Quantum enhanced optical sensing

Schäfermeier, Clemens; Andersen, Ulrik Lund; Huck, Alexander

Publication date:
2016

Document Version
Publisher's PDF, also known as Version of record

Quantum enhanced optical sensing

A thesis submitted in partial satisfaction of the requirements for the degree of
Doctor of Philosophy

to the
Department of Physics
Technical University of Denmark

by
Clemens Schäfermeier

under supervision of
Prof. Ulrik Lund Andersen

Quantum enhanced optical sensing

Supervisor: Prof. Ulrik Lund Andersen
Co-supervisor: Associate Prof. Alexander Huck

Examiners: Prof. David Vitali
Università di Camerino, Italy
Prof. Nicolas Treps
Université Pierre et Marie Curie, France
Associate Prof. Kirstine Berg-Sørensen
Technical University of Denmark

Submitted to the Technical University of Denmark on August 31st 2016

Technical University of Denmark

Acknowledgement

"All the rivers run into the sea; yet the sea is not full; unto the place from whence the rivers come, thither they return again."

—Ecclesiastes 1:7

It is owed to Ulrik L. Andersen that I had the chance of spending three exciting years in a group of lively and dedicated people. It is not only his overview and insight into quantum optics, but also his personal engagement that made our discussions very valuable to this work. The dedication and patience he shows towards science comes along with a remarkable attention to each of his group member's skills and thoughts – which is also reflected by the chance of pursuing and exploring different projects during my thesis.

An invaluable support was given by Tobias Gehring on all squeezed light experiments: From developing new ideas to performing electronic magic, working with him had always been a great pleasure.

Especially the learning about the nitrogen vacancy centre was guided by Alexander Huck: As my co-supervisor, he showed great patience and interest discussing ideas and projects, usually coming up with a new point of view.

During different projects, I had the pleasure to enjoy various collaborations:

Miroslav Ježek's experimental and theoretical expertise made the super resolution experiment succeed, such that I am very grateful for his contributions. Miroslav, working at the Palacký University, gave help always on the right time and never without cheerfulness.

Fortunately, I could spent three months in Fedor Jelezko's group at the University of Ulm to explore the silicon vacancy centre. Learning from his advice on daily lab work and deep knowledge of quantum physics rendered my stay in Ulm more than worthwhile. It was further Lachlan J. Rogers, Andrea B. Kurz, Alexander Kubanek, Andreas Dietrich and Kay D. Jahnke who greatly contributed to the progress of the study on silicon vacancy centres – and my personal well-being.

Working on optomechanics, I found myself in the fortunate position to collaborate with Warwick P. Bowen from the University of Queensland. The effort he put into our communication sped up the project, and it helped me to make a cold-start into a new topic less troublesome. Hugo Kerdoncuff introduced me into the details of delicate microtoroid experiments. I am very thankful for the help he provided by sharing his expertise with me.

With Jonas S. Neergaard-Nielsen, I discovered the art of shooting and analysing optical fibres. Especially his curiosity made him a regular partner for fruitful discussions – and a receiver of many questions. By his search for correct and clear explanations, Ulrich B. Hoff made a large contribution to write the optomechanics publication. Furthermore, I'd like to acknowledge: Amine Laghaout for the deep and fruitful discussions on quantum measurement and its philosophy, and Timur Iskhakov for lending a hand in the CV lab. The hours Christian Scheffmann Jacobsen and I spent together on various projects and construction works ended up in a lab with some distinguished features, capable of compensating a flooding, electric hazards

and broken lasers.

Hugo Kerdoncuff, Rasmus Jensen, Mads Boll, Ulrich B. Hoff, Haitham El-Ella and Sepehr Ahmadi spent their time on reading parts of this manuscript. Their effort helped me to focus the questions which guided my writing. Mikkel Maag Pedersen and Mads Boll gave vital support for polishing my Danish.

For their time spent with me on professional and personal discussions, I acknowledge especially Jørn Otto Bindslev Hansen and Haitham El-Ella for their sincerity.

For everyone who shared their questions with me, I am very glad about your trust and the chance you gave me to learn something new.

The group's laboratories had undergone a number of serious changes in the past three years, and a lot of time for planning and execution went into the change. I am grateful for everyone helping and supporting it, trying to prepare our labs for new exciting challenges. And, well, to transition from classical to quantum mechanics.

It is especially Kristian Hagsted Rasmussen and Ruben Grigoryan who contributed to important improvements in the clean room and the electronic workshop. Ruben has to be credited for his reliable support on electronics and for building useful (and good looking) lab helpers which shed a better light on our experiments. Kristian's knowledge of clean room techniques and chemistry prevented from major technical and personal issues.

To realise most of the mechanical devices, I am glad for Erik Hansen's and Poul Erik Andersen's work. With patience and accuracy they handled my drawings and requests, providing stable tools for our experiments. From printing periscopes to shields, Erik's service on the 3D printer meant a lot of new possibilities for me.

Tine Hougaard Klitmøller and Helle Wedel Wellejus were the most important colleagues when it came to reduce all kinds of (classical) uncertainties. Their help kept things actually running, and whenever no one else knew what to do, I knew whom to ask.

Finally, it is the group's spirit which was one of most important influences during my thesis. None of the attempted works progressed without various contributions, whether they were of personal or technical character.

Besides my colleagues, I was blessed with meeting some very remarkable persons: Thank you Michael Løiten Magnussen and Lenka Magnussen for sharing your thoughts with me, and for taking me to foreign countries. Rasmus Jensen, Mette Høy Jakobsen, Hugo Kerdoncuff and Mads Boll put me in the time of writing always on the right and joyful track. For climbing walls with me, I owe Mads a special β.

My brother Felix deserves a very special gratitude for keeping my wheels turning and constantly equipped with new tubes and tires. To my parents, whose support is more than I could have ask for.

You don't see the stars until it's really dark!

Abstract

The work in this thesis is embedded in the framework of quantum metrology and explores quantum effects in solid state emitters and optical sensing. Specifically, the thesis comprises studies on silicon vacancy centres in nanodiamonds, phase measurements and cavity optomechanics utilising optical squeezed states, and a theoretical study on quantum amplifiers.

Due to its similarity to single atoms, colour centres in diamond are ideal objects for exploring and exploiting quantum effects, because they are comparably easy to produce, probe and maintain. While nitrogen vacancy centres are the most renowned colour centres, we studied the silicon vacancy (SiV^-) centre. In bulk diamond it features strong zero-phonon-line emission and, at cryogenic temperatures, a linewidth of hundreds of MHz, but it displays a weak spin coherence in the order of ns. To suppress the relaxation process which limits the coherence time, we utilised SiV^- centres in nanodiamond. By means of confocal microscopy and resonant excitation at cryogenic temperatures, we measured linewidths in recently developed nanodiamond which were an order of magnitude smaller compared to previous studies on SiV^- nanodiamonds. Furthermore, we identified spectral diffusion as the main hindrance in extending spin coherence times. Overcoming this issue will provide a promising candidate as an emitter for quantum information.

Next, the question of how squeezed states of light can improve optical sensing was addressed. For this purpose, a squeezed light source was designed and built from scratch, which achieved a noise suppression of $-8\,\mathrm{dB}$ at an optical pump power of $40\,\mathrm{mW}$. The generated squeezed light was first used to demonstrate how Gaussian states and detection can beat the shot noise limit and Rayleigh criterion in phase measurements simultaneously. Compared to quantum phase measurements based on single photon states, this approach is inherently deterministic. In addition, the applied homodyne detection enables close-to-unity detection efficiencies and thereby outperforms single photon state strategies which rely on comparably inefficient or demanding detection techniques.

A second experiment combined squeezed light and feedback control to cool an optomechanical system. This proof-of-principle study is the first reported squeezing enhanced optomechanical cooling experiment. Despite losses of more than $50\,\%$ (a resulting noise suppression of $-2\,\mathrm{dB}$), the mechanical resonator was cooled from room temperature to $130\,\mathrm{K}$. This represents a $12\,\%$ improvement compared to the use of a coherent state protocol.

Finally, we theoretically investigated the fundamental properties of quantum amplifiers. Such devices can be used in information and sensing technology to amplify signals to overcome e.g. technical detection limitations. Amplified communication channels were characterised by applying the measure of mutual information I, as it offers strict bounds on the maximum achievable performance, which enabled a fair comparison between different applications scenarios. As a result, we identified two peculiar configurations: A configuration where amplification does not affect I, and a configuration where quantum correlations do not always lead to an enhanced I.

Keywords Quantum metrology, Colour centres, Diamond optics, Squeezed states, Cavity optomechanics, Interferometry, Quantum information

Dansk resumé

På baggrund af de sidste fem årtiers opdagelser, er vejen til kvantemekanisk forbedrede optiske sensorer ikke kun mere tilgængelig, men også realiserbar for real-life applikationer. Grundlaget for denne udvikling er studiet af interaktioner, især dem af kohærent natur, mellem bestanddele i et meget grundlæggende system, bestående af stof på den ene side og lys på den anden. Denne afhandling har til formål at benytte kvanteeffekter til at studere begge aspekter.

Til studiet af kvanteeffekter i stofbaserede sensingteknikker, er de spektrale egenskaber af vakancecentre i diamant blevet undersøgt. På grund af deres lighed med et enkelt atom, er vakancecentre ideelle objekter til at udforske og udnytte kvanteeffekter, da de er relativt nemme at producere, at måle på og at vedligeholde. Vakancecentre kommer naturligt sammen med et allerede interessant miljø: Blandt andet kernespin af omkringliggende atomer og felter produceret af overfladeladninger, som centret interagerer med. Mens nitrogen-vakancecentre, studeredet siden 1997 som en isoleret optisk emitter, er de mest velkendte vakancecentre, koncentrerede vi undersøgelsen omkring silicium-vakancecentre. Deres optiske egenskaber er siden 2006 blevet undersøgt på en lignende måde som nitrogen-vakancecentret, og det anses for at være en lovende kandidat til applikationer såsom enkelt-fotonkilder. For at udvikle forståelsen af henfaldsprocesser i silicium-vakancecentre og udforske potentielle anvendelser, er de spektrale egenskaber af enkelte silicium-vakancecentre i nanodiamanter blevet undersøgt. Konkret har vi forsøgt at formindske dekohærens af dets elektroniske spin. Det var muligt at opnå dette, dog karakteriserede vi skadelige effekter.

Dernæst blev det undersøgt hvordan kvantemekaniske tilstande af lys kan forbedre optiske måleteknikker. Til det formål blev en lyskilde af klemte tilstande designet og bygget. I modsætning til en almindelig laserkilde, har en sådan kilde støjegenskaber der ikke kan opnås ved nogen klassisk metode. Dette skyldes at korrelationer på feltexcitationsniveau gør det muligt at overvinde almindelige støjgrænser. Denne egenskab blev anvendt eksperimentelt til at måle et faseskift i et interferometer med højere opløsning og følsomhed. Endvidere blev den mekaniske vibration af en mikroskopisk ringkerne undersøgt mere præcist ved hjælp af klemt lys. Oplysningerne indhentet om mikro-toroidens bevægelse blev til sidst brugt til at styre den med en feedback-mekanisme til effektivt at køle sin tilstand.

Endelig har vi teoretisk undersøgt fundamentale egenskaber af kvanteforstærkere. Sådanne komponenter kan anvendes i informations- og måleteknologi til at forstærke signaler, eksempelvis for at overvinde tekniske begrænsninger i detektoren. Vi anvendte mutual information til karakterisering, fordi det giver strenge grænser for den maksimale opnåelige ydeevne. Dette muliggjorde en rimelig sammenligning mellem forskellige scenarier. Som følge heraf er to ejendommelige tilfælde blevet identificeret der tilbyder fordele i forhold til almindelige tilgange.

Abbreviations, acronyms and symbols

AC / DC	Alternating / direct current
APD	Avalanche photodiode
AOM	Acousto-optic modulator
BS	Beam splitter or beam sampler
c.c.	Complex conjugate
D	Photodetector
EOM	Electro-optic modulator
FEM	Finite element method
FFM	Fundamental flexural mode
FI / FR	Faraday isolator / Faraday rotator
FWHM	Full width half maximum
h.c.	Hermitian conjugate
HD	Homodyne detector
HWHM	Half width half maximum
LO	Local oscillator
P	Piezo element
PBS	Polarising beam splitter
PL(E)	Photoluminescence (excitation)
PSD	Power spectral density
SNR	Signal-to-noise ratio
SN(L/U)	Shot noise (limit / unit)
ZPL	Zero-phonon-line

e	Euler's number, i.e. the outcome of $\sum_{n=0}^{\infty} \frac{1}{n!}$.
$\imath$	The imaginary unit defined by $i^2 = -1$.
π	A quarter of $\sum_{n=0}^{\infty} \frac{(-1)^n}{2n+1}$.
$\hbar$	Planck's constant divided by 2π. In SI units, $\hbar \approx 1.055 \cdot 10^{-34}\,\mathrm{J\,s}$.
k_B	Boltzmann constant. In SI units, $k_B \approx 1.380 \cdot 10^{-23}\,\mathrm{J\,K^{-1}}$.
ϵ_0	The vacuum permittivity. Its unit is $\frac{\mathrm{A^2 s^4}}{\mathrm{kg\,m^3}}$.
μ_0	The vacuum permeability. Its unit is $\frac{\mathrm{V\,s}}{\mathrm{A\,m}}$.
c_0	The speed of light in vacuum, equal to $299\,792\,458\,\mathrm{m\,s^{-1}}$.

$\star^\dagger$	The adjoint, also termed as Hermitian conjugate, of $\star$.
$\star^*$	The complex conjugate of $\star$.

$\hat{\star}$	An operator.
$\boldsymbol{\star}$	A vector quantity.
$\lvert\star\rvert$	The absolute value of $\star$.
$\lVert\star\rVert$	The norm of $\star$, which is to be considered as a map to a real-valued scalar.
$\hat{\boldsymbol{1}}$	A general representation of the identity, to be read as an operator or a matrix.
$\lvert\star\rangle$	A ket vector, which is a representation of a pure state and an element of $\mathcal{H}$, a Hilbert space.
$\langle\star\rvert$	A bra vector, an element of the dual vector space of a Hilbert space.
$\langle\star\rvert\lvert{}^{\star}_{\star}\rangle$	An inner product of a ket and a bra vector.
$\lvert\star\rangle\langle{}^{\star}_{\star}\rvert$	An outer or tensor product of a ket and a bra vector.
$\lvert\star, {}^{\star}_{\star}\rangle$	A composite ket vector. It is an element of the Hilbert space formed by a tensor product of the underlying Hilbert spaces, e.g. suppose $\lvert\star\rangle \in \mathcal{H}_1,\ \lvert{}^{\star}_{\star}\rangle \in \mathcal{H}_2$, then $\lvert\star, {}^{\star}_{\star}\rangle \in \mathcal{H}_1 \otimes \mathcal{H}_2$.
$\langle{}^{\star}_{\star}\rvert\hat{\star}\rvert{}^{\star}_{\star}\rangle$	The expectation value of an operator's ($\hat{\star}$) action on a state $\lvert{}^{\star}_{\star}\rangle$.
$\langle\hat{\star}\rangle$	Same as $\langle{}^{\star}_{\star}\rvert\hat{\star}\rvert{}^{\star}_{\star}\rangle$, used if the context makes the choice of $\lvert{}^{\star}_{\star}\rangle$ obvious.
$\mathrm{p}(\star\rvert{}^{\star}_{\star})$	The probability to measure an eigenvalue $\star$ of its operator $\hat{\star}$ when applied on a state $\lvert{}^{\star}_{\star}\rangle$. If there is no ambiguity about $\lvert{}^{\star}_{\star}\rangle$, it reads $\mathrm{p}(\star)$.
$\mathrm{Var}(\hat{\star})$	The variance of an operator's expectation value when applied on some state. As long as the context is clear, the state will be omitted. Otherwise it reads: $\mathrm{Var}(\hat{\star}, {}^{\star}_{\star})$.
$\sigma(\hat{\star})$	The standard deviation of an operator's expectation value when applied on some state. Like for the variance, the state will only be written out as $\sigma(\hat{\star}, {}^{\star}_{\star})$ if the context is ambiguous.
$\mathrm{tr}(\hat{\star})$	The trace of an operator.
$\left[\hat{\star}, {}^{\hat{\star}}_{\star}\right]$	The commutator of two operators.
$\left\{\hat{\star}, {}^{\hat{\star}}_{\star}\right\}$	The anti-commutator of two operators.
$\hat{X}, \hat{Y}$	The dimensionless quadrature operators. Used for phase space representations and can be probed via homodyne techniques.
$\hat{a}, \hat{a}^{\dagger}$	An annihilation and a creation operator – or just the 'ladder operators'.
$\hat{n}$	A number operator. Also used as a generator for a phase shift.
$\hat{H}$	A Hamilton operator. It is the generator for time evolution.
$\hat{D}$	A displacement operator, producing $\hat{D}(\alpha)\lvert 0\rangle = \lvert\alpha\rangle$.
$\hat{S}$	A squeezing operator, producing $\hat{S}(\xi)\lvert 0\rangle = \lvert\xi\rangle$.
$\lvert n\rangle$	A number state, i.e. an eigenstate of the number operator. Also referred to as Fock state.
$\lvert\alpha\rangle$	A coherent state resembling a classical-like electromagnetic field. It is an eigenstate of the annihilation operator.
$\lvert\xi\rangle$	A squeezed state exhibiting, compared to $\lvert\alpha\rangle$, a reduction in the variance of a certain quadrature.

$\bar{n}$	The average photon number of a Gaussian state.
η	Loss or efficiency.
ν	A frequency, given in units of Hz.
ω	An angular frequency, equalling $2\pi\nu$.
$\mathcal{Q}$	Quality factor of an oscillator, defined as the ratio between the resonance frequency to bandwidth.
$\mathcal{V}$	Visibility of interference fringes, defined as $(v_{\max} - v_{\min})/(v_{\max} + v_{\min})$, where $v_{\max}$ and $v_{\min}$ is the maximum and minimum of the oscillations.
V_s, V_a	The degree of squeezing and anti-squeezing in units of dB.
W	A Wigner function.

Selected chapter-specific symbols

Chapter 2

$\hat{\mathcal{L}}$	A Lindblad superoperator used to describe dissipative effects in an equation of motion. The notion 'superoperator' is used to distinguish it from other operators which are not acting on operators.
${}^2E_g$	The ground state of the centre with an even wavefunction and a two-fold orbital- and spin degeneracy. The orbital degeneracy is lifted by virtue of spin-orbit coupling.
${}^2E_u$	The first excited state of the centre with an odd wavefunction. Its other features are similar to ${}^2E_g$.
T_1	The energy decay or relaxation time.
T_2	The total decoherence time.
T_2^*	The pure dephasing time.
γ	A decay rate.

Chapter 3

σ	The sensitivity of a phase measurements. As it is derived from the variance, a lower value of σ means a better sensitivity.
F	The Fisher information.
Φ	An estimator of the phase shift parameter. We consider unbiased estimators, such that the estimated phase parameter approaches asymptotically the true phase parameter.
H	The quantum Fisher information.
$\hat{\Pi}_d$	The operator describing the binning procedure. Also referred to as dichotomy operator.

Chapter 4

C	The optomechanical cooperativity which compares optomechanical coupling to optical and mechanical losses. An additional subscript 'eff' denotes the effective optomechanical cooperativity.
$\hat{Q}, \hat{P}$	The dimensionless "mechanical" position and momentum operator.
$\hat{q}, \hat{p}$	The position and momentum operator in SI units.
κ	An optical loss rate given in angular frequencies.
Γ_m	The mechanical loss rate given in angular frequencies.

S A power spectral density.

Chapter 5

g Gain of the amplifier. In case of no gain, $g = 1$.

I Mutual information, given in bits per channel use.

Graphs and uncertainties

The axes of graphs are labelled like a/b, where a is the quantity which is plotted and b is the dimension of a. Thus $b = 1$ when a is dimensionless.

Uncertainties of measurement results are written as $1.23(40)$, which means that the mantissa's first digit is known within ± 4.

Contents

1 | Introduction

What is the motivation to enhance sensing techniques? To answer this question, we will outline its development, that is the development of metrology.

Metrology is the science of measurement, and thus a fundamental principle of every scientific experiment. The modern approach to it was probably formulated by N. de Condorcet during the French revolution in 1791: According to de Condorcet, the meter is an "unité qui dans sa détermination, ne renfermait rien ni d'arbitraire ni de particulier à la situation d'aucun peuple sur le globe" [87], which can be translated as an 'unit determined with neither an arbitrary nor a specific dependence on the situation of any person on the planet'. It is very likely fair to state that, from the perspective of people during the French revolution, the aspect of local as well as the s o c i a l independence in this definition were of similar importance. We might conclude that metrological studies seek to define, if necessary, and refine, if possible, units and measurement techniques to promote a common understanding of science and the phenomena it tries to describes.

Focussing on optical metrology, the development of the microscope and telescope can be said to be major discoveries in the 17th century [133]. Since then, the microscope was popularised, first by biologists and then by scientists interested in the microscopic world of animate and inanimate objects.

Hand in hand with the popularisation, much effort has been taken to explore the boundaries in resolution, shading light on smaller and smaller structures of the world we inhabit.

Up to the present day, a multitude of approaches surpassing the long-standing fundamental limit of resolution, namely the diffraction limit confirmed experimentally by Ernst Abbe in 1883 [1], have been devised. The ongoing journey was just highlighted by the Nobel Prize 2014 in chemistry for scaling up the resolution by combining the knowledge of the specimen's energetic states with two cleverly engineered laser beams, enabling the detection of particles of only a few tens of nanometres. This development usually comes under the heading of 'super resolution', which is also a technique studied during this thesis.

Many of the so-far applied techniques enabling super resolution employ classical states of electromagnetic radiation, that is: The radiation employed in these techniques may have specially engineered spatial- or temporal features. However the description of the very constituents of this radiation – the photons – requires an at most semiclassical model. Thus, the additional degrees of freedom quantum mechanics offer haven't been fully utilised. Exploiting these additional degrees leads to form the electromagnetic field itself to a state that is optimal for its purpose. One of the advantages of quantum enhanced techniques is that the amount of photons used for sensing is literally "a handful", such that the influence on the (possibly animate) specimen is inherently decreased over classical methods.

Another path towards quantum enhanced sensing focusses on the properties of the p a r t i c l e s emitting radiation. In 1952, E. Schrödinger argued that "we *never* experiment with just *one* electron or atom or (small) molecule" [252]. Already thought experiments based on

such an individual control would entail "ridiculous consequences" [252]. Schrödinger's prediction turned out to be false, at least when taken literally. Outstanding experimental efforts have enabled the extraction and control of individual atoms and molecules, and this to an extend that atom interferometry became a common means throughout metrology and is, in some cases, close to field application [97, 271]. However, when examining, for example, the properties of single photon states such as their phase or field amplitude, his statement is everything else than far fetched[1].

A major challenge in the application of single atoms remains the need to acquire and control them experimentally. What is required is some sort of environment that encapsulates that emitter, potentially in a way that is convenient to maintain. It turned out that colour centres in diamond pose a solution for this: Foreign atoms, such as nitrogen or silicon, combined with vacancies in the crystal lattice of diamond create defects called 'colour centres' or 'vacancy centres' which resemble a single atom. Such vacancy centres occur naturally in diamond, but can also be implanted. This allows for a creation of single optical emitters to a precision of a few nanometres [253].

So to answer – or in the attempt of – the introductory question: Improved sensing techniques have ever since shed new light on phenomena which were either disputed or yet-to-be discovered. And, following-up on de Condorcet, it led to conceptual changes in science. Even further, de Condorcet's motive of unification still applies – no longer on social aspects, but on the aspect of a growing separation in scientific research.

The progress in the mentioned fields gave us the opportunity to study and advance techniques of optical sensing from a broad point of view. Considering that the topics of this thesis can be seen as individual projects, it demonstrates that technological and scientific progress allow for both starting and conducting experiments in fields which were individually hard to access experimentally a few years ago.

1.1 Thesis structure

The following chapters are presented in a similar and mostly self-contained way, such that a reader may address each chapter individually without following cross-references. Each chapter commences with a brief introduction and motivation before the main work is presented. If required, a mathematical framework introduces the most important concepts applied for the analysis. A summary and outlook concludes the chapter.

In the appendix, the reader will find a summary of some of the tools developed during this thesis. The selection was based on the importance of those developments for a successful experimental operation.

The thesis is addressed to a readership familiar with basic concepts of quantum mechanics, classical and quantum optics. Foundation material treating these topics is available in a large number of thesis, books and papers. References to such material are given throughout. To provide a common ground for definitions used in later chapters, a mathematical description of the relevant concepts of quantum optics is outlined next. As detailed derivations can be found in the cited material, the theoretical parts are focussed on concepts and applications. Some passages of the next section can be found in a more elaborate form elsewhere [246].

[1] A rather strict point-of-view took W. E. Lamb, Jr. on the use of the word 'photon'. From his view, "there is no such thing as a photon. Only a comedy of errors and historical accidents led to its popularity among physicists and optical scientists" [168].

1.2 A brief mathematical description of light

To describe light and its properties by classical means, Maxwell's equations have to be solved [34]. A common approach to achieve that is to consider the vector potential $\boldsymbol{\mathcal{A}}$ inside a perfectly conducting cube of volume V. In a superposition of plane waves, one can find [114]:

$$\boldsymbol{\mathcal{A}} = \frac{1}{2}\sum_j \sum_{d=1}^{2} \Big(A_{j,d} \exp\Big(\imath\big(\boldsymbol{k}_j \boldsymbol{x} - \omega_j t\big)\Big) + \text{c.c.}\Big)\boldsymbol{e}_{j,d}, \quad \text{with} \quad [A] = \frac{\text{kg m}}{\text{s}^2\text{A}}, \tag{1.1}$$

where $A_{j,d}$ is the j-th complex amplitude plane of a wave in one of the two directions of polarisation $\boldsymbol{e}_{j,d} \in \mathbb{R}^3$, with $\boldsymbol{e}_{j,1} \times \boldsymbol{e}_{j,2} = \boldsymbol{k}_j/|\boldsymbol{k}_j|$. While $\boldsymbol{k}$ denotes the wave vector, $\boldsymbol{x}$ refers to a point in space. $A_{j,d}$ must be complex to provide for a local phase difference. The factor of $1/2$ just cancels the factor of two due to the complex conjugate (c.c.).

Given the condition of a vanishing electric potential one may apply $\boldsymbol{E} = -\frac{\partial}{\partial t}\boldsymbol{\mathcal{A}}$, whereby the electric field[2] is readily derived as

$$\boldsymbol{E} = \frac{\imath}{2}\sum_j \sum_{d=1}^{2} \Big(A_{j,d} \exp\Big(\imath\big(\boldsymbol{k}_j \boldsymbol{x} - \omega_j t\big)\Big) - \text{c.c.}\Big)\omega_j \boldsymbol{e}_{j,d}. \tag{1.2}$$

While the factor ω_j introduces the proper physical unit of the electric field amplitude, the global phase[3] of $\imath$ makes the electric field to be real. One may also define the real quantities

$$C = \frac{1}{\sqrt{2}}(A + A^*) \quad \text{and} \quad S = \frac{\imath}{\sqrt{2}}(A - A^*), \tag{1.3}$$

which are identified as the classical field quadrature. Omitting the summation over j in equation (1.2), a single-mode plane wave reads

$$\boldsymbol{E}_j = \frac{\imath}{2}\sum_{d=1}^{2} \big(A_d \exp\big(\imath(\boldsymbol{k}\boldsymbol{x} - \omega t)\big) - \text{c.c.}\big)\omega \boldsymbol{e}_d \tag{1.4a}$$

$$\equiv \frac{1}{\sqrt{2}}\sum_{d=1}^{2} \big(C_d \cos(\boldsymbol{k}\boldsymbol{x} - \omega t) - S_d \sin(\boldsymbol{k}\boldsymbol{x} - \omega t)\big)\omega \boldsymbol{e}_d. \tag{1.4b}$$

The Hamiltonian, applied to calculate the time evolution of the electromagnetic field, can be rewritten in terms of A [114]:

$$H = \frac{1}{2}\epsilon_0 V \sum_j \sum_{d=1}^{2} \omega_j^2 A_{j,d} A_{j,d}^*. \tag{1.5}$$

This compact form emphasises that, first, a global phase term will always cancel out and, second, that the complex field amplitude describes (under the given conditions) the electromagnetic field entirely. To complete the discussion and compare the classical with the quantum mechanical formulation, C and S are substituted into the latter Hamiltonian:

$$H = \frac{1}{4}\epsilon_0 V \sum_j \sum_{d=1}^{2} \omega_j^2 \big(C_{j,d}^2 + S_{j,d}^2 \big). \tag{1.6}$$

[2] The magnetic part $\boldsymbol{B} = \nabla \times \boldsymbol{\mathcal{A}}$ of the radiation field will be neglected throughout this work, since, first, most coupling to the matter is through the electric field [114], second, the total radiation energy can be readily written in terms of A, and, finally, in vacuum it is just weaker by $1/c_0$ than the electric part.

[3] See Gerry and Knight for an elaborate discussion of the optical phase [114, pp. 33]. Mlak and Słociński also treat the quantum phase operator in a concise and more technical way [198].

1.2.1 Quantisation of the electromagnetic field

By virtue of the correspondence principle [220], equation (1.6) identifies the quantities C and S as a pair of canonical variables to quantise the electromagnetic field. Therefore, besides the fact that the field amplitude A as well as the fields themselves become operators, all characteristics of a quantum harmonic oscillator [86] apply equally to the electromagnetic field. The operators correspond to their classical quantities according to

$$A \to \hat{a}\gamma, \quad A^* \to \hat{a}^\dagger\gamma, \tag{1.7a}$$

and equivalently for

$$C \to \hat{X}\gamma, \quad S \to \hat{Y}\gamma. \tag{1.7b}$$

with $\gamma = \sqrt{2\hbar/(\epsilon_0 V\omega)}$. We will refer to $\hat{X}$ as the amplitude- and $\hat{Y}$ as the phase quadrature. This choice is arbitrary, but follows the usual convention.

Most important, since it represents Heisenberg's uncertainty principle, is the canonical commutation relation [33]. For the introduced operators, it reads

$$\left[\hat{a}, \hat{a}^\dagger\right] = \hat{\boldsymbol{1}}, \tag{1.8a}$$

$$\left[\hat{X}, \hat{Y}\right] = \imath\hat{\boldsymbol{1}}, \tag{1.8b}$$

whereas $\hat{\boldsymbol{1}}$ denotes the identity operator. In further discussions, we will make an explicit use of the latter only if necessary.

The quantised single-mode plane wave from equation (1.4) reads[4]

$$\widehat{\boldsymbol{E}}_j = \imath\sqrt{\frac{\hbar\omega}{2\epsilon_0 V}}\sum_{d=1}^{2}\Big(\hat{a}_d \exp\big(\imath(\boldsymbol{k}\boldsymbol{x} - \omega t)\big) - \text{h.c.}\Big)\boldsymbol{e}_d \tag{1.9a}$$

$$\equiv \sqrt{\frac{\hbar\omega}{\epsilon_0 V}}\sum_{d=1}^{2}\Big(\hat{X}_d \cos(\boldsymbol{k}\boldsymbol{x} - \omega t) - \hat{Y}_d \sin(\boldsymbol{k}\boldsymbol{x} - \omega t)\Big)\boldsymbol{e}_d, \tag{1.9b}$$

where the Hermitian conjugate (h.c.) is required to maintain a Hermitian, and thus observable, field operator. This plane wave model is a mathematical useful, but rather delicate approximation: Outside the model of a perfectly conducting cube of volume V, or rather in a "free space" cube with $\lim_{V\to\infty}$, such a single-mode plane wave would show no lessening and thereby consume an infinite amount of energy. Thus, a self-consistent model of light is always expected to be a superposition like equation (1.9a). In the experiment, a single-mode plane wave is a suitable model as long as the detection of light is confined time- and space-wise. More precisely, the measurement interval should always be smaller than the change of the radiation field.

In relation to the measurement details, there is also the question of when it is allowed to treat the radiation field as classical. Berestetskii et al. [26, eq. (5.2)] obtain the inequality

$$\|\boldsymbol{E}\|^2 \gg \frac{\hbar c_0}{(c_0\tau)^2}, \tag{1.10}$$

where τ is the averaging time of the measurement. The field can be treated as classical if the inequality is true. From this, it follows that – for a valid classical treatment – a weak field has to be averaged over a longer time compared to a strong field. However, "variable fields [that is any variation in addition of the phase of a single-mode plane wave], if sufficiently weak, can never be quasi-classical" [26, p. 15].

[4] For a time-dependent evaluation, one can readily regard $\hat{a}$, $\hat{a}^\dagger$ as operators in the Heisenberg picture, i.e. extract $\imath\omega t$ from the exponential function and recast it like $\hat{a}(t) = \hat{a}(0)\exp(-\imath\omega t)$.

Quantum mechanical basis states of light

Essentially, there are two different sets of quantum mechanical basis states for the description of light or any other excitation of a harmonic oscillator:

Fock states One of them is the number state, or Fock state, basis. A Fock state can be compared to a system containing exactly n photons, i.e. n quanta of energy. Since $\hat{a}^\dagger\hat{a}|n\rangle = \hat{n}|n\rangle = n|n\rangle, n \in \mathbb{N}$ [86], the expectation value of a "photon-counting experiment" equals n and the variance is zero. Experiments, especially in quantum information processing, based on Fock states are therefore said to be based on discrete variables, simply because the outcome of a detection takes a number from a discrete set.

A special state is $|0\rangle$, referred to as the vacuum state. According to the Hamiltonian[5]

$$\widehat{H} = \sum_j \hbar\omega_j \left(\hat{n}_j + \frac{1}{2}\right), \tag{1.11}$$

the energy eigenvalue of the j-th mode is $1/2\hbar\omega_j$. The expectation value of the quadrature operators in vacuum is $\langle 0|\hat{X}_j|0\rangle = \frac{1}{\sqrt{2}}\langle 0|(\hat{a} + \hat{a}^\dagger)_j|0\rangle = 0$, which holds equally for $\hat{Y}_j$. The variance yields

$$\mathrm{Var}\big(\hat{X}_j, 0\big) = \langle 0|\hat{X}_j^2|0\rangle - \langle 0|\hat{X}_j|0\rangle^2 = \mathrm{Var}\big(\hat{Y}_j, 0\big) = \frac{1}{2}, \tag{1.12}$$

hence the signal of a quadrature measurement shows fluctuations even if the incoming field is (on average) zero: This signal characterises the shot noise. Technically, such a measurement can be performed via a homodyne detection [16, 114] which will be explained later.

The variance of a Fock state scales proportional with its occupation number: In a single mode scenario, hence dropping j, $\mathrm{Var}\big(\hat{X}, n\big) = \langle n|\hat{n} + \frac{1}{2}|n\rangle = n + \frac{1}{2}$. This is not true for the expectation value, that is $\forall n : \langle n|\hat{X}|n\rangle = 0$. The latter suggests that there is no mean electromagnetic field. A laser beam thought of a number state is hence a rather unphysical picture.

Coherent states To resemble the electromagnetic field of a laser beam in a more realistic way, another kind of basis states is used: The coherent states, deemed to be the "'most classical' quantum states" [114, p. 43]. A coherent state is defined as an eigenstate of the annihilation operator:

$$\hat{a}|\alpha\rangle = \alpha|\alpha\rangle, \quad \text{likewise} \quad \langle\alpha|\hat{a}^\dagger = \alpha^*\langle\alpha|, \tag{1.13}$$

where $\alpha \in \mathbb{C}$ is referred to as the coherent amplitude. This definition is quite peculiar, as it implies that even a repeated annihilation of photons will not change the state. A consequence of this can be seen when evaluating the moments of $\hat{X}$ and $\hat{Y}$. From the latter equation, it follows

$$\langle\alpha|\hat{n}|\alpha\rangle = |\alpha|^2 = \bar{n}, \tag{1.14}$$

thus $|\alpha|^2$ is the average number of photons of a coherent state.

Due to the fact that the number states form a complete set, a coherent state may be expanded in terms of $|n\rangle$. The linear combination reads [117]

$$|\alpha\rangle = \mathrm{e}^{-\frac{1}{2}|\alpha|^2} \sum_{n=0}^{\infty} \frac{\alpha^n}{\sqrt{n!}}|n\rangle. \tag{1.15}$$

[5] The Hamiltonian may be identified, via the correspondence principle, as the quantum mechanical formulation of equation (1.5). For an ease of notation, we include the summation over the polarisation modes d in j.

From this equation, the probability to find a certain number of photons in a coherent state is

$$\mathrm{p}(n|\alpha) = \mathrm{e}^{-|\alpha|^2}\,\frac{|\alpha|^{2n}}{n!}. \tag{1.16}$$

This is a Poisson distribution with a fractional uncertainty in the photon number of

$$\frac{\sigma(\hat{n})}{|\alpha|^2} = \frac{1}{|\alpha|} = \frac{1}{\sqrt{\bar{n}}}. \tag{1.17}$$

Thus, a strong laser beam shows less relative fluctuations in the photon number than a weak beam. From this point of view, the classical limit is $\lim_{|\alpha|^2\to\infty}$, which is in agreement with equation (1.10). Since a beam of 1 mW and a wavelength of 800 nm contains about 10^{15} photons per second, the fractional uncertainty in the photon number is ca. $3.2\cdot10^{-6}\,\%$. The fact that $\mathrm{p}(n)$ is a Poisson distribution originates from definition (1.13): A process that obeys such a distribution describes events which are uncorrelated [44]. This explains the "peculiar" behaviour of $|\alpha\rangle$ when a photon is removed from it.

Regarding the quadrature operators, one finds that the expectation values

$$\big\langle\alpha\big|\hat{X}\big|\alpha\big\rangle = \frac{1}{\sqrt{2}}(\alpha+\alpha^*) \quad\text{and}\quad \big\langle\alpha\big|\hat{Y}\big|\alpha\big\rangle = \frac{\imath}{\sqrt{2}}(\alpha-\alpha^*). \tag{1.18a}$$

So they are proportional to the real and imaginary part of the coherent amplitude. Moreover, by factoring the oscillating term from equation (1.9b) into the operators, the expectation values read

$$\sqrt{2}\Re(\alpha)\cos\big(\boldsymbol{kx}-\omega t\big) \quad\text{and}\quad -\sqrt{2}\Im(\alpha)\sin\big(\boldsymbol{kx}-\omega t\big), \tag{1.18b}$$

emphasising the classical notion of light as a wave. The variance of the quadratures result to

$$\mathrm{Var}\big(\hat{X},\alpha\big) = \frac{1}{2}. \tag{1.19}$$

The standard deviation of $1/\sqrt{2}$ (which changes amongst literature) also defines a 'shot noise unit'.

By virtue of the general uncertainty relation for two observables $\hat{O}_1, \hat{O}_2$ [231]

$$\sigma\big(\hat{O}_1\big)\,\sigma\big(\hat{O}_2\big) \geq \frac{1}{2}\Big|\big\langle\psi\big|\big[\hat{O}_1,\hat{O}_2\big]\big|\psi\big\rangle\Big|, \tag{1.20}$$

a simultaneous measurement of the quadratures obeys the relation

$$\sigma\big(\hat{X}\big)\,\sigma\big(\hat{Y}\big) \geq \frac{1}{4}. \tag{1.21}$$

Coherent states therefore always show the minimum fluctuations, independent from the number of photons in that state.

The probability distribution over the variable X can be calculated via[6]

$$\langle X|\alpha\rangle = \frac{1}{\sqrt[4]{\pi}}\exp\!\left(-\frac{1}{2}\Big(\alpha^2+|\alpha|^2+X^2-\alpha X/\sqrt{2}\Big)\right), \quad\text{thus} \tag{1.22a}$$

$$\mathrm{p}(X|\alpha) = \frac{1}{\sqrt{\pi}}\exp\Big(-\big(X-\underbrace{\tfrac{1}{\sqrt{2}}(\alpha+\alpha^*)}_{=\langle\alpha|\hat{X}|\alpha\rangle}\big)^2\Big), \tag{1.22b}$$

[6] The distribution can be calculated in various ways: Compare, e.g., Walls and Milburn [280, p. 42] with Bachor and Ralph [16, p. 71], but the latter one with minding that equations (4.3.9) and (4.3.10) have a wrong scaling in relation to their definitions.

with $X \in \mathbb{R}$ being an eigenvalue of $\hat{X}$. Probing an arbitrary quadrature of a coherent state many times, one should expect to find a normal distribution as the outcome. Its average value equals the mean number of photons in that state, while the standard deviation characterises the quantum shot noise [16]. Due to the characteristics of a normal distribution, only the first and second moment have to be known to completely describe $|\alpha\rangle$.

As we can see, apart from the first moment, a vacuum and a coherent state have equal moments. A coherent state can be thus seen as a displaced vacuum state. The unitary displacement operator [114, 280]

$$\hat{D}(\alpha) = \exp(\alpha\hat{a}^\dagger - \text{h.c.}) \tag{1.23}$$

is thus, in analogy to $\hat{a}^\dagger$ for a Fock state, the creation operator of a coherent state.

1.2.2 Squeezed states

A coherent state exhibits an equal uncertainty in both quadratures. However, to be conform with quantum mechanics, a state just has to obey relation (1.21). That is $\sigma(\hat{X})$ maybe found to be much smaller than a shot noise unit, as long as the uncertainty in the other quadrature is large enough. The area in phase space "covered" by a coherent state is circular, if one circumscribes it by $\sigma(\hat{X})$ and $\sigma(\hat{Y})$, such that a way to produce – at least conceptually – a state with less uncertainty along one quadrature is simply by squeezing the circle to an ellipse. A state following such a description is thus termed a squeezed state. When centred about the origin of phase space, it is a squeezed vacuum state. Usually, the axes in a phase space representation are related to the amplitude and phase of the optical field, such that the terms 'phase squeezed' and 'amplitude squeezed' are used to specify the squeezing direction.

The unitary operator producing a squeezed state is given by [114, 280]

$$\hat{S}(\xi) = \exp\Big(-\frac{1}{2}\big(\xi(\hat{a}^\dagger)^2 - \text{h.c.}\big)\Big), \tag{1.24}$$

where $\xi \in \mathbb{C}$ is the 'squeeze' parameter. ξ is commonly expanded as $\xi = r\exp(\imath\varphi)$ with $r, \varphi \in \mathbb{R}$. Compared to $\hat{D}$, its generator is proportional to the second power of $\hat{a}^\dagger$, which gives a hint about two properties: First, that its phase space distribution c a n be elliptic, i.e. multivariate. Second, that such a state has a special photon number distribution.

The latter can be directly seen when evaluating a squeezed vacuum state in the Fock basis [114, 280]:

$$\hat{S}(\xi)|0\rangle = |\xi\rangle = \frac{1}{\sqrt{\cosh(r)}} \sum_{n=0}^{\infty} (-1)^n \,\mathrm{e}^{\imath n\varphi}\, \frac{\sqrt{(2n)!}}{2^n n!} \tanh(r)^n |2n\rangle, \tag{1.25}$$

that is, a squeezed vacuum state only comes in twins, quadruplets, ..., of photons. Even though called v a c u u m squeezed state, it actually contains photons. Thus, to squeeze a vacuum state (or a coherent state in general) requires energy. To obtain the expectation value of the photon number and other properties such as the quadrature variances, the following relations can be applied [114, 280]:

$$\hat{S}^\dagger\hat{a}\hat{S} = \cosh(r)\hat{a} - \sinh(r)\,\mathrm{e}^{\imath\varphi}\,\hat{a}^\dagger, \quad \hat{S}^\dagger\hat{a}^\dagger\hat{S} = \cosh(r)\hat{a}^\dagger - \sinh(r)\,\mathrm{e}^{-\imath\varphi}\,\hat{a}. \tag{1.26}$$

An expansion in the form of $\hat{a}|\xi\rangle = \hat{S}\hat{S}^\dagger\hat{a}\hat{S}|0\rangle$ helps to find

$$\langle\xi|\hat{n}|\xi\rangle = \sinh(r)^2, \tag{1.27a}$$

$$\mathrm{Var}(\hat{n}) = \sinh(r)^2\cosh(r)^2 = \langle\hat{n}\rangle + \langle\hat{n}\rangle^2 \tag{1.27b}$$

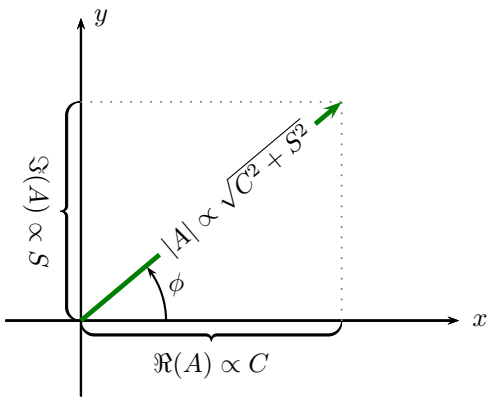

(a) Classical field

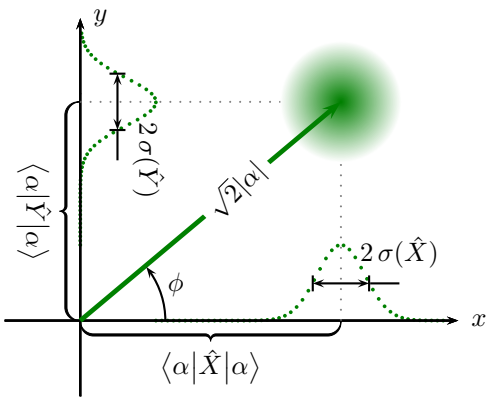

(b) Coherent state

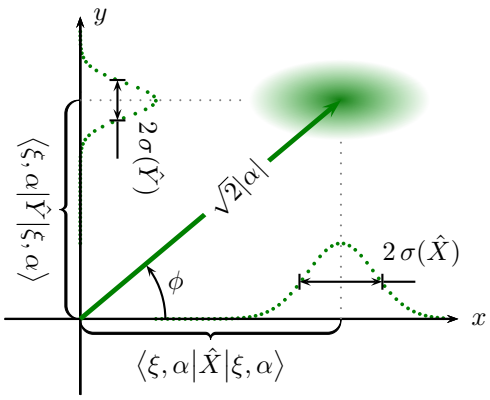

(c) Squeezed and displaced state

Figure 1.0: Phase space representation of three different states of light. In the simplest case, a time evolution corresponds to a rotation about the origin. (a) A diagram of the classical field quadratures. Amplitude and phase are perfectly determined, that is: Nothing prevents from telling the position of the pointer to an arbitrary precision. (b) A coherent state in phase space calculated via the Wigner function. Some authors apply the term "ball and stick diagram" here [37]. The area of uncertainty is equally distributed about the mean. Against the quadrature axes, a marginal distribution was plotted. Unlike for the classical field, the uncertainty of a coherent state is an inherent feature and not due to a limited measurement precision. (c) A squeezed and displaced state, created by $\hat{D}\hat{S}|0\rangle$. The area of uncertainty turned into an ellipse and shows more fluctuations along the y quadrature. This quadrature is usually labelled as the phase quadrature, hence this is a phase squeezed state.

and

$$\mathrm{Var}(\hat{X}) = \frac{1}{2}(\cosh(r)^2 + \sinh(r)^2 - 2\cos(\varphi)\sinh(r)\cosh(r)), \tag{1.28a}$$

$$\mathrm{Var}(\hat{Y}) = \frac{1}{2}(\cosh(r)^2 + \sinh(r)^2 + 2\cos(\varphi)\sinh(r)\cosh(r)). \tag{1.28b}$$

The degree of squeezing is often expressed in decibel via

$$V_s = 10\log_{10}\left(\frac{\mathrm{Var}(\hat{X})}{1/2}\right). \tag{1.29}$$

A comparison of a coherent state, a squeezed state and a classical field in phase space is given in figure 1.0.

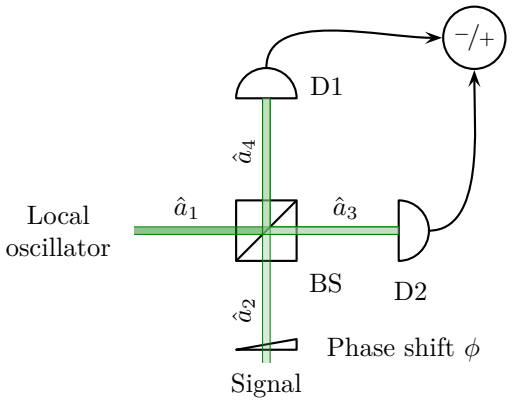

Figure 1.1: Scheme of an optical homodyne detection setup. A strong field, the local oscillator, and a weak field, the signal, are commonly derived from the same light source [219]. The signal is sent into some system to be probed while the local oscillator stays unchanged. Then, the beams are recombined by means of a beam splitter (BS), i.e. the signal interferes with the local oscillator. Both outputs of the beam splitter are detected by a photodiode (D1, D2). Finally, their signals are subtracted by a differential amplifier. Thereby classical noise contained in both beams cancels out. A wedged plate symbolises a relative phase shift between local oscillator and signal. Labels for the modes are used to derive the beam splitter transformation.

1.2.3 Homodyne detection

As described by the probability distribution (1.22), a coherent state of light may be entirely characterised by measuring the amplitude and phase of $|\alpha\rangle$ repeatedly, i.e. often enough to built-up the probability distribution. We also saw that a projection on the quadrature operators resembles this measurement. The physical measurement scheme which is able to do so is the homodyne detection, a concept derived from electrical engineering to detect a beat frequency between two (usually radio frequency) signals [142]. The whole detection stage consists of a beam splitter, two photodiodes and a differential amplifier. An illustration of the setup and further explanation can be found in figure 1.1.

For a mathematical description, the fields leaving the beam splitter have to be related to the incoming ones first. This is done in terms of the single-mode annihilation operators $\hat{a}_1, \hat{a}_2, \hat{a}_3, \hat{a}_4$. A beam splitter transformation is [114, 181]:

$$\begin{bmatrix} \hat{a}_3 \\ \hat{a}_4 \end{bmatrix} = \begin{bmatrix} t_{13} & r_{23} \\ r_{14} & t_{24} \end{bmatrix} \begin{bmatrix} \hat{a}_1 \\ \hat{a}_2 \end{bmatrix}, \tag{1.30}$$

where the indices of the coefficients of reflectivity r and transmission t indicate the "connection" between the modes. There are two constraints the coefficients r and t have to obey [181]: Energy conservation, which demands $|r_{13}|^2 + |t_{23}|^2 = |r_{24}|^2 + |t_{14}|^2 = 1$, and the commutation relation $\left[\hat{a}_i, \hat{a}_j^\dagger\right] = \delta_{ij}$, $i, j \in \{1, 2, 3, 4\}$.

When parametrising the beam splitter transformation by [181, 280]

$$r \to \imath \exp(\imath\eta) \sin(\eta), \tag{1.31a}$$
$$t \to \exp(\imath\eta) \cos(\eta), \tag{1.31b}$$

a beam splitter may also be represented via an unitary operator. It reads

$$\hat{U}_b(\eta) = \exp\Big(\imath\eta(\hat{a}_1^\dagger \hat{a}_2 + \hat{a}_2^\dagger \hat{a}_1\Big). \tag{1.32}$$

and is of use when operating in the Heisenberg picture.

For our purposes, we consider the case of a balanced homodyne detection, where the moduli of the coefficients are all equal to $1/\sqrt{2}$. By demanding that the coefficients are either real or complex valued, the matrix is found. For the (experimental) outcome however, the choice is

irrelevant [133]. Here, the real valued matrix is chosen, i.e.

$$\begin{bmatrix} t_{13} & r_{23} \\ r_{14} & t_{24} \end{bmatrix} = \frac{1}{\sqrt{2}} \begin{bmatrix} 1 & 1 \\ -1 & 1 \end{bmatrix} \tag{1.33}$$

Now the number operators, which resemble the intensity of the field [16], for the outputs are calculated to

$$\hat{n}_3 = |t_{13}|^2 \hat{n}_1 + t_{13}^* r_{23} \hat{a}_1^\dagger \hat{a}_2 + t_{13} r_{23}^* \hat{a}_2^\dagger \hat{a}_1 + |r_{32}|^2 \hat{n}_2 = \frac{1}{2}\big(\hat{n}_1 + \hat{a}_1^\dagger \hat{a}_2 + \hat{a}_2^\dagger \hat{a}_1 + \hat{n}_2\big), \tag{1.34a}$$

$$\hat{n}_4 = |r_{14}|^2 \hat{n}_1 + t_{24} r_{14}^* \hat{a}_1^\dagger \hat{a}_2 + t_{24}^* r_{14} \hat{a}_2^\dagger \hat{a}_1 + |t_{24}|^2 \hat{n}_2 = \frac{1}{2}\big(\hat{n}_1 - \hat{a}_1^\dagger \hat{a}_2 - \hat{a}_2^\dagger \hat{a}_1 + \hat{n}_2\big). \tag{1.34b}$$

The difference and sum number operator results to

$$\hat{n}_- = \hat{n}_3 - \hat{n}_4 = \hat{a}_1^\dagger \hat{a}_2 + \hat{a}_2^\dagger \hat{a}_1, \tag{1.35a}$$

$$\hat{n}_+ = \hat{n}_3 + \hat{n}_4 = \hat{n}_1 + \hat{n}_2. \tag{1.35b}$$

Hence, the difference signal is an observable of the correlations between the incoming fields. Switching from a differential to a summing amplifier means measuring the overall photon number, which is proportional to the total intensity.

Next, the incoming fields are identified as the signal and local oscillator, as shown in figure 1.1. As we will see, helpful mathematical approach is to introduce the so-called noise operator $\delta\hat{a}$ first. Thereby, the field $\hat{a}$ is split up into a complex valued amplitude α and an operator representing quantum noise (cf. figure 1.0) [16].

$$\hat{a}_1 = \alpha_L \hat{\boldsymbol{1}} + \delta\hat{a}_L \quad \text{and} \quad \hat{a}_2 = \mathrm{e}^{\imath\phi}\big(\alpha_S \hat{\boldsymbol{1}} + \delta\hat{a}_S\big). \tag{1.36}$$

In the general case, the signal $\hat{a}_S$ has an additional phase which is relative to the local oscillator. To shorten the expressions, the unity operator will be omitted. Substituting the latter definitions into equations (1.35) results to

$$\hat{n}_- = \mathrm{e}^{\imath\phi}\Big(\alpha_L^* \alpha_S + \alpha_L^* \delta\hat{a}_S + \alpha_S \delta\hat{a}_L^\dagger + \mathcal{O}(\delta^2)\Big) + \text{h.c.}, \tag{1.37a}$$

$$\hat{n}_+ = |\alpha_L|^2 + \alpha_L^* \delta\hat{a}_L + \alpha_L \delta\hat{a}_L^\dagger + \mathcal{O}(\delta^2) + \hat{n}_S. \tag{1.37b}$$

Since $|\alpha_S| \ll |\alpha_L|$,

$$\begin{aligned} \hat{n}_- &\approx \mathrm{e}^{\imath\phi}(\alpha_L^* \alpha_S + \alpha_L^* \delta\hat{a}_S) + \text{h.c.} \\ &= |\alpha_L|\Big(\underbrace{\mathrm{e}^{\imath(\phi+\phi_L)}\,\delta\hat{a}_S + \text{h.c.}}_{\equiv\sqrt{2}\delta\hat{X}_S}\Big) + 2|\alpha_S||\alpha_L|\cos(\phi + \phi_L + \phi_S), \end{aligned} \tag{1.37c}$$

$$\hat{n}_+ \approx |\alpha_L|^2 + |\alpha_L|\Big(\underbrace{\mathrm{e}^{\imath(\phi+\phi_L)}\,\delta\hat{a}_L + \text{h.c.}}_{\equiv\sqrt{2}\delta\hat{X}_L}\Big). \tag{1.37d}$$

The action of these operators on a coherent state $|\alpha_S, \alpha_L\rangle$ yields the following expectation values and variances:

$$\langle\hat{n}_-\rangle \approx 2|\alpha_S||\alpha_L|\cos(\phi + \phi_L + \phi_S), \qquad \mathrm{Var}\big(\hat{n}_-\big) \approx 2|\alpha_L|^2\,\mathrm{Var}\big(\delta\hat{X}_S\big), \tag{1.38a}$$

$$\langle\hat{n}_+\rangle \approx |\alpha_L|^2, \qquad \mathrm{Var}\big(\hat{n}_+\big) \approx 2|\alpha_L|^2\,\mathrm{Var}\big(\delta\hat{X}_L\big). \tag{1.38b}$$

While the expectation value of $\hat{n}_+$ equals approximately the intensity of the local oscillator, the expectation value of $\hat{n}_-$ comprises the relative phase of the signal (plus the phase terms of the amplitudes ϕ_L, ϕ_S). Furthermore, this phase scales with the amplitude of the local oscillator: Even if the signal is very weak, its phase can be probed with a strong local oscillator. This characteristic scaling, or rather amplification, of the signal can also be seen in the variance of $\hat{n}_-$. Here, the variance of the signal is amplified by the local oscillator's amplitude. This shows that a balanced homodyne detection can effectively probe the quantum noise of a vacuum state, where $\alpha_S = 0$, but $\mathrm{Var}(\delta\hat{X}_S) = 1/2$. The variance of $\hat{n}_-$ is further used to quantify the shot noise unit. In contrast to $\mathrm{Var}(\hat{n}_-)$, the variance of the summation operator will not only contain quantum-, but also classical noise. Supposed that the electronic noise of the detector is negligible, this variance is a test if the laser source is shot noise limited or not. In case that the radiation is shot noise limited, $\mathrm{Var}(\hat{n}_+) = \mathrm{Var}(\hat{n}_-)$. Any excess of the former variance can then be given in terms of the shot noise unit [16].

Next to the electronic noise, another requisite of homodyne detection is that the interference of the input fields has to be as good as possible. To achieve this, the beams need to be matched in their frequency and spatial mode structure. Any deviation from that will decrease the visibility of the interference and hence deteriorate the phase information. A lack in visibility is thus equivalent to optical losses. To model these, a beam splitter transformation can be applied to the interfered modes. Important to note is that, as it arises due to the interference between local oscillator and signal, the visibility has to be squared when calculating the equivalent loss term [16, eq. (8.1.12)]. As we were experimentally able to dial in visibilities of $\geq 98\,\%$, losses due to a low visibility were usually negligible.

Another more likely cause for a degradation in the detection of the quantities (1.38) are losses in the signal mode. As an example, the signal beam suffers from losses when coupled in- and out of an optical fibre. Again, losses can be modelled by a fictitious beam splitter. Using equation (1.31), $\hat{n}_-$ from equation (1.37c) reads

$$\hat{n}_- \propto |\alpha_L|\Big(\sqrt{\eta}\delta\hat{X}_S + \sqrt{1-\eta}\hat{X}_{\mathrm{vac}}\Big), \tag{1.39}$$

where the vacuum mode is represented by the operator $\hat{X}_{\mathrm{vac}}$.

If we consider the variance of $\hat{n}_-$ from equation (1.38a), we find that loss enters linearly:

$$\mathrm{Var}(\hat{n}_-) \propto |\alpha_L|^2\Big(\eta\,\mathrm{Var}(\delta\hat{X}_S) + (1-\eta)\,\mathrm{Var}(\hat{X}_{\mathrm{vac}})\Big) = |\alpha_L|^2\Big(\eta\,\mathrm{Var}(\delta\hat{X}_S) + (1-\eta)/2\Big). \tag{1.40}$$

For a coherent state $\mathrm{Var}(\hat{n}_-)$ is independent of η, because the variance of a vacuum- and a coherent state are equal. However, a squeezed state can not be fully detected in the presence of losses, as the squeezed variance is effectively increased by virtue of the vacuum noise contribution. Some more details on squeezed states and losses will be given in chapter 3.

Various authors treated the theory of homodyne detection in greater detail. To name a small selection: Collett et al. [70] elaborate on the count distributions of the various signals, Yuen and Chan [298] treat the nature of the noise and Kumar et al. [167] present the theory more extensive and give a layout of a homodyne detector. A brief summary of homodyne detection on squeezed states can be found in a review by A. I. Lvosvsky [185].

1.2.4 Wigner quasiprobability distribution

A phase space representation is a common way to describe mathematically and – if possible – visually the configurations a physical system can take on. Such a representation thus follows the rules for a probability distribution [44]. In classical mechanics, where the phase space was

applied in first, the coordinate system is spanned by the system's degrees of freedom, that is the canonical position and momentum variables [212]. As these variables are however non-commutable in quantum mechanics – there is no sense in referring to a certain point in a quantum phase space –, the representation of a quantum state in phase space required novel concepts. Several approaches have been developed to map a wavefunction $\psi(x) = \langle X|\psi\rangle$ or a density matrix $\hat{\rho} = \sum_i p_i|\psi_i\rangle\langle\psi_i|$ to phase space[7] [48, 114]. It is thus common to choose a map which is most convenient for a certain application.

For our purpose, this is the Wigner quasiprobability distribution or just 'Wigner function'. This is because its marginal distribution directly corresponds to a measurement technique applied in several of our experiments: The homodyne detection described above. Like all quantum phase space representations, the Wigner function is a quasiprobability distribution, as it does not obey the definition of a common probability distribution. A Wigner function for example can take on negative values, some other representations may also be singular. Important for a coherent treatment is to agree on the definition of the shot noise unit, since it affects also the normalisation of the Wigner function [114, 280]. As defined previously, the shot noise unit is set to $1/\sqrt{2}$. Then, the mapping reads

$$W(x,y) = \frac{1}{2\pi}\int_{-\infty}^{\infty} \psi\Big(x+\frac{z}{2}\Big)\psi^*\Big(x-\frac{z}{2}\Big)\,\mathrm{e}^{\imath yz}\;\mathrm{d}z \tag{1.41}$$

and can be recognised as an autocorrelation with an additional kernel. For a mixed state represented by a density operator,

$$W(x,y) = \frac{1}{2\pi}\int_{-\infty}^{\infty} \Big\langle x+\frac{z}{2}\Big|\hat{\rho}\Big|x-\frac{z}{2}\Big\rangle\,\mathrm{e}^{\imath yz}\;\mathrm{d}z. \tag{1.42}$$

For example, given $\hat{\rho} = \sum_i^2 p_i|\psi_i\rangle\langle\psi_i|$, that is a mixture of two pure states assigned to a probability p_i,

$$W(x,y) = \frac{1}{2\pi}\int_{-\infty}^{\infty} \Big(p_1\psi_1\Big(x+\frac{z}{2}\Big)\psi_1^*\Big(x-\frac{z}{2}\Big) + p_2\psi_2\Big(x+\frac{z}{2}\Big)\psi_2^*\Big(x-\frac{z}{2}\Big)\Big)\,\mathrm{e}^{\imath yz}\;\mathrm{d}z. \tag{1.43}$$

For a squeezed vacuum and a coherent state, the Wigner function reads

$$W(x,y,r,\varphi) = \frac{1}{\pi}\exp\big(\sinh(2r)((y-x)(y+x)\cos(2\varphi) - 2yx\sin(2\varphi)) - \cosh(2r)(y^2+x^2)\big), \tag{1.44a}$$

$$W(x,y,\alpha) = \frac{1}{\pi}\exp\Big(-2|\alpha|^2 - y^2 + \imath 2\sqrt{2}\alpha y + 2\sqrt{2}(x-\imath y)\Re(\alpha) - x^2\Big). \tag{1.44b}$$

Applications for Wigner functions The previously mentioned relation between the marginal distribution probed via homodyne detection and a Wigner function is

$$\int_{-\infty}^{\infty} W(x,y)\;\mathrm{d}y = |\psi(x)|^2 = \mathrm{p}(x) = |\langle X|\psi\rangle|^2, \tag{1.45}$$

which holds equally for the other quadrature. The series of expressions just clarifies the link between the different notations. To learn about the expectation value of a pure or mixed state,

[7] When starting from a density matrix, we note that all $|\psi_i\rangle$ must be given in the basis of coherent states for a direct application of the following formulas.

we can apply

$$\langle \hat{X} \rangle = \int_{-\infty}^{\infty} xW(x,y)\,\mathrm{d}x\,\mathrm{d}y, \tag{1.46}$$

which is a property that Wigner functions and "common" probability distributions share. The same applies for all higher moments m:

$$m(\hat{X}, i) = \int_{-\infty}^{\infty} \left(x - \langle \hat{X} \rangle\right)^i W(x,y)\,\mathrm{d}x\,\mathrm{d}y. \tag{1.47}$$

Hence a quantum state, mixed or pure, can be fully described by its statistical moments in the coherent-state basis set. To extract other characteristics such as the photon number distribution, Wigner functions associated with the number and phase operator have been developed [275, 276].

As outlined above, a homodyne detection projects a state into a coherent-state basis: Thus the Wigner function can be experimentally reconstructed via homodyne detection under various phase angles[8], i.e. by changing ϕ in figure 1.1.

The Wigner function is a convenient means for characterising quantum states. As an example, we may consider an apparently squeezed state: If a pure, squeezed state experiences losses, e.g. due to a propagation through a beam splitter, it becomes a mixed state – as it gets literally mixed with the vacuum state which enters through the second input port of the beam splitter (cf. equation (1.39)). Depending on how much loss a squeezed state experiences, the measurable degree of squeezing lessens. A common way to quantify the losses is by comparing the marginal distributions along the squeezed and the so-called 'anti-squeezed' quadrature. The squeezed and anti-squeezed quadrature are given by the minor and major axis of the ellipse, respectively. A pure state shows an equal amount of squeezing and anti-squeezing (e.g. $\pm 3\,\mathrm{dB}$), a mixed state has a higher amount of the latter.

Wigner functions are also useful to propagate a state through various elements, e.g. a beam splitter: First, the transformation of the quadrature operators are identified, then they are substituted into the Wigner function. If more than one mode (like it is the case for a beam splitter) is involved, the phase space needs to be expanded.

All these operations are especially simple when the transformations and the states are Gaussian. The coherent state is a prominent member of Gaussian states, i.e. states which, when described via a Wigner function, obey a multivariate normal distribution. Thus, the same holds for squeezed states. A transformation or operation qualifies itself as Gaussian when it does not turn a Gaussian into a non-Gaussian state. The displacement operation $\hat{D}$ is an example of a Gaussian operation: From (1.22) the quadratures are transformed according to

$$\hat{X} \to \hat{X} - \sqrt{2}\Re(\alpha), \tag{1.48a}$$

$$\hat{Y} \to \hat{Y} + \sqrt{2}\Im(\alpha). \tag{1.48b}$$

Thereby, a Wigner function displayed in figure 1.0(c) can be created from equation (1.44a).

For a concise and detailed description of Gaussian states in quantum optics, the reader may refer to Ferraro et al. [99] or Weedbrook et al. [285].

[8] The heterodyne detection technique provides another means for a phase space reconstruction and might be in some cases more precise than homodyne detection, as Müller et al. pointed out recently [201].

2 | Silicon vacancy centres and their electronic spin coherence

2.1 Introduction

One of the main precursors for quantum enhanced sensing are atomic clocks. Decades before quantum features of light were harnessed for precision measurements, the use of electronic transitions of atoms offered novel ways to measure and define time [263]. Until today, the quantum features of atoms and ions play a major role in the improvement of sensing techniques. Even though the advances in experimental techniques allows for the control of single atoms, the requirements for such techniques hamper applications outside of well-controlled and isolated environments.

Over the past decades, quantum systems in solids became a promising alternative, as they naturally come in a (potentially) controllable and stable environment. This potential can since then be explored because of advances in nanotechnology which rendered the fabrication of single quantum emitters in solids feasible.

An established type of solid state emitters are diamond defects. Studied as a single emitter in 1997, the best known diamond defect is the negatively charged nitrogen vacancy (NV^-) centre [90, 127]. Similar to its host material, the NV^- centre offers a few unique features, such as very good photostability and a spin coherence time of more than 1 ms at room temperature [19, 25, 162]. Used as a sensor for magnetic fields, sensitivities of ca. $4\,\mathrm{nT}/\sqrt{\mathrm{Hz}}$ have been reported for a single NV^- centre[1] [19]. To allow for such features, the synthesis of isotropically pure diamond and techniques to decouple the spin from its environment are necessary [90, 131], however the fact that room temperature experiments yield these figures is an outstanding property. Next to various sensing applications, NV^- centres served as a platform for quantum computation [15], e.g. single photon sources and quantum memories [204], and ground-breaking loophole-free Bell tests [137].

While in the beginning the creation process of NV^- centres in synthetic diamond, e.g. via electron irradiation and annealing [127, 258], offered little control over the transversal positioning, novel fabrication techniques led to a change. The actual conversion from just a vacancy and a nitrogen atom into a NV^- centre can not yet be called deterministic, but fabrication techniques now allow for a positioning of an "unconverted" defect with nanoscale precision [170, 253].

All that turns the NV^- centre into a potential system for the 'second quantum revolution', which denotes the transition from quantum mechanics as a description of a physical reality to quantum mechanics as an engineering platform [92].

Apart from the NV^- centre, several hundreds of other diamond defects are known[2] [4, 301].

[1] Sensitivities as low as $0.9\,\mathrm{pT}/\sqrt{\mathrm{Hz}}$ were achieved by using ensembles of NV^- centres [289].

[2] In 1997, Gruber et al. cited a count of "over 100" [127]. Three years later, A. M. Zaitsev stated that "more than 500" [301] luminescence centres in diamond have been recorded.

Since a few years, the negatively charged silicon vacancy (SiV^-) centre has caught attention and is known as a promising candidate, which outperforms the NV^- centre in certain applications [208, 282]. A drawback of NV^- centres is that broadband phonon interactions set the probability of collecting 'zero-phonon-line' (ZPL) photons in bulk diamond to ca. 3 % [20, 124]. Photons from the ZPL maintain optical coherence features which are otherwise lost, or at least weakened, via phonon interactions. This loss of coherence is disadvantageous for all techniques which rely on narrowband emission – in fact for quantum information protocols based on NV^- centres the ZPL fluorescence efficiency is usually the major figure to improve [24, 28] –, but also the mentioned sensing techniques potentially benefit from a more pronounced ZPL in terms of a higher signal-to-noise ratio[3] [289]. With 70 % of fluorescence from the ZPL, the SiV^- centre clearly excels in this perspective [71].

To further determine the application range of SiV^- centres, our study focussed on the extension of electronic spin coherence time. Two arguments motivated this endeavour: First, just as for the NV^- centre, the electronic spin coherence time is a critical figure when it comes to efficiently sense (readout) and store spin-state information. Thus, the comparably short electronic spin coherence time of SiV^- centres thus appears to be a limiting factor. Second, the underlying decoherence mechanism had been identified recently, which gave us an indication of the possibility to control the spin coherence time.

The study presented herein was conducted during a three-month stay at Fedor Jelezko's group in Ulm, Germany. Work performed without my contribution will be noted accordingly.

Chapter structure The historical development and a few important properties of the SiV^- centre will be outlined first. This leads to the introduction of the energy level scheme which is important for the understanding of the experimental technique we applied. Next, we explain the two main parameters of our study, which are the spin relaxation- and the dephasing time. Given this information, the experimental scheme will be introduced before the actual experimental setup is described. After the experimental details are given, we present the results and conclude this chapter with a summary and outlook.

2.1.1 The silicon vacancy in diamond

It was in 1980 that the luminescent properties of silicon implanted into natural diamond were recognised [300]. By cathodoluminescence studies a strong signal at 1.684 eV (736.25 nm) was found, which is close to the zero-phonon-line (ZPL) signal at 1.68 eV (737 nm).

The direct identification of the emitter as a vacancy centre was provided by Clark and Dickerson in 1991 who implanted not only silicon atoms, but also deliberately created vacancies via electron beam irradiation [64]. Consecutive annealing of the synthetic diamond samples at different temperatures led them to the conclusion that the emitter is a "silicon and vacancy" centre, hence the name. In the following years, spectroscopic studies [65, 71, 98, 121, 149, 260] gave Goss et al. experimentally verified support to conduct a theoretical modelling of the SiV^- centre [123]. In 2005, Goss et al. elaborated on this model and further explained the nowadays accepted ZPL at 737 nm [122] which was verified experimentally by Edmonds et al. in 2008 [95].

[3] We note that sole "reshuffling" of emission into the ZPL can not enhance the SNR. The premise for a benefit is that a more pronounced ZPL emission also implies Purcell enhancement [161], or, more generally, effects that suppress non-radiative processes.

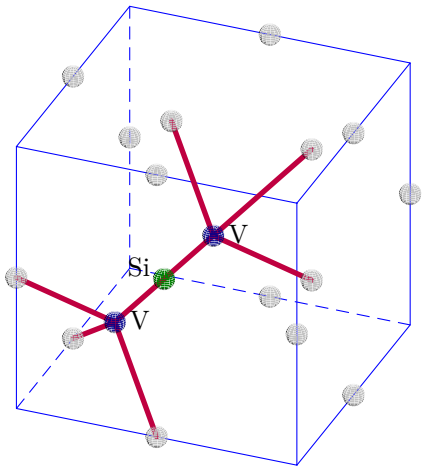

Figure 2.1: Structure of the SiV^- centre in a unit cell of the diamond lattice. In between two vacancies (V) a silicon (Si) atom rests. All other atoms are carbon. The symmetry of the centre in Schoenflies notation reads D_{3d}, which means it has a three-fold rotation axis and three two-fold axes perpendicular to the rotation axis. In addition, there are three vertical mirror planes passing through the two-fold axes.

Symmetry and spectral properties

The actual symmetry of the SiV^- centre was experimentally studied in various works [45, 83, 138, 205, 261], all indicating that – as predicted by Goss et al. [123] – the D_{3d} point group is the correct geometrical description. A representation of the physical structure is given in figure 2.1.

By a study of the irreducible representations of symmetry operations in the D_{3d} point group, the electronic level scheme can be derived [270]. Four irreducible representations exists for this group and are used to label the energy levels: A_1, A_2 and E, whereas all of them are allowed to come in an even (subscript g) or odd wave (subscript u) function [270]. The latter states have a lower energy, the same applies for A compared to E levels [123, 283]. According to the energy hierarchy, the level scheme can be filled with the supplied electrons. Four electrons are contributed by the silicon atom, a fifth one is donated – which results to the centre's negative charge. From the "dangling" carbon bonds, six electrons are supplied, which makes up for 11 electrons bound to the SiV^- centre. Thereby, the ground state is found to be ${}^2E_g$ characterised by a two-fold orbital- and spin degeneracy[4]. To find the first excited state, an electron may be promoted to the next level. The first excited state is also a spin- and orbital doublet, but of odd parity, thus it reads ${}^2E_u$. Figure 2.2 shows an illustration of the level scheme for the ground- and the first excited state.

In the illustration, the ZPL fine structure and the according transition strength is shown. Rogers et al. concluded by polarisation measurements that the fine structure is due to spin-orbit coupling [234]. Photoluminescence (PL) spectra resolved the individual lines, ranging between 736.4 nm to 737 nm. The spectral uniformity, stability and finally the ability to selectively access the ZPL fine structure of SiV^- centres in bulk diamond was demonstrated in a Hong–Ou–Mandel experiment by Sipahigil et al. in 2014 [256]. Another demonstration of the uniformity was given by Dietrich et al.: With a distribution spread over 8 GHz, the inhomogeneous broadening of individual SiV^- centres in synthetic diamond, overgrown in a chemical vapour deposition (CVD) process, was an order of magnitude smaller than the shift of the ZPL induced by the silicon isotope (^{28}Si, ^{29}Si, ^{30}Si). Thus, Dietrich et al. were able to conclude from PL spectra which isotope was involved in a certain SiV^- centre [85].

[4] This contrasts the spin-triplet state of the NV^- centre's ground- and excited state. Due to zero-field splitting, sensing magnetic fields with an NV^- centre doesn't require to initially lift a spin degeneracy.

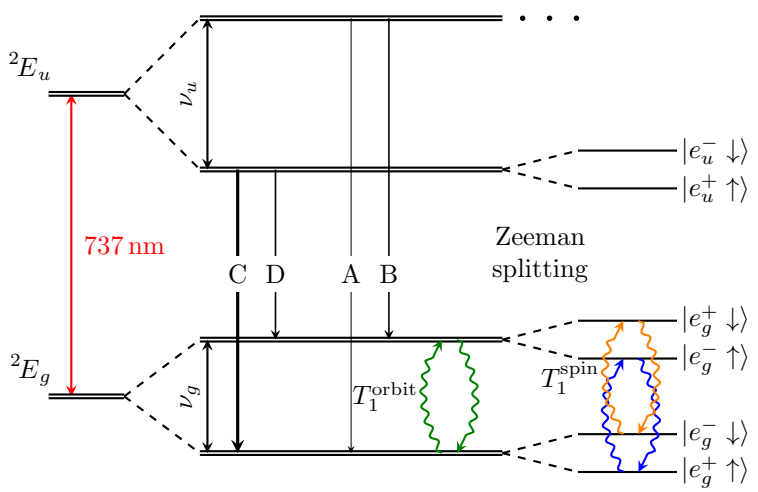

Figure 2.2: Energy level diagram with the fine structure lines of the ZPL. The orbital degeneracy is lifted by spin-orbit coupling. An external magnetic field leads to a splitting of the spin states. The spin- and orbital relaxation times are highlighted. Arrows in the electronic spin states printed to the right of the energy levels indicate the electron spin. The frequency differences are $\nu_g \approx 47\,\text{GHz}$ and $\nu_u \approx 258\,\text{GHz}$ [234]. The labelling of the fine structure lines and the electronic spin states is in accordance with Rogers et al. [233]. A variation in linewidth shall indicate the relative PL strength.

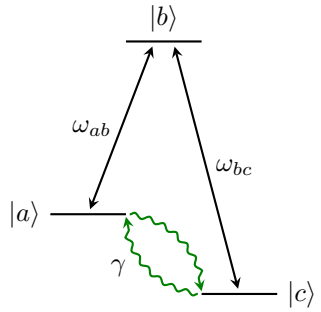

Figure 2.3: An energy level diagram following the Λ scheme. The transition from $|b\rangle$ to $|a\rangle$ or $|c\rangle$ might be driven resonantly with a laser tuned to ω_{ab} or ω_{bc}. By virtue of e.g. thermal processes, the system might be initially found in either $|a\rangle$ or $|c\rangle$. As an example, consider an energy difference between $|a\rangle$ and $|c\rangle$ of $\gamma = 50\,\text{GHz}$. According to the Boltzmann distribution the probability to find the system in $|a\rangle$ is 30.9 % when probed at 5 K.

Electronic structure and the issue of pure dephasing

To explore the electronic spin structure of the centre, which might serve as a basis for a qubit [126], Rogers et al. [233] applied an external magnetic field to lift the spin degeneracy. The spin splitting introduced a so-called Λ scheme [296], exemplified in figure 2.3. To clarify the correspondence to figure 2.2: $|a\rangle$ is $|e_g^+ \downarrow\rangle$, the excited state $|b\rangle$ is $|e_u^- \downarrow\rangle$ and $|c\rangle$ is $|e_g^- \uparrow\rangle$. With an optical driving- and readout-pulse, each one tuned to one of the transitions, Rogers et al. could access the spin state optically and found, at 5 K, a spin relaxation time of $T_1^{\text{spin}} = 2.4(2)\,\text{ms}$ [233]. To deduce the spin pure dephasing time T_2^* – which will be discussed in the following –, both lasers continuously drove the mentioned transition which lead to 'coherent population trapping', a special case of electromagnetically induced transparency [101, 233]. They found $T_2^* = 35(3)\,\text{ns}$, which limits the total spin coherence time T_2^{spin} via [2, 257]

$$\frac{1}{T_2} = \frac{1}{2T_1} + \frac{1}{T_2^*} \tag{2.1}$$

to ca. 35 ns. An explanation for the short T_2^* time was provided by a study of electron-phonon processes: Jahnke et al. demonstrated that the orbital relaxation time is $T_1^{\text{orbit}} \approx 38\,\text{ns}$ [153]. As they stated, $T_1^{\text{orbit}} \ll T_1^{\text{spin}}$ indicates the orbital relaxation process must conserve the electron spin. However, in the process of orbital relaxation, the spin coherence is lost, which results in a short T_2^* time.

Motivated by the mentioned benefits of a long T_2^* time, our goal was to increase the total

coherence time to, if possible, a lifetime-limited ($T_2^* \to \infty$) case. We had strong evidence that the orbital relaxation is the main cause of decoherence, and furthermore knew that, at cryogenic temperatures, the silicon atom supports purely local phonon modes [85, 152]. The latter implies that, in case of a single local phonon mode, only this mode has to be suppressed to cancel pure dephasing. To achieve such a suppression, there are two basic possibilities:

- Operate at temperatures at which the thermal population of the corresponding mode is negligible. The energy of the orbital splitting is, as shown in figure 2.2, about 50 GHz. According to the Boltzmann distribution $\exp(\Delta E/(k_B T))$, where ΔE is the energy difference and T the temperature, it requires temperatures of less than 700 mK to decrease the probability of populating the excited state to less that 1 %. Due to a lack of equipment capable of reaching these temperatures, this approach was ruled out.

- Place the SiV^- centre in an environment which does not support frequencies of ca. 50 GHz, that is: Create a phononic band gap around this frequency [46]. Assuming a speed of sound in diamond of $12\,000\,\mathrm{m\,s^{-1}}$, the smallest cavity length that is resonant for 50 GHz is ca. 120 nm.

As we were provided with nanodiamonds containing SiV^- centres, we chose the latter approach.

Studies with nanodiamonds In fact, a number of studies investigated the optical properties of SiV^- centres in nanodiamonds [202, 206, 207, 208, 302] down to a size of 1.6 nm [279]. The interest in nanodiamonds was however spurred by other applications, such as studies of the centre's local environment or applications where a manual placement of the emitter is beneficial, which applies for, e.g., micro cavities [6, 230].

So far, the reported SiV^- linewidths for nanodiamonds of a few GHz deviate strongly from the linewidths reported for bulk diamond [202, 206, 207]. At cryogenic temperatures, the linewidth in bulk diamond was reported to range between 119 MHz to 409 MHz [232]. The issue with linewidths on the order of GHz is that strong magnetic fields are required to individually address the spin states. As reported by Rogers et al. [233], 450 mT is required to lift the spin degeneracy by ca. 6 GHz. Because the SiV^- nanodiamonds provided by our collaborators were fabricated by a technique which is known to also yield high optical qualities for NV^- centres [80], investigation of the linewidth of SiV^- PL posed a second aspect of our study.

Experimental scheme

As stated previously, we aimed to extend T_2^*, and eventually the total coherence time T_2^{spin}, by increasing T_1^{orbit}. To verify this link between T_2^* and T_1^{orbit}, we planned to initially measure T_1^{orbit} before using coherent population trapping to deduce T_2^*. The experimental scheme to measure T_1^{orbit} is sketched in figure 2.4 and can be summarised as follows:

1. A laser pulse resonantly excites the SiV^- centre. As an example, we assume to drive transition D in figure 2.2. The resonant excitation will prepare the state in the lowest branch of the level diagram. To drive a single transition, the experiment needs to be conducted at ca. 5 K. Neglecting Zeeman splitting, the system can be seen as a Λ scheme like in figure 2.3, where $|a\rangle$ and $|c\rangle$ represent the orbital states in ${}^2E_g$ and $|b\rangle$ is the lower state in ${}^2E_u$.

2. After a short waiting time, another laser pulse drives the same transition. At the same time, the fluorescence is recorded. If the phonon mode at ca. 50 GHz is inhibited, the probability of finding the system in the upper branch of ${}^2E_g$ will remain low. Thus, the

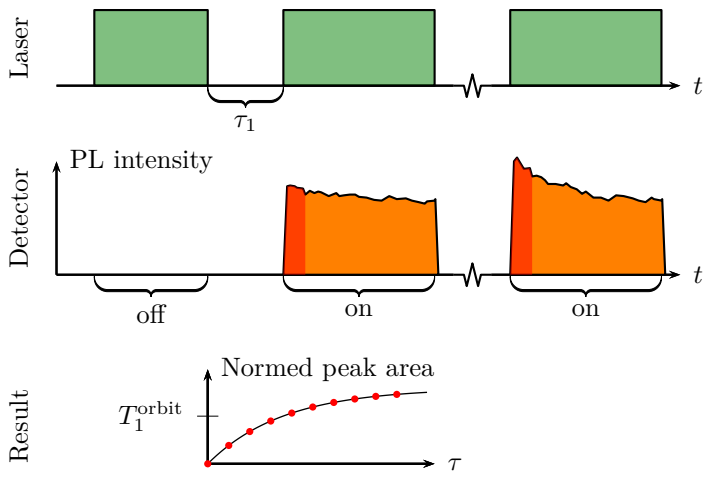

Figure 2.4: T_1^{orbit} measurement scheme. The blocks on the upper time axis represent the switching of laser pulses to drive resonant PL. The first block initialises the system in a "dark" state, which is not accessed by the laser pulse. After a certain waiting time τ_1, another laser pulse is sent. At the same time, the PL intensity is recorded. Given that the system is still in the dark state prepared by the first pulse, the detected signal only contains technical noise. As the waiting time increases, the system equilibrates and the probability to find it in a state resonant to the laser pulse will eventually yield PL. Repeating this scheme numerous times to build up reliable statistics results in signals similar to the ones sketched in the middle graph. The analysis of the detected signal is exemplified in the bottom graph.

detected signal may contain technical noise, but the chance to detect resonance fluorescence is very low.

3. The second step is repeated and the waiting time might be slightly increased. Over time, relaxation processes eventually re-populate the upper branch of ${}^2E_g$. If this happens, resonance fluorescence will be detected. As the expected count rates are very low, the whole process has to be iterated several million times.

4. Finally, by analysing the recorded PL, T_1^{orbit} can be derived. This can be achieved by integrating over a certain fraction of the PL signals recorded for different waiting times. The integrated area is highlighted in figure 2.2. Commonly, also a fraction of the last part of each signal is integrated and used for normalisation.

To be able to resolve and thus address the individual orbital states, cryogenic temperatures are required. The experimental realisation of this scheme will be explained in a following section.

Concept of the T_1, T_2 and T_2^* time

Before continuing with the experimental details, we outline the two key concepts of our study: That is relaxation and decoherence. For the purpose of explanation, we will develop the equation of motion of a two-level model system and discuss its solution. A rigorous derivation may be found elsewhere [29, 247, 257].

The most general equation governing the evolution of a quantum system is the von Neumann equation [43, 247]

$$\frac{\mathrm{d}}{\mathrm{d}t}\hat{\rho}_{\mathrm{t}} = \frac{\imath}{\hbar}\left[\hat{\rho}_{\mathrm{t}}, \hat{\mathcal{H}}_{\mathrm{t}}\right], \tag{2.2}$$

where $\hat{\rho}_{\mathrm{t}}$ is the density matrix of the total system and $\hat{\mathcal{H}}_{\mathrm{t}}$ its Hamiltonian. Here 'total' means that $\hat{\mathcal{H}}_{\mathrm{t}}$ is comprised of a 'system' – in our case the qubit –, a '(thermal) bath' and the coupling

between the the two. The von Neumann describes a closed system, i.e. by solving it one is able to study the evolution of the qubit and the bath. No information can be lost. However, usually one is neither interested in keeping track of the bath's evolution, nor able to actually do so, because the degrees of freedom are to numerous to handle. By virtue of certain approximations[5], the Lindblad master equation can be derived from equation (2.2) [119, 178]. In the process of derivation, the bath is traced out of the total system, such that, during the evolution of the remaining system, information may get lost. Thus, a Lindblad master equation is the equation of motion of an open quantum system. Setting $\hbar$ to unity, it reads

$$\frac{\mathrm{d}}{\mathrm{d}t}\hat{\rho} = \imath\big[\hat{\rho}, \hat{\mathcal{H}}\big] + \hat{\mathcal{L}}(\gamma, \hat{\rho}, \hat{o}), \tag{2.3}$$

where $\hat{\rho}$ is the reduced density matrix describing only the system and $\hat{\mathcal{L}}$ denotes a Lindblad superoperator acting on $\hat{\rho}$ and an operator $\hat{o}$. At a rate γ, the latter is influenced by the bath which establishes a bath-system coupling. The Lindblad superoperator takes the form [43, 247, 288]

$$\hat{\mathcal{L}}(\gamma, \hat{o}, \hat{\rho}) = \gamma\left(\hat{o}\hat{\rho}\hat{o}^\dagger - \frac{1}{2}\big\{\hat{o}^\dagger\hat{o}, \hat{\rho}\big\}\right) \tag{2.4}$$

and governs the non-unitary part of the equation of motion.

To outline the effects of relaxation and decoherence, we consider a simple qubit (spin 1/2) system with a Hamiltonian of

$$\hat{\mathcal{H}} = \omega_z \hat{s}_z, \tag{2.5}$$

where $\hat{s}_z$ is a spin operator and ω_z the associated frequency. The $\hat{s}_z$ spin operator is an observable with two eigenvalues, $\pm\frac{1}{2}$, and represents a spin measurement in the z direction [86]. Along with the other two spin operators [26, 114]

$$\hat{s}_x = \frac{1}{2}\begin{pmatrix} 0 & 1 \\ 1 & 0 \end{pmatrix} \quad \text{and} \quad \hat{s}_y = \frac{1}{2}\begin{pmatrix} 0 & \imath \\ -\imath & 0 \end{pmatrix}, \tag{2.6a}$$

it is given by

$$\hat{s}_z = \frac{1}{2}\begin{pmatrix} 1 & 0 \\ 0 & -1 \end{pmatrix}. \tag{2.6b}$$

As we will see next, $\hat{s}_z$ causes a rotation about the z axis. When defining the $+\frac{1}{2}$ eigenstate of $\hat{s}_z$ as the excited state $|e\rangle$ and the $-\frac{1}{2}$ eigenstate as the ground state $|g\rangle$, another representation of $\hat{s}_z$ is

$$\hat{s}_z = \frac{1}{2}(|e\rangle\langle e| - |g\rangle\langle g|), \tag{2.7}$$

[5]Three approximations are implied in a master equation in Lindblad form: (1) The Born approximation, which requires that the bath does not become entangled with the system, i.e. bath and system are separable. This also requires that the bath is not changing its state caused by the interaction. (2) The Markov approximation, demanding a memoryless bath, at least compared to the time scale of the system. (3) Finally, the secular approximation, which, in simple terms, assumes that decay rates of excited states are much smaller than transition frequencies and thus justifies the omission of terms with fast oscillations. For closed systems, a similar approximation is known: The rotating-wave approximation. A detailed derivation and application of the Lindblad and other master equations is given by G. Schaller [247].

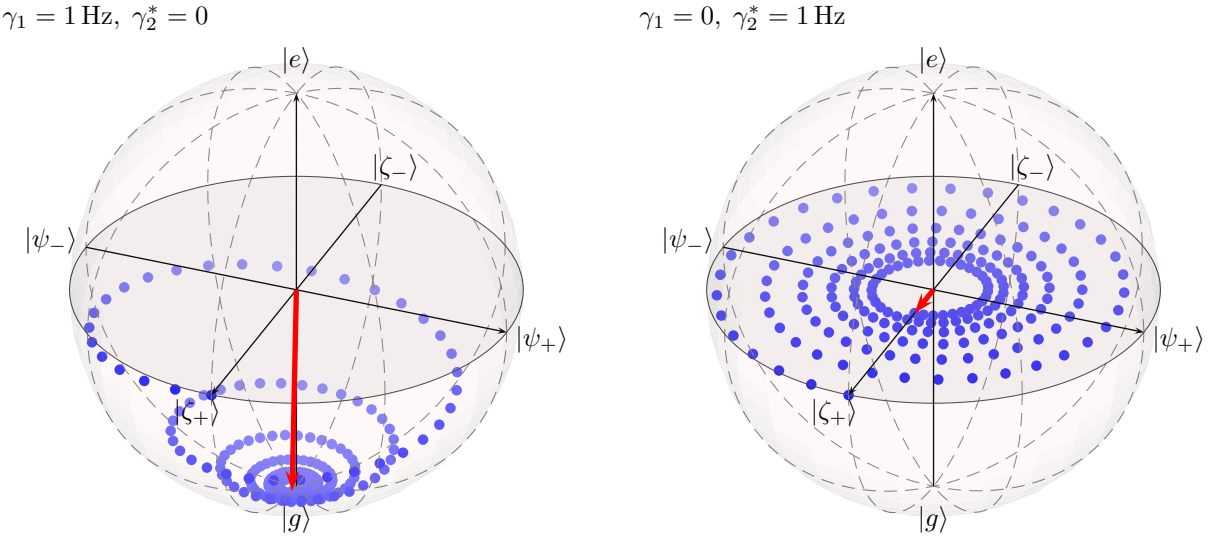

(a) T_1 process (b) T_2^* process

Figure 2.5: Bloch sphere representation of a qubit (spin 1/2) system evolving in time. The axes represent the ground- and excited state, and the superposition states $|\zeta_\pm\rangle = 1/\sqrt{2}(|e\rangle \pm |g\rangle)$, $|\psi_\pm\rangle = 1/\sqrt{2}(|e\rangle \pm \imath|g\rangle)$. We note that $\langle\psi_+|\psi_-\rangle = \langle\zeta_+|\zeta_-\rangle = \langle g|e\rangle = 0$. Points represent the state in terms of $(\langle\hat{s}_x\rangle, \langle\hat{s}_y\rangle, \langle\hat{s}_z\rangle)$ each time the equation of motion was solved. A red arrow points to the last step of the evaluation. If $\gamma_1 = \gamma_2^* = 0$, the qubit will evolve according to equation (2.5) and spin thereby around the centre while remaining on the Bloch sphere's shell.

which is why $\hat{s}_z$ is also called inversion operator [114]. Important to notice is that $\hat{s}_z$ only "queries" the system's energy without changing it.

Next, we add two Lindblad superoperators to model a relaxation (T_1) process and a pure dephasing (T_2^*) process. This is achieved by including [29, 268]

$$\hat{\mathcal{L}}(\gamma_1, \hat{s}_-, \hat{\rho}) \tag{2.8a}$$

and

$$\hat{\mathcal{L}}(\gamma_2^*/2, \hat{s}_z, \hat{\rho}), \tag{2.8b}$$

where $\hat{s}_-$ is the system's annihilation operator equal to $|g\rangle\langle e|$ and the dissipation rates are denoted by $\gamma_{1,2^*} = (T_{1,2^*})^{-1}$.

To point out the difference between the two processes, we can solve the equation of motion for a system subject either to a T_2^* or a T_1 process. The system is initially prepared in a superposition state

$$|\zeta_+\rangle = \frac{1}{\sqrt{2}}(|e\rangle + |g\rangle) \tag{2.9}$$

and then evolved numerically for 6 s in 200 time steps [157]. The results are visualised for $\omega_z = 2\pi\,\mathrm{Hz}$ in figure 2.5. Using a Bloch sphere representation, we can directly follow the time evolution of the state. After each time step, the expectation values of $\hat{s}_z$, $\hat{s}_y$ and $\hat{s}_x$ are evaluated

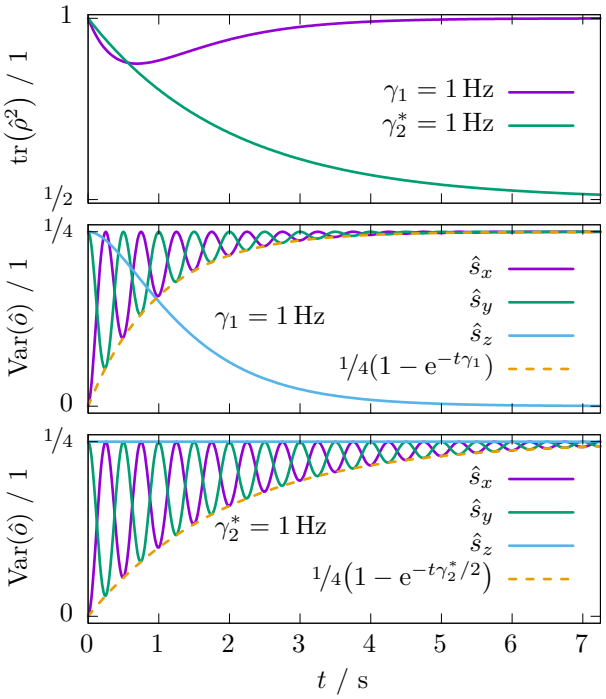

Figure 2.6: Additional illustration of the qubit shown in figure 2.5. The purity of the state is plotted in the upper graph. In the T_1 process, the final state is $|g\rangle$, thus the purity recovers asymptotically. In case of pure dephasing, purity is gradually lost ($1 \leq \mathrm{tr}(\hat{\rho}^2) \leq 1/d$, where d is the dimension of $\hat{\rho}$). The middle and lower graph show the spin variance for the T_1 and T_2^* process, respectively. Apart from the different decay rate, one can see that the variance oscillates at twice the frequency ω_z. We note that the expectation values of $\hat{s}_{x,y}$ decay according to $1/2 \exp(-t(\gamma_1 + \gamma_2^*/2)/2)$, while the envelope of $\langle \hat{s}_z \rangle$ follows $1/2(-1 + \exp(-t\gamma_1))$.

and marked as a point on (or in) the Bloch sphere. Figure 2.5(a) shows that the T_1 process leads to a decay from $|\zeta_+\rangle$ to $|g\rangle$. Eventually the coherence is lost as well, as $|g\rangle$ can not carry a (relative) phase. This just emphasises equation (2.1): Relaxation causes decoherence. In the T_2^* processes presented in 2.5(b), the state remains on the "equator", but is spiralling inwards over time. Thus, the energy is unperturbed in the course of the process, but the coherence, i.e. the information about the relative phase of the superposition, becomes less and less determined. Another way of relating the coherence of a system to the Bloch sphere representation is the norm of the vector pointing to a state: If the state is located on the shell of the Bloch sphere, it is a pure state, while mixed states are found on the inside [114]. The time evolution of purity, as well as the variance for each spin operator, is presented in figure 2.6.

2.2 Experiment

This section begins with a presentation of experimental details. These entail the optical setup and sample characteristics. Next we discuss off- and on-resonant spectra of SiV^- nanodiamonds at cryogenic temperatures. The results achieved during the period of the stay are summarised, before we conclude this chapter with an outlook.

2.2.1 Experimental setup

The implementation of the scheme outlined on page 21 was based on confocal microscopy [195, 214]. This technique allows to resolve, according to Abbe's criterion [133], structures with a radius of $d = \lambda/(2\mathrm{NA})$, where λ denotes the wavelength and NA is the objective's numerical aperture. An overview of the experimental setup, which was re-built at the beginning to improve efficiency and stability, is given by figure 2.7. More information on the experimental equipment

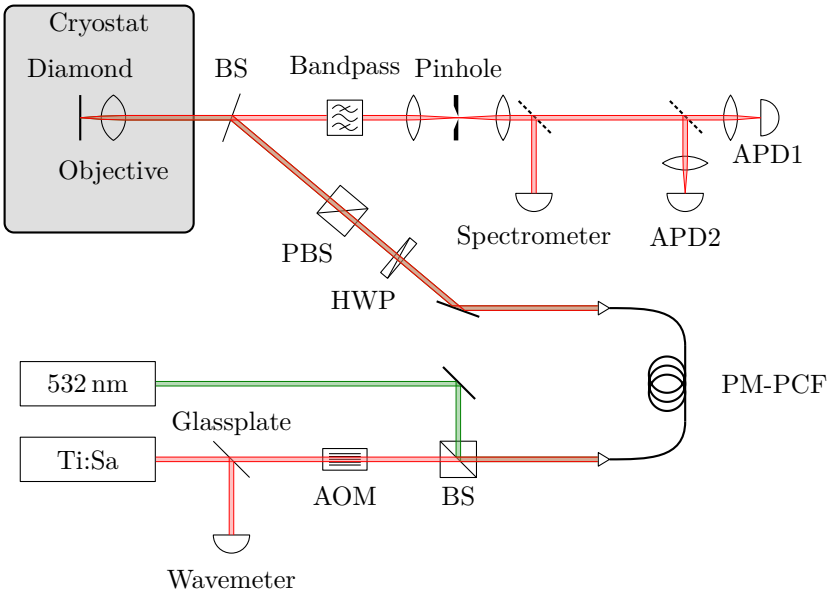

Figure 2.7: Scheme of the confocal microscope setup including the most important components. A polarisation maintaining photonic crystal fibre (PM-PCF) was used to prepare both beams in a similar spatial mode. The objective inside the flow cryostat was mounted on a 3D piezo scanner.

is listed in table 2.1. To excite the SiV^- centres in our sample, two laser sources were used: A 532 nm diode laser to drive off-resonant PL and a titanium-sapphire (Ti:Sa) laser for resonant excitation.

The Ti:Sa laser was tunable from 700 nm to 780 nm and was stabilised to an external Fabry–Pérot cavity to yield a linewidth limit of 50 kHz. A small fraction of the Ti:Sa laser beam was coupled to a wavemeter. Its absolute accuracy was 30 MHz. By synchronising the wavemeter with our recording software [273], PL excitation (PLE) spectra could be recorded. An acousto-optical modulator (AOM) with a rise and fall time of ca. 60 ns was placed in the beam path of the Ti:Sa laser to prepare pulses. Both lasers were coupled with an efficiency of 63 % into a polarisation maintaining photonic crystal fibre. The fact that both laser beams shared the same fibre mode facilitated the alignment of the confocal microscope. After outcoupling the light, a 750 nm short-pass filter limited fluorescence caused by scattering effects in the fibre. Next, half wave plate (HWP) / polarising beam splitter (PBS) combination was used to adjust the optical power. The reflected beam was recorded to monitor power drifts.

A beam sampler (BS) directed a fraction of the incident beam into the microscope objective mounted in a helium flow cryostat. The objective was mounted on a piezo scanner which enabled a translation of the focal spot through the diamond sample. The sample was moulded into a coin-sized indium chip and then fixed to the cold finger of the cryostat. Even though the latter reached a temperature of ca. 4.2 K, heat flow from surrounding elements increased the sample's temperature to ca. 5 K. A vacuum pump provided a pressure of 10^{-7} mbar.

Fluorescence of the sample was collected by the objective. Given the incident beam was focussed onto a SiV^- centre, the emitted fluorescence left the objective collimated. It passed through the anti-reflection coated side of the BS and a band-pass filter. To detect the whole spectrum of the SiV^- centre, a 750/40 filter was placed in the beam path. When measuring PLE spectra, a 780/60 filter was used to block laser light. Information about the state of the centre was thereby read off from fluorescence with a wavelength larger than 750 nm, which is, as it will be also shown, emission associated to the phononic sideband [153].

Table 2.1: Components involved in the experiment.

Component	Company	Model (Specifications)
Ti:Sa laser	*Sirah*	Matisse TS, MOS-1
Diode laser	*Laser Quantum*	gem 532
Wavemeter	*High Finesse*	WS Ultimate 30
AOM	*Crystal Technology Inc.*	AOMO 3200-146
PM-PCF	*NKT Photonics*	LMA-PM-10
BS	*Thorlabs*	BSF20-B
Objective	*Olympus*	UMPlan Fl (100×, 0.95 NA)
Piezo scanner	*Physik Instrumente GmbH & Co. KG*	P-562.6CD PIMars (3D travel range: 200 µm)
Flow cryostat	*CryoVac*	KONTI (mod., He)
Spectrometer	*Princeton Instruments*	Acton SP2500 (1200 L/mm, Pixis 100 Model 7515-0015)
Counting card	*Fast ComTec*	MCS6A-2T2
APD	*Excelitas Technologies*	SPCM-AQRH 14

To complete the confocal microscope, the beam was focussed through a 25 µm pinhole. After collimating the beam again, it was directed either to a spectrometer or to one or two avalanche photodiodes (APDs). Two APDs were used to record second order correlations $g^{(2)}$ [114, 181].

2.2.2 Nanodiamond preparation and characteristics

The nanodiamonds used for this experiment were provided by Davydov et al. who employed a technique similar to the high-pressure high-temperature (HPHT) technique [80]. HPHT techniques are known to yield low crystal distortion and thereby more uniform optical features compared to other techniques to synthetically grow nanodiamonds [72, 205]. During the growth process, Davydov et al. introduced SiH_4 compounds which enabled a formation of SiV^- centres. According to their report, the nanodiamond size range from nm to µm. Thus it was important to dilute and spread the nanodiamonds evenly over a substrate.

As substrate, a synthetic type-IIa diamond slide was used. In addition to very low fluorescence, its thermal conductivity is five time higher than the one of copper [284], which leveraged an effective cooling of the sample in our cryostat. Before spin-coating the nanodiamonds onto the diamond substrate, a H_2O_2 / H_2SO_4 (1:3) acid mix was prepared to remove compounds which might cause fluorescence. Next, ca. 1 µL of the beforehand diluted nanodiamond solution and held in an ultra-sonic bath to mitigate agglutination. Immediately after taking the diluted solution out of the ultra-sonic bath, it was spin-coated on the substrate.

To characterise the nanodiamond size, several substrates were prepared and examined under a scanning electron microscope (SEM). A SEM image is shown 2.8 and verifies that nanodiamonds smaller than 100 nm could be found. However, we also detected nanodiamonds of a few µm and agglutinated nanodiamonds. Because the resolution of our confocal microscope was limited to ca. 300 nm, smaller particles were not distinguishable. Thus, we decided to embed markers into the diamond substrate via focussed ion beam (FIB) milling. Such markers allow to localise appropriately sized nanodiamonds via SEM imaging first and identify the same site by confocal microscopy. The FIB process was carried out by U. Jantzen. Marked substrates were utilised after my stay.

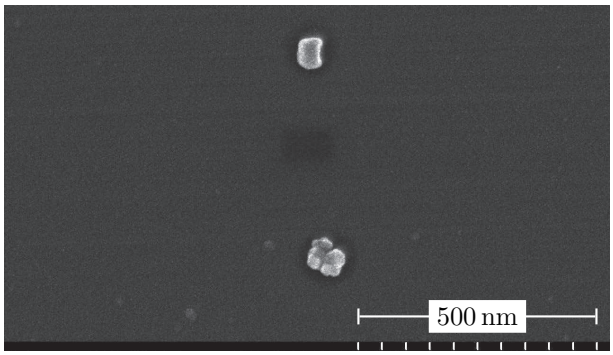

Figure 2.8: SEM image of SiV^- nanodiamonds on platinum coated type-IIa diamond substrate. The imaged nanodiamonds have a size of ca. 80 nm. While the upper particle is a single nanodiamond, the lower one is formed of agglutinated nanodiamonds. Paul Walther, head of the electron microscopy institute at the University of Ulm, granted us access to the SEM and gave advice for its use.

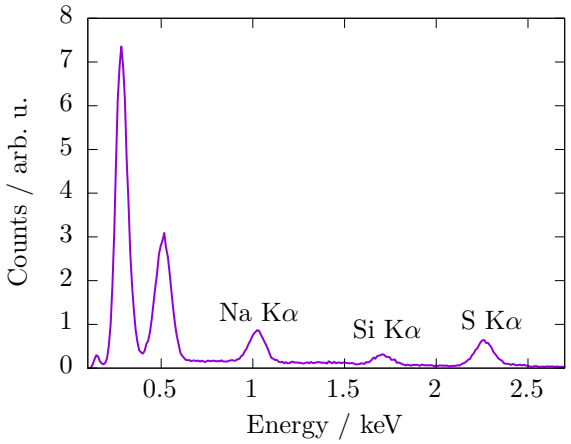

Figure 2.9: EDXA of SiV^- nanodiamond on type-IIa diamond substrate. The sample was not coated with conducting components prior to the analysis, because we did not intend to take high resolution SEM images. The electron beam was focussed on nanodiamonds similar to the ones shown in figure 2.8. Elements with low masses (atomic number less than 11) can not be routinely characterised via EDXA [118]. The first two strong peaks stem probably from carbon and oxygen (0.5 keV).

In addition to SEM, energy-dispersive X-ray spectroscopy (EDXA) was utilised for an elemental analysis of the sample. As the results in figure 2.9 proof, silicon was found in the nanodiamonds. Besides silicon, sulphur and sodium were detected in the spectrum. We assumed that sulphur and sodium stem from buffer solutions to stabilise the pH value of the original nanodiamond solution.

2.2.3 Spectral properties of SiV^- nanodiamonds at cryogenic temperatures

Off-resonant excitation

Spectral properties at cryogenic temperatures were first investigated via off-resonant excitation to study the full spectrum of SiV^- emission. After localising bright and diffraction limited spots, the 532 nm laser was used to excite PL. Fluorescence was recorded with the optical spectrometer. A typical spectrum is presented in figure 2.10. Here, the characteristics of a SiV^- PL spectrum for bulk diamond can be seen: Pronounced ZPL emission and a phonon sideband of ca. 20 nm width. To characterise the spectral distribution of our SiV^- nanodiamonds, ten PL spectra of different nanodiamonds were recorded and averaged. The averaged spectrum, shown in figure 2.11, was fitted to the Lorentz distribution

$$f(\lambda) = a + b\frac{\ell^2}{(\lambda - \lambda_0)^2 + \ell^2}, \tag{2.10}$$

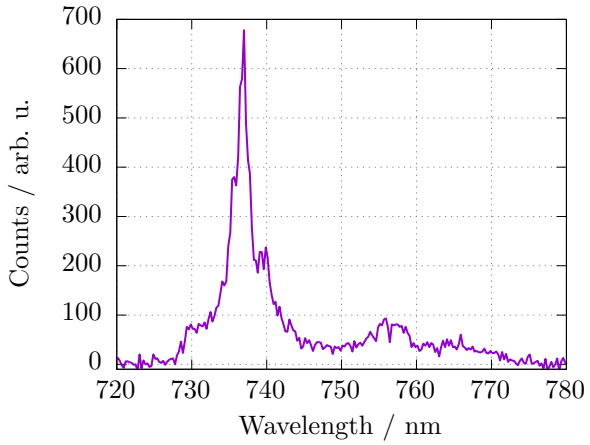

Figure 2.10: PL spectrum of a nanodiamond containing SiV^- centres, recorded at 5 K with 25 µW optical pump power at 532 nm. Optical power was measured in front of the microscope objective. The spectrum was acquired over 100 s and corrected for dark counts. A 750/40 bandpass filter was placed in front of the detection stage. Most noticeable is the peak at the ZPL. The peaks at longer wavelengths stem from the phonon sideband.

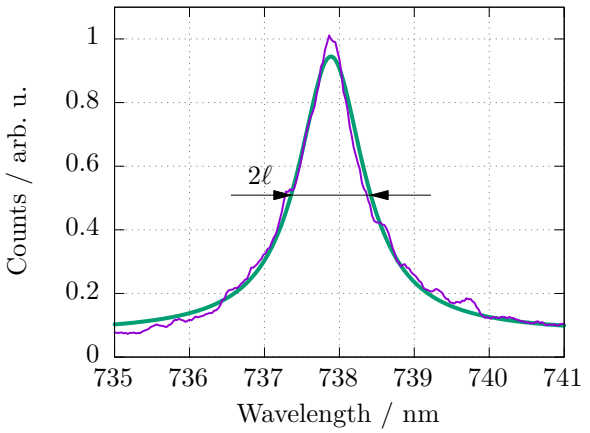

Figure 2.11: Averaged PL spectrum of ten SiV^- nanodiamonds. Individual spectra were excited with 532 nm light. The solid line is derived from a fit to equation (2.10). Parameters were estimated to $a = 0.074(3)$, $b = 0.87(1)$, $\lambda_0 = 737.89(1)$ nm and $\ell = 0.53(1)$ nm.

where ℓ is the half-width-half-maximum (HWHM) linewidth, λ_0 is the median of the distribution and a, b are parameters to correct for data offset. From the fit, we found $\lambda_0 = 737.89(1)$ nm, and $\ell = 0.53(1)$ nm. The linewidth is broader than for SiV^- centres in low-strain bulk diamond, but almost five-times more narrow than for previous ensemble-studies on SiV^- nanodiamond [11]. This indicates that the fabrication technique applied by Davydov et al. yields more uniform optical properties.

In a consecutive study by A. B. Kurz and U. Jantzen, the actual number of SiV^- centres contained in nanodiamonds was estimated via $g^{(2)}$ intensity autocorrelation [114]. It was found that at least six centres contributed to PL [154]. However, the PL from most SiV^- nanodiamonds did not yield a $g^{(2)}$ signal which exhibited single-photon characteristics, implying that much more SiV^- centres contributed to the emission.

Resonant excitation

By using a resonant excitation instead and probing PLE spectra, we were able to resolve individual lines in the fluorescence of SiV^- nanodiamonds. Despite the fact that multiple SiV^- centres were contained in nanodiamond, resonant excitation allows for addressing individual emitters assuming that the individual emission lines of the centres are not overlapping and broader

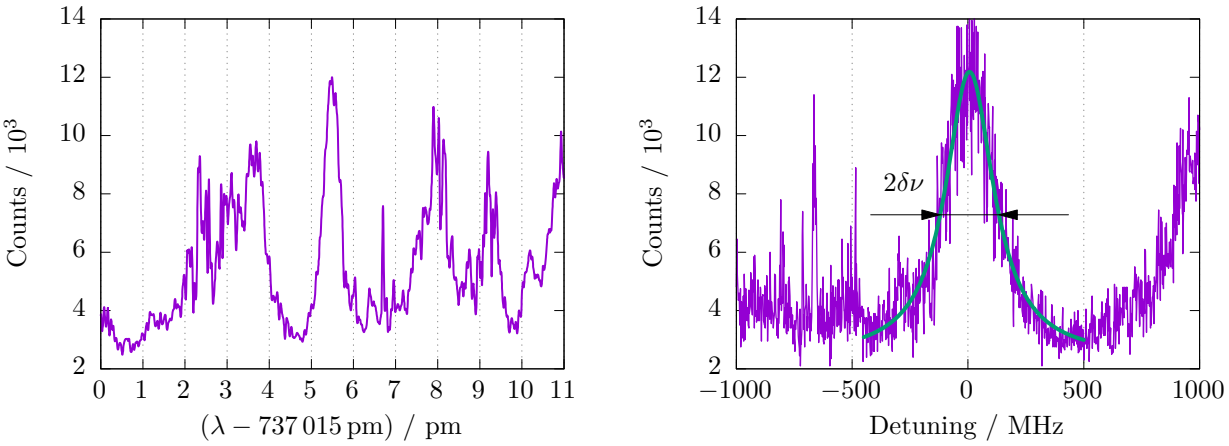

(a) PLE spectrum (b) Relative detuning

Figure 2.12: (a) Low-pass filtered PLE spectrum of SiV^- nanodiamond. To mitigate power broadening, the optical excitation power was set to less than 50 nW [152, 232]. The laser frequency was swept at a rate of 100 MHz s^{-1} over the shown spectrum. (b) The raw PLE spectrum in terms of a relative frequency shift. The solid line is derived from a fit to the Lorentz distribution (2.10) with $a = 2.38(12)$, $b = 9.80(16)$, $\nu_0 = 6.7(19)$ MHz and $\delta\nu = 127.0(44)$ MHz, where ν_0 is the frequency shift from the null position (406.763 THz ≡ 737 020.5 pm) and $\delta\nu$ the HWHM linewidth.

than the excitation linewidth. The latter assumption certainly applied for our measurement, as the Ti:Sa laser had a linewidth of ca. 50 kHz. To distinguish between scattered laser light and SiV^- PL, we used a 780/50 band-pass filter and thus detected emission from the phonon sideband. Figure 2.12 illustrates a typical PLE spectrum. Two features are prominent in the spectrum: A clear peak in the centre and other less defined peaks. In figure 2.12(b), the linewidth $\delta\nu$ of the central peak is shown and estimated to 127.0(44) MHz. Compared with the smallest SiV^- linewidth in bulk diamond, $\delta\nu$ is about two-times wider and underlines thereby the promising features of the novel fabrication technique. The other peaks, such as the spike to the right, were found to blink strongly, i.e. switching on and off, over time. Thus, the less defined peaks just partly uncover their actual spectrum. In fact, we found that none of the recorded PLE spectra exhibit a temporal stability. This instability can be seen in figure 2.13. The plot shows a PLE spectrum where the laser frequency was manually scanned six times. As it can be seen, the PLE spectrum shifts in a range of ca. 5 pm. In addition, the PLE intensity and line shape changed.

By switching to off-resonant excitation at 532 nm between the scans, we investigated whether it was possible to initialise the SiV^- state. This method did however not yield any observable difference.

After my colleagues automatised the laser-frequency tuning to cover in each scan the same frequency range, PLE spectra of different SiV^- nanodiamonds were recorded in this fashion. We interpreted the line shift as spectral diffusion, so they shifted each scan block and averaged them. It was found that the averaged linewidth was around 350 MHz [154] and hence consistent with the herein presented results.

The nature behind the observed spectral diffusion, which is strong compared to SiV^- in bulk

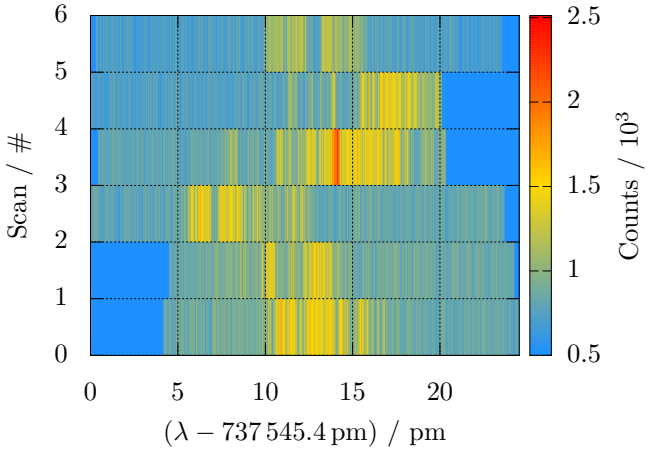

Figure 2.13: Six consecutively recorded PLE spectra of a SiV^- nanodiamond covering a wavelength range of 25 pm. Each horizontal block is a spectrum similar to spectrum 2.12(a). After a block was recorded, the laser frequency was swept in the other direction. The recording took 600 s, i.e. on average 100 s per block. As the change of laser frequency was controlled manually, the frequency range and offset was not kept constant.

diamond, and blinking effects has not been understood yet. A hypothesis for blinking is that, in analogy to the NV^- / NV^0 system, photo-ionisation transfers the SiV^- centre to its neutral charge state SiV^0. The SiV^0 centre is known and associated with a ZPL at 946 nm [199]. As the SiV^0 ZPL is furthermore only weakly fluorescent, we could not check for its presence in our setup.

Another hypothesis, which also explains the observed spectral diffusion, comes from the fact that multiple SiV^- centres were contained in a nanodiamond and thus interact with each other. A similar reasoning is that other photo-activated effects interact with the SiV^- centre. In bulk, SiV^- centres are known to be comparably insensitive to electric field and strain perturbations, but by virtue of the close proximity to the enlarged effective surface area, the centre might become more susceptible to such effects [232, 256]. The footprint of sulphur and potassium found via EDXA (cf. figure 2.9) poses a potential reason for surface effects causing an electric field perturbation. In summary, an improved control over the nanodiamond growth process seems to be required to harness the potential of SiV^- centres in nanodiamond.

2.2.4 Extended orbital relaxation time

Due to the spectral shifting and blinking, the prospects of measuring an extended orbital relaxation time were rather modest. However, as the experimental scheme described on page 21 relies on numerous repetitions, we conducted the experiment – given that the spectral instabilities occur randomly and at rates faster than the measurement, an extended T_1^{orbit} could still be measurable.

The pulse scheme sketched in figure 2.4 was implemented as a series of 30 pulses. Each laser / detection pulse was 1 µs long and repeated after a pause time incremented in steps of 0.1 µs. Thus, a complete pulse sequence took $30 \cdot 1\,\mu s + \sum_{i=0}^{29} 0.1\,\mu s(1+i) = 76.5\,\mu s$ and was sampled every 0.8 ns. This provides to an effective T_1^{orbit} "detection range" of approximately 4 µs to 70 µs. At a laser power of 30(3) nW, which was chosen to mitigate power broadening effects, more than $120 \cdot 10^6$ pulse sequences were acquired in 5.3 h. Every 60 s, an automatised process mapped out the PL over a volume of $0.8^3\,\mu m^3$. The centroid of the PL intensity map was estimated and used to re-focus the microscope objective. The largest drift was measured in the longitudinal direction. Over the measurement time, the focal spot was re-adjusted by ca. 10 µm.

To analyse the acquired data according to our scheme, each pulse had to be extracted first. Instead of manually selecting each pulse, we picked the first pulse and used it to calculate a cross-

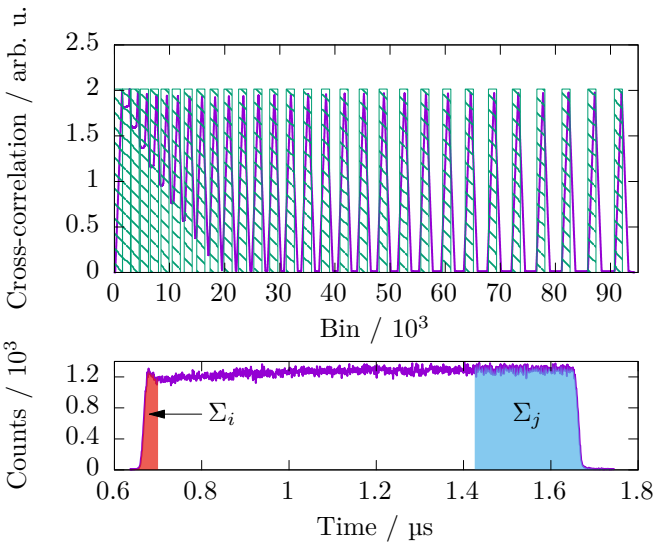

Figure 2.14: The lower plot shows the first detected pulse. It was manually selected and then used to calculate a cross-correlation with the acquired data. Filled areas highlight the sums used in the analysis shown next.
The upper plot presents the cross-correlation between the shown pulse and the complete acquired data. Hatched areas label regions where each pulse was, according to our pulse pattern, known to be found. To localise a pulse, the maximum in each region was extracted.

correlation with the whole sequence. The result can be seen in figure 2.14. Next, the maxima in the cross-correlation were extracted, which provided an exact localisation of each pulse.

Finally, the counts in the leading peak of every pulse were summed. To provide a normalisation measure, counts in the pulse tail were summed as well. As it can be observed in figure 2.15, the ratio of the two latter sums does not correspond to the expected behaviour which is illustrated in the lower panel of figure 2.4. In fact, the ratio develops somewhat opposite to our expectation. Only looking at the ratio, one might conclude that a process with a characteristic time of less than 5 µs governs the evolution. However, the summed counts in the last bins, shown in the middle plot, stress that this can not be the sole process: The dip of ca. 3 % at 10 µs recovers with a characteristic time of another 10 µs.

Due to the long recording time, the stability of the setup and the individual normalisation of each pulse we have no evident suspicion that the observed features stem form technical issues. The features might indicate that the basic Λ scheme is insufficient to describe the physical system properly. As of today, the experiment has not been repeated, such that no additional evidence could vindicate this assumption.

2.3 Conclusion and outlook

In this study, spectral properties of SiV^- centres in nanodiamond were investigated. The initial goal to extend the spin decoherence T_2^* by suppressing phonon vibrations at 50 GHz using SiV^- nanodiamond was not reached, however we identified limiting factors and furthermore promising features. First, we have measured a spectral distribution of the SiV^- ZPL across several nanodiamonds of 1.06 nm (FWHM). Second, via resonant excitation, transition linewidths of 350 MHz were demonstrated. Both features have not been reported for SiV^- nanodiamond before and thus highlight that the novel nanodiamond fabrication technique yields improved crystal qualities. Due to spectral diffusion and blinking effects which are likely caused by the interaction with near-by defects or surface effects, the direct application of SiV^- nanodiamond is limited. Yet, this issue is not unique for the utilised SiV^- nanodiamonds and is expected to be tackled by surface treatment.

Given that advances in nano fabrication can solve the reported challenges, the narrow optical

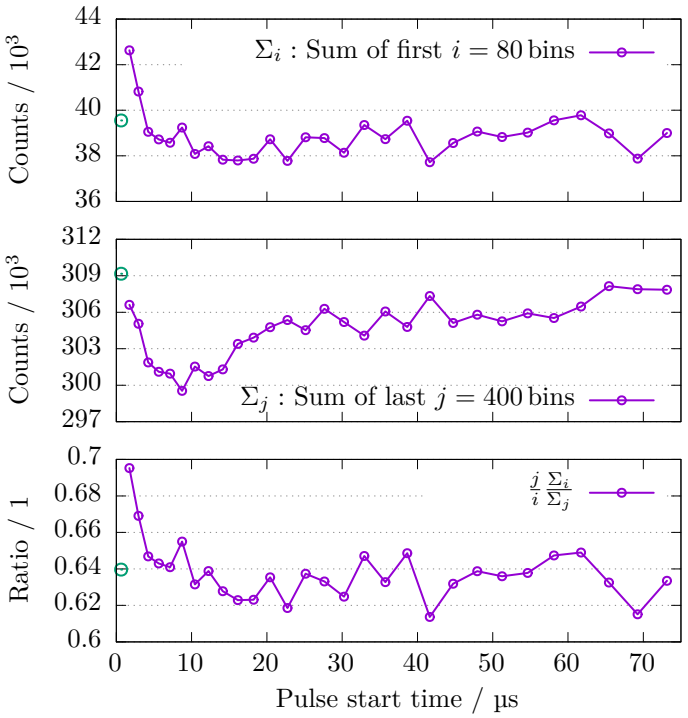

Figure 2.15: Data analysis of the T_1^{orbit} measurement. A green circle corresponds to the 'off' detection pulse in figure 2.15. The upper figure shows the sum of the counts in the first 80 bins, which contained the important leading edge feature. The middle figure shows the count-sum of the last 400 bins. The normalised ratio of the sums is presented in the last plot.

linewidth qualify SiV^- nanodiamond as highly attractive emitters for use in quantum optics. The ability to move and place nanodiamonds manually led already to experiments where NV^- nanodiamonds in micro cavities were used to demonstrate Purcell enhancement and narrowband single photon sources [6, 160]. The use of SiV^-- instead of NV^- nanodiamonds offers certain benefits. First, the inherently stronger ZPL allows for higher quantum efficiency and, second, the fact that the SiV^- ZPL is ca. 100 nm above the NV^- ZPL (637 nm) makes the fabrication of high finesse micro cavities less demanding, because detrimental scattering effects scale as $\sim 1/\lambda$. The ability to fabricate high finesse micro cavities[6] is the main challenge to enter the strong coupling regime, which enables the study of fundamental aspects and applications in quantum optics, e.g. triggered single photon sources and such fascinating phenomena as photon blockade [30, 42, 277].

[6]The prospects for optical micro cavities have also motivated us to initialise cavity experiments. During the thesis, an automatised interferometer and a special assembly required for the storage and coating of optical elements was designed and built from scratch. Details about these projects can be found in appendix A.4.

3 | Quantum enhanced phase measurements

3.1 Introduction

Phase measurements by optical interferometry is a ubiquitous tool, with applications ranging from biological studies [266], over profiling surfaces [187], to sensing gravitational waves for fundamental research [177]. Optical interferometry gained success quickly after A. A. Michelson's invention of a setup now known as the Michelson interferometer [192]. The Michelson–Morley experiment performed in 1887 to probe "the relative motion of the Earth and the luminiferous ether" [193] yielded a negative result, in that the predicted relative motion was not measurable. However, it supported earlier experimental findings by H. Fizeau that caused controversy about luminiferous (meaning light-bearing) ether theories [259]. And it stirred up the search for new theories about the relationship between space and time – which eventually led to the special theory of relativity.

A cornerstone in interferometry, and metrology in general, was then set by quantum mechanics: Due to Heisenberg's uncertainty relation, a definite limit of the measurement's certainty was found. The name giver of this relation himself put forth a thought experiment [134], now known as Heisenberg's microscope. It pedagogically depicts the constraint of knowing a particle's position when probed by photons. Even though the original explanation showed to be misleading [237], an extension of his picture vindicates the usage of it [47]. In retrospective, this thought experiment was challenged in various ways ever since, either by preparing the probe state in ways only accessible by quantum mechanics, or by measuring the state after the interaction.

Achievements of these attempts are techniques which enhance the sensing of phase changes, referred to as super sensitivity and super resolution. From an experimental point of view, the limits which have to be surpassed to qualify a measurement of being super sensitive or -resolved is set by an interferometer configuration which employs the "'most classical' quantum state" [114, p. 43], namely a coherent state, and whose output is probed in the "most classical" way, which is realised by directly monitoring the beam's power as it leaves the device. In this configuration, the interaction between photons and sample can be pictured as a passing of individual, uncorrelated, photons through the sample. To achieve an enhanced sensing, one might change either the properties of the input state or the detection process, which comprises a physical detection, i.e. absorption of photons, and a processing of the acquired data.

Even though our study is restricted to sensing a phase shift in an optical interferometer, we note that the general concept of overcoming 'classical limits' by harnessing quantum effects applies to other types of interferometry, such as atom interferometers [76], and further also spatial resolution concepts such as the Rayleigh criterion [34, 133] which may find application in, amongst others, lithography [36]. From another point of view, phase measurements and

quantum computation are on equal footing. This connection is based on the insight that quantum algorithms can be related back to estimating the phase of the quantum bit as it's tracing through the quantum computer's clockwork [96]. New results in either field might thereby influence each other and help to harness the resources for quantum computation most effectively.

Chapter structure We will specify the resolution and sensitivity criteria further and name experimental concepts to meet those criteria. Based on the challenges faced by the latter, a motivation of our approach will be given. Before analysing the technique we applied, an introduction to phase estimation and the concept of Fisher information starts the theoretical part. The reader will also find a short summary of squeezed states of light, as it is an essential element of the experiment. Next, the experimental section starts with a description of the generation of squeezed light before explaining the actual interferometer setup. A summary of the results and an outlook concludes this chapter.

3.1.1 Motivation of our measurement scheme

In a standard single-pass interferometer, as depicted in figure 3.1(a), the interference effect arising from the coherence of electromagnetic waves creates a fringe pattern with a periodicity set by half of the wavelength [133]. The full width half maximum (FWHM) of the fringe determines the resolution. When attained by classical means, the resulting FWHM is commonly referred to as the Rayleigh criterion. Figure 3.1(b) visualises this measure. Overcoming the Rayleigh criterion is termed as super resolution and was achieved with entangled photons created by spontaneous parametric down-conversion [197, 227], post-selection techniques [197, 228] and a post-processing technique put forth by Distante et al. [88]. It is an extension of the latter technique our approach is based on.

Next to the fringe resolution, the quantum shot noise limit (SNL) is another boundary of interferometry, setting the sensitivity of the measurement. Unlike the resolution feature, this boundary can not be termed as classical any more, as the SNL is due to quantum fluctuations [114, 181]. Thus, to visualise this characteristic, figure 3.1 needs to be redrawn: A "quantum picture" can be seen in figure 3.2 and 3.3 on page 37 and will be theoretically elaborated in a next section. Beating the SNL qualifies the measurement for being super sensitive. According to quantum estimation theory [136], the quantum Cramér–Rao bound, or equally the Heisenberg limit introduced in the following section, constitutes the ultimate bound of the sensitivity, which can be saturated by, e.g., squeezed input states [55, 116].

Combining both super sensitive and super resolving features is known to be achievable via "NOON" states [240], defined as a coherent superposition of n photons passing through either arm of the interferometer:

$$|\psi\rangle = \frac{1}{\sqrt{2}}(|n,0\rangle - |0,n\rangle). \tag{3.1}$$

We will shortly see what the reasoning behind this is. Another proposal was put forth by Anisimov et al. It is based on parity detection [10], where one needs to tell apart an even from an odd photon number state.

The fundamental drawback of using NOON states is their susceptibility to losses [115, 145]. A number of detailed studies investigated the influence of losses mathematically and experimentally [79, 82, 91, 159]. Photon losses can occur in the setup itself, e.g. due to absorption at optics. The largest contribution to losses can however usually be attributed to detection efficiencies: Depending on the wavelength, standard single photon counting detectors offer efficiencies in the range of 20 % to 40 %. State of the art photon counting detectors can have efficiencies of 95 %,

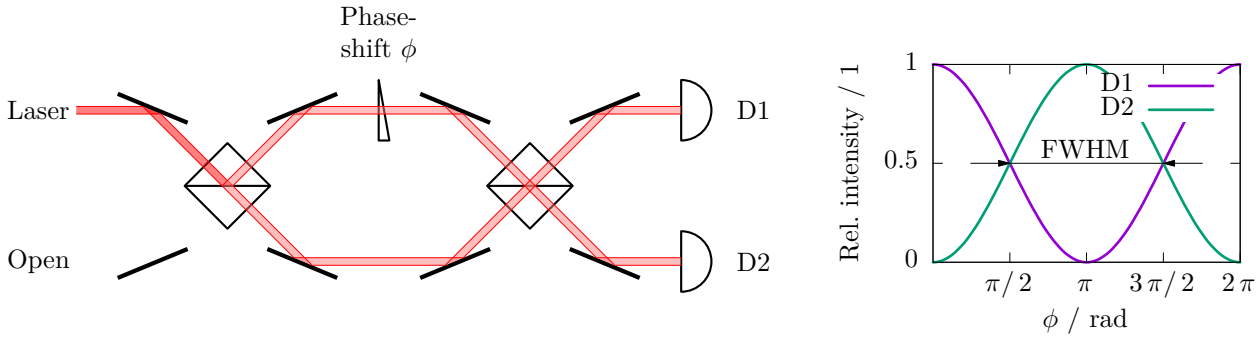

(a) Single pass Mach–Zehnder interferometer

(b) Fringe pattern for a classical description

Figure 3.1: (a) A scheme of a single pass Mach–Zehnder interferometer from a classical point of view. 'Single pass' means that the phase shifting element is passed only once. A laser beam is sent into the upper mode. The second input mode is left unused. A phase shift is imparted on the mode travelling through the upper arm. It can be realised by various means: As depicted, by a wedged glass plate, or, more generally, a sample with a variation in refractive index. Another means is to actuate one of the four mirrors between the two beam splitters by a piezoelectric device. At the output, two photodetectors, D1 and D2, record the intensity.
(b) The observed fringe pattern, assuming that the in- and output is treated as classical. The recorded intensity is normed to the input intensity. Given a perfect alignment, and unity transmission and detection efficiencies, the fringe visibility is 100 %, that is the relative intensity is modulated between zero and one. The full width half maximum (FWHM) marks the attainable resolution.

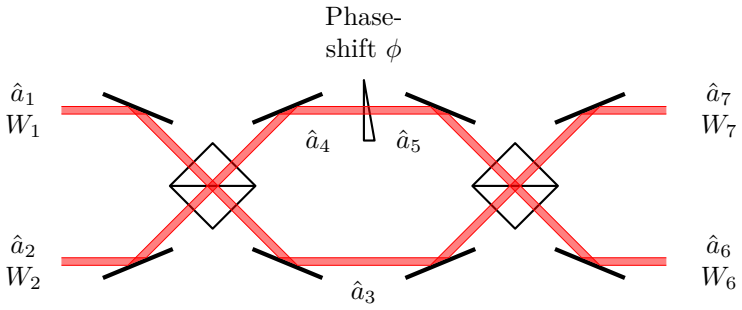

Figure 3.2: Indexing of modes and Wigner functions in a Mach–Zehnder interferometer applied for a quantum mechanical treatment. The modes are denoted by annihilation operators $\hat{a}$. To visualise the in- and output modes, Wigner functions W are used.

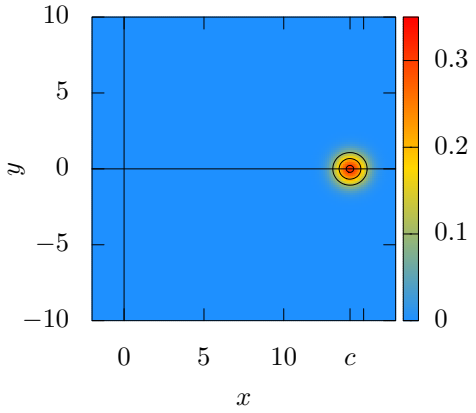

(a) W_1: Amplitude-displaced coherent state

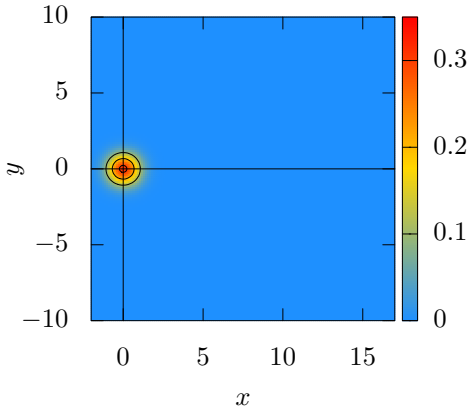

(b) W_2: Vacuum state

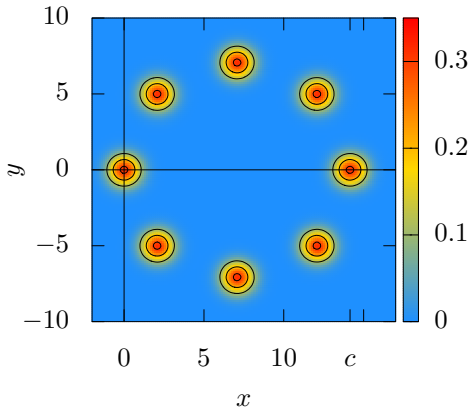

(c) W_7: Output mode undergoing a phase change

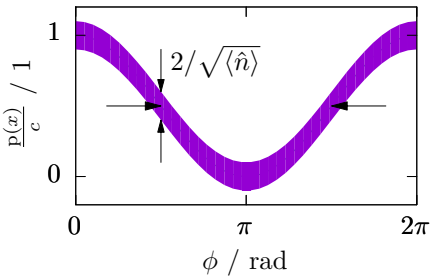

(d) Marginal distribution of W_7 along $\hat{X}$ quadrature

Figure 3.3: (a) Wigner function of the input state in mode 1. The indexing is in accordance with figure 3.2. The amplitude of the displacement (section 1.2.1 introduces the terminology) is $c = \sqrt{2}\Re(\alpha)$ with $\alpha = 10$.
(b) Wigner function of the second input mode. As it is left unused in this configuration, it shows the vacuum state.
(c) Wigner function of the output mode 7 under a change of the phase ϕ. Eight "snapshots" visualise the Wigner function at $\phi = \frac{n}{4}\pi$, $n \in \{0, \ldots, 7\}$. At $\phi = 0$, W_2 is mapped directly to W_7. At $\phi = \pi$, W_1 can be detected in this mode. For mode 6, the opposite applies, however with an additional sign change. That is the whole distribution of W_6 is displaced by c along the amplitude quadrature.
(d) The marginal distribution along the amplitude quadrature normed to c. It recreates the behaviour shown in figure 3.1(b) in terms of resolution, but now shot noise is imprinted on the signal. When normed to c, the standard deviation is, according to equation (1.17), $1/\sqrt{\langle\hat{n}\rangle}$.

but an operation at 100 mK is required to reach this value [179]. In addition, to fully characterise NOON states, i.e. to perform a state tomography, one can either attempt to perform a homodyne detection or to resolve the actual photon number [150]. On the one hand, technical difficulties render a homodyne detection on single photon states inefficient: Lvovsky et al. reported 55 % for a single photon state $|1\rangle$ [5, 186]. On the other, photon number resolving detectors can reach efficiencies of 43 % and also rely on an operation at cryogenic temperatures [50]. This issue of detection (in)efficiencies applies for the proposal of Anisimov et al. as well, since it requires parity detection.

Finally, schemes employing NOON states, or, more general, states with a discrete photon number, require a reliable and preferably on-demand single photon source.

To overcome the named hurdles, post-processing techniques are commonly applied to omit those events where a photon was lost or the creation of the input state failed [156, 197]. This implies that the sample which causes the phase shift in the interferometer was subject to more photons than taken into account. It not only poses a concern in scenarios where the input power has to be minimal to prevent from optical damage, which applies when examining the phase shift induced by a biological samples [266, 267], it is also a fundamental issue: As we will see, the sensitivity is derived from the number of photons which experience a phase shift. If those are omitted which get lost after a phase shift was imprinted on them, the sensitivity is artificially increased.

Our motivation was to experimentally achieve super resolution and super sensitivity and to address the mentioned issue by harnessing the advantages of Gaussian states and detection techniques[1]. Due to the continuous nature of Gaussian states, this should yield a fully deterministic approach. Furthermore, the detection of such states via the homodyne technique, described on page 7, allows for efficiencies larger than 98 % without requiring cooling or otherwise expensive components [16, 94]. On top of that, a homodyne setup has shown to be optimal in terms of sensing – when used for the coherent state in particular, but also for Gaussian states in general [200].

3.2 Theoretical framework

The theoretical analysis starts by describing the special challenges met when measuring a phase shift. Next the transformation of quadratures due to a phase shift will be derived. To be able to quantify phase measurement techniques, the Fisher information is discussed. Then the relation between Fisher information and the measure of sensitivity is given. By these means, a few interferometer configurations are compared. Thereby readers familiar with one or the other concept can relate the experimental results to the respective measure.

Based on the introduced operations and measures, our approach is finally treated.

The emphasis in the theoretical section is put on concepts and fundamental properties of phase measurements, rather than technical details. Readers unfamiliar with this topic might find thereby an easier access to it, as the works we refer to usually assume an understanding of such concepts and properties.

3.2.1 Challenges of phase measurements

This section describes how information of a phase shift on a quantum state can be gained.

[1] These states and detection strategies can be represented by Gaussian operators, which are defined as operators that transform Gaussian states only in Gaussian states [99]. Refer also to page 15.

Most often for reasons of convenience, the suffix 'shift' is omitted in literature and unless an ambiguous understanding might occur, it will be dropped herein as well. Nonetheless, we would like to remind that the measurement of the phase is inherently connected with delicate issues: One of the obvious problems is the periodicity of the phase; without any other (arbitrary) static reference the outcome is rendered meaningless. From an experimental point of view, the need for a reference already implies that only by means of an interferometer a phase can be measured. This problem is not inherently a quantum mechanical one, but it brings forth trouble when "looking" for a Hermitian phase operator and its complementary observable. For a comparison of different approaches towards a Hermitian phase operator, the reader may refer to Gerry and Knight [114].

The obstacles of defining a Hermitian phase operator are however not a hurdle when dealing with the estimation of a phase shift as a p a r a m e t e r. Here, one does not seek to realise an apparatus that measures an eigenvalue of the phase operator, but rather utilises an estimator which finally relates another (accessible) quantity to the parameter – the phase ϕ. The design of the estimator constraints how much information we can infer about ϕ. On the baseline of an estimator is a function which tells how probable it is to have measured a certain quantity, given a certain value of ϕ. For a meaningful estimation, the measured quantity hence needs to be correlated to the phase. Figure 3.3(d) shows clearly that an interferometer probed via homodyne detection is a way to gather information about ϕ. So the question an estimator in this case answers is: How probable is it to measure $\mathrm{p}(x)/c = 1$ given $\phi = 0$?

From what is stated above – and in dependence of the terminological standpoint –, the notion of phase m e a s u r e m e n t might be misleading. The term 'phase measurement by inference' is certainly less ambiguous. Due to its length (and common practice) we will stick with the short form and mind that knowledge about the phase is only gained indirectly.

3.2.2 Operator representation of a phase shift transformation

When trying to learn something about a phase, the first question might be: How does one model the phase shift? An answer can be given in the Heisenberg picture, by describing the interaction in terms of a transformation of the ladder operators $\hat{a}$ and $\hat{a}^\dagger$ which are introduced on page 7. Assuming a lossless case, one can understand the interaction as an annihilation of the incoming photon followed by the creation of a photon with its phase shifted by ϕ. This is the single-mode analogue of a beam splitter transformation (cf. equation (1.32)). Thus the unitary operator reads

$$\hat{U}_\phi = \exp\big(\imath\phi\hat{a}^\dagger\hat{a}\big) = \exp(\imath\phi\hat{n}). \tag{3.2}$$

The dependence on $\hat{n}$ is the reason why NOON states achieve super resolution: A $|n,0\rangle$ state launched into the interferometer in figure 3.2 makes a NOON state after the first beam splitter. As the phase shift in the sensing arm is of the given form, the state in front of the second beam splitter reads

$$|\psi\rangle = \frac{1}{\sqrt{2}}\big(|n,0\rangle + \mathrm{e}^{\imath\phi n}|0,n\rangle\big), \tag{3.3}$$

that is, a set of n photons picks up a phase shift n times[2].

To discuss different (experimental) realisations that infer something about ϕ, a convenient way is to work with Wigner functions introduced in section 1.2.4. Starting from a known Wigner

[2] To achieve this with a classical interferometer, a laser with half the wavelength can be employed. This suggests that the energy deposited by a NOON states increase in the same way as doubling the frequency does.

function at the interferometer's input, the Wigner function at the output is found by transforming the conjugate quadrature operators $\hat{X}$ and $\hat{Y}$, i.e. by a transformation of the initial coordinate system [53, 285]. This simple recipe only applies when Gaussian operations are to be handled, so operations that do not send a Gaussian to a non-Gaussian state. To figure out how the quadratures are transformed by (3.2), we need to find $\hat{U}_\phi^\dagger \hat{X} \hat{U}_\phi$. For $\hat{X}$, this reads

$$\mathrm{e}^{\imath\phi\hat{n}}\,\hat{X}\,\mathrm{e}^{-\imath\phi\hat{n}}\,. \tag{3.4}$$

The Baker–Campbell–Hausdorff lemma [239]

$$\mathrm{e}^{\imath\vartheta\hat{A}}\,\hat{B}\,\mathrm{e}^{-\imath\vartheta\hat{A}} = \hat{B} + \imath\vartheta[\hat{A},\hat{B}] + \frac{(\imath\vartheta)^2}{2!}[\hat{A},[\hat{A},\hat{B}]] + \frac{(\imath\vartheta)^3}{3!}[\hat{A},[\hat{A},[\hat{A},\hat{B}]]] + \cdots \tag{3.5}$$

may be applied to find the solution. With the commutator relation (1.8a) and

$$\hat{X} = \frac{\hat{a}+\hat{a}^\dagger}{\sqrt{2}}, \tag{3.6a}$$

$$\hat{Y} = \frac{\hat{a}-\hat{a}^\dagger}{\imath\sqrt{2}}, \tag{3.6b}$$

we arrive at

$$\big[\hat{n},\hat{X}\big] = \frac{\hat{a}^\dagger-\hat{a}}{\sqrt{2}} = -\imath\hat{Y}, \tag{3.7a}$$

$$\big[\hat{n},\hat{Y}\big] = \frac{-\hat{a}^\dagger-\hat{a}}{\imath\sqrt{2}} = -\frac{1}{\imath}\hat{X}. \tag{3.7b}$$

Checking for the "second order" nesting of the commutator returns the initial quadratures:

$$\big[\hat{n},-\imath\hat{Y}\big] = \hat{X}, \tag{3.8a}$$

$$\big[\hat{n},-\hat{X}/\imath\big] = \hat{Y}. \tag{3.8b}$$

Next these results are arranged according to their power:

$$\begin{aligned}\hat{U}_\phi^\dagger\hat{X}\hat{U}_\phi &= \hat{X} + \imath\phi\Big(-\imath\hat{Y}\Big) + \left(-\frac{\phi^2}{2!}\hat{X}\right) + \left(-\imath\frac{\phi^3}{3!}\right)\Big(-\imath\hat{Y}\Big) + \left(\frac{\phi^4}{4!}\hat{X}\right) + \cdots \\ &= \sum_{j=0}^{\infty}\frac{\phi^{2j}}{(2j)!}(-1)^j\hat{X} + \sum_{j=0}^{\infty}\frac{\phi^{2j+1}}{(2j+1)!}(-1)^j\hat{Y} \\ &= \cos(\phi)\hat{X} + \sin(\phi)\hat{Y}, \end{aligned} \tag{3.9a}$$

similarly we find

$$\hat{U}_\phi^\dagger\hat{Y}\hat{U}_\phi = \cos(\phi)\hat{Y} - \sin(\phi)\hat{X}. \tag{3.9b}$$

Thus the original coordinate system is undergoing a rotation. As an example, $\phi = \pi/2$ leads to $\hat{X} \mapsto \hat{Y}$ and $\hat{Y} \mapsto -\hat{X}$.

3.2.3 Estimation of the phase shift and the Fisher information

As outlined, we can not access the phase directly, so another means has to be employed. This means is a statistical estimator Φ, i.e. a measure that relates a quantity we k n o w to the phase,

which is the quantity we w a n t to know. Such a "knowable" quantity is, e.g., the amplitude $|\alpha|^2$, that is the average photon number $\langle\hat{n}\rangle = \bar{n}$ of a coherent state which leaves one of the interferometer's outputs.

The relation an estimator Φ builds is then described as follows: First, we assume to measure $\bar{n}$ photons given a phase of ϕ. We write the condition as '$\bar{n}|\phi$'. Since this measurement must come with an uncertainty – due to statistical and systematic uncertainties, and finally non-commuting operators–, a repeated measurement reveals the probability of $\bar{n}|\phi$, which we write as $\mathrm{p}(\bar{n}|\phi)$. Second, the way to infer knowledge from $\mathrm{p}(\bar{n}|\phi)$ defines the estimator $\Phi(\bar{n})$. This could be, e.g., the mean of $\mathrm{p}(\bar{n}|\phi)$. Finally, the estimator returns an estimate of the phase: $\Phi(\bar{n}) = \tilde{\phi}$.

When the estimator is set, a vital question is how well it performs in telling us ϕ. A good estimator should react quickly to a small change in the phase, so one asks how much $\mathrm{p}(\bar{n}|\phi)$ changes to $\mathrm{p}(\bar{n}|\phi + \delta\phi)$. To quantify the change, it is common to take the derivative of the logarithm of the conditional probability, i.e. $\frac{\partial}{\partial\phi} \ln \mathrm{p}(\bar{n}|\phi)$ [44]. Using the chain rule, $\frac{\partial}{\partial\phi} \ln \mathrm{p}(\bar{n}|\phi) = 1/\,\mathrm{p}(\bar{n}|\phi) \frac{\partial}{\partial\phi} \mathrm{p}(\bar{n}|\phi)$, which makes the interpretation easier: The result, in statistics known as the score, is a "normalised sensitivity".

To arrive at positive values for the score, it is squared. Then weighting the squared score by $\mathrm{p}(\bar{n}|\phi)$ and summing over all $\bar{n}$ defines the Fisher information [75]:

$$F(\phi) = \sum_{\bar{n}} \mathrm{p}(\bar{n}|\phi) \left(\frac{\partial}{\partial\phi} \ln \mathrm{p}(\bar{n}|\phi) \right)^2 = \sum_{\bar{n}} \frac{1}{\mathrm{p}(\bar{n}|\phi)} \left(\frac{\partial}{\partial\phi} \mathrm{p}(\bar{n}|\phi) \right)^2 \tag{3.10}$$

Changing from a summation to an integration, this definition equally applies for continuous variables. The Fisher information quantifies the information content that $\bar{n}$ carries about the (unknown) parameter ϕ.

3.2.4 Bounds of the estimation process

An important property of the Fisher information is that it provides the lower bound on the uncertainty of an estimator under a given probability function p, that is [75]

$$\mathrm{Var}(\Phi) \geq \frac{1}{F(\phi)}. \tag{3.11}$$

There might be another p that performs better, thus puts less uncertainty on the estimated parameter. The lowest reachable, in that sense optimal, constraint is named the Crámer–Rao bound, in reminiscence of the mathematicians who proved the inequality [75]. One way to derive it is by means of the Cauchy–Schwartz inequality [44] $|\langle x, y\rangle| \leq \|x\| \cdot \|y\|$.

$$\mathrm{Var}(\Phi) = \|x\| = \sum_{\bar{n}} \mathrm{p}(\bar{n}|\phi)(\Phi(\bar{n}) - \phi)^2, \tag{3.12a}$$

$$F(\phi) = \|y\| = \sum_{\bar{n}} \frac{1}{\mathrm{p}(\bar{n}|\phi)} \left(\frac{\partial}{\partial\phi} \mathrm{p}(\bar{n}|\phi) \right)^2, \tag{3.12b}$$

and so for the cross term

$$|\langle x, y\rangle| = \sum_{\bar{n}} (\Phi(\bar{n}) - \phi) \left(\frac{\partial}{\partial\phi} \mathrm{p}(\bar{n}|\phi) \right) = \frac{\partial}{\partial\phi} \sum_{\bar{n}} \Phi(\bar{n})\, \mathrm{p}(\bar{n}|\phi), \tag{3.12c}$$

which equals ϕ for an u n b i a s e d estimator, as the sum converges to 1. Assembling the last three equations yields equation (3.11).

In an experimental realisation one will probably measure $\bar{n}$ repeatedly. This is certainly true for a phase measurement, where a repetition means: Send i uncorrelated photons through the phase shifting element, i.e. the sample. To account for a repetition, the additivity of F has to be investigated. To derive it, we write out the Fisher information as

$$F_{a,b}(\phi) = \sum_{a,b} \mathrm{p}(a,b|\phi)\left(\frac{\partial}{\partial\phi}\ln \mathrm{p}(a,b|\phi)\right)^2. \tag{3.13}$$

For statistically independent variables, $\mathrm{p}(a,b|\phi) = \mathrm{p}(a|\phi)\,\mathrm{p}(b|\phi)$. Substituting it, we find

$$\begin{aligned} F_{a,b}(\phi) &= \sum_{a,b} \mathrm{p}(a,b|\phi)\left(\frac{\partial}{\partial\phi}\ln \mathrm{p}(a,b|\phi)\right)^2 \\ &= \sum_{a,b} \mathrm{p}(a|\phi)\,\mathrm{p}(b|\phi)\left(\frac{\partial}{\partial\phi}\ln(\mathrm{p}(a|\phi)\,\mathrm{p}(b|\phi))\right)^2, \end{aligned} \tag{3.14a}$$

and by introducing $\mathrm{p}(n|\phi) = p_n$, $\frac{\partial}{\partial\phi}p_n = p'_n$, and using the chain rule again,

$$\begin{aligned} &= \sum_{a,b} p_a p_b\left(\frac{\partial}{\partial\phi}(\ln p_a + \ln p_b)\right)^2 \\ &= \sum_{a,b} p_a p_b\left(\left(\frac{p'_a}{p_a}\right)^2 + \frac{2p'_a p'_b}{p_a p_b} + \left(\frac{p'_b}{p_b}\right)^2\right) \\ &= \sum_{a,b} \frac{p_b}{p_a}p'^2_a + 2p'_a p'_b + \frac{p_a}{p_b}p'^2_b. \end{aligned} \tag{3.14b}$$

Comparison to equation (3.10) and the completeness $\sum_i p_i = 1$ yields

$$= F_a(\phi) + \sum_{a,b} 2p'_a p'_b + F_b(\phi). \tag{3.14c}$$

Finally, the point symmetry of p'_i makes the middle term disappear, such that

$$F_{a,b}(\phi) = F_a(\phi) + F_b(\phi). \tag{3.14d}$$

The implication of the additivity is best exemplified by an interferometer with a certain configuration: Assuming a single photon input and a "photon or no photon" (known as 'click') detection, we find $F(\phi) = 1$. Sending in a second photon – uncorrelated to the first one – yields $F(\phi) = 2$, and so forth. Thus, dividing by the number of attempts is necessary when comparing the scaling of equation (3.11) for different input states. From another point of view, using a quantum state with uncorrelated photons, i.e. a coherent state with $\langle\hat{n}\rangle = \bar{n}$, this finding already suggests that $\mathrm{Var}(\Phi) \propto 1/\bar{n}$.

3.2.5 Quantum Fisher information and the Heisenberg limit

The Fisher information is a measure derived from classical probability distributions. Also in quantum mechanics, as Born's rule tells [35], any direct measurement outcome will follow such a distribution. Thus, in any case, F is a perfectly valid concept. However, the issue with F applied on quantum parameter estimation is that F does not cover all the available information on the

parameter, as it does not account for non-classical correlations. The extractable information of ϕ might be higher than it appears, thus F will no longer be a lower bound.

To account for this, a quantum version of F has been derived, called the quantum Fisher information H. The concept is to follow equation (3.10) and apply Born's rule

$$\mathrm{p}(x|\phi) = |\langle x|\psi\rangle|^2 = \mathrm{tr}\big(\hat{\rho}\hat{\Pi}_x\big), \tag{3.15}$$

where $\hat{\Pi}_x = |x\rangle\langle x|$ are elements of a positive-operator valued measure describing the measurement process of the quantum state represented by a density matrix $\hat{\rho}$ [23]. The reason for choosing the latter representation is because it applies to both mixed and pure states and general detection strategies.

The right hand side of equation (3.15) may then be substituted into equation (3.10). G. W. Helstrom employed the symmetric logarithmic derivative [135]

$$\frac{\partial}{\partial\phi}\hat{\rho} = \frac{1}{2}\Big(\hat{\Lambda}\hat{\rho} + \hat{\rho}\hat{\Lambda}\Big) \tag{3.16}$$

to substitute the derivative in equation (3.10) with quantum operators. Solving for $\hat{\Lambda}$ yields

$$\hat{\Lambda} = 2\imath(\hat{\rho}\hat{n} - \hat{n}\hat{\rho}). \tag{3.17}$$

By virtue of two inequalities, Helstrom arrived at

$$H(\phi) = \mathrm{tr}\big(\hat{\rho}\hat{\Lambda}^2\big). \tag{3.18}$$

This finding is important, as it is not, in comparison to F, dependent on the measurement process any more. The bound H constitutes reads

$$\mathrm{Var}(\Phi) \geq \frac{1}{F(\phi)} \geq \frac{1}{H(\phi)} \tag{3.19}$$

and is referred to as the quantum Cramér–Rao bound. In general, one can only show whether or not this bound is saturated. It does not provide the means to determine the measurement itself.

The homodyne detection technique introduced in section 1.2.3 in combination with coherent states has shown to achieve the Cramér–Rao bound [144], while the use of squeezed vacuum states yields a saturation of the quantum Cramér–Rao bound [200]. As outlined, we based the experiment on Gaussian states and detection techniques, such that these features played an important role for our approach. Neglecting the experimental difficulties outlined in the introduction of this chapter, the same can be reached with NOON states defined in equation (3.1) and photon counting detectors [115].

A calculation of H for pure states, which satisfy $\hat{\rho} = \hat{\rho}^2$, yields

$$H(\phi) = 4\,\mathrm{Var}(\hat{n}), \tag{3.20}$$

and is thus independent of ϕ. More general cases of thermal states have been analysed by, amongst others, A. A. Berni [27]. Considering a Mach–Zehnder interferometer as shown in figure 3.2, the photon number variance $\mathrm{Var}(\hat{n})$ has to be evaluated for the s e n s i n g arm. Taking the NOON state as an example, one will find $H(\phi) = 4\frac{n^2}{4} = n^2$. Substitution into equation (3.19) and taking the square root reads

$$\sigma(\Phi)_{\mathrm{HL}} \propto 1/n, \tag{3.21}$$

which is known as the Heisenberg limit. For coherent states with a mean excitation of $\bar{n}$ in the sensing arm, one can achieve at best the shot noise limit

$$\sigma(\Phi)_{\mathrm{SNL}} \propto 1/(2\sqrt{\bar{n}}). \tag{3.22}$$

For a squeezed vacuum state, characterised in section 1.2.2,

$$\sigma(\Phi)_{\xi} \propto 1/(2\sqrt{2}\sqrt{\bar{n}+\bar{n}^2}). \tag{3.23}$$

The proportionality sign in the last three equations reminds that the number of measurement repetitions has to be accounted for.

We note that the Heisenberg limit is usually understood as a scaling rather than a limit, such as the quantum Cramér–Rao bound. That is, equation (3.23) reaches asymptotically the Heisenberg limit, but a squeezed vacuum state and a homodyne detection can, for all $\bar{n}$, saturate the quantum Cramér–Rao bound.

3.2.6 Fisher information and sensitivity

Next to the Fisher information another measure to quantify a parameter estimation is by means of a common tool in data analysis, namely the method of uncertainty propagation. This approach yields an estimate on the uncertainty $\sigma(a)$ of a parameter a given a model of the measurement, that is a functional $f(\mathbf{b}) = a$, where $\mathbf{b}$ is the set of i parameters influencing measurement. To estimate the uncertainty on a, the uncertainty propagation [44]

$$\sigma(a) = \sum_i \left| \frac{\partial f(\mathbf{b})}{\partial b_i} \right| \sigma(b_i) \tag{3.24}$$

can be employed. The method is a sum of the the first derivatives of the model with respect to a parameter b_i multiplied by the a priori knowledge of its uncertainty $\sigma(b_i)$.

To apply this method for our study, equation (3.24) has to be solved for $\sigma(b_i)$, because we know $\sigma(a)$ – namely the standard deviation of the homodyne measurement – and seek to know the uncertainty of the estimated phase parameter $\Phi(x)$. This yields

$$\sigma(\Phi) = \frac{\sqrt{\mathrm{Var}(\mathrm{p}(x|\phi))}}{\left| \frac{\partial}{\partial \phi} \langle \mathrm{p}(x|\phi) \rangle \right|}. \tag{3.25}$$

Given that $\langle \mathrm{p}(x|\phi) \rangle$ is only punctually vanishing, both the latter expression and $\sqrt{1/F}$ are equivalent [60, 75]. From here on we will adopt the common practice and refer to the result of equation (3.25) as the sensitivity. Whether sensitivity or F is used to evaluate a phase measurement differs amongst authors. It appears to be easier to read off the shot noise limit in a sensitivity plot, thus we prefer the latter.

3.2.7 Comparing Fock with Gaussian states in a Mach–Zehnder interferometer

From the viewpoint of a "quantum mechanic", a natural test case for a measurement is to use a single photon as the input state. The other input mode of the interferometer is left free, thus we have $|1,0\rangle$. As another case, we send $|1,1\rangle$ into the interferometer drawn in figure 3.2. Finally a coherent state input $|\alpha,\beta\rangle$ and a squeezed vacuum state $|\xi\rangle$ formed the input state.

To compare those cases, the Fisher information and the sensitivity were calculated for the output modes 6 and 7, that is the modes leaving the second beam splitter in the assembly. As the measurement strategy, a homodyne technique was applied to all scenarios. This is the best choice for a Gaussian state scenario, but for the Fock state this is rather unusual, and as such an interesting technique to explore.

The Wigner function, as summarised on page 15, was applied to solve for F and the sensitivity σ. By virtue of equation (3.9) and the beam splitter transformation (1.30), $\mathrm{p}(x|\phi)$ was computed via

$$\mathrm{p}(x|\phi) = \frac{\int_{-\infty}^{\infty} W(x''', y''', \phi)\,\mathrm{d}y'''}{\int_{-\infty}^{\infty} W(x''', y''', \phi)\,\mathrm{d}x'''\,\mathrm{d}y'''}, \tag{3.26}$$

where $W(x''', y''', \phi)$ denotes the Wigner function after three transformations: (a) The first beam splitter, (b) the phase shift in one mode, (c) the last beam splitter. The result was then substituted into equation (3.25) and, to arrive at F directly, the integral form of equation (3.10).

For the Gaussian states, this approach delivered a symbolic expression for F. In the case of $|1\rangle|0\rangle$, symbolic expressions have been found as well. For the double photon input $|1\rangle|1\rangle$, complex analysis was required to extract a symbolic expression in F for one of the two output modes. As it was however always feasible to calculate a symbolic expression for the integration kernel of (3.10), numerical integration was found to be convenient for higher order photon number states. The results are presented in figure 3.4. Appendix A.5 summarises the expression evaluated for the different input states.

3.2.8 Approach to deterministic super resolution and super sensitivity

Building on the fundamental concepts presented in the preceding section, we will next elaborate on our approach to combine super resolution and super sensitivity. The approach is based on an experimental verification of super resolution by Distante et al. [88]. Using coherent states and a Mach–Zehnder interferometer, a post-processing technique of the data acquired via homodyne detection led to fringes narrowed by a factor of 12. However, their configuration prevented from surpassing the shot noise limit. By combining a coherent- with a squeezed vacuum state and extending their mathematical model, this limit could be surpassed. The idea of sending a squeezed vacuum state in the second input mode of an interferometer goes back to a proposal of C. M. Caves [55]. It is thus fair to state that our approach is of an eclectic nature.

Super resolution with parity detection

At the very bottom of the post-processing technique we applied is the idea to measure a NOON state, instead of generating it. This somewhat reflects the time-reversal symmetry of quantum mechanics [228]. Gao et al. elaborated on this idea and developed a proposal based on coherent states and photon number resolving detectors[3] [108]. The reasoning here is as follows: We consider $|\alpha, 0\rangle$ as the input state. By propagating the state through the first beam splitter using equation (1.30) and the phase shifting element,

$$|\psi\rangle = \left|\mathrm{e}^{\imath\phi}\,\frac{\alpha}{\sqrt{2}}, \frac{\alpha}{\sqrt{2}}\right\rangle = \mathrm{e}^{-\bar{n}/2} \sum_{i}^{\infty}\sum_{j}^{\infty} \frac{\left(\mathrm{e}^{\imath\phi}\sqrt{\bar{n}/2}\right)^{i}\left(\sqrt{\bar{n}/2}\right)^{j}}{\sqrt{i!j!}}|i,j\rangle \tag{3.27}$$

is found. A constant phase offset due to the beam splitter interaction was added to ϕ. The expansion in the Fock state basis (1.15) makes it explicit that $\mathrm{e}^{\imath i\phi}|i,0\rangle + |0,i\rangle$ states as well as

[3] In fact, Gao et al. considered that a parity detection might be sufficient to establish super resolution.

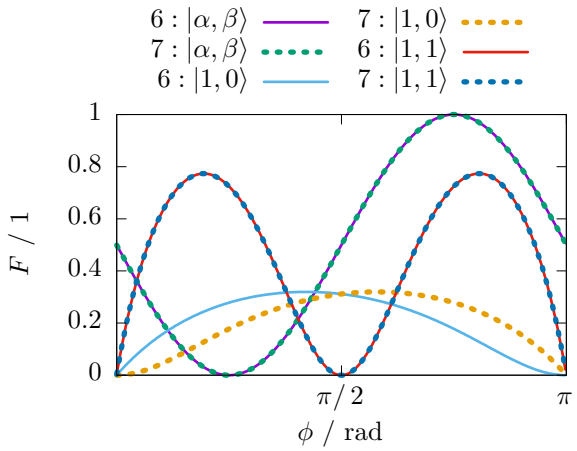

(a) Fisher information of various states

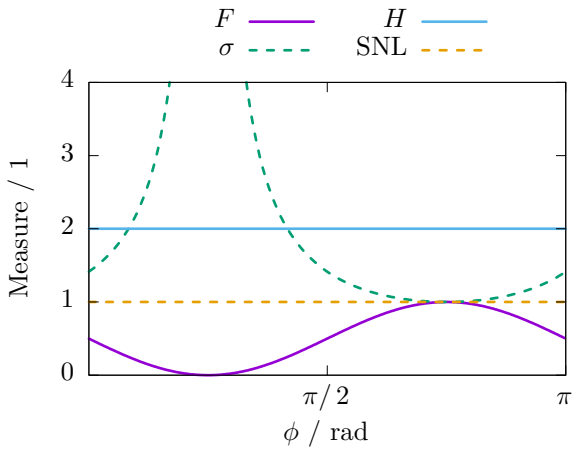

(b) Sensitivity and Fisher information of coherent state

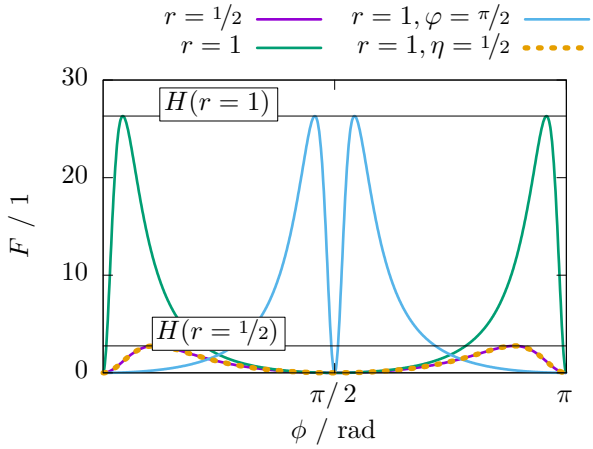

(c) Fisher information of squeezed vacuum state

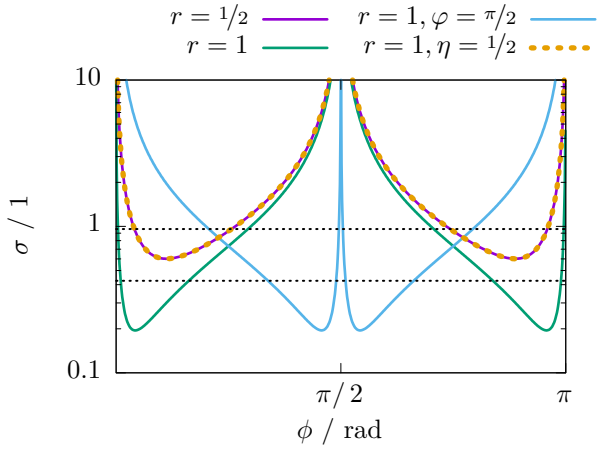

(d) Sensitivity of squeezed vacuum state

Figure 3.4: (a) Fisher information for three input states. Modes are numbered in accordance to figure 3.2. The coherent state amplitudes are $\alpha = 1/\sqrt{2}$, $\beta = -\imath/\sqrt{2}$. Only for the latter, F also exists in mode 5 – it's $F_5 = F_6 + F_7$. For Fock states $F_5 = 0$, which reveals the (missing) feature of a single photon state, namely a phase. By interfering mode 5 with the bypassing mode 3, ϕ becomes measurable. Lines which can not be identified directly are covered by another line; this applies for $|1,1\rangle$ and $|\alpha,\beta\rangle$. An apparent feature is the asymmetry of F for $|1,0\rangle$: Depending on the working point, probing one of the modes would be thus preferential. The doubled periodicity of $|1,1\rangle$ corresponds to the finding that fringe spacing can be decreased by correlated photons. (b) Fisher information and sensitivity compared in one graph. The results stem from $|\alpha,\beta\rangle$. The shot noise limit (SNL) is given by equation (3.22). The quantum Cramér–Rao bound can not be reached with this configuration. (c) Fisher information for a squeezed state under variation of the squeezing parameters r and φ. A lossy transmission ($\eta = 1/2$), yields the same F as if $r = 1/2$. As a reference, the quantum Cramér–Rao bound is depicted as a solid line. The fact that this bound can always be reached at some φ led to the idea of combining phase estimation with feedback control [27]. (d) The sensitivity of the cases shown in graph (c). Dotted lines present the sensitivities reached by coherent states with $\bar{n} = \sinh(r)^2$.

$\mathrm{e}^{\imath i\phi}|i,j\rangle + \mathrm{e}^{\imath j\phi}|j,i\rangle$ are present in the sum – both exhibit super resolution [148, 155]. Thus, the task is to realise a measurement described by

$$\hat{\pi} = \sum_{i,j}^{\infty} |i,j\rangle\langle j,i|. \tag{3.28}$$

The solution provides the parity operator

$$\hat{\Pi}_{\pm} = (-1)^{\hat{n}} = \exp(\imath\pi\hat{n}), \tag{3.29}$$

which clearly resembles the phase operator (3.2), but with a fixed phase. As $\hat{\Pi}_{\pm}$ has only two eigenvalues, it performs a dichotomy of the state it is applied on.

First, we note that the state in equation (3.27) is found before the second beam splitter. To reach super resolution, $\hat{\pi}$ should be applied to it at this stage. Second, motivated by a comparison to the phase shift operator, $\hat{\Pi}_{\pm}$ is propagated from the output of the second beam splitter to where $|\psi\rangle$ is known. This yields

$$\langle\psi|\hat{\pi}|\psi\rangle = \big\langle \alpha,0\big|\hat{U}_b^{\dagger}(\hat{U}_{\phi}\otimes\hat{\mathbf{1}})^{\dagger}\hat{\pi}(\hat{U}_{\phi}\otimes\hat{\mathbf{1}})\hat{U}_b\big|\alpha,0\big\rangle = \big\langle \alpha,0\big|\hat{U}_b^{\dagger}(\hat{\Pi}_{\pm}\otimes\hat{\mathbf{1}})\hat{U}_b\big|\alpha,0\big\rangle \tag{3.30}$$

and shows that a parity detection at the interferometer's output is equivalent to applying $\hat{\pi}$ inside, i.e. before the second beam splitter. The result Gao et al. found reads $\langle\psi|\hat{\pi}|\psi\rangle = \exp(-2\bar{n}\sin(\phi/2)^2)$, hence achieves a fringe narrowing dependent on the average photon number $\bar{n}$.

This finding raised the question whether a similar 'dichotomy technique' can be applied for homodyne detection, which is (at least at the present status quo) technically more efficient than the various types of single photon detectors.

A processing of the detected signal which mimics the 'dichotomy operation' of $\hat{\Pi}_{\pm}$ has been found and originates from a theoretical study of Wigner functions and the parity operator. In 1977, A. Royer proofed a relation between $\hat{\Pi}_{\pm}$ and the Wigner function [236]. Specifically, he showed that $\langle\hat{\Pi}_{\pm}\rangle = \frac{\pi}{2}W(0,0)$.

To utilise this relation via homodyne detection is simple: The acquired signal is, as shown in figure 3.3(d), a projection on one of the quadratures. Let us assume to measure $\mathrm{p}(y,\phi=\pi)$ for mode 7, that is the $\hat{X}$ quadrature is traced out and the output is a vacuum state. To finally arrive at an information about $W(0,0)$, the acquired signal $\mathrm{p}(y)$ has to be sorted into two bins: $\mathrm{p}(y=0)$ and $\mathrm{p}(y\neq 0)$.

To cast this idea in equations, the Wigner formalism, outlined in section 1.2.4, can be used to propagate a coherent state $|\alpha,\beta\rangle$ through the interferometer. At the output, one finds

$$\begin{aligned}
&W(x_6,y_6,x_7,y_7) = \\
&\frac{1}{\pi^2}\exp\Bigg(\frac{1}{2}\Bigg(\mathrm{e}^{-\imath\phi}\Big(-\mathrm{e}^{\imath\phi}\big(4|\beta|^2+2\sqrt{2}2\Re(\beta)(x_6-x_7-\imath y_6+\imath y_7)+\\
&2x_6^2-\sqrt{2}\alpha x_6+2(x_7^2+y_6^2+y_7^2)+\sqrt{2}(\alpha x_7-\imath(\alpha-2\beta)(y_6-y_7))\big)+\\
&\sqrt{2}(\alpha+\beta)^*(x_6+x_7-\imath(y_6+y_7))+\sqrt{2}\,\mathrm{e}^{2\imath\phi}(\alpha+\beta)(x_6+x_7+\imath(y_6+y_7))\Big)+\\
&\alpha^*(-4\alpha+\sqrt{2}x_6-\sqrt{2}x_7-\imath\sqrt{2}y_6+\imath\sqrt{2}y_7)\Bigg)\Bigg).
\end{aligned} \tag{3.31}$$

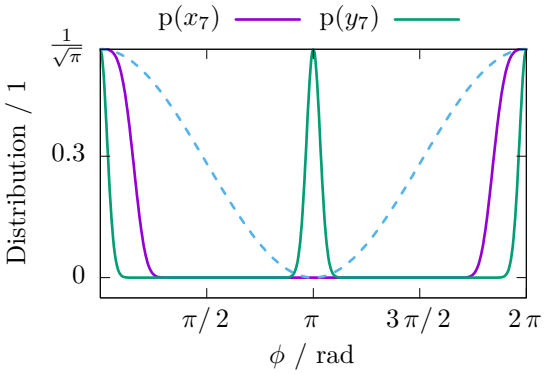

Figure 3.5: The result of equation (3.32). The dashed line follows a cos-function to compare the acquired signal with a standard detection scheme. For this simulation, $\alpha = 10$. The response differs between the measured quadrature: This behaviour stems from the way the state revolves about its centre in phase space, as it can be seen in figure 3.3(c).

Then by tracing out mode 6 and $\beta = 0$, the measurable probability distributions are

$$\mathrm{p}(x_7 = 0, \phi) = \frac{1}{\sqrt{\pi}} \exp\left(-\frac{1}{8}\,\mathrm{e}^{-2\imath\phi}(-1+\mathrm{e}^{\imath\phi})^2(\alpha^* - \alpha\,\mathrm{e}^{\imath\phi})^2\right), \tag{3.32a}$$

$$\mathrm{p}(y_7 = 0, \phi) = \frac{1}{\sqrt{\pi}} \exp\left(\frac{1}{8}\,\mathrm{e}^{-2\imath\phi}(-1+\mathrm{e}^{\imath\phi})^2(\alpha^* + \alpha\,\mathrm{e}^{\imath\phi})^2\right). \tag{3.32b}$$

Figure 3.5 presents the outcome and shows the super resolving features of this detection strategy.

Dichotomy strategy widened

The problem with this strategy however is that such a dichotomy would take forever, as strictly speaking the chance to only measure at $y = 0$ takes an infinite amount of resources. Another way to look at this impossibility is that this measurement is a projection on the eigenstate $|y = 0\rangle$ which is a projection onto an infinitely squeezed state. As such a state is not physical[4] the binning has to be relaxed. This measurement strategy can be described by two projectors [88]

$$\hat{\Pi}_0 = \int_{-a}^{a} |y\rangle\langle y|\,\mathrm{d}y, \tag{3.33a}$$

and its complement

$$\hat{\Pi}_1 = \hat{\boldsymbol{1}} - \hat{\Pi}_0. \tag{3.33b}$$

to fulfil

$$\hat{\Pi}_p = c_2\hat{\Pi}_0 + c_1\hat{\Pi}_1 = \hat{\boldsymbol{1}}, \tag{3.34}$$

where c_1 and c_2 are the eigenvalues of the operators. To find the eigenvalues, one calculates the expectation value $\langle 0|\hat{\Pi}_0|0\rangle$ for a vacuum state. The integration to be solved is thus $\int_{-a}^{a}\int_{-\infty}^{\infty}\langle 0_7|y\rangle\langle y|0_7\rangle\,\mathrm{d}x\,\mathrm{d}y$, where $|0_7\rangle$ is the vacuum state in mode 7. It is a basic Gaussian integral and yields $c_1 = \mathrm{erf}(a)^{-1}$, $c_2 = 0$. Care has to be taken for these values, as they depend on the normalisation of the state. Distante et al. preferred a shot noise unit of $1/2$, which leads to $c_1 = \mathrm{erf}(\sqrt{2}a)^{-1}$. Normalising the results to shot noise units makes however both definitions equal. The smaller a, the more narrow the fringes becomes, eventually recovering the result (3.32). However, the drawback is that, as analysed by Distante et al., the sensitivity drops with

[4] According to equation (1.27) an infinitely squeezed state has an infinite amount of photons.

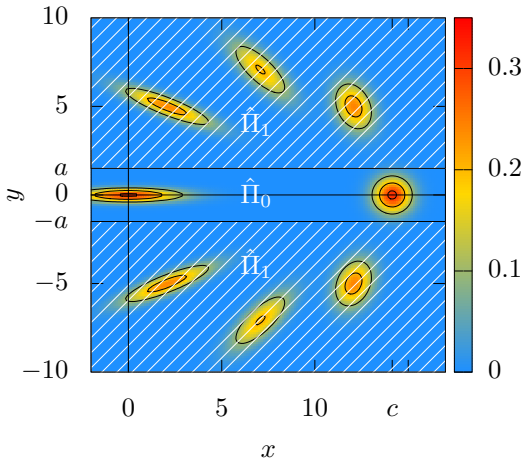

Figure 3.6: The evolution of the state in mode 7 visualised by a combination of Wigner functions. In comparison to figure 3.3(c), the vacuum state found at $\phi = \pi$ is replaced by a phase squeezed vacuum state. The dichotomy strategy is represented by their operators $\hat{\Pi}_0$ and $\hat{\Pi}_1$, while a marks the bound set for $\hat{\Pi}_0$. As in the previous plot, $c = \sqrt{2}\Re(\alpha)$. The squeezing parameters are $r = 1$ (equivalent to $-8.7\,\mathrm{dB}$) and $\varphi = \pi/2$.

a small a. To reach the shot noise limit, $a \to \infty$, but then the resolution feature disappears obviously.

Thus, in any case, the restriction to a coherent state input prevents super sensitive measurements. So, following the mentioned proposal of C. M. Caves [55] which achieves super sensitivity, our configuration and detection strategy looks as depicted in figure 3.6.

Extension of the approach with squeezed vacuum states

To analyse and provide the model to post-process the data, the approach follows the scheme presented above: Determine the Wigner function at the output of the interferometer first. Then, apply the projection (3.33). Calculating $\langle\hat{\Pi}_p\rangle$ and $\mathrm{Var}(\hat{\Pi}_p)$ yields the finally sensitivity.

To simplify the calculations, the Wigner function model was modified: According to figure 3.6, the coherent state is amplitude modulated, such that $\alpha \in \mathbb{R}$. Next, when experimentally generating a squeezed vacuum state, it suffers from losses. These losses, as motivated in introduction 1.2.3 and 1.2.4, lead to anti-squeezing, such that the degree of squeezing is different along the conjugate quadratures. As an example, one might find $-3\,\mathrm{dB}$ of noise reduction and $6\,\mathrm{dB}$ of noise increase. Furthermore, the squeezing ellipse should be oriented such that the noise is reduced in the phase quadrature.

The Wigner functions which account for this are

$$W(x, y, \alpha) = \frac{1}{\pi}\exp\big(-\big(y^2 + (x-\alpha)^2\big)\big), \tag{3.35a}$$

$$W(x, y, \wp, \varsigma) = \frac{\wp}{\pi}\exp\left(-\left(\frac{y^2}{\varsigma^2} + \wp^2\varsigma^2 x^2\right)\right), \tag{3.35b}$$

where $\varsigma = \mathrm{e}^{-r}$, and $\{\wp \in \mathbb{R} \mid 0 < \wp \leq 1\}$. The parameter $\wp$ determines the purity of the state. The degree of squeezing (which we rewrite here from equation (1.29)) and anti-squeezing are

$$V_s = 10\log_{10}(\varsigma^2), \tag{3.36a}$$

$$V_a = 10\log_{10}\big(1/(\varsigma\wp)^2\big), \tag{3.36b}$$

respectively. How V_a and V_s are affected by losses is presented in figure 3.7. The average photon

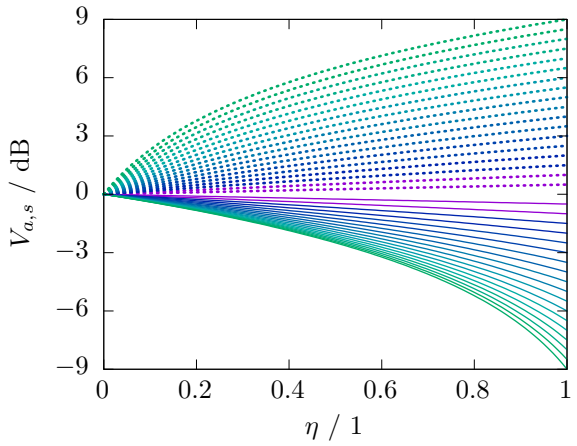

Figure 3.7: Influence of optical loss η on the degree of (anti-)squeezing. Dashed lines refer to the degree of anti-squeezing V_a. The loss dependence can be readily derived from equation (1.40). 18 values from $\pm$ 1/2 dB to $\pm$ 9 dB are plotted. Most important is the finding that losses have a more pronounced effect on squeezing than on anti-squeezing. This effect becomes the stronger the higher the initial degree of squeezing is and somewhat illustrates the fragility of quantum correlations compared to thermal excitations (found in the anti-squeezed quadrature).

number of the input state represented by the Wigner functions is

$$\bar{n} = |\alpha|^4 + 1/4(-2 + (\wp\varsigma)^{-2} + \varsigma^2). \tag{3.37}$$

Propagating the Wigner functions (3.35) through the interferometer and tracing out mode 6, the function reads

$$W(x_7, y_7, \alpha, \wp, \varsigma, \phi) = 2\wp\varsigma \frac{\exp(f_n)}{f_d} \tag{3.38}$$

with

$$\begin{aligned} f_d = {} & \pi\sqrt{\cos(2\phi)(1-\wp^2\varsigma^4) + \wp^2\varsigma^4 - 4(\varsigma^2-1)\cos(\phi) + 4\varsigma^2 + 3}\times \\ & \sqrt{\frac{((\varsigma^2-1)\cos(\phi) - \varsigma^2 - 1)(\cos(\phi)(\wp^2\varsigma^2-1) + \wp^2\varsigma^2 + 1)}{\cos(2\phi)(\wp^2\varsigma^4-1) - \wp^2\varsigma^4 + 4(\varsigma^2-1)\cos(\phi) - 4\varsigma^2 - 3}}, \end{aligned} \tag{3.39a}$$

$$\begin{aligned} f_n = {} & \Big(4\cos(\phi)\big(y_7^2\big(\wp^2\varsigma^2-1\big) - \wp^2\varsigma^2(-\alpha+\varsigma x_7 + x_7)(\alpha + (\varsigma-1)x_7)\big) + \\ & y_7^2\big(\wp^2\big(\varsigma^2+4\big)\varsigma^2+3\big) + \cos(2\phi)\times \\ & \big(-(y_7-x_7)(y_7+x_7)\big(\wp^2\varsigma^4-1\big) + \alpha^2\big(\wp^2\varsigma^2-1\big) - 2\alpha x_7\big(\wp^2\varsigma^2-1\big)\big) + \\ & 4y_7\sin(\phi)\big(\alpha + x_7\big(\wp^2\varsigma^4-1\big) + \alpha\wp^2\varsigma^2\big) + \\ & 2y_7\sin(2\phi)\big(-\wp^2\varsigma^4 x_7 + \alpha\big(\wp^2\varsigma^2-1\big) + x_7\big) + \\ & \wp^2\varsigma^2\big(3\alpha^2 + \big(3\varsigma^2+4\big)x_7^2 - 6\alpha x_7\big) + x_7^2 + \alpha(\alpha - 2x_7)\Big)/ \\ & \big(2\big(\big(\varsigma^2-1\big)\cos(\phi) - \varsigma^2 - 1\big)\big(\cos(\phi)\big(\wp^2\varsigma^2-1\big) + \wp^2\varsigma^2+1\big)\big). \end{aligned} \tag{3.39b}$$

Next the exception value $\langle\hat{\Pi}_d\rangle$ and the sensitivity can be calculated. After some algebra, this yields

$$\langle\hat{\Pi}_d\rangle(a, \varsigma, \wp, \phi, \alpha) = \frac{f_1}{2\,\mathrm{erf}\big(\sqrt{2}a/\varsigma\big)}, \tag{3.40}$$

with the abbreviations

$$f_1 = \operatorname{erf}\Big(f_- \sqrt{2/f_2}\Big) + \operatorname{erf}\Big(f_+ \sqrt{2/f_2}\Big), \tag{3.41a}$$

$$f_2 = \frac{\wp^2\varsigma^2\big(\varsigma^2(1+\cos(\phi))^2 + 2(1-\cos(\phi))\big) - \cos(\phi)^2 + 1}{4\wp^2\varsigma^2}, \tag{3.41b}$$

$$f_\pm = a \pm |\alpha| \sin(\phi)/2. \tag{3.41c}$$

Solving for equation (3.25) returns a sensitivity of

$$\sigma(a,\varsigma,\wp,\phi,\alpha) = \left| \frac{f_2^{3/2}\sqrt{(2-f_1)f_1\pi/2}}{\exp\big(-2f_-^2/f_2\big)(f_2' f_- + \alpha f_2 \cos(\phi)) + \exp\big(-2f_+^2/f_2\big)(f_2' f_+ - \alpha f_2 \cos(\phi))} \right| \tag{3.42}$$

with

$$f_2' = \frac{\partial}{\partial\phi} f_2 = \frac{2\cos(\phi)\sin(\phi) + \wp^2\varsigma^2\big(2\sin(\phi) - 2\varsigma^2(1+\cos(\phi))\sin(\phi)\big)}{4\wp^2\varsigma^2}. \tag{3.43}$$

Figure 3.8 illustrates $\langle\hat{\Pi}_d\rangle$ and σ for various parameter settings. In general, both the resolution and sensitivity profit from an increase of $|\alpha|$. The resolution feature scales, for finite a, always proportional to $1/|\alpha|$. In addition, a smaller a yields higher resolution. This does not hold for the sensitivity, as the examples in figure 3.8(b) proof. Hence one might focus on the optimisation of the sensitivity under variation of ς and a. It was found that for $|\alpha| = 10$, already more than $-13\,\mathrm{dB}$ of squeezing are required[5]. Under realistic constrains, it is thus sensible to set the degree of squeezing constant and optimise for a. It can be found that the optimum of a changes only slightly with $|\alpha|$ and was $\approx 1/2$, thus we fixed a to $1/2$ for processing the experimental data. In fact, this choice also showed to be preferable for the experiment of Distante el al. which did not exploit squeezed states [88].

The limit of phase sensitivity of our input configuration is set by the proposal of C. M. Caves [55] and can be recovered by $a \to \infty$ and a pure state $\wp = 1$. For a squeezing parameter $r = {}^1\!/_4 \ln\Big(1 + 4|\alpha|^2\Big)$ the optimum sensitivity for Cave's proposal is achieved. It reads

$$\sigma_{\mathrm{CL}} \propto \sqrt{\frac{\sqrt{1+4|\alpha|^2}-1}{2}} \frac{1}{|\alpha|^2} \tag{3.44}$$

and scales as $1/|\bar{n}|^{3/4}$ in the limit of large $\bar{n}$.

For an analysis of the experimentally acquired data, all properties and models are hereby stated. Before going over to the experimental section, the process of generating squeezed vacuum states will be outlined next.

3.2.9 Generating squeezed states of light

Firstly treated in the framework of quantum optics in the 1970s [262, 299], the generation of squeezed states of light attracted much attention. This was caused be the (back-then predicted) impact of squeezed states on metrology and information technology [59, 293]. In principle any

[5] As of today, the highest degree of squeezing recorded is $-12.7\,\mathrm{dB}$ [94].

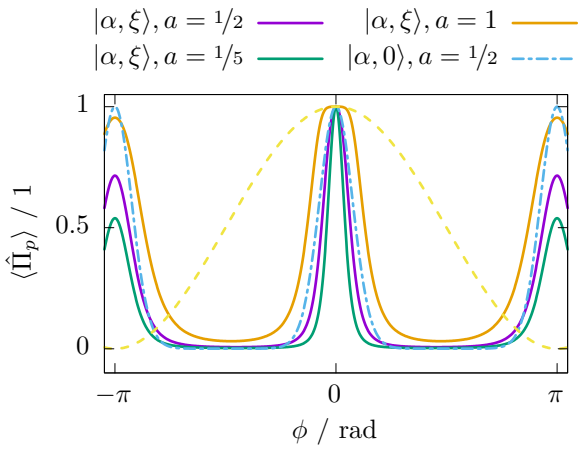

(a) Expectation value for two input states and three bin sizes

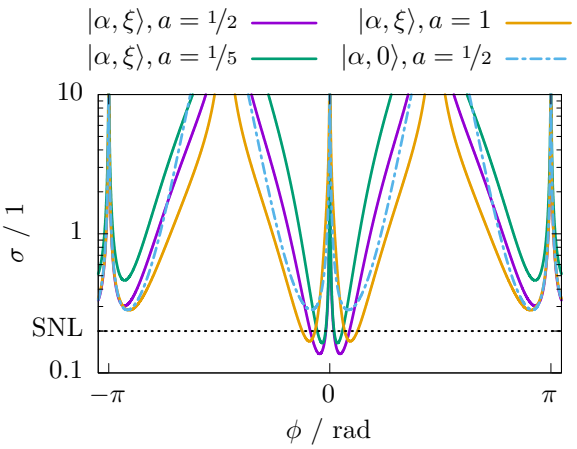

(b) Sensitivity for the configurations in figure (a)

Figure 3.8: (a) Expectation value of the post-processing technique with a coherent- and squeezed state input, and a single coherent state input, denoted by $|\alpha,\xi\rangle$ and $|\alpha,0\rangle$, respectively. The parameters are $\alpha = 5$, $\varsigma = 0.5$, $\wp = 0.7$, that is $V_s = -6\,\mathrm{dB}$ and $V_a = 9.1\,\mathrm{dB}$. A cos-function (dashed light yellow line) is shown for visual comparison. The FWHM of it defines the Rayleigh criterion which is set by the standard interferometer configuration. For the value of $a = 1/2$, a coherent state scenario was added. Apart from the latter case, the central fringe shows an increased resolution, while the next fringes are less resolved. A qualitative reasoning can be given by the evolution in phase space plotted in figure 3.6: The response of $\hat{\Pi}_0$ becomes affected by the amplitude noise of the phase squeezed state. This noise is represented by the elongation of the squeezing ellipse which is rotated by 90° just before the state enters the region covered by $\hat{\Pi}_0$. A general statement can be given on the value of a: Lowering a leads, in any case, to a higher fringe resolution.
(b) Sensitivity for the parameters used in figure (a). The SNL set by equation (3.22) shows the limit reachable by $|\alpha,0\rangle$. Compared to the resolution, the value of a can be used to optimise the sensitivity. Its optimum value is close to 1/2 and changes only slightly with respect to α and ς. For $a \to \infty$, the $|\alpha,0\rangle$ input reaches the SNL, while for $|\alpha,\xi\rangle$ the 'Caves limit' (3.44) can be achieved.

kind of Hamiltonian which exhibits higher order terms in the creation and annihilation operators can lead to a "squeezed feature". That is, apart from the single-mode squeezed state depicted above and refereed to herein, the concept of squeezing can be applied on any kind of canonical system of non-commutable variables [114].

To generate single-mode squeezed vacuum states we used the process of spontaneous parametric down-conversion [183, 255, 294], as its Hamiltonian is the generator of equation (1.24) with a quadratic term of $\hat{a}^\dagger$ and $\hat{a}^\dagger$. There are various approaches, or better to say starting points, for explaining the actual physical process that leads to the features of squeezed light summarised in section 1.2.2. Here we start from the classical equations of motion for what will be termed as the signal and idler fields. This approach does not cover all aspects of our experimental realisation, but it grants an understanding of the underlying physical process. In fact, the generation of squeezed states of light is described extensively by various authors, such that we refer the interested reader to the early publications of Collet and Gardiner [68], and Collet and Loudon [69], the book of Gardiner and Zoller [110], or review articles from Andersen et al. [8] and A. W. Lvovsky [185] whose work we based the following discussion on.

The main "ingredient" for our approach to generate squeezed light is a crystal with a second-order nonlinear susceptibility χ^2_{eff} [38, 255]. We use the subscript to remind that the susceptibility is a tensor, so the 'effective' component of it is determined by the orientation of the incident light and its polarisation. The coefficient χ^2_{eff} characterises the response of an optical medium to an incident field of frequency 2ω, i.e. it characterises $\boldsymbol{E}(2\omega) \propto \chi^2_{\text{eff}}\boldsymbol{E}(\omega)\boldsymbol{E}(\omega)$. Exactly this behaviour of generating two photons (with frequency ω) from a single 'pump' photon (at 2ω) is what is demanded to provide a Hamiltonian with second order terms[6].

For our purpose the incident field of frequency 2ω is referred to as pump field. For a general description, the field oscillating at half the frequency (that is where 'down-conversion' comes from) is split into an idler and signal field. To facilitate the model, we approximate the situation as follows:

1. All fields E_p, E_i and E_s are continuous in time and travel along z.

2. Only the amplitude of E_i and E_s are allowed change when propagating through the crystal of length l, which implies there is no effect of pump depletion. Also $|E_p| \gg |E_{i,s}|$, such that the pump field can be treated as classical.

3. There is some means provided to match the phase between the fields. This is usually less trivial than it sounds, as the material's refractive index n may be frequency dependent. It will cause the fields to propagate at different velocities, which deteriorates the down-conversion efficiency. A simple means is to use a crystal short enough to prevent from a dispersion, however the longer the crystal the higher the yield of signal and idler photons.

4. E_i and E_s are spatially degenerate. This will lead to single-mode squeezing. However they oscillate at $\omega \pm \varpi$ with $\varpi \ll \omega$. The energy scheme associated to a down-conversion or second harmonic process may be described by a transition between virtual energy levels, thus in principle "everything is allowed" as long as the model is conform with energy and momentum conservation.

5. The slowly varying envelop approximation applies [12]. When dealing with electromagnetic waves which are frequency-wise and spatially well defined, this approximation facilitates the wave equation greatly.

[6] In 1961, a landmark experiment by Franken et al. verified that the opposite also holds: The nonlinear susceptibility can also be used to generate light at twice the frequency of the pump field [104], an effect known as second harmonic generation. An extensive study of nonlinear optics is given by R. W. Boyd [38].

Following these points, the classical equation of motion for E_i and E_s read [38]

$$\frac{\partial}{\partial z}E_{i,s} = \imath\frac{\omega \pm \varpi}{2\epsilon_0 n c_0}P_{\mathrm{nl}}(\omega \pm \varpi), \tag{3.45}$$

where the nonlinear polarisation amplitude

$$P_{\mathrm{nl}}(\omega \pm \varpi) = 2\epsilon_0\chi^2_{\mathrm{eff}}E_p E^*_{i,s}(z) \tag{3.46}$$

was introduced. ϵ_0 denotes the vacuum permittivity given in units of $\frac{\mathrm{A^2 s^4}}{\mathrm{kg\,m^3}}$. Under the given assumptions, we may find

$$E_s(l) = E_s(0)\cosh(r) + E^*_i(0)\sinh(r), \tag{3.47a}$$
$$E_i(l) = E_i(0)\cosh(r) + E^*_s(0)\sinh(r), \tag{3.47b}$$

where

$$r = \frac{\chi_{\mathrm{eff}}\omega}{n c_0}|E_p|l. \tag{3.47c}$$

A quantisation of the field as in equation (1.7) leads to a result which resembles equation (1.26) on page 10:

$$\hat{a}_{s,i}(l) = \hat{a}_{\omega\pm\varpi}(l) = \hat{a}_{\omega\pm\varpi}(0)\cosh(r) + \hat{a}^\dagger_{\omega\pm\varpi}(0)\sinh(r). \tag{3.48}$$

However, the difference here is that two modes are present, i.e. if the signal and idler mode are in a vacuum state before the crystal, they leave as an entangled-, also known as two-mode squeezed-, state [58]. The entanglement can be found between the sidebands at $\pm\varpi$ of the carrier frequency. This feature of entangled sidebands was in fact demonstrated by Huntington et al. [146]. To detect this type of two-mode squeezing, they employed homodyne detection and measured the detector's photocurrent with an electronic spectrum analyser. Prior to this measurement, the optical field had to be separated spatially such that the sidebands could be addressed individually via two homodyne detectors. Otherwise, this common frequency-domain measurement technique rules out the distinction between symmetric sidebands, because the analyser probes the mean squared power of the detector's photocurrent [16, 37].

If one decides to measure the temporal behaviour of squeezed light instead, e.g. by just recording the photocurrent with an oscilloscope, it turns out that the m a t h e m a t i c a l description of such process leads to a single-mode picture. This was concisely pointed out by A. W. Lvovsky [185], who described the measurement by introducing a temporally limited version of $\hat{a}$. Such a limited duration mode $\hat{a}_{\mathrm{ld}}$ may be derived via a transformation of $\hat{a}$ with a filter kernel $f(t) \in \mathbb{R}$ summarising physical and technical causes for a limited duration as $\int_{-\infty}^{\infty}\hat{a}(t)f(t)\,\mathrm{d}t$. Under certain constrains, the limited duration mode operator reads [185]

$$\hat{a}_{\mathrm{ld}}(l) = \hat{a}_{\mathrm{ld}}(0)\cosh(r) + \hat{a}^\dagger_{\mathrm{ld}}(0)\sinh(r), \tag{3.49}$$

which is in the familiar form of a single-mode squeezed field.

We emphasise that the outlined approach to generate squeezed light corresponds to a 'single-pass configuration', where all fields propagate through the nonlinear crystal only once. To enhance the generation of squeezed light, it is common to built an optical cavity around the crystal. Such a configuration is known as optical parametric oscillator and has been realised in our experiment. The theoretical description of optical parametric oscillators used for squeezed light generation has been developed by Savage and Gardiner [111].

3.3 Experiment

This section begins with a description of the squeezed light source built for the experiment. Next, a report of the actual phase measurement setup will be given, before the results are presented.

3.3.1 Squeezed light source

The design and implementation of a source for squeezed states posed the main experimental challenge for our demonstration of quantum enhanced phase measurements. Basic requirements for a high degree of squeezing and stable operation are clean conditions to mitigate optical losses and mechanically stable mounts for various optical elements. To meet those demands and provide access to squeezed light also for future experiments, the laboratory was rebuilt from scratch and equipped with flow modules and rack assemblies similar to the enclosure illustrated in the appendix A.4.

Figure 3.9 illustrates the actual setup of all optical and electro-optical components. The electronic components involved in the control of cavity and phase locks are shown in figure 3.10. Details omitted in the following text are given in the figure caption.

A Nd:YAG laser (*Innolight GmbH* Diabolo) with an emission at 1064 nm and a spectral linewidth of ca. 1 kHz served as the main light source. An internal module for second harmonic generation provided 532 nm radiation used as a pump for the generation of squeezed light.

First, we describe the path of the pump beam with a wavelength of 532 nm, before we describe the 'squeezer', and finally follow the infrared 'steering' beam.

Pump beam A Faraday isolator (FI) acting as an optical diode prevented from back reflection into the laser cavity. The pump light was filtered spatially and frequency-wise by means of a mode cleaning cavity with a finesse of 230. Figure 3.11 illustrates and explains this measure. To stabilise the cavity, a Pound–Drever–Hall lock [31, 93, 106] was applied. A phase modulation at 12 MHz, generated inside the laser module, served as the electronic local oscillator for this lock. Photodetector D2 picked up the reflection from the first mirror of the cavity. We implemented an internal electronic mixer, such that all electronics necessary for the generation of an error signal were contained in the detector housing. Figure 3.12 illustrates a typical transmission spectrum and error signal. As for all other locks, the servomechanism described in appendix A.3 was applied to control the feedback system. Detector D1 was used to monitor the transmission of the cavity. A lens configuration was designed to shape the spatial profile of the mode leaving the cavity to match the spatial mode of the "squeezer" cavity. For tasks which required a precise knowledge of the transversal beam profile and its propagation properties, such as the design of telescopes, a software had been written capable of analysing the profile recorded with a camera in real-time. Details about the software are given in appendix A.1. Next we focus on the key component of the setup:

Squeezer module The squeezer is an assembly of a Fabry–Pérot cavity containing a 10 mm long periodically poled potassium titanyl phosphate (ppKTP, *Raicol*) crystal. Its nonlinear optical properties lead to the process described in section 3.2.9. One of the crystal's flat end facets was coated with an anti-reflective coating for 1064 nm and 532 nm. A high-reflection coating for both wavelengths was applied to the other facet. To form a cavity, a mirror with a reflectivity of 90 % and 20 % for 1064 nm and 532 nm, respectively, was mounted 13 mm away from the crystal. The figure on page 157 presents the architecture of the squeezer module. The coating yielded a bandwidth of about 80 MHz at a finesse of ca. 80. A piezo actuator between the crystal and the mirror was controlled by means of another Pound–Drever–Hall lock. Here,

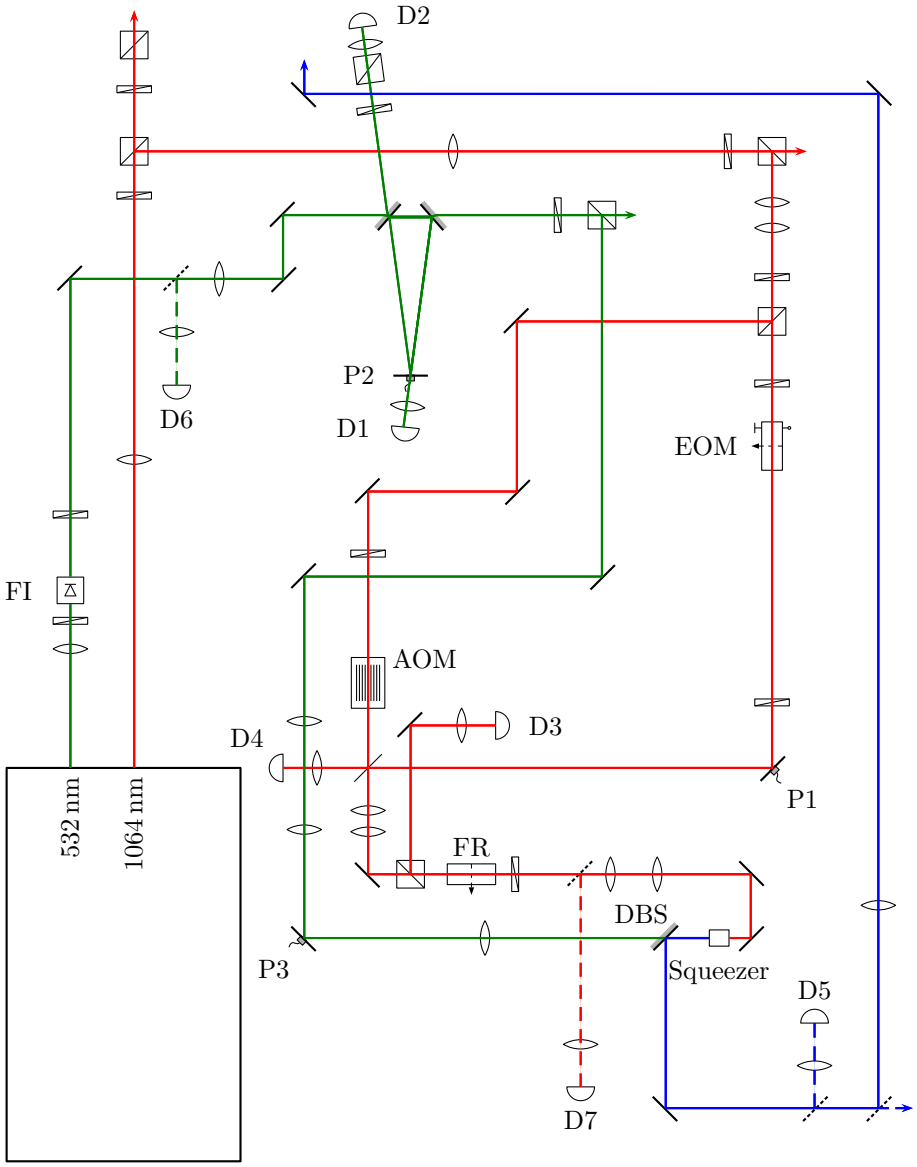

Figure 3.9: Complete optical setup of the squeezed light source. The scheme is drawn to scale: The long side measures 1.5 m. All cubes represent polarising beam splitters. Only half wave plates were used. The letter P labels piezoelectric devices which actuate mirrors. Mirrors in dashed lines are removable. The dichroic beam splitter (DBS) reflects infrared light only.

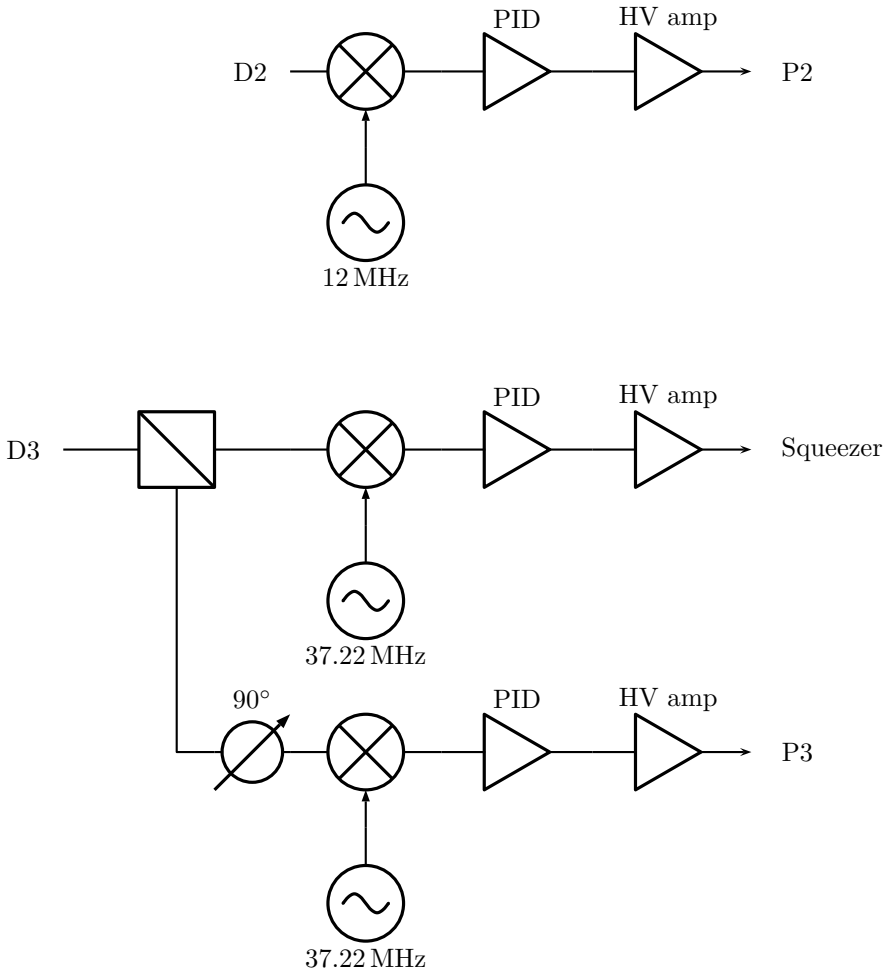

Figure 3.10: Conceptual schematic of the electronic stages used for controlling the mode cleaning cavity, the squeezer cavity and the pump phase lock. The upper scheme refers to the mode cleaning cavity lock. First, the photocurrent of detector D2 was down-mixed with a 12 MHz signal derived from the laser module. Thereby an error signal was provided which was sent into a servomechanism (PID). Then, to drive the piezo element P2 actuating a mirror of the cavity, the signal of the PID was amplified by means of a high voltage amplifier.
The lower scheme refers to the locking scheme for the squeezer. Here, the signal from photodetector D3 was split up first. One half was processed in the same sense as it was done for signal D2. This part provided a Pound–Drever–Hall lock for the squeezer cavity. A frequency generator, developed in-house and based on an *Analog Devices* AD9959 digital synthesizer, set to 37.22 MHz drove an electro-optic modulator (EOM) to generate sidebands necessary for this scheme. The same generator provided the local oscillator for the down-mixing process. The second half was phase shifted by 90° before a similar processing. This part was employed to control the relative phase shift between the pump- and the infrared steering beam. By inverting the phase of the signal generated by the PID, we could effectively control whether phase- or amplitude squeezed light was generated.

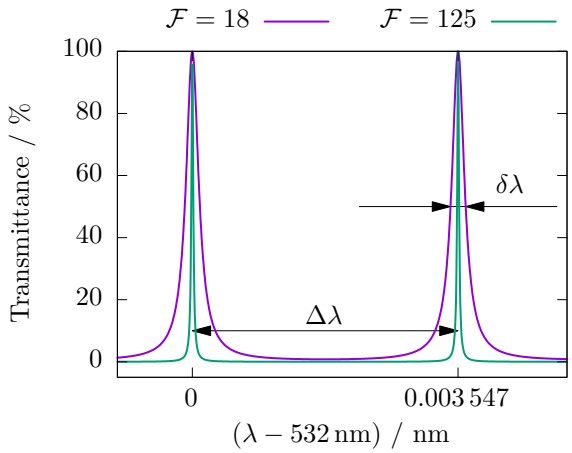

Figure 3.11: Simulated transmission spectrum of a Fabry–Pérot cavity to illustrate the measure 'finesse'. The formula to describe the spectrum may be found in various literature on optics. We assumed a cavity length of 3.99 cm and changed the reflectivity of the cavity mirror to achieve a low and a high finesse. The higher the reflectivity, the more narrow the peaks and the higher the finesse. The horizontal axis is given in relation to 532 nm and shows the absolute shift between the transmission peaks. $\Delta\lambda$ is usually referred to as the free spectral range, $\delta\lambda$ is the bandwidth. The finesse $\mathcal{F}$ is then defined as $\Delta\lambda/\delta\lambda$. As a comparison, the $\mathcal{Q}$ factor is given by $\lambda/\Delta\lambda$. Experimentally, $\mathcal{F}$ is readily measured by shifting the cavity length linearly and recording the transmission signal over time. To resolve also narrow peaks of a high finesse cavity, the speed at which the cavity length is changed may be adjusted. The finesse can then be read off from the recorded signal.

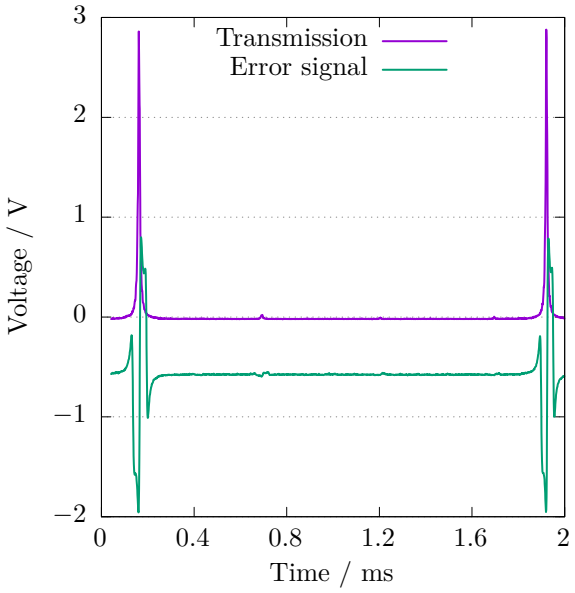

Figure 3.12: A transmission spectrum and error signal from the mode cleaning cavity. To ease the identification, the error signal was shifted by −0.5 V. The transmission signal was picked up by photodetector D1, while the error signal was derived as shown in figure 3.10. To record this spectrum, the cavity mirror was displaced by piezo P2, which was itself driven with a high voltage amplifier. A triangular signal moved the piezo in a linear fashion back and forth. A close inspection of the transmission shows a "bump" around 0.7 ms which stems from the second polarisation mode of the ingoing beam. Even smaller irregularities arise due to a mismatch between the mode determined by the cavity and the ingoing beam. The experimentalists task is to optimise the mode matching to provide for a maximum power throughput. When moving over a resonance, the error signal becomes strongly sloped. This enables (a) a sensitive control, as a small fluctuation results in a large change and, due to zero-crossing on resonance, (b) a "which-way" information, which is not provided by the peak itself.

the reference signal was generated with an external electro-optic modulator[7] (EOM) driven at 37.22 MHz. An overview and explosion view of the squeezer can be found in appendix A.4, page 156. To establish a phase-match condition between the pump- and the infrared steering beam, the crystal's temperature was actively stabilised with a servomechanism (*Wavelength Electronics* LFI3751), temperature sensor and a Peltier element. Another common type of cavities used for the generation of squeezed light are 'bow-tie' (as it resembles the mirror placement) cavities. Due to the presence of four instead of two mirrors, this type offers more flexibility and an easier access to the crystal. On the other hand, a linear Fabry–Pérot cavity requires less space and is, due to the smaller number of components, less prone to optical losses and mechanical instabilities. It requires, however, a precise alignment as little room for adjustments is given by this approach, especially when saving the second mirror by coating the crystal itself. To pump the crystal efficiently, the spatial mode of the pump beam has to match the mode given by the squeezer cavity geometry. We achieved this by the mentioned lens configuration. For a precise alignment, we set the infrared steering beam (entering the squeezer from the right in figure 3.9) to 50 mW. This optical power was sufficient to generate the second harmonic at 532 nm, which was then back-seeded into the mode cleaning cavity and finally detected at detector D6. For the stable generation of phase- or amplitude squeezed light, the phase between the pump- and the steering beam had to be locked[8]. By displacing a mirror via piezo P3, the phase of the pump beam was changed. A fast actuation of the mirror was necessary to counteract disturbances over a large frequency range, hence special care had to be taken about the mirror's housing. A mechanical drawing in appendix A.4 illustrates our solution. The phase relation between pump- and steering beam basically determines the orientation of the squeezing ellipse relative to the steering beam and enables a controlled detection for later experiments. Depending on the phase relation, the steering beam was either amplified or de-amplified [255, 294]. De-amplification is defined to generate amplitude squeezing, while amplification leads to phase squeezing. The lock itself is based on the same Pound–Drever–Hall technique also employed for the other two locks. However, this type of lock does commonly not provide any phase information. To generate an error signal, the photocurrent from photodetector D3, which was also used to lock the squeezer cavity, was phase shifted by 90°. This allowed for detecting a change in the sidebands modulated at 37.22 MHz due to the (de-)amplification in the nonlinear crystal. Furthermore, it effectively reduced the amount of electronics by one photodetector. The design of detector D3 is based on a schematic developed by Gehring and Steinlechner [112]. Figure 3.13 exemplifies the reaction of the error signal when changing the pump beam's phase.

A drawback of this technique, documented by B. Hage [130], is that we could effectively lock only to phase or amplitude squeezing; for an arbitrary squeezing angle another reference signal would be required. This can be provided by an acousto-optical modulator (AOM) in combination with another detector (D4) and a phase shifter (P1). All parts are included in the design, but they have not been fully implemented during our work.

Steering beam The infrared steering beam was used, as its name suggests, as a means to steer the generated squeezed vacuum state. It can be seen as a DC field or carrier of the squeezed state. From previous works, it is known that the employed laser works at the quantum shot noise limit above ca. 2 MHz [27, 130]. A polarising beam splitter (PBS) / half wave plate (HWP)

[7] A *New Focus* 4004 had been modified with a passive network resonant at the driving frequency. Thereby the required power to generate a sufficiently strong phase modulation decreased, and we could use a home-built digital frequency generator with an output of 6 dBm without additional amplification.

[8] Squeezed light will also be generated without a stable phase relation, but, as a consequence, the (anti-)squeezed quadrature follows stochastic fluctuations caused by, e.g., microscopic mechanical vibrations. Assuming that the fluctuations are faster than the detection rate, the squeezed- and the anti-squeezed variance will be averaged. At best (if the squeezed state is pure), the detected variance would look like as if it came from a coherent state.

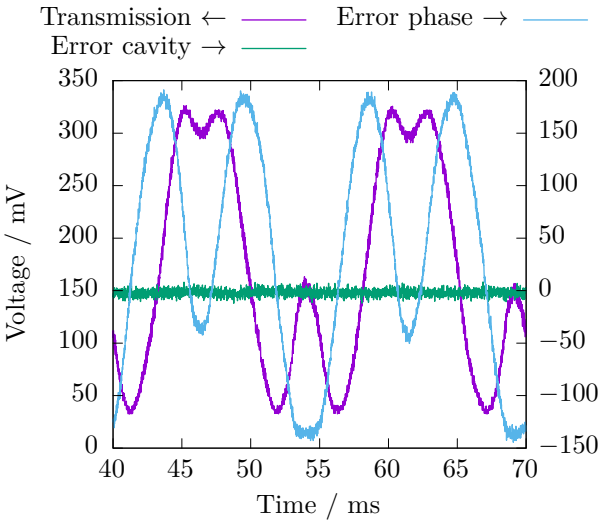

Figure 3.13: Examples of the error- and transmission signals of the squeezer. Arrows indicate the vertical axis the signal is referred to. For this recording, the mode cleaning cavity as well as the squeezer cavity was locked, while piezo P3 was displaced linearly via a high voltage "triangle" signal. The transmission signal was picked up by detector D5. Both error signals were derived from D3. Depending on the pump phase, the signal was amplified or de-amplified. Switching off the pump beam decreased the transmission signal to ca. 55 mV. As can be observed from the 'Error cavity' signal, the servomechanism did not respond to a phase shift of the pump. This was important to lock the cavity and the pump phase individually. The 'Error phase' signal shows a direct correspondence to the amplification of the transmission: Each time this error signal crosses zero, the transmission is either minimal or maximal. Depending on the settings of the pump phase servomechanism, we operated at de-amplification or amplification.

combination controlled the optical power sent to the squeezer and other experiments. Two lenses shaped the beam's mode for a low-loss propagation through the previously mentioned EOM. HWPs controlled the polarisation of the beam to prevent unwanted modulations of the beam's amplitude[9]. A Faraday rotator (FR) in combination with a PBS and HWP enabled a separation between the beam entering and leaving the squeezer, such that detector D3 probed the reflected beam and provided the signal for the cavity and phase lock. Finally, the steering beam was focussed into the squeezer. Due to the hemispherical cavity, the waist of the incident beam had to be positioned at the flat surface of the crystal. The geometry of the cavity led to a waist size[10] of 43(1) µm. A dichroic beam splitter (DBS) reflected only infrared light such that 532 nm light did not propagate to consecutive experiments. For monitoring purposes, photodetector D5 was placed after a removable mirror.

Performance of the squeezer

We will present selected properties of the squeezer to characterise stability and the attainable degree of squeezing.

Mechanical stability For successful experiments, the most important feature of the squeezer (and similar optical cavities) is mechanical stability. As described – and further elaborated in appendix A.2 –, we designed, built and optimised feedback control systems to stabilise the devices. An inherently stable mechanical design however can facilitate the operation significantly. The more unstable the passive component is, the more difficult it is to guarantee a stable operation[11]. Computer simulations of the mechanical design and comparison with other approaches to Fabry–

[9] If the polarisation vector of the beam does not match with the crystal axis, the EOM effectively modulates the phase and amplitude of the polarisation vector parallel and perpendicular to the crystal axis.

[10] Figure A.2 on page 131 illustrates the waist size and other properties of a laser beam.

[11] A stable operation here means that the respective device can be actively controlled on a certain bias point under normal disturbances, such as vibrations and human interferences.

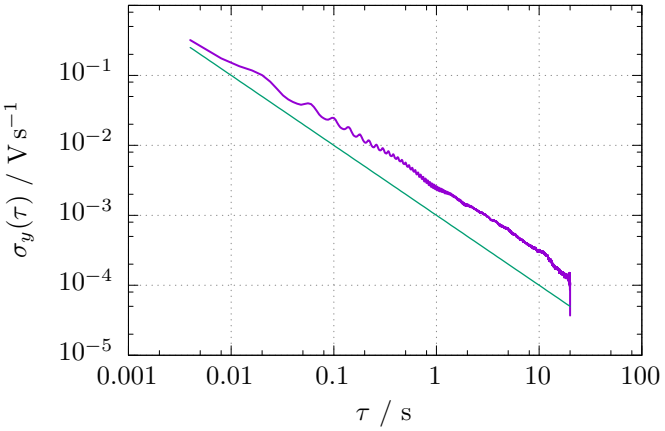

Figure 3.14: Allan deviation applied to a transmission signal of the locked squeezer cavity. The signal was picked up by detector D5 in figure 3.9. The thin solid line follows $1/\tau$ and matches approximately the slope of the measurement. The kink at the very last data point is a numerical artefact. A C program was used for data processing [244].

Pérot cavities [112, 130] led to the design shown in appendix A.4. To characterise the stability of the squeezer cavity, we employed the Allan variance $\sigma_y(\tau)^2$ which is a measure of frequency stability in oscillators, especially clocks [7, 22]. Mathematically, the Allan variance (or sometimes Allan deviation $\sigma_y(\tau)$) for a continuous signal is defined by [7]

$$\sigma_y(\tau)^2 = \frac{1}{2}\Big\langle \big(\bar{y}(t+\tau) - \bar{y}(t)\big)^2 \Big\rangle, \tag{3.50}$$

where τ is the binning time and $\bar{y}(t)$ is the average frequency deviation given by

$$\bar{y}(t) = \frac{1}{\tau}\int_t^{t+\tau} y(t')\,\mathrm{d}t'. \tag{3.51}$$

Care has to be taken when translating it to a time series, that is, a signal which is not originally recorded as a frequency. An algorithm for discrete data which may also be applied to data in time deviation is illustrated by L. Galleani [107]. A translation into a C program can be found elsewhere [244]. The Allan variance is a useful tool to visually identify different types of noise [143, 188]: Depending on the slope of $\sigma_y(\tau)^2$, random noise and technical noise can be differentiated. What we were looking for is whether or not $\sigma_y(\tau)$ follows the $1/\tau$ power law, as it implies that the noise stems from random processes. To explain this behaviour: If $\sigma_y(\tau)$ continuous to decrease over the binning time τ, then the noise source must be random ('white'), because averaging a random signal results in a lower and lower deviation. To compute $\sigma_y(\tau)$, we locked the squeezer cavity on resonance and recorded the output of photodetector D5. As it can be observed in figure 3.14, the Allan deviation follows approximately $1/\tau$ over five decades. The slightly increased slope can be attributed to technical noise.

First gain measurements and homodyne tomography After the squeezer had been assembled, we measured the gain of the (de-)amplification as it is an indication of the achievable degree of squeezing [218, 286]. For this purpose, the steering beam was set to 800 µW and the output was monitored at D5 for different pump powers. By shifting the pump phase, the steering beam was either de-amplified or amplified. The gain of this parametric amplification process was measured via

$$g_{\text{max, min}} = v_{\text{max, min}}/v_0, \tag{3.52}$$

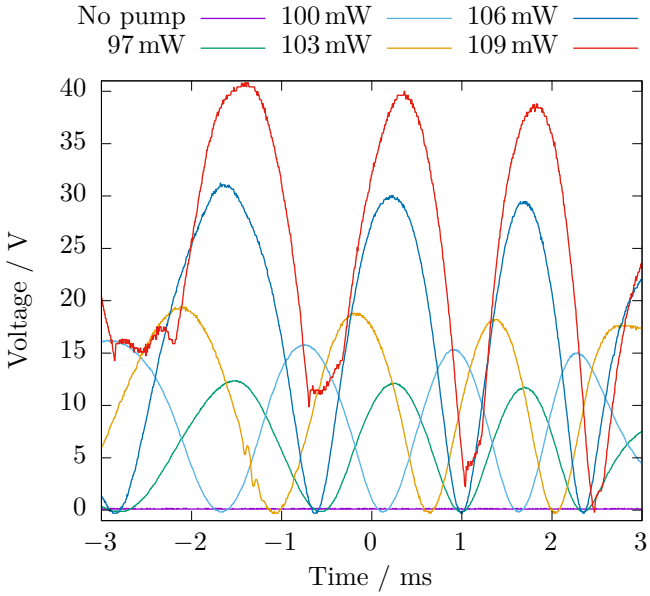

Figure 3.15: Parametric amplification of the steering beam for five pump powers. The signal shown here was picked up by photodetector D5 from figure 3.9. A frequency generator produced a triangular wave at 40 Hz to displace the mirror mounted to P3. Due to the high power of the transmitted beam, a filter was placed in front of the diode. Its absorption was taken into account by rescaling the vertical axis. Compared to a sinusoidal curve, a slight asymmetry already appears at 103 mW, suggesting that the threshold of the spontaneous down-conversion was close to be reached. At more than 109 mW of pump power, the squeezer worked as an optical parametric oscillator above threshold [255].

Power	$g_{\max}$	$g_{\min}$
97 mW	104(2)	0.09(3)
100 mW	133(2)	0.09(4)
103 mW	160(6)	0.09(6)
106 mW	256(10)	0.09(6)

Table 3.1: Gain values derived from the measurement shown in figure 3.15. The distance between the crystal and cavity mirror was here set to 14 mm which corresponds to a beam waist of ca. 39 µm. We note the increase of the uncertainty for high pump powers which rendered a reliable prediction of squeezing parameters impossible.

where v_0 is the transmission signal in absence of pump light. The amplified output for different pump powers is presented in figure 3.15. Values for $g_{\max,\,\min}$ are documented in table 3.1. We note that, in principle, the degree of squeezing and anti-squeezing can be derived from the gain measures [286]: The degree of squeezing is $V_s = 10\log_{10}\left(\sqrt{g_{\max}g_{\min}} + g_{\min} - 1\right)$. That is, if $g_{\max}g_{\min} = 1$, V_s is maximal. As we were operating at very high $g_{\max}$, a precise estimation of $g_{\min}$ was necessary but eventually limited by the resolution of our instruments. At 109 mW, the threshold of the spontaneous down-conversion process was reached, and the squeezer cavity started lasing. An actual homodyne tomography of the squeezed state was not performed, as the spatial output mode exhibited an ellipticity of ca. 1.8. Thus we decided to decrease the air gap between the crystal and mirror by 1 mm to finally 13 mm. In this way, the beam waist of the cavity mode increased from 39 µm to 42 µm which in turn reduced the demand for high focussing power. In the end, a circular beam profile was achieved. Due to the increased beam waist and thereby reduced intensity at a given pump power, the threshold increased to 135 mW.

The initially high gain values were a promising indication of high degrees of squeezing. After a readjustment of the focussing optics, a 'homodyne tomography' was performed. Homodyne tomography refers to performing a homodyne detection while sweeping the local oscillator's phase and recording the detected photocurrent with an electronic spectrum analyser (cf. section 1.2.3). The homodyne detector was built from scratch, based on a design published by T. Gehring [112]. It featured a direct subtraction of the individual photocurrents, which is a concept developed earlier to improve the common mode rejection ratio [167]. This ratio tells the detector's capability of removing unwanted classical noise from the local oscillator [242]. The employed indium-

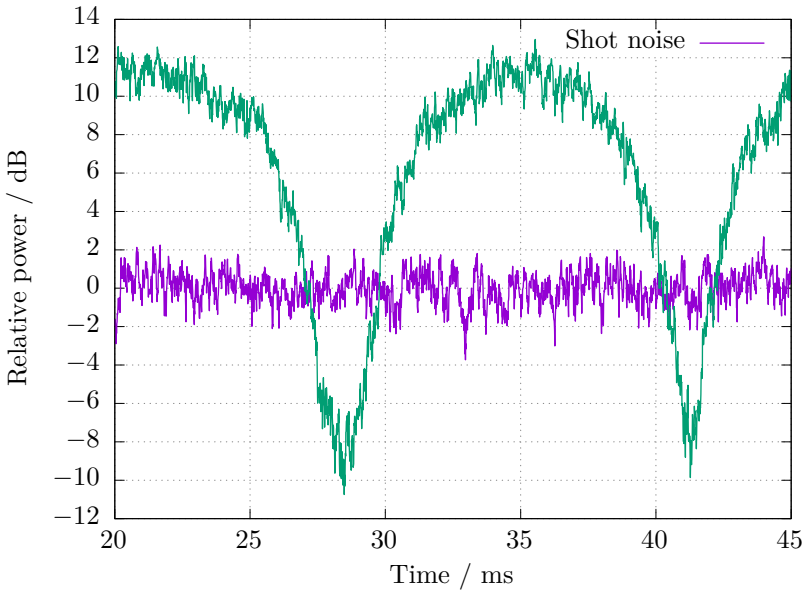

Figure 3.16: Homodyne tomography of the squeezed state immediately after the source. The local oscillator power was set to 12 mW, which yielded an electronic noise clearance of more than 13 dB. Electronic noise was subtracted for this visualisation. The data was acquired at 5.5 MHz with a resolution bandwidth of 300 kHz and video bandwidth of 3 kHz. The interference visibility $\mathcal{V}$ between local oscillator and squeezed beam measured to 98.8 %, which is equivalent to a mode matching efficiency of 97.6 %.

gallium-arsenide photodiodes[12] had a quantum efficiency of $\eta_{\mathrm{qe}} > 99\,\%$. At a pump power of 40 mW and a mode matching efficiency, introduced in section 1.2.3, between local oscillator and squeezed beam of $\eta_{\mathrm{vis}} = 97.6\,\%$, we recorded $V_s = -8.2(2)\,\mathrm{dB}$ and $V_a = 11.0(2)\,\mathrm{dB}$. The signal, recorded by an electronic spectrum analyser (*Agilent* N9000A CXA), is shown in figure 3.16.

As of today, six months past recording 3.16, the squeezer is operational and used for various experiments. During the alignment process of a later experiment, infrared light was sent into the squeezer from the opposite direction (thereby detecting it on photodetector D7). Afterwards, a drop in the degree of squeezing was measurable; the initial value of $-8.2(2)\,\mathrm{dB}$ at 40 mW decreased to $-6.0(2)\,\mathrm{dB}$. We attribute the decrease to intra-cavity losses: The gap between the cavity mirror and the nonlinear crystal is created by a PMMA (known as acrylic glass) spacer with a circular cut-out for the beam to pass[13]. Hitting the edge of the cut out with the tightly focussed, and thus intense, beam might have caused evaporation of the spacer. Due to the small volume of the squeezer cavity, it is likely that the condensing material settled on either of the optics. After the assembly of a second cavity of the same design, it was found that the PMMA spacer can be replaced with an aluminium version, while still maintaining the crystal temperature at more than 38 °C. With the present status of the squeezer we conclude this section and turn to the experimental setup of the quantum enhanced phase measurement.

3.3.2 Interferometer setup

To perform the quantum enhanced phase measurement scheme presented in the theoretical section 3.2, a Mach–Zehnder interferometer had to be built. Instead of using the standard configuration shown, e.g. on page 36, we implemented a polarisation based Mach–Zehnder interferometer where the two spatial modes are replaced by orthogonal polarisation modes. This means that only one spatial mode comprises the to-be-interfered beams and inherently increases the mechanical stability, as demonstrated experimentally in similar interferometers [194].

[12] Purchased in 2011 from *Laser Components*. Unlabelled and packaged in a SOT9 head. Its protection window was removed.

[13] For more details, we refer the reader to appendix A.4.

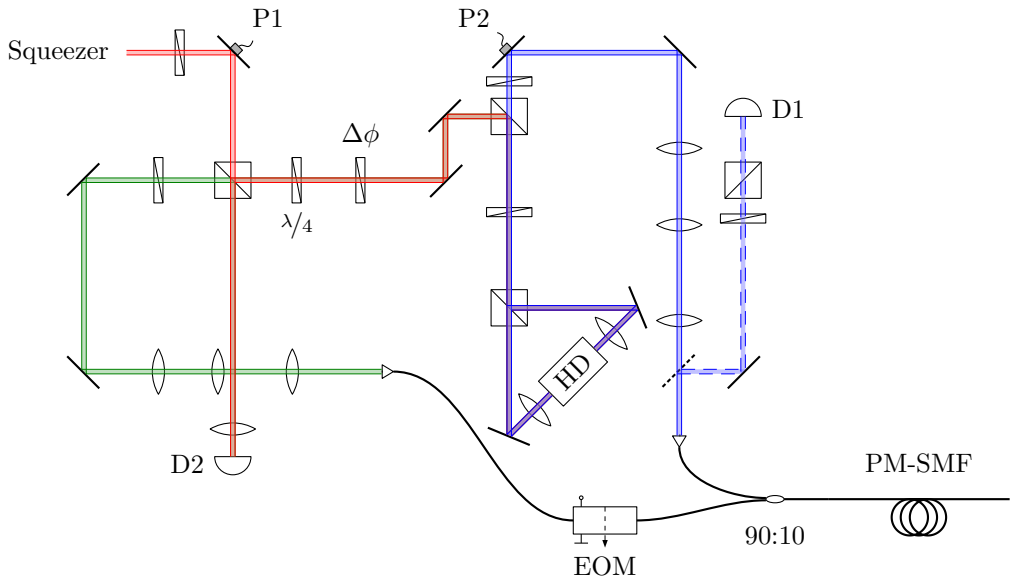

Figure 3.17: To-scale schematic of the optical setup. The short side measures 0.75 m, the long side 1.5 m. All cubes represent polarising beam splitters. If not labelled otherwise, HWPs were used. The HWP labelled by $\Delta\phi$ was mounted in a remote-controlled rotation stage. Both the squeezed beam as well as the beam launched into the fibre were derived from the setup illustrated in figure 4.6 on page 90. The corresponding incoupling stage can be found in a central position of figure 4.6. Detector D1 was used to check the power and the polarisation of the local oscillator. The interference between a fraction of the coherent- and the squeezed beam was measured by detector D2. Its signal was part of a feedback loop to establish a stable phase stabilisation between the the squeezed- and the coherent state. Detector D2 of the same design as detector D2 used to lock the mode cleaning cavity shown in figure 3.9 and originally developed by Gehring and Steinlechner [112]. A mechanical drawing of the mirror mounts containing piezo elements P1 and P2 can be taken from appendix A.4, page 155.

Figure 3.17 illustrates a scaled version of the optical setup. The electronic components involved to stabilise the measurement are shown in figure 3.18. A specification of the commercial components is given in table 3.2.

It is convenient to separate the description into three parts: The beam representing the squeezed state (drawn in red), the one representing the coherent state (green) and finally the local oscillator (blue).

The local oscillator and the coherent state were derived from the infrared beam which was coupled into a polarisation maintaining single-mode fibre (PM-SMF). The corresponding incoupling stage can be found in the centre of figure 4.6. A fibre-based beam splitter sent 90 % of the power directly to a fibre collimator. To control optical power and polarisation properties, photodetector D1 was placed after a removable mirror and a HWP / PBS combination. The interference visibility between local oscillator and signal beam, i.e. the combination of a squeezed and a coherent state, was optimised by means of a telescope. For the measurement run, the visibility read 97 %, mainly limited by the large beam waist of 3.4 mm of the signal beam due to a

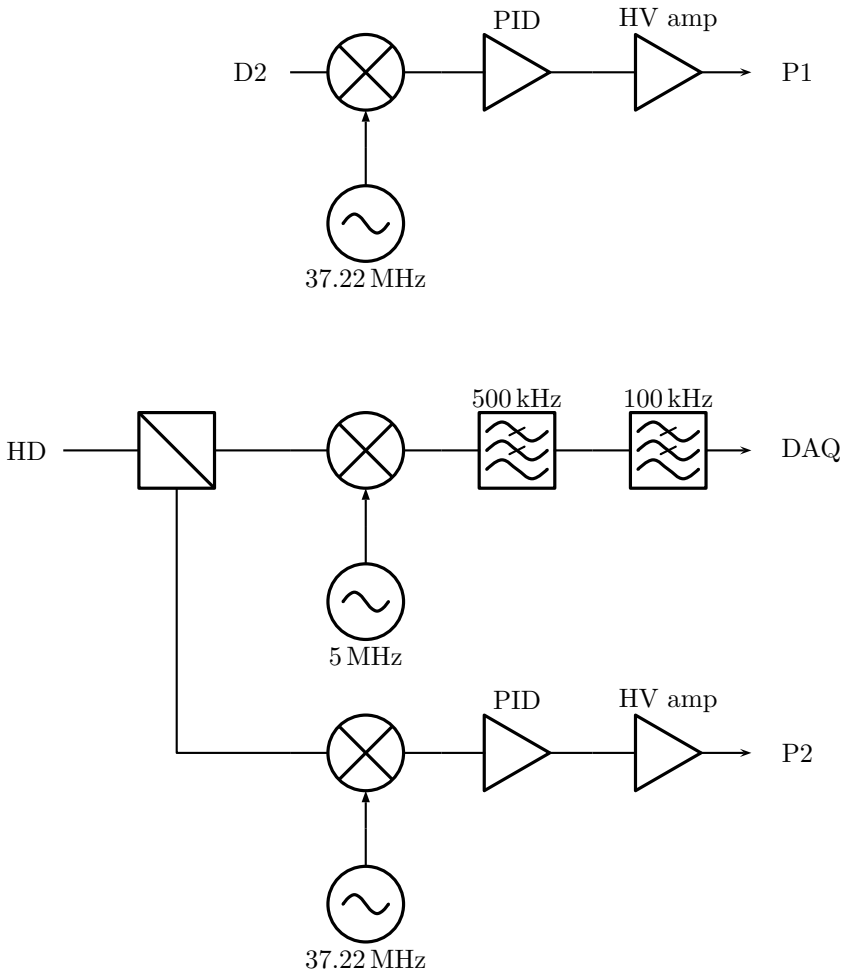

Figure 3.18: Diagram of the electronics applied in the experiment. The external frequencies were generated by a digital synthesiser based on a *Analog Devices* AD9959 chip. All shown devices were built in-house. The photocurrent from D2 was mixed with an electronic oscillator at the same frequency as was used for the phase modulation of the steering beam. Thereby we could reference the coherent state and the steering beam containing the squeezed state to the beam providing the local oscillator. This applies, as the steering beam and local oscillator were derived from the same source. The AC-coupled output of the homodyne photocurrent was split in two: The first half was mixed with a sinusoidal signal at 5 MHz and low-pass filtered. This scheme mimics a spectrum analyser set to 5 MHz. After down-mixing the signal, it was acquired by a 14-bit data acquisition (DAQ) card. To match the bandwidth of the card, a low-pass filter of 100 kHz was connected between the output of the homodyne detector and the DAQ card. The second half served for locking the homodyne detection on the amplitude quadrature. It guaranteed a stable measurement of the amplitude quadrature via a feedback loop.

Component	Company	Model (Specifications)
Fibre patch cable	*Thorlabs*	P3-1064PM-FC-2
Fibre 90:10 PBS	*Thorlabs*	PBC1064SM-APC
Fibre collimator	*Thorlabs*	TC12APC-1064
Fibre EOM	*Photline*	NIR-MPX-LN-0.1-P-P-FA-FA (phase modulator)
Rotation stage	*Thorlabs*	K10CR1/M (USB interface)
PBS	*Bernhard Halle*	$R_s > 99.9\,\%$ at 1064 nm (facets anti-reflection coated)
Data acquisition	*GaGe*	CSE8384 (14 bit digitiser, eight channels, 50 MS/s, 100 MHz bandwidth, PCI Express)
Turning mirrors	*Layertec*	100717 ($R > 99.9\,\%$)

Table 3.2: Commercial components involved in the experiment.

propagation length of ca. 6.5 m measured from the squeezer cavity[14]. Piezo P2 actuated a mirror to control the local oscillator's phase. A HWP set the local oscillator power before combining it spatially with the signal beam. The next HWP in conjunction with a PBS rotated both the local oscillator's and the signal beam's polarisation state, thereby splitting up the two beams into equal halves. Finally, a homodyne detector turned the interference signal into a photocurrent. Following the discussion in the theoretical section 3.2, the amplitude quadrature of the signal beam had to be detected. Hence, the local oscillator and signal beam had to be locked at a fringe maximum or minimum[15]. For locking at this interference point, we implemented an electronic mixer to detected the interference at 37.22 MHz, which was the modulation frequency of the steering beam's phase. This technique is usually referred to as 'AC lock', whereas a stabilisation on a mid fringe position can be achieved without an electronic mixer and is hence termed 'DC lock' [106].

The smaller fraction of light split by the fibre-based PBS travelled through an electro-optical modulator (EOM) driven at 5 MHz before coupled out by a fibre collimator. The EOM modulated the phase of the field, such that we prepared, at the given frequency, a coherent state in the phase quadrature [51, 196]. In terms of a Wigner function $W(x, y)$, whose axes are defined with respect to the local oscillator of the homodyne detection, it means that the state is displaced along the y axis. This contrasts the concept illustrated in figure 3.6, where an amplitude-displaced coherent state enters the interferometer. In fact, as we prepared an amplitude squeezed state, also the squeezed state does not correspond to the configuration in figure 3.6. Hence, the phase of both input states had to be rotated by 90° to match the configuration. Similar to the locking technique outlined in the previous paragraph, a rotation of the relative phase can be achieved by implementing either a DC or an AC lock. To provide the shift of 90° relative to the local oscillator, an AC lock had to be used. Equal to the homodyne detection lock, the reference signal

[14] A large beam waist is beneficial to decrease the divergence of a beam, however it renders the localisation of the waist difficult. The less precise the waist and its localisation is known, the more adjustment is required to match such a beam to a second beam. In principle, the use of a telescope in the signal beam path could have decreased the waist to a smaller size, but to reduce the optical losses we tried to maintain a low count of optics.

[15] The basic idea behind this reasoning is: If the output of an interferometer is initially null, which is the position between minimum and maximum called 'mid fringe', and it changes, the only cause of this change is a p h a s e shift. On its minimum or maximum, where the slope of the output signal vanishes, the a m p l i t u d e of one of the interfering beams has to change to alter the output. To stabilise an interferometer at a 'mid fringe' is readily accomplished, as the signal's slope at this point already provides a "which-way" information. To stabilise on a maximum, however, requires a technique such as the described 'AC lock'.

Table 3.3: Parameter values set or measured during the experiment. The visibility $\mathcal{V}$ was measured for the inference between the local oscillator (LO) and beam for the coherent state ($|\alpha\rangle$) and squeezed state ($|\xi\rangle$). The degree of (anti-)squeezing and purity $\wp$ was characterised via a fit to a homodyne tomography.

Set		Measured	
Parameter	Value	Parameter	Value
Crystal temperature	36.2 °C	Dark noise clearance	18 dB
Pump power	45 mW	$\mathcal{V}(\mathrm{LO} \to \|\alpha\rangle)$	99 %
Steering beam power	400 µW	$\mathcal{V}(\mathrm{LO} \to \|\xi\rangle)$	97 %
Local oscillator power	5 mW	V_s	−6.4(1) dB
Down-mix frequency	5 MHz	V_a	11.1(1) dB
EOM driving frequency	5 MHz	$\wp$	0.582(1)

was provided by the phase modulation at 37.22 MHz of the steering beam. The interference visibility with the local oscillator measured 99 % at the homodyne detector. Depending on the amplitude of the applied modulation signal, the coherent state's average photon number was controlled. To calibrate the voltage-to-photon-number conversion, a homodyne tomography was performed.

Next, we turn to the beam transferring the squeezed state, which we term "squeezed beam". As mentioned above, the squeezer was operated at amplitude squeezing. This operation is beneficial to the noise features of the steering beam, as an operation at amplification also leads to an increase of technical noise from the laser source [130]. Furthermore, the decreased power prevented saturation of the homodyne detector. The crystal temperature for phase matching was 36.6 °C. In front of the squeezer cavity, the optical power of the steering beam measured 400 µW. The pump beam at 532 nm had a power of 45 mW. To split a small fraction from the squeezed beam for interference with the "coherent beam" at detector D2, a HWP was placed in front of the PBS which combined the two beams spatially. After this PBS, the squeezed beam is in s polarisation, orthogonal to the p polarisation of the coherent beam. However, they share the same spatial mode, which was guaranteed by a visibility of 99 % at detector D2. In this situation, the two polarisation modes constitute the interferometer arms. To delay one mode with respect to the other, i.e. create the phase shift, a HWP was used. Mounted in a remote-controlled rotation stage, we could control the experiment from a PC. To exactly mimic a common Mach–Zehnder interferometer, the relative phase shifts from reflections at beam splitters have to copied to our polarisation interferometer. An analysis be means of the Jones formalism [133, 255] shows that an additional quarter wave plate is required to mimic the spatial Mach–Zehnder configuration. Its polarisation axis should be oriented parallel to either of the beams.

The important experimental parameters are summarised in table 3.3.

Electronics and data processing

Here we will summarise details on the photodetectors and the data acquisition.

The photodetector D2 with a built-in circuit for error signal generation was based on the same schematic as detector D2 in figure 3.9 and originally designed by Gehring and Steinlechner [112].

The homodyne detector was, as mentioned on page 62, a direct photocurrent subtraction design and photodiodes with a quantum efficiency of $\eta_{\mathrm{qe}} > 99\,\%$. The detector circuit featured three outputs: A DC output with a bandwidth of 330 kHz, an AC output with a high-pass filter of 1 MHz and an output of a signal created by mixing the AC signal with an electronic oscillator. The latter signal was low-pass filtered at 500 kHz to provide a down-mixed signal for data acquisition. In this way, the data was recorded on a PC without using an electronic

spectrum analyser. The coherent state was prepared by means of the EOM driven at a frequency of 5 MHz. Accordingly, the electronic local oscillator was set to the same frequency. To minimise the required electrical power for the mixing process, the input for the electronic local oscillator was equipped with a resonant filter.

A digital oscilloscope with a PCIe interface (*GaGe* CSE8384) sampled the data from the homodyne detector. It featured a bandwidth of 100 kHz at a sampling rate of 50 MS/s and resolution of 14 bit. Per measurement point, 10^6 samples were acquired. A measurement point was defined by the setting of the motorised HWP. Centred about the null phase, 57 points were recorded every 0.9° (15.7 mrad). Beyond this central region, 40 points were taken with an increment of 2°. These points were used to validate the response of the stage actuating the HWP. The overall procedure was repeated for seven different coherent state amplitudes.

The actual data processing was done as follows:

1. Characterise the squeezed- and coherent state individually via homodyne tomography.

2. Null the data for a correct zero phase. This step is important for further processing, as it symmetrises the data such that the 0° setting implies detecting a squeezed state.

3. Choose a value for a and sort the data of each measurement point according to equation (3.34). As mentioned on page 51, a was set to 1/2. This step yields $\langle \hat{\Pi}_d \rangle$.

4. Fit the function $\langle \hat{\Pi}_d \rangle$, given by equation (3.40), to the experimental results.

5. Calculate the variance at each data point. With an analytic expression of $\langle \hat{\Pi}_d \rangle$, the derivative in equation (3.25) may be calculated. Given the variance and derivative at each data point, the sensitivity is computed. From the fit to $\langle \hat{\Pi}_d \rangle$ from the previous step, a comparison to an analytic expression can be derived.

3.3.3 Results

In our demonstration of quantum enhanced phase measurements we combined a coherent and squeezed vacuum state in a polarisation dependent Mach–Zehnder interferometer. With a fixed −6.4 dB of squeezing, seven coherent states with a different amplitudes were used to investigate the sensitivity and resolution feature. By virtue of homodyne detection the output of the interferometer was monitored. The digitised signal was sorted according to the strategy presented in section 3.2. From the output of the binning, the resolution and sensitivity were derived. Figure 3.19 shows the results for an input state with an average photon number of $\bar{n} \approx 357.8$, calculated according to equation (3.37). Here, we beat the Rayleigh criterion by a factor of 11.6 and the shot noise limit by a factor of 1.7. From the fit to the experimental data, it can be seen that the measurement matches well with the theoretical prediction. This is furthermore verified by figure 3.20, where all results are summarised and compared to our and other approaches to quantum enhanced phase measurements. For all coherent state excitations, we attained super resolution and super sensitivity. The resolution is compared to the Rayleigh criterion, while the sensitivity feature is compared with three different limits: The shot noise, the Heisenberg and the Caves limit. The SNL was clearly beaten by our measurements. As expected, the Heisenberg- as well as the Caves limit were not in reach for our scenario. The limitation for much higher average photon numbers arose due to saturation effects of the detector when the relative phase reached π.

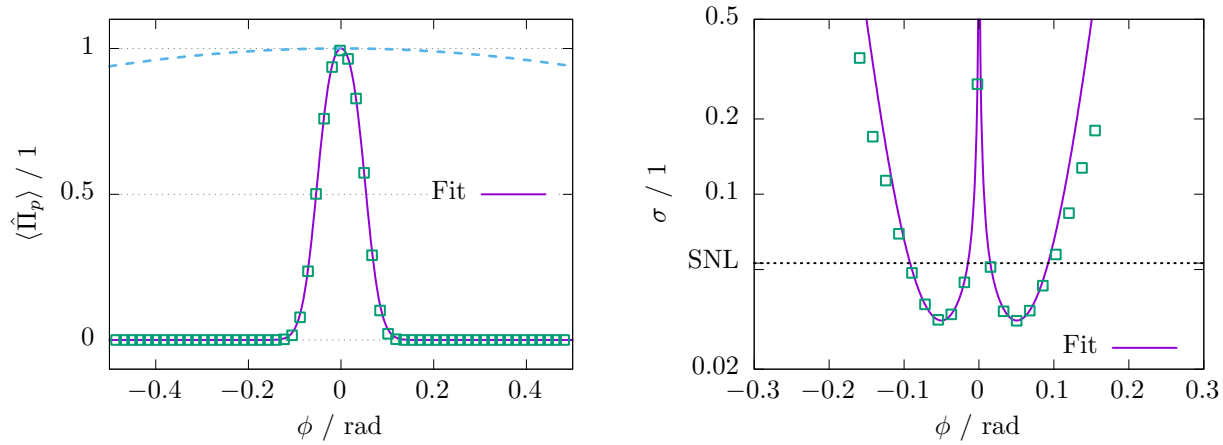

(a) Main fringe (b) Sensitivity around null phase

Figure 3.19: Results achieved for an input state with $|\alpha|^2 = 355$ and a total of $\bar{n} \approx 357.8$. (a) The fringe after applying the dichotomy operator $\hat{\Pi}_d$. A dashed line describes the resolution of a standard interferometer. Its FWHM is 11.6 larger compared to our result. (b) The sensitivity derived from the experimental data. In a range of about ± 0.1 rad, the SNL was surpassed by a factor of 1.7. The uncertainty of each data point is well within the □ symbol. We attribute the symmetric deviations at the wings to a systematic anomaly in the set phase-shift controlled by the HWP.

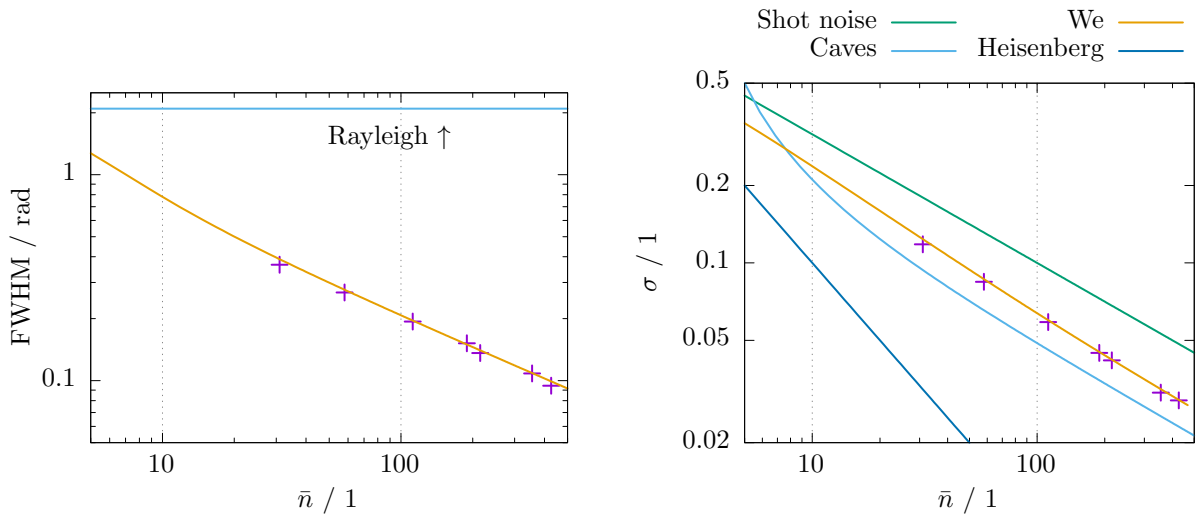

(a) Fringe resolution (b) Comparison of sensitivities

Figure 3.20: (a) The FWHM under variation of the total average photon number of the input state. For comparison, the theoretically predicted FWHM is shown as well and proofs the stable performance of the setup. (b) A comparison to three sensitivity limits. As for the resolution, the theoretical prediction affirms our experimental results. The Caves limit corresponds to the case where $a \to \infty$, thus it does not achieve super resolution.

3.4 Conclusion and outlook

By operating a polarisation based Mach–Zehnder interferometer with a squeezed- and a coherent state input, combined with a post-processed homodyne detection scheme, we demonstrated that phase measurements can overcome Rayleigh's resolution criterion and beat the quantum shot noise limit simultaneously.

With more than $-6\,\mathrm{dB}$ of squeezing and a coherent state with mean photon number of 427, the shot noise limit and the Rayleigh criterion were surpassed by a factor of 1.7 and 23.3, respectively. To achieve these results, a squeezed light source had been designed and implemented from scratch.

Our approach relies only on Gaussian states and detection, and is furthermore fully deterministic. Compared to the discussed technical intricacies in phase measurements based on NOON states, we believe that the features of our approach render it favourable for practical applications.

Depending on the application and the accessible resources, the experimental parameters can be varied continuously: Probing e.g. light-sensitive samples puts an upper bound on the number of photons, thus a low photon number is demanded. This can be achieved by simply changing the coherent-state amplitude. When being confronted with an unknown sample a higher fringe resolution might be advantageous over higher sensitivity. For detectors working on a bias point, the shot noise limit might be more important to beat. Both latter points can be covered easily by varying the post-processing scheme without re-running the experiment.

As the experimental execution could be done in a stable and repeatable manner, our approach can be implemented in more complex scenarios, such as actual microscopes. Another test case is a multi-pass interferometer to evaluate especially the loss performance and to compare with classical multi-pass configuration which naturally yield a higher fringe count.

With respect to direct enhancements of our approach, we aim to extend our theoretical model to a "multi-fringe" theory, which can be accomplished by adding more selection windows to the post-processing. This is a concept applied by Distante et al. for a coherent state input [88] and sketched in figure 3.21. Due to the increase in model parameters, the mathematical modelling for our input configuration gains in complexity.

Finally, with a future experiment we'd like to draw the attention to the benefits of squeezed vacuum states: When sent directly through a phase shifting sample, a comparison of the attainable sensitivities suggests that squeezed vacuum states are capable of outperforming NOON states. This is observed from a comparison of the quantum Fisher information (equation (3.21) and (3.23)). For a significant improvement, the average photon number of the squeezed vacuum state should be larger than 1, i.e. $V_s < -7.7\,\mathrm{dB}$. To achieve this performance, we intend to further enhance and characterise the squeezed light source.

It appears to us that this advantage of squeezed vacuum states is commonly overlooked. This is probably justified by the comparison of a NOON state in a Mach–Zehnder interferometer with a squeezed vacuum state sent into a Mach–Zehnder interferometer. As can be seen from Caves' limit (3.44), sending a vacuum squeezed state into a Mach–Zehnder type interferometer does not reach the absolute sensitivity of a NOON state. While this two-mode configuration is necessary for a NOON state to exist, it is not for a squeezed vacuum state. Because the local oscillator in a homodyne detection provides a phase reference, a squeezed vacuum state can sense a phase shift without relying on a common two-mode interferometer.

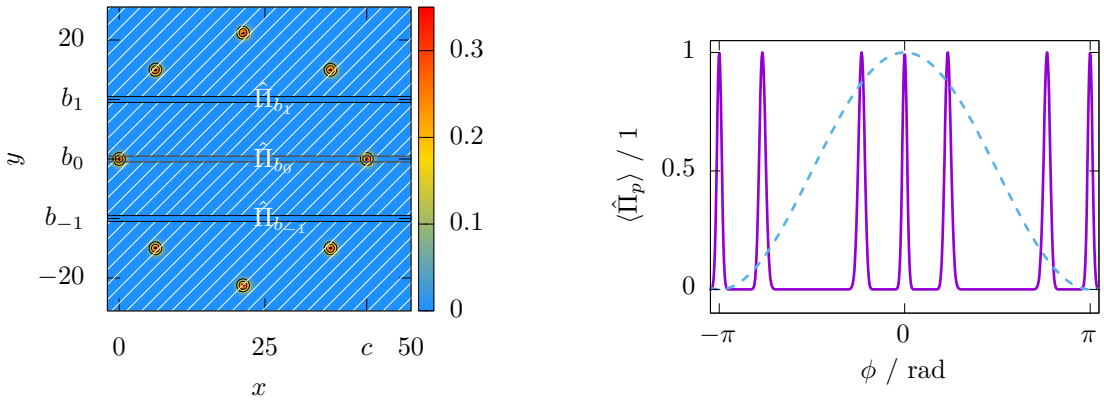

(a) Phase space picture of multi fringe theory

(b) Multiple super resolved fringes

Figure 3.21: (a) Phase space representation of the multi fringe post-processing technique using only a coherent state. Instead of a single window, this technique uses multiple $2a$-sized windows centred at b_i. An experimental verification for up to 20 fringes is given by Distante et al. [88]. (b) Simulation of the super resolved fringes. The parameters are $|\alpha| = 30$ ($c = \Re(\alpha)\sqrt{2}$), $b_1 = b_{-1} = 10$, $a = 1/2$ and correspond exactly to the phase space presentation. We aim to further expand this model to cover also squeezed states for achieving multiple fringes which beat the shot noise limit.

4 | Sensing and feedback cooling of a micro resonator

4.1 Introduction

How massless photons interact with massive objects is the central question of quantum optomechanics. At least from our human perception, this already implies the need for very delicate objects, as we expect the momentum of light to be rather subtle. The probably most popular attempt to utilise and study this interaction dates back to 1873 and is credited to Sir William Crookes: The so-called light mill. Crookes explained the movement of the vanes by radiation pressure – which was eventually proved wrong [77]. However, it took a rather long standing debate, and the involvement of prominent persons such as J. C. Maxwell, A. Einstein and O. Reynolds [180, 229]. Their contributions to experiments and theoretical considerations finally led to the right conclusion about the vane's movement [291]. Almost 30 years later, E. F. Nichols and G. F. Hull conceived an apparatus to observe radiation pressure [209].

The step towards exploring – and eventually utilising – optomechanical effects was to realise that the assembly of an optical cavity around the mechanical object greatly enhance the coupling between the optical field and mechanics. The first works in this field, now known as cavity optomechanics, were motivated by an experimental study which has been shown to be very successful just recently, namely the observation of gravitational waves using optical interferometers [177]. To reach the required sensitivity, a study of various noise sources was and is still undertaken [21]. This has led to the finding that radiation pressure has in fact a detrimental effect on the sensitivity of the mentioned experiment [39, 40, 56].

Since then, the attempts to actually enhance optomechanical effects seem to have outnumbered the occasions where its effect ought to be decreased: This can be attributed to the promise of testing predictions of quantum mechanics on 'macroscopic' objects, i.e. mechanical systems that consist of a large number of atoms. How such systems decohere [191, 210, 235], if they can deliver insight into quantum gravity [222], what role they will play in quantum computation [63, 303] and how they can be used for metrology [17, 81, 278] are, amongst others, questions that attracted much attention.

Chapter structure First, we start with a motivation of our study and a description of the experimental system to focus the proceeding study. A brief introduction to the theoretical framework of cavity optomechanics and feedback control can be found next. It provides the reader with necessary details for the analysis; readers who are interest in a rigorous mathematical study are kindly referred to the work of Bowen and Milburn [37], Wiseman and Milburn [288], Jacobs [151], or a comprehensive review by Aspelmeyer et al. [14]. The main section on the experimental setup follows next and presents measurements and calibration details. The chapter

closes with a summary of the results and an outlook to motivate further investigations.

4.1.1 Motivation towards the cooling scheme

We have investigated one aspect which is often considered as a prerequisite for most of the previously named applications of optomechanical systems [14]: Cooling the mechanical object, better-to-say mechanical oscillator, by means of an active control scheme. Usually, the intention of cooling schemes is to prepare the mechanical oscillator in its motional ground state. The subject of this work was to combine various concepts of quantum optics and apply them in the field of cavity optomechanics: Rather than cooling the mechanical oscillator to its lowest temperature, which has been demonstrated by others, we demonstrated experimentally a novel aspect feedback cooling.

Depending on the system parameters, different methods towards cooling the mechanical oscillator have been devised [14, 113, 295]. Feedback cooling [189], the method we applied, can be itself implemented in various ways: Radiation pressure force was shown to be usable [67, 165, 287], although it is rather weak; its effectiveness is limited by the optical power required to actuate the mechanical oscillator – the beam used for cooling will eventually lead to excessive heating. Several non-optical schemes had been devised, for example piezo driven cantilevers [224], optical tweezers [173], coil actuators [73, 176], and the use of dielectric gradient forces [169, 274]. Motivated by its feasibility and strong influence, our study is based on a feedback scheme using the last named dielectric gradient forces.

The cooling efficiency is first of all limited by the ability to probe the mechanical oscillator with high sensitivity, thus it is of special interest to increase this ability. As for gravitational wave detectors, an increased power to probe the oscillator does increase the sensitivity, but it also increases the afflicted noise due to radiation pressure and additional detrimental effects due to absorption [251] and nonlinear effects [250, 272]. To be able to probe the mechanical oscillator's movement more efficiently, we combine a feedback technique with an optical squeezed-state probe. The fact that squeezed light, introduced briefly on page 10, can be employed to enhance laser cooling of atoms was proposed already in the early 1990s [62, 125]. An experiment of a cooling scheme based on squeezed light and dielectric gradient force feedback had, to our knowledge, not been realised.

4.1.2 Overview of the optomechanical system

The actual optomechanical system of our study is sketched in figure 4.1. An optical fibre, tapered to ca. 1 µm, provides coupling of light into and out of the optical cavity. The latter is formed by a silica microtoroid. Due to its shape, this type of optical cavity is also referred to as a whispering gallery mode resonator. To fix the microtoroid mechanically, a pillar of silicon is fabricated onto a chip of the same material. A thin disc-like region in the centre of the toroid serves to combine the latter with the silicon pillar. The silicon chip itself only serves as a basis of the overall fabrication process.

The silica microtoroid also constitutes a mechanical oscillator; silica's high elastic module in combination with a mass on the order of a few micro gram yields mechanical frequencies on the order of 10^6 Hz to 10^8 Hz [52, 248, 249].

An electrode placed in close vicinity above the microtoroid provides the dielectric gradient force, controlled with a real-time feedback by detecting the output of the tapered fibre. Common sewing needles were used as electrodes.

As the fabrication of the fibre and the microtoroid were not part part of our study, details can be found elsewhere [13, 18, 250]. The toroid fabrication was undertaken within the Queensland

Node of the Australian Nanofabrication Facility, while the fibre tapering was carried out in W. P. Bowen's group at the University of Queensland. Similar devices had been used in previous experiments [141, 163].

4.2 Theoretical framework

For a correct analysis and description of the experimental finding, two subjects are treated next: How the motion of the mechanical oscillator can be sensed with an optical probe, and how this information can be used to cool the mechanics. A broader theoretical study of cooling techniques and their fundamental boundaries was carried out by, amongst others, H. Kerdoncuff [163] and Genes et al. [113].

In terms of notation, we will adopt the usage of hats to mark quantum operators; classical quantities come with them. As one means to facilitate the shift between the classical and quantum description, it is common to split an operator $\hat{O}$ into an amplitude $O \in \mathbb{C}$ and a so-called noise operator $\delta\hat{O}$ [16, 37]:

$$\hat{O} \to O + \delta\hat{O} \tag{4.1}$$

4.2.1 Sensing the mechanical motion via an optical probe

Before applying information from the mechanical motion to eventually control it, the motion has to be sensed. The probe which reads out this information is an optical field sent into the tapered fibre, as depicted in figure 4.1. To understand the process of optomechanical sensing, a sketch of the interaction will be given next. A concise introduction into quantum mechanics applied to optical and mechanical systems can be found in the review of Aspelmeyer et al. [14] and a book chapter of G. S. Agarwal [3]. As previously cited, the work of Bowen and Milburn [37] provides an extensive treatment of quantum optomechanics.

Dynamics of the optomechanical system

To describe the time evolution of a generic cavity optomechanical system, we first gather the energy terms for the Hamiltonian:

$$\hat{\mathcal{H}} = \hat{\mathcal{H}}_c + \hat{\mathcal{H}}_m + \hat{\mathcal{H}}_i. \tag{4.2}$$

It is comprised of the energy in the optical cavity c, the mechanical oscillator m, and the interaction i between them. The notation introduced below corresponds to the quantities visualised in figure 4.1.

Using the position and momentum operator, $\hat{q}$ and $\hat{p}$, respectively, and the optical ladder operators $\hat{a}^\dagger$ and $\hat{a}$, we find[1] [37, 114, 181]

$$\hat{\mathcal{H}} = \frac{1}{2}\left(\frac{\hat{p}^2}{m_{\text{eff}}} + m_{\text{eff}}\Omega_m^2\hat{q}^2\right) + \hbar\omega_c\left(\hat{a}^\dagger\hat{a} + \frac{1}{2}\right) + \hat{\mathcal{H}}_i, \tag{4.3}$$

where m_{eff} symbolises the effective mass of the optomechanical system. The concept of effective mass will be explained later; in general terms it is the mass of the mechanical oscillator which is both in motion and in interaction with the optical mode.

Similar to the electromagnetic field (cf. equation (1.7)), ladder operators can also be introduced for the mechanical oscillator. Furthermore, it is convenient to use a dimensionless set of

[1] Identity operators in the form of $\hat{a} \otimes \hat{\mathbf{1}}$ or $\hat{\mathbf{1}} \otimes \hat{b}$ to complete the Hilbert space will be omitted.

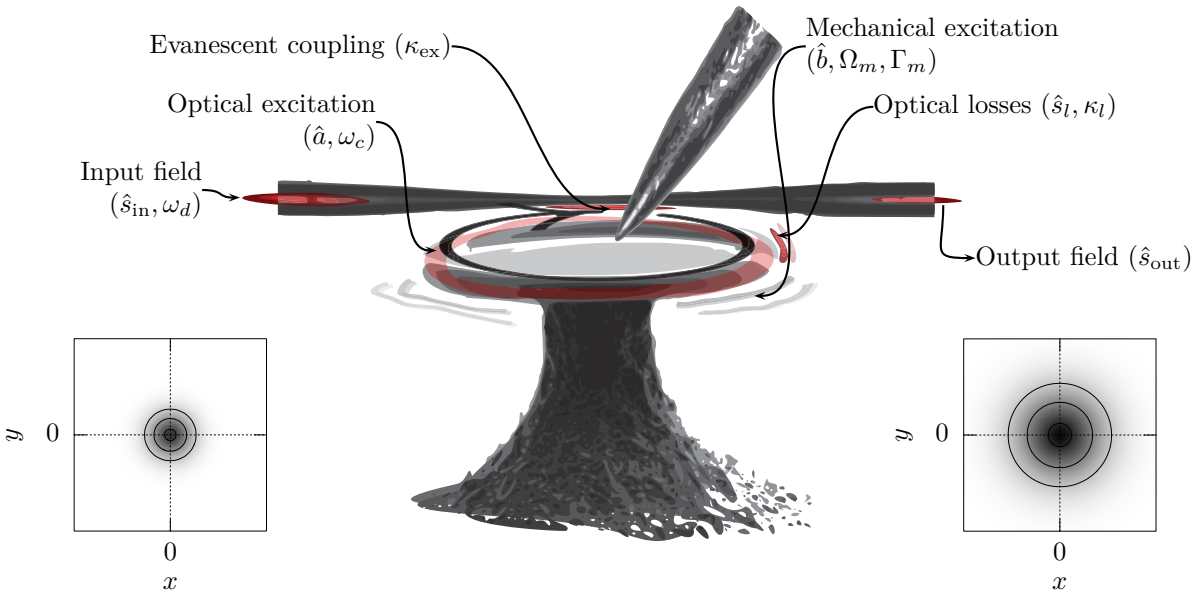

Figure 4.1: Illustration of the effects and physical parts constituting the experiment. Although a scaling of the various parts was not the primary aim, the drawing captures the most important dimensions. As an indication, the width of the pillar is about 20 µm at its thinnest part. After accomplishing the desired coupling between the optical cavity- and the tapered fibre mode via evanescent coupling, an electrode tip was brought a few micrometres above the microtoroid.
A probe beam with a frequency ω_d was injected into the fibre, described by the operator $\hat{s}_{in}$. At a rate of κ_{ex}, an optical field was excited inside the cavity, represented by the annihilation operator $\hat{a}$. The frequency ω_c of the mode is set by the refractive index n and the geometry of the microtoroid, approximately given by $c_0/(nr)$, where r denotes the toroid's radius. Optical losses at a rate of κ_l, caused by irregularities on the facet and absorption, broadened the effective cavity width to $\kappa_c = \kappa_l + \kappa_{ex}$. To describe the mode of the losses, we denoted it as $\hat{s}_l$. The mechanical excitation – always present as the experiment was conducted at room temperature – is described by the annihilation operator $\hat{b}$. A consequence of the mechanical excitation at a frequency of Ω_m is a length change of the optical cavity. Γ_m specifies the width of the mechanical resonance. Induced by the changing length, the outgoing optical field features a phase shift. This is equivalent to say that sidebands are modulated onto the carrier signal. We will mathematically describe this effect and the readout in a following section. The sideband modulation can be also be pictured as a Raman-like scattering process where Stokes and anti-Stokes sidebands are populated by photons bouncing on the mechanical oscillator [14, 37].
The readout of the mechanical state is visualised by the two plots of the Wigner function $W(x, y)$ (for an introduction see page 15), inset at the bottom: On the left side, the state of the probe field is shown – at the sideband frequency Ω_m – before the interaction. By virtue of optomechanical coupling, the state of the mechanical oscillator is transduced to the probe field. On the right side, we see that the vacuum state was populated and forms now a thermal state. The information drawn from probing the optical mode at the output yields information about the oscillator's motion, which was used as the control signal in the feedback loop. To close the feedback loop, a voltage was applied over the microtoroid by an electrode. The electric ground was formed by a conductive baseplate.

operators. The conversion between the mechanical oscillator ladder operators, the dimensionless-, and the "standard" position and momentum operators reads

$$\frac{1}{\sqrt{2}}\left(\hat{b}^\dagger + \hat{b}\right) = \hat{Q} = \frac{\hat{q}}{\sqrt{2}q_{\mathrm{zpf}}}, \tag{4.4a}$$

$$\frac{\imath}{\sqrt{2}}\left(\hat{b}^\dagger + \hat{b}\right) = \hat{P} = \frac{\hat{p}}{\sqrt{2}p_{\mathrm{zpf}}}, \tag{4.4b}$$

and directly resembles the optical quadrature operators $\hat{X}$ and $\hat{Y}$ introduced on page 7. In terms of the commutation relation, the optical and mechanical quadratures are equal: $[\hat{Q}, \hat{P}] = \imath$. The quantities q_{zpf} and p_{zpf} are the vacuum state standard deviations (often referred to as 'zero-point fluctuations') of the respective operator. Their values may be derived from equation (4.3) and read

$$q_{\mathrm{zpf}} = \sqrt{\frac{\hbar}{2m_{\mathrm{eff}}\Omega_m}}, \tag{4.5a}$$

$$p_{\mathrm{zpf}} = \sqrt{\frac{\hbar m_{\mathrm{eff}}\Omega_m}{2}}. \tag{4.5b}$$

Thus a high mechanical frequency increases the position fluctuation amplitude q_{zpf}, which is eventually convenient to increase if one aims to be (at least theoretically) able to resolve zero-point fluctuations. The challenge is that usually high frequencies are associated with very light systems, and as mass and frequency are on equal footing here, there is no gain in aiming only at high frequencies. This challenge has attracted scientists to design intricate optomechanical systems, some of which may be found in a review article by Aspelmeyer et al. [14].

What is missing yet is the description of the interaction between the optical field in the cavity and the mechanical oscillator. However, looking at drawing 4.1, we can recognise the mechanical oscillation as a deformation of the optical cavity. Thus ω_c in equation (4.3) is not static, but a function of $\hat{q}$. The actual function of $\omega_c(\hat{q})$ depends on the cavity geometry and can be complex to derive analytically, especially for a microtoroid. Approximate solutions for simple geometries have been found [147], but for length shifts smaller than the cavity length l, a truncated Taylor expansion also provides a good approximation. Such an approximation yields

$$\omega_c(\hat{q}) \approx \omega_c(1 + \hat{q}/l). \tag{4.6}$$

By substitution the latter into the equation (4.3), the Hamiltonian reads

$$\hat{\mathcal{H}} = \frac{1}{2}\left(\frac{\hat{p}^2}{m} + m_{\mathrm{eff}}\Omega_m^2\hat{q}^2\right) + \hbar\omega_c\left(1 + \frac{\hat{q}}{l}\right)\left(\hat{a}^\dagger\hat{a} + \frac{1}{2}\right). \tag{4.7}$$

The interaction Hamiltonian $\hat{\mathcal{H}}_i$ thereby is $\hbar\omega_c\hat{q}\left(\hat{a}^\dagger\hat{a} + \frac{1}{2}\right)/l$, that is linearly depended on the position $\hat{q}$. Next, we can replace $\hat{q}$ and $\hat{p}$ by virtue of equation (4.4) with the mechanical ladder operators to arrive at

$$\hat{\mathcal{H}} = \hbar\omega_c\hat{a}^\dagger\hat{a} + \hbar\Omega_m\hat{b}^\dagger\hat{b} + \hbar g_0\hat{a}^\dagger\hat{a}\left(\hat{b}^\dagger + \hat{b}\right). \tag{4.8}$$

First, all constant terms are removed, as they do not contribute to the evolution of the system. Second, the vacuum optomechanical coupling rate

$$g_0 = \omega_c q_{\mathrm{zpf}}/l \tag{4.9}$$

has been introduced. It is a fundamental parameters in cavity quantum electrodynamics as it determines how fast $\hat{a}$ and $\hat{b}$ interchange energy [281]. For our system, it both tells how the mechanical displacement shift the optical frequency and how a single photon "kicks" the mechanical oscillator.

For a simulation of the latter Hamiltonian, we would have to take into account a large time span from mechanical to optical rates. To facilitate the (numerical) treatment, the Hamiltonian can be transformed into a frame rotating at the laser frequency ω_d used to drive or probe the system. The transformation is done by $\hat{\mathcal{H}} \to \hat{U}^\dagger \hat{\mathcal{H}} \hat{U} - \hat{V}$, where the generator of $\hat{U}$ is $\hat{V} = \hbar\omega_d \hat{a}^\dagger \hat{a}$ [114]. Applying the transformation to equation (4.8) changes

$$\omega_c \hat{a}^\dagger \hat{a} \to (\omega_c - \omega_d)\hat{a}^\dagger \hat{a} = \Delta \hat{a}^\dagger \hat{a}, \tag{4.10}$$

whereas Δ denotes the detuning between the input field, oscillating at ω_d, and the cavity field.

For g_0 to have a significant effect on the dynamics of the system, the decay rates κ and Γ_m have to be at least on equal footing. Otherwise a coherence between $\hat{a}$ and $\hat{b}$ will quickly dissipate. To enhance the coupling, the optical cavity can be driven with an external coherent optical field. It is readily introduced into to the Hamiltonian, assuming the drive field is unitary, via

$$\hat{\mathcal{H}} = \hbar\Delta \hat{a}^\dagger \hat{a} + \hbar\Omega_m \hat{b}^\dagger \hat{b} + \hbar g_0 \hat{a}^\dagger \hat{a}\left(\hat{b}^\dagger + \hat{b}\right) + \hbar d\left(\hat{a}^\dagger + \hat{a}\right). \tag{4.11}$$

Here d symbolises the rate at which the optical field is populated. By this Hamiltonian, the unitary evolution of an arbitrary optomechanical system can be described. It is a valid description for a single optical and mechanical mode, if the shift in cavity length is much shorter than its length "at rest".

Relation between the cavity- and input field

While the optical field in the cavity $\hat{a}$ is obviously important for the optomechanical interaction, it can be more interesting to derive it from the input field. Experimentally, we have direct access to the latter and the output; for the intracavity field this does not apply. Thus, it is of importance to built a relation between what leaves and enters the cavity. This is achieved by means of the input-output formalism [109] and can account for additive dissipative, i.e. non-unitary, effects. In contrast to the previously description in terms of Hamiltonian, i.e. following the Heisenberg picture, the input-output formalism grounds on the Schrödinger picture where the dynamics are associated to the operators, not the state. Especially steady state conditions can be developed easier by this means. Next, we will apply the input-output formalism to draw a connection between the mechanical oscillation and its optical detection.

First, energy conservation requires

$$\hat{s}_{\mathrm{out}} = \hat{s}_{\mathrm{in}} - \sqrt{\kappa_{\mathrm{ex}}}\hat{a}, \tag{4.12}$$

that is: The output field is what is left from the input, because $\hat{s}_{\mathrm{in}}$ couples at a rate of κ_{ex} to the optical cavity[2]. An illustration of the quantities is given by figure 4.1. The dynamics of the

[2]We adopted the convention of treating the in- and output field observable $\hat{s}^\dagger_{\mathrm{in}}\hat{s}_{\mathrm{in}}$ and $\hat{s}^\dagger_{\mathrm{out}}\hat{s}_{\mathrm{out}}$, respectively, in the dimension of a flux, while the corresponding observable $\hat{a}^\dagger\hat{a}$ of the intracavity field is a number. To recognise the difference, we prefer to use $\hat{s}_{\mathrm{out}}$ over $\hat{a}_{\mathrm{out}}$.

cavity field amplitude, by virtue of the input-output formalism, reads [3, 37, 109]

$$\frac{\mathrm{d}\hat{a}}{\mathrm{d}t} = -\Big(\imath\Delta + \imath\sqrt{2}g_0\hat{Q} + \frac{\kappa}{2}\Big)\hat{a} + \sqrt{\kappa_{\mathrm{ex}}}\hat{s}_{\mathrm{in}} + \sqrt{\kappa_l}\hat{s}_l, \tag{4.13a}$$

$$\frac{\mathrm{d}\hat{Q}}{\mathrm{d}t} = \Omega_m\hat{P}, \tag{4.13b}$$

$$\frac{\mathrm{d}\hat{P}}{\mathrm{d}t} = -\Omega_m\hat{Q} + \frac{\sqrt{2}q_{\mathrm{zpf}}}{\hbar}\hat{F}_{\mathrm{th}} - \Gamma_m\hat{P} - \sqrt{2}g_0\hat{a}^\dagger\hat{a}. \tag{4.13c}$$

At a rate of $\sqrt{\kappa_l}$, photons can leak out of the cavity. It has to be noted that also an addition to the cavity population can enter via this port, e.g. due to the thermal bath the cavity is situated in. At optical frequencies, the latter is negligible even at room temperature. However, at mechanical frequencies in the range of kHz to GHz, stochastic fluctuations generating a force F_{th} will certainly affect the motion.

Semiclassical evaluation and identification of system parameters In general, the set (4.13) of equations is difficult to solve. In the attempt of gaining more insight into the coupling, one can constrain the dynamics to a semiclassical picture. Instead of evaluating the complete statistics of the operators, the expectation values can be taken. This implies, with the reasoning given above, $\langle\hat{s}_l\rangle = \langle\hat{F}_{\mathrm{th}}\rangle = 0$. In addition, all correlations between the operators are neglected, such that $\langle\hat{O}_1\hat{O}_2\rangle = \langle\hat{O}_1\rangle\langle\hat{O}_2\rangle$. Applying the expansion of $\hat{O}_1$ according to equation (4.1) yields $\big\langle(O_1 + \delta\hat{O}_1)(O_2 + \delta\hat{O}_2)\big\rangle$, and helps to check the validity of the latter simplification: Only if the correlations $\big\langle\delta\hat{O}_1\delta\hat{O}_2\big\rangle$ are smaller compared to the amplitudes, the simplification is sound. This holds when dealing with an optomechanical system probed with a laser beam, such that the intracavity photon number is on the order of 10^6, and no other process[3] amplify the fluctuations.

Finally, the given assumptions reduces the set (4.13) to

$$\frac{\mathrm{d}\langle\hat{a}\rangle}{\mathrm{d}t} = -\Big(\imath\Delta + \imath\sqrt{2}g_0\langle\hat{Q}\rangle + \frac{\kappa}{2}\Big)\langle\hat{a}\rangle + \sqrt{\kappa_{\mathrm{ex}}}\langle\hat{s}_{\mathrm{in}}\rangle, \tag{4.14a}$$

$$\frac{\mathrm{d}\langle\hat{Q}\rangle}{\mathrm{d}t} = \Omega_m\langle\hat{P}\rangle, \tag{4.14b}$$

$$\frac{\mathrm{d}\langle\hat{P}\rangle}{\mathrm{d}t} = -\Omega_m\langle\hat{Q}\rangle - \Gamma_m\langle\hat{P}\rangle - \sqrt{2}g_0\langle\hat{a}^\dagger\hat{a}\rangle. \tag{4.14c}$$

Considering a coherent input field $\langle\hat{s}_{\mathrm{in}}\rangle = s_{\mathrm{in}}$, $\langle\hat{a}\rangle$ equals a coherent amplitude α. Thereby we identify $g_0|\alpha|^2$ in equation (4.14c) as the optomechanical coupling rate enhanced by the number of photons in the cavity, defined as

$$g = g_0|\alpha|^2 = g_0 n_c. \tag{4.15}$$

This leads to the introduction of another derived quantity of optomechanical systems: The cooperativity[4]

$$C = \frac{4g_0^2 n_c}{\kappa\Gamma_m}. \tag{4.16}$$

A large cooperativity implies that the coherent interaction between the optical and the mechanical mode is faster than their decay. Thereby it also tells how strong optical shot noise heats the

[3] Driving the optomechanical system at an instability, the quantum fluctuations can amplified and rule out the discussed simplification [292].

[4] It has to be noted that the numerical factor in the cooperativity differs amongst authors, compare for example Bowen and Milburn [37], with Aspelmeyer et al. [14].

mechanical oscillator. We also note that C depends on the intracavity photon number n_c, i.e. it scales quadratically with the input power.

Equation (4.14a) offers additional insight into two aspects of our experiment.

Optical cavity without mechanical coupling First, the equation (4.14a) is solved for an optical system without coupling to a mechanical oscillator, that is $g_0 = 0$. With the initial condition of an empty cavity, we find

$$|\alpha|^2 = s_{\text{in}}^2 \frac{4\kappa_{\text{ex}}\, \mathrm{e}^{-t\kappa}\left(-2\,\mathrm{e}^{\frac{\kappa t}{2}}\cos(t\Delta) + \mathrm{e}^{\kappa t} + 1\right)}{\kappa^2 + 4\Delta^2}, \tag{4.17a}$$

$$\arg(\alpha) = \arg\left(\frac{1 - \mathrm{e}^{-\frac{1}{2}t(\kappa + 2\imath\Delta)}}{\kappa + 2\imath\Delta}\right), \tag{4.17b}$$

$$|\alpha|^2_{t\to\infty} = s_{\text{in}}^2 \frac{4\kappa_{\text{ex}}}{4\Delta^2 + \kappa^2}, \tag{4.17c}$$

$$\arg(\alpha)_{t\to\infty} = \arg\left(\frac{1}{2\imath\Delta + \kappa}\right). \tag{4.17d}$$

By virtue of equation (4.12), the amplitude and phase of α can further be related to the output[5]. Analysing the behaviour of the steady state solutions, the optical coupling efficiency defined as

$$\eta_c = \kappa_{\text{ex}}/\kappa \tag{4.18}$$

is of importance for sensing of the mechanical motion, as we will shortly see. Three different optical coupling regimes can be considered. Figure 4.2 visualises all regimes.

1. The overcoupled regime where $\eta > 1/2$. Energy exchanges at a faster rate than it decays via losses. Light enters the cavity at a high rate, but it also leaves it in the same way. Thus, the intracavity field won't reach its maximum. Tuning over the resonance, the phase shift of the outgoing filed is maximal: 2π. We will shortly see in detail that the microtoroid's mechanical motion causes a phase modulation of the optical field. From this point of view, an operation in the overcoupled regime seems to be optimal, as it yields the strongest phase shift and hence extracts most of the information.

2. The undercoupled regime where $\eta < 1/2$. Light that enters the cavity is more likely to get lost than coupled out. Accordingly, the intracavity amplitude again won't reach its maximum, and it might be even lower than the output field. This applies for the case $\eta_c = 0.13$ shown in the middle amplitude plot in figure 4.2, for slightly higher η_c it is no longer true. On resonance, the phase shift imprinted on the output field is always the smallest compared to the other regimes.

3. When $\eta = 1/2$ the cavity is said to be critically coupled or 'impedance matched'. The loss- and energy exchange rate are equal: $\kappa_l = \kappa_{\text{ex}}$. This allows for the maximal intensity built-up inside the cavity. The phase shift experienced by the output field spans π. On resonance ($\Delta = 0$), the transmitted field vanishes. As our experimental approach relied on detecting a transmitted field, the critically coupled regime was avoided.

[5]We remind that $|\alpha|^2$ is the mean number of photons and $|s_{\text{out}}|^2$ a flux. In an experimental setting, the power $P_{\text{out}} = \hbar\omega_d|s_{\text{out}}|^2$ instead of the field amplitude can be accessed directly. For the intracavity power, $P_c = \hbar\omega_d|\alpha|^2/\tau_c$, where τ_c is the round trip time for a photon. In the analysis however, we will stick to $|\alpha|^2$ and $|s_{\text{out}}|^2$ without loss of generality.

Even though the properties of the undercoupled regime appear to be disadvantageous, it is useful to operate in it when quantum noise features of the input field are tried to be preserved: By the analysis of homodyne detection on page 12, illustrated also in figure 3.7 on page 50, it can be told that the presence of losses degrades the noise suppression due to squeezed light, which is our means of enhanced sensing. Surprisingly, it was proofed theoretically that the arguments for and against one of two coupling regimes are balanced, such that the choice is irrelevant [163, 164]. However, in relation to the experiment, it is more convenient to work in the undercoupled regime: It is realised by widening the gap between the fibre taper and the toroid, thereby it is less likely to contact the former with the latter.

Regardless of the coupling regime, a detuning leads to a phase shift of the outgoing field. By virtue of the optomechanical coupling (described by the Hamiltonian (4.11)) mechanical motion causes detuning. Thus we can expect to sense this motion by detecting the phase shift imprinted on the light leaving the cavity.

Optical cavity with a mechanical oscillation To check how exactly the described mechanically-induced phase shift affects the cavity field, we will conclude the study by adding a harmonic mechanical displacement in equation (4.14a). Thus we substitute $\langle\hat{Q}\rangle = Q\sin(\Omega_m t)$, but leave the momentum and position uncoupled. The full solution reads

$$\alpha(t) = s_{\mathrm{in}}\sqrt{\kappa_{\mathrm{ex}}}\exp\left(\imath\left(\frac{\sqrt{2}g_0 Q}{\Omega_m}\cos(t\Omega_m) - \Delta t\right) - \frac{\kappa t}{2}\right) \times \left(\int_0^1 \exp\left(-\imath\left(\frac{\sqrt{2}g_0 Q}{\Omega_m}\cos(\tau\Omega_m) + \Delta\tau\right) + \frac{\kappa\tau}{2}\right)\mathrm{d}\tau + \int_1^t \exp\left(-\imath\left(\frac{\sqrt{2}g_0 Q}{\Omega_m}\cos(\tau\Omega_m) + \Delta\tau\right) + \frac{\kappa\tau}{2}\right)\mathrm{d}\tau\right) \tag{4.19}$$

The first integral yields a constant factor. That the second integral converges, in case all parameters are real, can be seen by factoring-in the term $\exp\left(-\frac{\kappa t}{2}\right)$ of the prefactor. What is important to notice is the modulation $\imath\cos(t\Omega_m)$, driven with a strength of $d = \sqrt{2}g_0 Q/\Omega_m$. This is a characteristic of phase modulation which is often studied in the context of devices like electro-optical modulators [31]. In case of small $d \ll 1$ and $t \gg 1/\kappa$, such that a steady state regime has been reached, a Taylor expansion yields (cf. H. Kerdoncuff's thesis [163, p. 62])

$$\alpha(t) \approx |\alpha|^2\,\mathrm{e}^{-\imath\Delta t}\left(1 + \frac{\Omega_m}{\kappa - 2\imath(\Delta+\Omega_m)}d\,\mathrm{e}^{-\imath\Omega_m t} + \frac{\Omega_m}{\kappa - 2\imath(\Delta-\Omega_m)}d\,\mathrm{e}^{\imath\Omega_m t}\right). \tag{4.20}$$

The terms oscillating at $-\Omega_m$ and $+\Omega_m$ represent the anti-Stokes and Stokes sidebands, respectively [255]. Figure 4.3 illustrates the behaviour of the exact solution (4.19) to justify the validity of the approximation.

In conclusion, equation (4.20) tells quantitatively how a mechanical oscillation modulates the intracavity field. By virtue of equation (4.12) it is readily connected to the output field. To measure the transduced mechanical motion, a standard homodyne detection, introduced in section 1.2.3, can be employed to meter the phase fluctuation. Based on these finding, it will be outlined how the knowledge about the oscillator's motion can be employed to control its state.

4.2.2 Controlling and feedback cooling the mechanical oscillator

For cooling the mechanical oscillator, two main approaches can be taken: Feedback cooling, also termed as cold damping, or sideband cooling, sometimes referred to as cavity-assisted cooling [14,

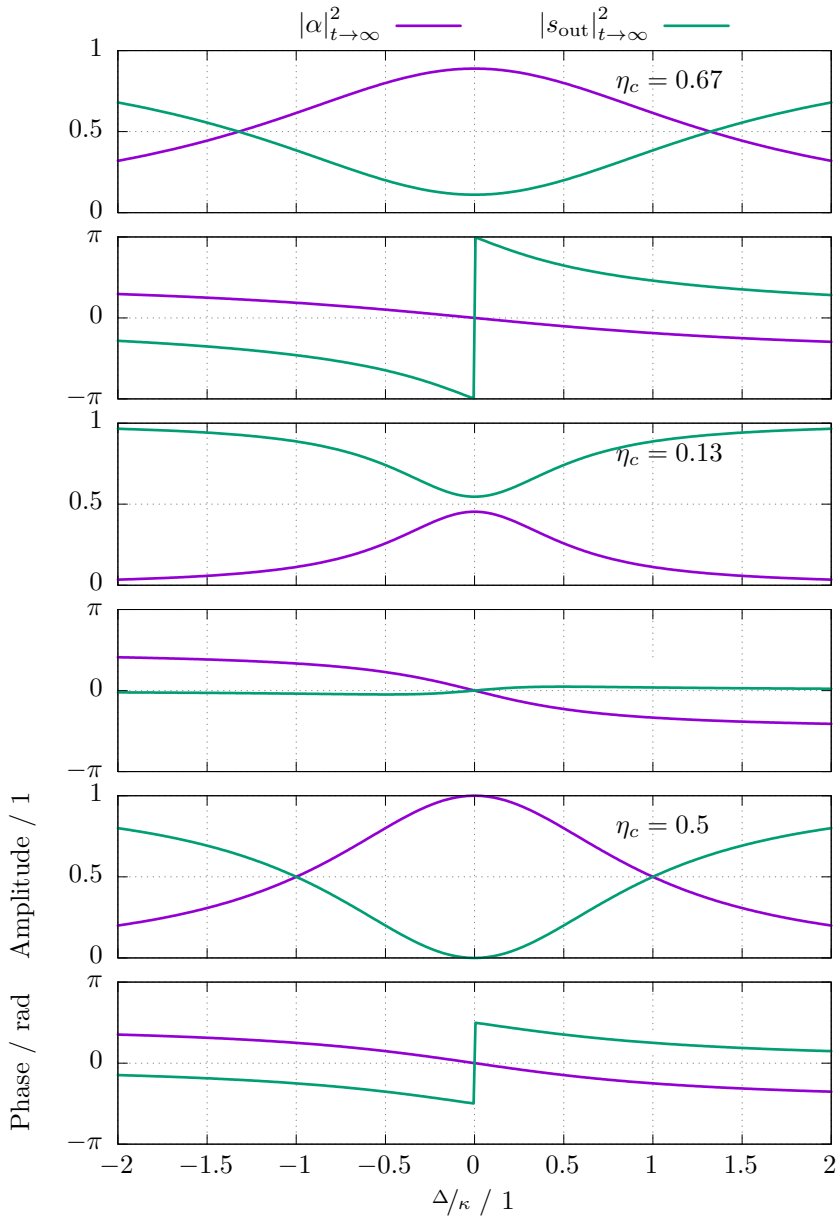

Figure 4.2: Amplitude and phase diagram for three cavity-coupling regimes. From top to bottom: Overcoupled, undercoupled, impedance matched. The horizontal axis represents the detuning $\Delta = \omega_c - \omega_d$ normalised to the cavity decay $\kappa = \kappa_{\mathrm{ex}} + \kappa_l$. This way the loss rate κ_l is set by the choice of η_c. The phase exhibits a discontinuity as the output of the arg function is wrapped in the interval $(-\pi, \pi)$. To compare the steady-state field amplitudes directly, all other parameters were set to unity such that the quantities are effectively normalised.
Considering a Fabry–Pérot cavity instead, the notion of 'out' has to be reversed, as it corresponds to the field reflected from the incoupling mirror [106, 255].

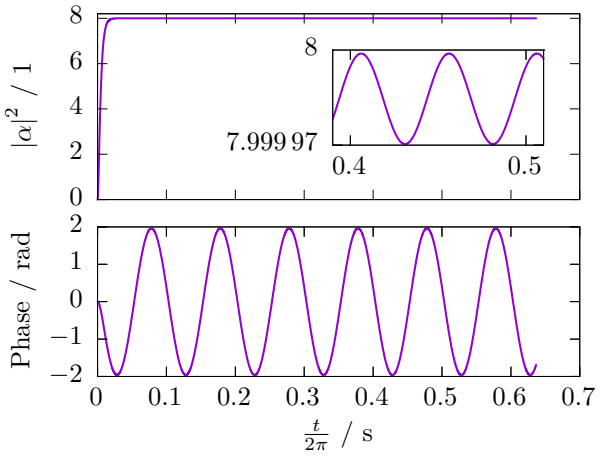

Figure 4.3: Numerical solution of equation (4.19). For the sake of readability, the vertical axes are scaled by a factor of 100. The parameters are $s_{\text{in}} = 1$, $\sqrt{2}g_0Q = 1/10\,\text{Hz}$, $\Omega_m = 10\,\text{Hz}$, $\Delta = 0\,\text{Hz}$, $\kappa = 100\,\text{Hz}$, and $\kappa_{\text{ex}} = 20\,\text{Hz}$. Thus the system is qualified as under-coupled and probed on resonance which resembles our experimental configuration. After a time of about $1/\kappa$, the amplitude reaches almost a steady state behaviour. It is only almost, as a close inspection exhibits an oscillation at a rate of κ_{ex}. This feature is lost in the approximation (4.20). The phase evolution however shows a very pronounced oscillation with a periodicity of $1/\Omega_m$ and justifies the approximation.

295]. Which of these is more suitable depends on whether or not the sidebands at Ω_m transduced onto the optical carrier are larger or smaller than κ. The two regimes this comparison constitutes are called resolved- or unresolved sideband regime for which $\Omega_m \gg \kappa$ and $\Omega_m \ll \kappa$, respectively.

What this intuitively means is that an operation in the resolved sideband regime requires a fast mechanical oscillator or a "good" optical cavity. What an operation in that regime leads to is that the information transduced onto the optical field lessens, the more the sidebands are resolved, i.e. the greater Ω_m compared to κ is. However, probing an optomechanical system in this regime with a red detuned laser has shown to achieve ground state cooling [61].

Feedback cooling, also termed as cold damping, utilises the imprint of information on the optical probe, thus operates in the unresolved sideband regime. As for our system $\Omega_m < \kappa$, we will focus on the feedback cooling approach further on.

A classical analogy By metering the mechanical oscillator's position $\hat{q}$, a negative feedback force $\hat{F}_{\text{Fb}}$ proportional to the velocity $\frac{\mathrm{d}}{\mathrm{d}t}\hat{q}$ can be applied to dampen the motion of the mechanical oscillator [189]. A transfer function model of the interactions can be found in figure 4.4. We sketch the idea by a classical description of the evolution of a mechanical oscillator subject to an external force F:

$$m\frac{\mathrm{d}^2}{\mathrm{d}t^2}q + m\Gamma_m\frac{\mathrm{d}}{\mathrm{d}t}q + m\Omega_m^2 q = F \tag{4.21}$$

The generic mass m was factored out to explicitly show the mechanical frequency and damping rate. When F is periodic, a convenient way to solve the differential equation is via a Fourier transformation. In frequency space,

$$q(\Omega) = \frac{1}{m(\Omega^2 - \Omega_m^2 - \imath\Omega\Gamma_m)}F(\Omega) = \frac{\chi_m(\Omega)}{m}F(\Omega), \tag{4.22}$$

where χ_m denotes the mechanical susceptibility. Exerting a force on resonance, such that $\Omega \approx \Omega_m$, χ_m becomes maximal and $\arg(\chi_m) = \pi/2$. The time-frequency relation $\mathscr{F}(\frac{\mathrm{d}}{\mathrm{d}t}y) = \imath\Omega y(\Omega)$ of the Fourier transformation $\mathscr{F}$ [44] lets us conclude that, as stated above, the feedback force can be set proportional to the velocity of the mechanical oscillator. We also identified the phase delay which is required to impose a viscous damping.

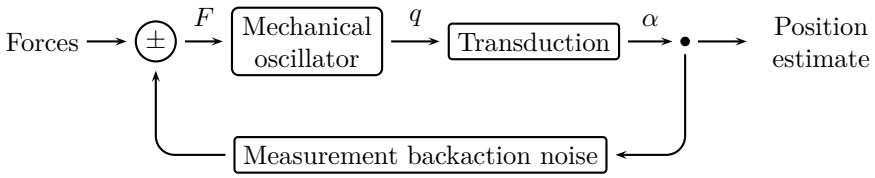

Figure 4.4: Block diagram of an optomechanical feedback control. Physical dimensions are placed above the connecting lines to denote the transformation caused by the individual block. F is a force, q a mechanical displacement (or equally position) and α an optical amplitude. The effects that contribute to the feedback path are the force controlled by, e.g., electromechanical components and quantum noise due to the measurement.

External force terms Next, we consider a mechanical oscillator and the external forces it can be subject to in more detail:

- Thermal Brownian force $\hat{F}_{\mathrm{th}}(\Omega)$ due to the ambient environment,
- a radiation pressure backaction force $\hat{F}_{\mathrm{ba}}(\Omega)$ associated with coupling of the oscillator to an optical probe field,
- and finally the feedback actuation force $\hat{F}_{\mathrm{Fb}}(\Omega)$.

For the microtoroid system we studied, the radiation pressure force is much weaker than the thermal Brownian force and remains hidden below the measurement noise. Thus, this contribution will henceforth be neglected. The effect of backaction force has only recently been observed in state-of-the-art experiments on macroscopic oscillators [221, 226, 238] and is challenging to achieve, as contribution to the mechanic's occupancy from the thermal bath and the radiation pressure shot noise have to be at least on equal footing.

The measurement backaction noise itself is not only given by the measurement outcome; quantum mechanics tells us that the measurement process perturbs the probed system. We account for the disturbance by adding a stochastic noise operator $\hat{q}_N$ as

$$\hat{F}_{\mathrm{Fb}}(\Omega) = m_{\mathrm{eff}} K(\Omega)(\hat{q}(\Omega) + \hat{q}_N(\Omega)). \tag{4.23}$$

The imprecision noise $\hat{q}_N(\Omega)$ of the displacement measurement includes all noise sources in the feedback loop, e.g. optical shot noise, detection- and electronic noise. The prefactor is composed of an effective mass, previously introduced as m_{eff} and to be explained shortly, and a transfer function $K \in \mathbb{C}$, characterising gain and phase lag of the feedback loop. K is, in analogy to χ_m in equation (4.22), the mechanical susceptibility to a feedback force. To achieve the optimal cooling via feedback cooling, the injected measurement noise has to be minimal and the amplification of the feedback signal not constraint by technical saturation effects. As we will see, the larger the signal from the mechanical oscillator, the higher the feedback gain is required to be for reaching the minimal temperature.

Concept of effective mass The concept of an effective mass is of importance in our study; as we will see, it determines the calibration of the mechanical oscillator and finally the inference of the temperature. It is used to distinguish between

- the actual mass of the physical object,

- the displaced mass, which is, for the microtoroid, approximately proportional to the volume of the torus, and
- the effective mass which is moving and guiding the optical mode. It is, so to speak, the mass we can extract information from via the optical probe. As the displaced mass changes for each mechanical mode, and the mechanical mode shape itself might have an impact on the optical mode, m_{eff} is dependent on the mechanical frequency Ω.

A formal way to describe the effective mass is given by Pinard et al. [223]. In a theoretical study they derive the effective mass term and highlight its influence on the optomechanical coupling. To motivate a formal description of m_{eff}, we will outline their study.

First, the time-dependent mechanical displacement of the resonator is expanded as a series of eigenmodes $\boldsymbol{u}_n$ via

$$\boldsymbol{u}(\boldsymbol{x},t) = \sum_n c_n(t)\boldsymbol{u}_n(\boldsymbol{x}), \tag{4.24}$$

where $c_n(t)$ is the time-dependent amplitude of the n-th mode. c_n is formally given by the scalar product $\frac{1}{V}\iiint_V \boldsymbol{u}(\boldsymbol{x},t)\boldsymbol{u}_n(\boldsymbol{x})\ \mathrm{d}^3\boldsymbol{x}$, evaluated over the volume V of the resonator. Regions of the resonator which are not displaced in any of the n eigenmodes do not contribute to c_n, such that V can be seen as the "displaced volume".

Next, the moving mass m_n associated to $\boldsymbol{u}_n$ is introduced by describing the potential energy of the resonator as a series of eigenfrequencies:

$$U(t) = \frac{1}{2}\sum_n m_n\Omega_n^2 c_n(t)^2. \tag{4.25}$$

The frequency of an eigenmode is denoted as Ω_n. Knowing $\boldsymbol{u}_n$ and the resonator material's density ρ, the moving mass can be evaluated via $\rho\iiint_V \|\boldsymbol{u}_n(\boldsymbol{x})\|^2\ \mathrm{d}^3\boldsymbol{x}$.

For an optomechanical quantum system, where the light field plays the split role of a probe and a disturbance, the physical mass of the mechanical oscillator is of minor importance – it is the displaced mass interacting with the optical field which forms the actual system.

To describe the mass which is both displaced and interacting with light one may introduce the spatial overlap

$$s_n = \frac{1}{V}\iiint_V \boldsymbol{v}^2(\boldsymbol{x})\boldsymbol{u}_n(\boldsymbol{x})\ \mathrm{d}^3\boldsymbol{x} \tag{4.26}$$

between $\boldsymbol{u}_n$ and the spatial amplitude distribution $\boldsymbol{v}$ of the electric field[6]. We may then associate an effective mass to each mechanical mode via

$$m_{\text{eff},n} = \frac{m_n}{s_n^2}. \tag{4.27}$$

As pointed out by Pinard et al., the effective mass can take on, depending on s_n, values which are less by more than order of magnitude compared the mechanical oscillator's physical mass, thereby enhancing the optomechanical coupling and optical noise spectra.

In our experimental study we address only a singly mechanical mode, such that for the following we omit the subscript n for m_{eff}.

[6] To give an example of $\boldsymbol{v}(\boldsymbol{x})$: Pinard et al. study the effective mass of a Fabry–Pérot cavity, whereas one of the two mirrors acts as a spring and its deformation is considered. In this case, both $\boldsymbol{v}$ and $\boldsymbol{u}_n$ are well approximated by scalar functions over cylindrical coordinates. Specifically, $\boldsymbol{v}$ takes a Gaussian- and $\boldsymbol{u}_n$ Laguerre–Gaussian form, such that closed expressions for s_n may be found.

Controlling the mechanical displacement Combining the contributions to the force which determines the mechanical displacement, we arrive at

$$\begin{aligned}\hat{q}(\Omega) &= m_{\text{eff}}^{-1}\chi_m(\Omega)\Big(\hat{F}_{\text{th}}(\Omega) + \hat{F}_{\text{Fb}}(\Omega)\Big) \\ &= m_{\text{eff}}^{-1}\chi_m(\Omega)\Big(\hat{F}_{\text{th}}(\Omega) + m_{\text{eff}}K(\Omega)(\hat{q}(\Omega) + \hat{q}_N(\Omega))\Big) \\ &= m_{\text{eff}}^{-1}\chi_{\text{eff}}(\Omega)\Big(\hat{F}_{\text{th}}(\Omega) + m_{\text{eff}}K(\Omega)\hat{q}_N(\Omega)\Big),\end{aligned} \tag{4.28}$$

where we have introduced an effective susceptibility:

$$\begin{aligned}\chi_{\text{eff}}(\Omega) &= \frac{\chi_m(\Omega)}{1 - K(\Omega)\chi_m(\Omega)} \\ &= \left(\Omega^2 - \Omega_m^2 - \Re(K(\Omega)) - \imath\Omega\Gamma_m\left(1 + \frac{\Im(K(\Omega))}{\Omega\Gamma_m}\right)\right)^{-1}.\end{aligned} \tag{4.29}$$

The real part of K contributes to the spring constant of the mechanical oscillator, resulting in a modified resonance frequency

$$\Omega_{\text{Fb}}^2 = \Omega_m^2 - \Re(K(\Omega)). \tag{4.30}$$

The dissipation of the mechanical oscillator is altered by the imaginary part of K, leading to a feedback induced damping rate

$$\Gamma_{\text{Fb}} = \Gamma_m(1 + G_{\text{Fb}}), \tag{4.31a}$$

with

$$G_{\text{Fb}} = \frac{\Im(K(\Omega))}{\Omega\Gamma_m}. \tag{4.31b}$$

Manipulating K thus allows for stiffening or softening the spring our mechanical oscillator forms. More interesting, it can affect the dissipative coupling to its environment, which is the essence of feedback cooling.

Starting from a representation of the feedback transfer function [184] in Laplace space[7], we can express

$$K = G_{\text{Fb}}(\Omega)\Omega\Gamma_m \exp(-\imath\Omega\tau_{\text{Fb}}) \tag{4.32}$$

where τ_{Fb} is the delay of the feedback loop. The exponential term represents a time shift, while the amplitude expresses the filter characteristics of the transfer function. In a following section, an experimental characterisation of the transfer function will be shown. It justifies that, for a further treatment, we can assume $\Omega\tau_{\text{Fb}} = \pi/2 + n2\pi, n \in \mathbb{N}$, corresponding to an ideal dissipative feedback force.

4.2.3 Displacement spectrum of the feedback actuated resonator

The power spectral density (PSD) for an operator $\hat{O}$ is generally defined as[8] [37]

$$S_{\hat{O}}(\Omega) = \int_{-\infty}^{\infty} \langle\hat{O}(t)\hat{O}(0)\rangle\, \mathrm{e}^{\imath\Omega t}\, \mathrm{d}t. \tag{4.33}$$

[7] Since we assume a linear and constant, i.e. time invariant, behaviour of K, a representation in Laplace space is valid.

[8] To explicitly show that the PSD is an autocorrelation, authors often denote it as $S_{\hat{O}\hat{O}}(\Omega)$. In this treatment, no crosscorrelation spectrum will be used, thus we will omit the second index for convenience.

In Fourier space

$$\hat{O}(\Omega,\tau) = \frac{1}{\sqrt{2\tau}} \int_{-\tau}^{\tau} \hat{O}(t)\, \mathrm{e}^{\imath\Omega t}\ \mathrm{d}t = \langle |\hat{O}(\Omega,\tau)|^2 \rangle, \tag{4.34a}$$

which relates to the PSD as

$$S_{\hat{O}}(\Omega) = \lim_{\tau\to\infty} \langle |\hat{O}(\Omega,\tau)|^2 \rangle. \tag{4.34b}$$

Under the assumption that the observation time τ is much larger than the relevant time scales of $\hat{O}$, we associate

$$S_{\hat{O}}(\Omega) = \langle |\hat{O}(\Omega)|^2 \rangle. \tag{4.35}$$

Using equation (4.28) and assuming that the noise terms are uncorrelated, the mechanical displacement PSD is given by

$$S_{\hat{q}}(\Omega) = \langle |\hat{q}(\Omega)|^2 \rangle = \frac{|\chi_{\mathrm{eff}}(\Omega)|^2}{m_{\mathrm{eff}}^2} \Big(S_{\hat{F}_{\mathrm{th}}}(\Omega) + m_{\mathrm{eff}}^2 |K|^2 S_{\hat{q}_N}(\Omega) \Big). \tag{4.36}$$

Substitution of equation (4.29) and (4.32) into the latter yields the following PSD for the mechanical displacement subject to feedback (cf. Poggio et al. [224]):

$$\begin{aligned} S_{\hat{q}}(\Omega) = {} & \frac{1/m_{\mathrm{eff}}^2}{\left(\Omega^2 - \Omega_m^2\right)^2 + \left(1 + G_{\mathrm{Fb}}\right)^2 \left(\Omega_m \Omega / \mathcal{Q}_m\right)^2} S_{\hat{F}_{\mathrm{th}}}(\Omega) \\ & + \frac{\left(\Omega G_{\mathrm{Fb}} \Omega_m / \mathcal{Q}_m\right)^2}{\left(\Omega^2 - \Omega_m^2\right)^2 + \left(1 + G_{\mathrm{Fb}}\right)^2 \left(\Omega_m \Omega / \mathcal{Q}_m\right)^2} S_{\hat{q}_N}(\Omega). \end{aligned} \tag{4.37}$$

Here, the first term represents driving of the mechanical oscillator by thermal Brownian noise, while the second term accounts for the mechanical position uncertainty introduced by imprecision noise in the feedback loop being fed back onto the oscillator. The mechanical quality factor is denoted as

$$\mathcal{Q}_m = \frac{\Omega_m}{\Gamma_m}. \tag{4.38}$$

Equation (4.37) evaluates the actual displacement of the feedback actuated oscillator, that is the displacement as it would be revealed by an ideal out-of-loop measurement.

An in-loop measurement, on the other hand, includes additional measurement imprecision noise. It is thus given by $\hat{q}(\Omega) + \hat{q}_N(\Omega)$. Gathering the terms from (4.28) and (4.37), the PSD reads

$$\begin{aligned} S_{\hat{q}}^{\mathrm{meas}}(\Omega) = {} & \frac{1/m_{\mathrm{eff}}^2}{\left(\Omega^2 - \Omega_m^2\right)^2 + \left(1 + G_{\mathrm{Fb}}\right)^2 \left(\Omega_m \Omega / \mathcal{Q}_m\right)^2} S_{\hat{F}_{\mathrm{th}}}(\Omega) \\ & + \frac{\left(\Omega^2 - \Omega_m^2\right)^2 + \left(\Omega \Omega_m / \mathcal{Q}_m\right)^2}{\left(\Omega^2 - \Omega_m^2\right)^2 + \left(1 + G_{\mathrm{Fb}}\right)^2 \left(\Omega_m \Omega / \mathcal{Q}_m\right)^2} S_{\hat{q}_N}(\Omega). \end{aligned} \tag{4.39}$$

It is important to distinguish the out-of-loop and in-loop measurement spectra as they suggest vastly different behaviour of the mechanical oscillator as function of G_{Fb}. To realise an out-of-loop measurement, two independent transduction measurements, e.g. detuned laser sources, can be used for feedback actuation and displacement spectrum characterisation [169]. Thereby the

actual displacement of the cooled oscillator and hence its temperature can be inferred. For the in-loop measurement, however, only one transduction measurement is used both for characterisation and generation of the feedback force. As the feedback gain is increased, the oscillator motion is progressively correlated with the inevitable imprecision noise of the measurement, resulting in an artificial noise suppression – called 'squashing' – in the measured displacement spectrum. For sufficiently large gain values the measured in-loop spectrum even suggests a mechanical noise below the measurement noise level. This effect will be shown and briefly discussed in the following experimental section.

Next, we will outline that the temperature of the mechanical mode is related to the integral of the displacement spectrum. In the presence of noise squashing this leads to inference of negative temperatures, which is obviously unphysical. Care should thus be taken when inferring the feedback cooled oscillator temperature from in-loop measurements. With the knowledge of equation (4.39), one can account for the noise contribution from the measurement and thereby infer the temperature even under the presence of squashing correctly.

4.2.4 Effective temperature of the feedback actuated resonator

According to the fluctuation-dissipation theorem [174] we can define an effective temperature from the PSD of the mechanical position fluctuations. The effective temperature T_{Fb} of a mechanical oscillator subject to a feedback actuation force can be calibrated relative to the effective temperature T_0 of the same oscillator in thermal equilibrium with its environment [37].

Assuming that the PSD of the position fluctuations under feedback actuation retains a Lorentzian profile with effective resonance frequency Ω_{Fb} and damping rate Γ_{Fb}, the effective temperature of the oscillator is given by

$$\frac{T_{\mathrm{Fb}}}{T_0} = \frac{\int_{-\infty}^{\infty} \left\langle |\hat{q}(\Omega)|^2 \right\rangle \mathrm{d}\Omega}{\int_{-\infty}^{\infty} \left\langle |\hat{q}(\Omega)|^2 \right\rangle_{G_{\mathrm{Fb}}=0} \mathrm{d}\Omega} = \frac{\Gamma_{\mathrm{Fb}} \left\langle |\hat{q}(\Omega_{\mathrm{Fb}})|^2 \right\rangle}{\Gamma_m \left\langle |\hat{q}(\Omega_m)|^2 \right\rangle_{G_{\mathrm{Fb}}=0}}. \tag{4.40}$$

Substituting equation (4.28) into equation (4.40), the effective temperature can be expressed in terms of experimentally accessible quantities as

$$\frac{T_{\mathrm{Fb}}}{T_0} = \left(1 + \frac{G_{\mathrm{Fb}}^2}{\mathrm{SNR}}\right) \frac{1}{1 + G_{\mathrm{Fb}}}, \tag{4.41}$$

where we have introduced the signal-to-noise ratio (SNR) as the level of the on-resonance mechanical position noise relative to the off-resonance measurement noise level:

$$\mathrm{SNR} = \frac{\left\langle |\delta\hat{q}(\Omega_m)|^2 \right\rangle_{G_{\mathrm{Fb}}=0}}{\left\langle |\delta\hat{q}_N(\Omega_m)|^2 \right\rangle_{G_{\mathrm{Fb}}=0}}, \tag{4.42}$$

The SNR can be determined directly from the PSD of the measured cavity output field fluctuations.

If the mechanical setup and the optical detection is unchanged such that the SNR is stable over the measurement, the lowest achievable temperature by cold damping is limited to

$$T_{\mathrm{min}} = 2T_0 \frac{\sqrt{1 + \mathrm{SNR}} - 1}{\mathrm{SNR}}, \tag{4.43}$$

for an optimised feedback gain of $G_{\mathrm{Fb}} = \sqrt{1 + \mathrm{SNR}} - 1$. When $G_{\mathrm{Fb}} > \sqrt{1 + \mathrm{SNR}} - 1$, the influence of the measurement noise overwhelms the position noise signal, which eventually leads to an increased effective temperature of the mechanical oscillator. Finally we note that to maximise the cooling efficiency, the SNR has to be increased.

Improving the detection efficiency by amplitude squeezing

In the backaction dominated regime ($C \gg n_{\mathrm{th}}$), the minimum achievable mechanical quadrature variances $\mathrm{Var}_{\hat{Q}}, \mathrm{Var}_{\hat{P}}$ is directly given by the transduction signal detection efficiency η, as [37]

$$\mathrm{Var}_{\hat{Q}} = \mathrm{Var}_{\hat{P}} = \frac{1}{2\sqrt{\eta}}. \tag{4.44a}$$

This condition also implies a minimum thermal state occupancy of

$$n_{\mathrm{min}} + 1/2 = \frac{1}{2\sqrt{\eta}}, \tag{4.44b}$$

which highlights the importance of achieving close to unity detection efficiency. Achieving high detection efficiencies has shown to be a major challenge in recent optomechanics experiments [287]. However, through a slightly unconventional use of squeezing, the effect of losses can be mitigated and high effective detection efficiencies reached. We start by considering the transduction of a mechanical oscillation mode with measurement noise variance Var_N and signal variance Var_S, both determined in the absence of losses, resulting in a total variance of $\mathrm{Var} = \mathrm{Var}_S + \mathrm{Var}_N$. For unity detection efficiency the corresponding SNR is given by

$$\mathrm{SNR}_0 = \frac{\mathrm{Var}_S}{\mathrm{Var}_N}. \tag{4.45}$$

The effect of signal loss can be modelled as an effective beam splitter with transmission efficiency η (introduced on page 12 and equation (1.40)), leading to

$$\mathrm{Var} \to \eta(\mathrm{Var}_S + \mathrm{Var}_N) + \frac{1-\eta}{2} = \eta\,\mathrm{Var}_S + \eta\,\mathrm{Var}_N + \frac{1-\eta}{2}, \tag{4.46}$$

and correspondingly, the finite efficiency SNR is given by:

$$\mathrm{SNR}_\eta = \frac{\eta\,\mathrm{Var}_S}{\eta\,\mathrm{Var}_N + (1-\eta)/2}. \tag{4.47}$$

Defining an effective detection efficiency as the ratio of the finite and unity efficiency SNR, we find

$$\eta_{\mathrm{eff}} = \frac{\mathrm{SNR}_\eta}{\mathrm{SNR}_0} = \frac{\eta\,\mathrm{Var}_N}{\eta\,\mathrm{Var}_N + (1-\eta)/2} = \frac{1}{1 + \frac{1-\eta}{2\eta\,\mathrm{Var}_N}}, \tag{4.48}$$

which approaches unity for $\mathrm{Var}_N \gg \frac{1-\eta}{2\eta}$. Using an amplitude-, rather than a phase-, squeezed probe beam this condition can be approximately fulfilled resulting in an effective enhancement of the detection efficiency. At the same time, the squeezed amplitude fluctuations lead to reduced heating of the oscillator due to less quantum backaction.

A rather figurative explanation for this effect is that the additional noise in the phase quadrature acts as a "buffer layer" and thereby protects the information from losses. Figure 4.5 presents the variation of η_{eff} for different degrees of squeezing.

4.3 Experiment

The experimental demonstration of quantum enhanced cooling outlined in the introduction was performed with the squeezed-light source described on page 56. In this section we will describe further parts and techniques applied in the experiment. We conclude by presenting the achieved cooling before summarising the project outcomes in the final section.

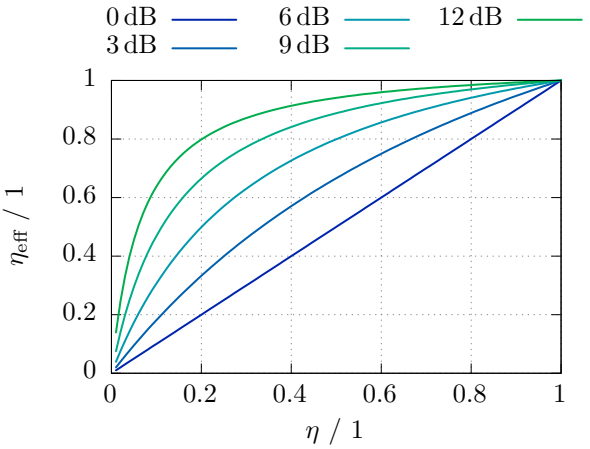

Figure 4.5: The effective detection efficiency in dependence of the efficiency set by a coherent-state scenario. Six lines represent different degrees of anti-squeezing given by $10\log_{10}(\mathrm{Var}_N/(1/2))$.

4.3.1 Experimental setup

A scaled schematic of the experimental setup is shown in figure 4.6 containing all optical and optoelectronic parts.

The optical source was a continuous-wave Nd:YAG laser (*Innolight GmbH* Diabolo) delivering an output beam at 1064 nm and a secondary beam at 532 nm produced by second harmonic generation from the fundamental wavelength. The fundamental beam was split into two, one serving as a seed for generation of bright squeezed probe states, the other, most intense part, was used as local oscillator for homodyne detection. Figure 3.9 on page 56 indicates where the local oscillator was split up from the laser.

Next to providing the local oscillator, the beam sent into the 'LO' port served two other purposes: First, to have a non-squeezed probe available. The power of the probe was conveniently adjusted via a combination of a half wave plate and a polarising beam splitter. Second, to match the spatial mode leaving the squeezer cavity to the spatial mode of the fibre coupler of the tapered fibre. This path is depicted by the dashed beam that is transmitted through the polarising beams splitter combining the signal and local oscillator beam before the detection stage.

For improved homodyne visibility the local oscillator was coupled into a polarisation maintaining single-mode fibre (PM-SMF) and recoupled into free space before being interfered with the probe field. Using equal lenses (*Thorlabs* C240TME-1064) for the outcoupling stages, a visibility of 99 % was achieved without additional telescopes in the signal and local oscillator path after outcoupling.

To allow for evanescent optical coupling to the microtoroidal resonator, the bright squeezed state was coupled into an adiabatically tapered single-mode fibre with a diameter at the taper waist of $< 1\,\mu\mathrm{m}$. For better mechanical stability and high coupling efficiency, the fibre was manually terminated with a FC/APC[9] connector on each side. The angled cut of the connector further prevents from standing waves, i.e. parasitic cavity effects. It was thereby easily feasible to determine the transmission through the tapered fibre without measuring the coupling efficiency by mating the tapered fibre with another patch cable. As mentioned above, the mode matching from free space to fibre was measured by back-seeding the tapered fibre and matching the output to the squeezing cavity. This yielded a mode matching efficiency of $\eta_{\mathrm{mm}} = 98.5\,\%$.

[9] The name FC/APC is an acronym for "Ferrule Connector / Angled Physical Contact". The improved coupling efficiency stems not only from the mentioned mechanical stability, but also from the polishing of the connector's tip which is involved in the manual termination.

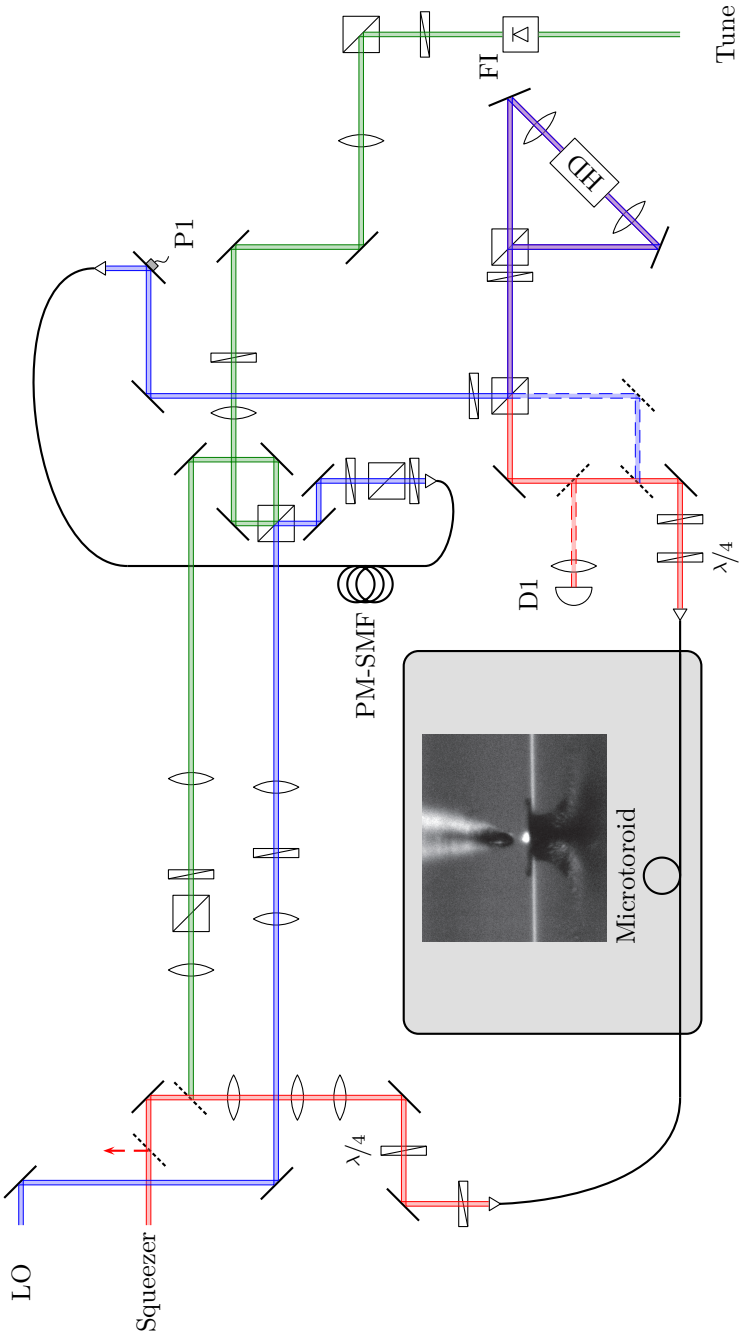

Figure 4.6: A schematic of the actual experimental setup. The schematic corresponds to the real placement; the short side of the setup measures 1.5 m, the long side 3 m. Dashed mirror symbols depict removable mirrors. Wave plates which are not labelled represent half wave plates. Dashed beams are paths that were used for alignment or calibration purposes. All beam splitters are polarising. The photo was taken by one of two microscope assemblies inside a clean enclosure containing the microtoroid.

Table 4.1: Overview of measured efficiencies and their notation.
[a]For cooling experiment only. Stronger coupling has been used for measurements as shown in figure 4.13.

Notation	Meaning	Value
η_c	Optomechanical coupling	2.8(1) %[a]
η_{taper}	Transmission through the tapered fibre	54.0(5) %
η_{trans}	Power transmission between squeezer output and detection stage input without optomechanical coupling	48.0(5) %
η_{mm}	Mode matching to the fibre coupler	98.5(2) %
η_{qe}	Quantum efficiency of photodiodes	> 99 %
η_{vis}	Mode matching between probe- and local oscillator beam at the homodyne detector	98.8(1) %

The transmittance through the fibre was measured to be 64 %. Contaminations of the tapered region were visible in the form of scattering effects and were deemed to be the cause of the losses. An overview of all measured efficiencies can be found in table 4.1.

The tapered fibre was kept at a fixed position while the microtoroid was held on a three-axes piezo stage (*Thorlabs* NanoMax MAX311D/M) providing control of the relative taper-to-toroid separation with nanometre resolution. The coupling efficiency to the microtoroid was controlled by changing

- the relative position between the tapered fibre and the micro-toroid,
- the polarisation of the incoupled beam, and
- the temperature of the toroid.

The toroid's temperature was actuated by means of a Peltier element underneath the chip, and stabilised using a controller (*Wavelength Electronics* LFI3751). For coarse and fast temperature tuning, the intensity of an incandescent lamp built into the microscope assembly was changed.

To detect the signal, the probe field was superimposed with the local oscillator beam on a half wave plate and polarising beam splitter. This combination was used to mimic a beam splitter with an accurately variable splitting ratio. The interference visibility $\mathcal{V}$ was measured to be 99.4 %, corresponding to a mode matching efficiency introduced in section 1.2.3 of $\eta_{\mathrm{vis}} = \mathcal{V}^2 = 98.8\,\%$. Two indium-gallium-arsenide photodiodes with $\eta_{\mathrm{qe}} > 99\,\%$ quantum efficiency (specified on page 63, footnote 12) were built into the homodyne detector, such that the overall losses were given by the transmission through the tapered fibre.

As the measurement required a stable phase quadrature measurement, the DC part of the homodyne detector (HD) photocurrent was used as error signal. The signal provided the input for a feedback loop controlling the phase of the local oscillator by means of piezo actuated mirror (P1). Details about the controller can be found in appendix on page 144.

For calibration purposes, a tunable diode laser was also launched into the setup. To prevent from back reflection into the laser cavity, a Faraday isolator (FI) was placed right after the laser module which is marked by 'Tune' in figure 4.6.

Electronic feedback circuit

Figure 4.7 illustrates the electronic circuit used for feedback actuation of the mechanical resonator. First, the AC component of the homodyne photocurrent was band-pass filtered, before splitting it into feedback and monitor / acquisition signals. The feedback signal was subsequently

amplified in two stages providing 10 and 30 dB gain, respectively. A variable signal delay was used to introduce the crucial 90° delay of the feedback force with respect to the mechanical motion. Two variable 10 dB attenuators set the electrical feedback gain. In principle, the *Femto* amplifier shown in figure 4.7 features a variable gain, however it was found that the phase is also affected by the gain setting. To prevent from varying the phase delay when changing the gain, attenuators were employed and the gain of the *Femto* amplifier set to 30 dB. Finally, a bias tee, modified to accept up to 300 V DC input, was used to add a bias voltage to the feedback electrode. This bias polarised the microtoroid to yield an improved electromechanical susceptibility [163].

Circuit characterisation Ideally, a flat frequency response of the feedback circuit is desired in the frequency band covering the mechanical resonance. To confirm that this was the case the transfer function of the employed combination of filters and amplifiers was measured using an electronic network analyser (*Agilent* E5061B). Figure 4.8 shows the measured S_{21} transfer function of the total feedback circuit.

Data acquisition

The data presented in the figures was recorded by sampling the AC coupled and band-pass filtered homodyne photocurrent using a digital sampling oscilloscope (*LeCroy* HDO6034). The signal was sampled at a rate of 50 MS/s yielding a Nyquist frequency of 25 MHz well above all relevant frequencies. For each measurement run the total sampling time was 100 ms resulting in $5 \cdot 10^6$ points per data set. In a subsequent post-processing step the data was binned and the corresponding power spectra were derived by a digital Fourier transformation.

Squeezing efficiency after fibre transmission

To characterise the efficiency of the squeezed light source, homodyne tomography of the generated state was performed. Without coupling the squeezed state into a fibre, a reduction of the shot noise level by −8 dB was observed. A free space measurement indicating this reduction is shown on page 63. Coupling to the microtoroid via the tapered fibre led to a reduction to −2 dB, as shown in figure 4.9. In the absence of coupling to the microtoroid, the total transmission efficiency through the tapered fibre was measured to be 54 %, including 4 % reflection ('Fresnel') loss from each of the uncoated fibre facets. At the fibre-to-microtoroid coupling strength used for both cooling experiments and the stated squeezing characterisation, the measured total transmission through the various optical elements and the tapered fibre was $\eta_{\mathrm{trans}} = 48\,\%$. By virtue of equation (1.40)[10], the corresponding loss-reduced degree of squeezing is given by

$$\mathrm{Var}_{\mathrm{out}} = \eta_{\mathrm{trans}}\,\mathrm{Var}_{\mathrm{in}} + (1 - \eta_{\mathrm{trans}}), \tag{4.49}$$

resulting in $V_{\mathrm{out}} = -2.25\,\mathrm{dB}$ for $V_{\mathrm{in}} = -8\,\mathrm{dB}$, consistent with the experimentally measured value.

4.3.2 Characterisation of the microtoroidal resonator

To detect mechanical resonances, the optical mode of the microtoroid had to be matched first to the probe laser frequency. When successfully matched, the mechanical spectrum was read out after adjusting for the required optomechanical coupling. All inferred system parameters can be found in table 4.2.

[10] We derived here the influence of losses on homodyne detection from the beam splitter transformation.

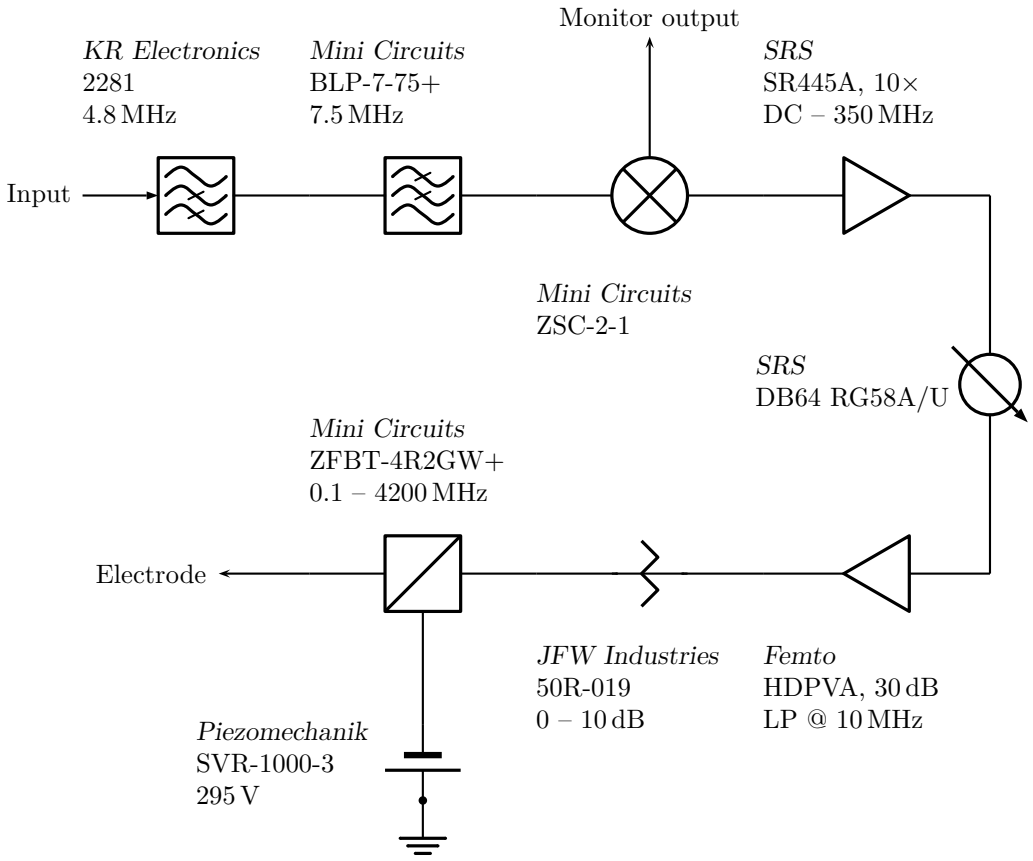

Figure 4.7: The electronic parts constituting the feedback circuit. The signal supplied by the homodyne detector was filtered by a low- and high-pass filter, before sending it to a power splitter. A delay circuit in between two amplifiers was used to accomplish a negative feedback. The amplifiers were set to a constant amplification, as it showed out that the amplification affects also the delay. To control the amplitude of the feedback signal, a set of attenuators was used. A bias tee combined a DC voltage with the actual feedback signal sent to the electrode. An aluminium plate underneath the silicon chip fixing the toroid served as ground. An electronic spectrum analyser (*Agilent* N9000A CXA) or an oscilloscope was connected to the monitor output for measuring the in-loop signal.

Table 4.2: Parameters of the optomechanical system.
[a] This value stems from the increased input power to measure the spectrum shown in figure 4.13(b).

Mechanical		Optical		System	
Symbol	Value	Symbol	Value	Symbol	Value
$\Omega_m/2\pi$	6.132(1) MHz	$\omega_c/2\pi$	281.8317(3) THz	T_0	295.0(1) K
$\Gamma_m/2\pi$	14.625(5) kHz	$\kappa^{\mathrm{uc}}/2\pi$	94.4(2) MHz	C	$2.50(5)\cdot10^{-5}$
m_{eff}	10(1) µg	$\kappa^{\mathrm{cc}}/2\pi$	203.6(2) MHz	C^a	$5.20(5)\cdot10^{-4}$
$n_{\mathrm{th}}(T_0)$	$1.0028(4)\cdot10^6$	$\mathcal{Q}_c^{\mathrm{uc}}$	$1.38(5)\cdot10^6$		
$\mathcal{Q}_m$	419.0(4)	$\mathcal{Q}_c^{\mathrm{cc}}$	$2.99(5)\cdot10^6$		

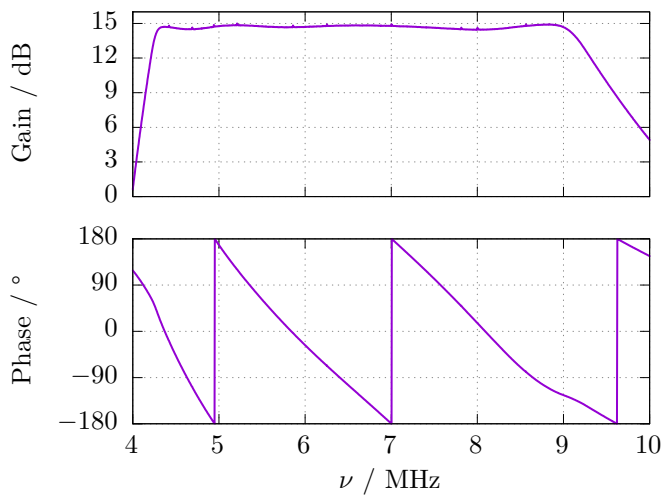

Figure 4.8: Measurement of the S_{21} transfer function of the total feedback circuit. In the region around the mechanical resonance, the gain was reasonably flat, the structure on top was found to be caused by reflections between the filter and the first amplifier. Due to the use of various filters a phase shift was however present. For very high cooling efficiencies, this shift has to be compensated, as with higher cooling the detected resonance broadens. Without a compensation, the tails of the resonance will experience a phase shift that leads to heating. The phase is referenced to an arbitrary offset and is shown in a wrapped format to facilitate the reading.

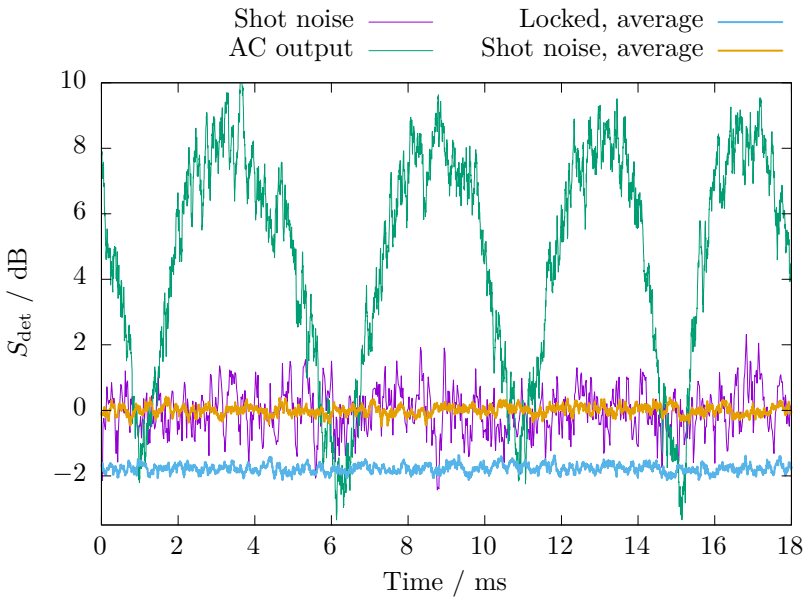

Figure 4.9: Homodyne tomography of the squeezed state after transmission through the tapered fibre and coupling to the microtoroid. For the measurement, the power of the local oscillator beam was set to 4.25 mW. The electronic noise, more than 13 dB below the shot noise level, had been subtracted. Data acquisition was done with a RBW of 300 kHz and a VBW of 3 kHz. Traces were recorded five times when averaging was applied. The 'Locked' trace was recorded by stabilising the local oscillator's phase with respect to the phase of the probe beam.

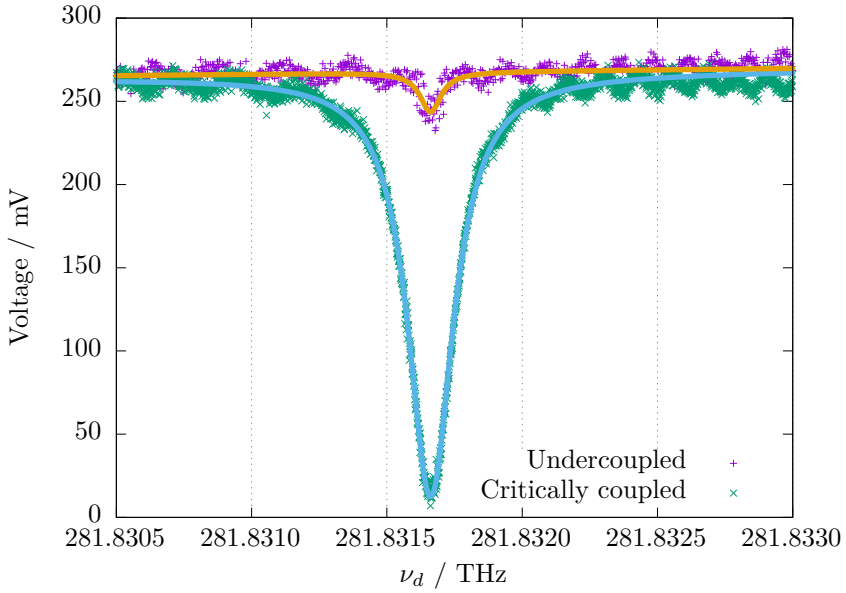

Figure 4.10: Transmission spectra of the optical resonance of the microtoroidal resonator in the case of critical- and under-coupling. The laser-frequency (ν_d) dependent modulation observed in the off-resonant parts of the spectra were attributed to parasitic cavity effects in the setup, most likely the tunable laser [297]. Contribution to this effect from the tapered fibre was mitigated by using FC/APC connectors. The optical signal was picked up by a photodetector. Inferring the resonance frequency ω_c from the measurement is straight forward; due to temperature changes affecting the microtoroid a calibration was repeated for every measurement run.

Optical mode

To characterise the optical mode of the microtoroid, we employed an external-cavity diode laser (*Newport* Velocity TLB-6721), tunable from 1050 nm to 1067 nm. Based on a Littman–Metcalf configuration [255] the laser frequency was controlled by means of piezo-electric tuning of the external cavity feedback mirror. Using the laser module's control-voltage input, the laser frequency was tuned by $10\,\mathrm{GHz\,V^{-1}}$. The frequency-swept laser was coupled to the microtoroid optical resonance by means of the tapered fibre. A direct detection using a photodiode (D1 in figure 4.6) recorded the transmission spectrum. Examples of transmission spectra for two different couplings to the optical resonance at $\omega_c/2\pi = 281.8317\,\mathrm{THz}$ are shown in figure 4.10. At near-critical coupling a Lorentzian fit to the transmission spectrum resulted in a FWHM resonance linewidth of $\kappa^{\mathrm{cc}}/2\pi = 204\,\mathrm{MHz}$. In the strongly undercoupled case, relevant to the cooling experiments, the resulting linewidth is $\kappa^{\mathrm{uc}}/2\pi = 94.4\,\mathrm{MHz}$. For the undercoupled regime, $\kappa^{\mathrm{uc}} \approx \kappa_l$ as the contribution of the coupling rate κ_{ex} becomes negligible. The corresponding optical quality factors are $\mathcal{Q}_c^{\mathrm{cc}} = 1.38 \cdot 10^6$ and $\mathcal{Q}_c^{\mathrm{uc}} = 2.99 \cdot 10^6$, respectively.

For the actual feedback cooling experiments the quoted Nd:YAG laser with noise characteristics superior to the tunable diode laser was used. However, the Nd:YAG laser had a limited frequency tuning range of $\pm 200\,\mathrm{MHz}$, insufficient to cover the $> 1\,\mathrm{THz}$ free spectral range of the microtoroid's optical mode spectrum. To compensate for this, the microtoroid was mounted on a Peltier element to enable thermal tuning of its optical resonance frequency into the range of the Nd:YAG laser. The mentioned controllable incandescent light source in the microscope assembly enabled further temperature tuning, thereby a fast means of localising the optical resonance.

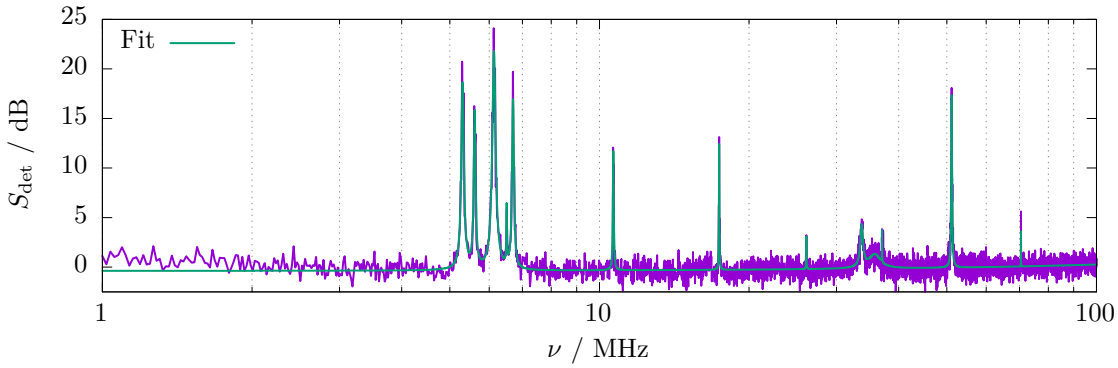

Figure 4.11: Spectrum of the transduced mechanical modes with resonance frequencies below 100 MHz. The fundamental flexural mode used for cooling appears at a frequency of 6.13 MHz. Dark noise was subtracted from the recording. The shot noise power spectral density was taken as the reference level.

Mechanical mode spectrum

The transduced mechanical motion, imprinted on the optical probe field as a phase modulation in the case of resonant probing, was recorded by homodyne detection of the probe field. A typical spectrum of the transduced mechanical motion for the particular micro-toroidal resonator is plotted in figure 4.11, showing a number of resonances in the frequency range from 1 MHz to 100 MHz. The strongest resonance, which, from mechanical finite element method (FEM) simulations of the microtoroid, can be identified as the fundamental flexural mode (FFM), was chosen for the feedback cooling experiments.

In order to calibrate the measured spectrum in terms of absolute mechanical displacement, we utilised that – in the unresolved sideband regime[11] and in the limit of negligible radiation pressure backaction heating[12] – the absolute position-measurement noise level $S_{\hat{q}_{\mathrm{det}}}$ is related to the optomechanical cooperativity C as [37, p. 76]:

$$S_{\hat{q}_{\mathrm{det}}} = 2q_{\mathrm{zpf}}^2 S_{\mathrm{det}} = 2q_{\mathrm{zpf}}^2\left(\frac{1}{8\eta\Gamma_m|C_{\mathrm{eff}}|} + 2\Gamma_m|\chi_m|^2|C_{\mathrm{eff}}|\right) \approx \frac{q_{\mathrm{zpf}}^2}{4\eta\Gamma_m C}, \tag{4.50}$$

where

$$\eta = \eta_{\mathrm{trans}} \cdot \eta_c \cdot \eta_{\mathrm{qe}} \cdot \eta_{\mathrm{vis}} \tag{4.51}$$

is the total optical detection efficiency and q_{zpf} the mechanical zero-point fluctuation amplitude from equation (4.5a). S_{det} introduces the normalised[13] detection noise PSD due to measurement and backaction effects. The last missing parameter is the effective cooperativity; it reads [37]

$$C_{\mathrm{eff}} = \frac{C}{(1 - 2i\Omega/\kappa)^2} \tag{4.52}$$

[11] As a reminder, this regime is characterised by $\kappa \gg \Omega_m$ and $\kappa \gg g_0$, that is the cavity field decays much faster than a mechanics oscillates and a single photon couples to the mechanics, respectively. What this leads to is an adiabatic elimination of optical cavity modes, that is the optical quadrature operators can be treated as stationary [37].

[12] This assumption is valid as the contribution of radiation pressure shot noise to the mechanical oscillator's mean occupancy was more than six orders of magnitude below the contribution from the thermal bath.

[13] It is normalised such that the dimension of S_{det} is Hz^{-1}

and can be approximately, as $\kappa \ll \Omega$ on resonance, set equal to C. Another useful equation which yields the (effective) cooperative can be found in the limit of negligible radiation pressure heating and with an on-resonance optical probe field, which applies for our measurement. According to Bowen and Milburn [37, eq. (A.17)]

$$C_{\mathrm{eff}} = \frac{1}{8\eta} \frac{S_i^{\mathrm{homo}} - 1/2}{n_{\mathrm{th}} + 1/2}. \tag{4.53}$$

S_i^{homo} denotes the normalised power spectral density of the homodyne photocurrent i measured at Ω_m. The PSD comprises all noise sources and is normalised to the detection bandwidth and shot noise level, i.e. it is dimensionless. n_{th} is the thermal occupancy of the mechanical mode which, in the high temperature limit, is given by [37, 174]

$$n_{\mathrm{th}} = \frac{1}{2} \coth\left(\frac{\hbar\Omega}{2k_B T}\right) \approx \frac{k_B T}{\hbar\Omega_m}, \tag{4.54}$$

The latter equation can be reformulated into

$$C_{\mathrm{eff}} = \frac{\mathrm{SNR}\,\mathrm{Var}_{\mathrm{det}}}{8\eta n_{\mathrm{th}}} = C, \tag{4.55}$$

whereas $\mathrm{Var}_{\mathrm{det}}$ denotes the variance of the detected degree squeezing[14]. Thus a relation between the SNR and the cooperativity is established which allows a straight forward experimental determination. Furthermore, substitution of the latter formula into equation (4.41) yields

$$T_{\mathrm{Fb}} = \left(1 + \frac{\mathrm{Var}_{\mathrm{det}}}{8\eta n_{\mathrm{th}} C} G_{\mathrm{Fb}}^2\right) \frac{1}{1 + G_{\mathrm{Fb}}} T_0, \tag{4.56}$$

to relate the effective temperature with actual system parameters.

Estimation of the effective mass The value of the effective mass m_{eff} in equation (4.5a) was determined via FEM simulations and a validation via equation (4.39):

First, the geometry of the microtoroid was estimated by previous microscopic studies [163] to compile a virtual model for the simulation. Assigning the material properties to model, the modes shown in figure 4.12 were found. Iterating the simulation for different geometries led to a matching between the simulated and measured mechanical spectrum. The frequency of the degenerate modes was assumed to be in between the modes shown depicted in figure 4.12. From the simulation, the moving mass was calculated. Then, via previously done optical simulations [163], the effective mass was inferred.

Second, the equations (4.39) and (4.50) were used as a validation. At the resonance peak, $S_{\hat{q}_{\mathrm{det}}}\,\mathrm{SNR} = S_{\hat{q}}^{\mathrm{meas}}$. By manipulating the formula, one may find that m_{eff} and $S_{\hat{q}_N}$ from equation (4.39) are free parameters. The isoline where the solution $S_{\hat{q}_{\mathrm{det}}}\,\mathrm{SNR} = S_{\hat{q}}^{\mathrm{meas}}$ can be found is hyperbolic, such that the set of solutions is open. However, as $S_{\hat{q}_N}$ changes rapidly over m_{eff} (e.g. for $m_{\mathrm{eff}} = 5\,\mu\mathrm{g}$, $S_{\hat{q}_N} > 2000\,\mathrm{am}^2\,\mathrm{Hz}^{-1}$), we can conclude that the value found via the FEM simulation is reasonable. An alternative of calibrating the effective mass is via a modulation of the optical probe field [120]. The drawback of this approach are the optical losses introduced to the probe beam, in case it is a squeezed state, the degree of squeezing degrades according to equation (4.46).

[14] According to our definition of the shot noise unit, $\mathrm{Var}_{\mathrm{det}} = 1/2$ if no squeezing is present.

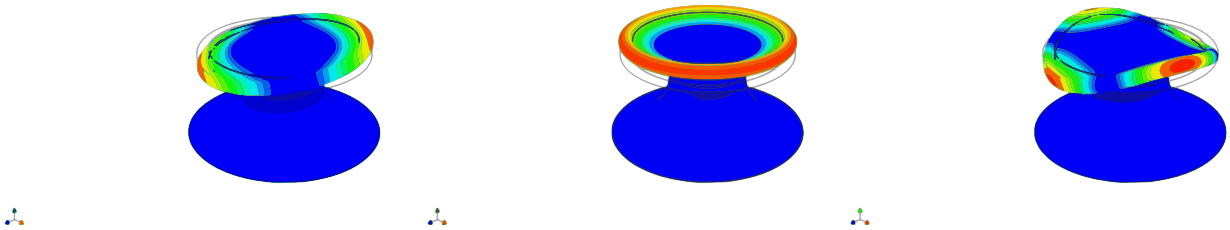

(a) First crown mode (b) Fundamental flexural mode (c) Second crown mode

Figure 4.12: Results of a FEM simulation of the microtoroid's mechanical eigenmodes. The first three modes are shown, with an increased eigenfrequency from (a) to (c). Mode (b) is the fundamental flexural mode we selected for cooling. The modes (a) and (c) are, due to their rotational symmetry, degenerate. Irregularities in the geometry cause a splitting of those modes. As asymmetries were optically visible on all tested microtoroids, we concluded that the transduced spectrum in figure 4.13(a) corresponds to the eigenmodes shown here. A detailed study of the mechanical modes was carried out by, amongst others, Schliesser et al. [248].

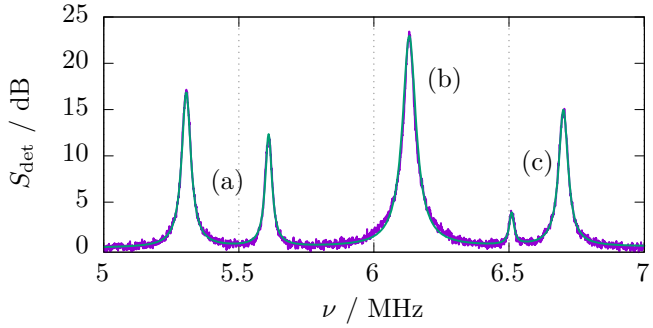

(a) Power spectral density

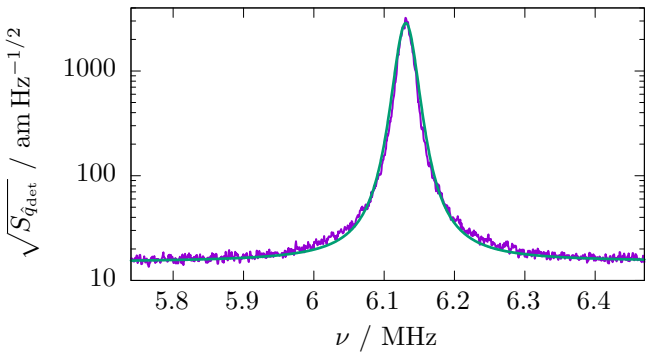

(b) Calibrated linear spectral density

Figure 4.13: (a) Uncalibrated, transduced spectrum of the mechanical modes within the filter window (cf. figure 4.8). The probe power and coupling efficiency do not correspond to the settings used for feedback cooling: For the latter, less power and a lower coupling was set to circumvent an immediate overlap between the modes when cooling. The letters correspond to the labels in figure 4.12. (b) Calibrated linear spectral density $\sqrt{S_{\dot{q}_{\mathrm{det}}}}$ of the mechanical fundamental flexural mode used for feedback cooling calibrated to the actual mechanical displacement amplitude.

Calibration summary Using the numerical values stated above, the SNR from figure 4.11 of 22.4 dB, and an effective mass for the FFM of $m_{\mathrm{eff}} = 10\,\mu\mathrm{g}$, we find: $q_{\mathrm{zpf}} = 11.6\,\mathrm{am}$, $n_{\mathrm{th}} = 10^6$, $C = 2.5 \cdot 10^{-5}$, and $\eta = 0.019$. Then, we arrive at a mechanical displacement sensitivity of

$$\sqrt{S_{\hat{q}_{\mathrm{det}}}} = \sqrt{2 q_{\mathrm{zpf}}^2 S_{\mathrm{det}}} = 14.6\,\mathrm{am}/\sqrt{\mathrm{Hz}}. \tag{4.57}$$

For an overview of the quoted values including uncertainty estimates, we refer to table 4.2 The correspondingly calibrated transduction spectrum for the FFM is plotted in figure 4.13.

Feedback gain calibration and effective temperature inference

Theoretically, the effect of the implemented feedback cooling technique is varied by the feedback gain G_{Fb}, cf. equation (4.43). However, experimentally, the controlled quantity is the electric gain given by the implementation of the feedback circuit. When the delay of the feedback signal is appropriately set for generating a dissipative cooling force, the feedback gain is related to the cooled mechanical resonator linewidth Γ_{Fb} by (cf. equation (4.31a))

$$G_{\mathrm{Fb}} = \frac{\Gamma_{\mathrm{Fb}}}{\Gamma_m} - 1, \tag{4.58}$$

which allows to deduce G_{Fb} from the transduced mechanical spectra as a function of the applied electric gain. The relation between the feedback gain and the electric gain is thus assumed to be linear. However, this approach breaks down for flat spectra, as Γ_{Fb} takes on very large values. Instead, we fit the measured spectra to the model equation (4.39), where the gain G_{Fb}, the resonance frequency Ω_m and the measurement noise $S_{\hat{q}_N}$ are taken as fit parameters. Given these parameters, the integral of the spectrum equation (4.37) can be used to determine the effective temperature. This relation is set by the fluctuation-dissipation theorem [37, 224]:

$$T_{\mathrm{Fb}} = \frac{m_{\mathrm{eff}} \Omega_m^2}{k_B 2\pi} \int S_{\hat{q}}(\Omega)\, \mathrm{d}\Omega. \tag{4.59}$$

As a complementary information, figure 4.14 shows the inferred feedback gain as a function of the applied electric gain. The conversion was not used as a calibration, but it stresses the behaviour of the electronic circuit under increasing gain.

Uncertainty propagation on the temperature estimate

To infer the out-of-loop temperature T_{Fb} shown in figure 4.18 on page 104, we evaluated equation (4.59) as explained above. The SNR was determined from the linear spectral density $\sqrt{S_{\hat{q}_{\mathrm{det}}}}$ when no feedback was applied. More precise, the SNR was derived by a fit to the data, using

$$f(\nu) = 2\pi a + (2\pi)^2 b\nu + 2\pi c \frac{(\Gamma/(4\pi))^2}{(\nu - \Omega/(2\pi))^2 + (\Gamma/(4\pi))^2}, \tag{4.60}$$

i.e. the Cauchy ("Lorentzian") probability density function with a linear term as an offset. The function is defined such that Γ yields the FWHM.

In total, seven parameters $a, b, c, \Gamma_m, \Omega_m, G_{\mathrm{Fb}}, S_{\hat{q}_N}$, extracted by a nonlinear fit, determined the effective temperature. Furthermore, we assumed an uncertainty of 10 % on the knowledge of the effective mass and an uncertainty of 0.1 K on the initial temperature. From the fit routine, uncertainties on the previously named parameters were estimated. Upon these results, the standard deviation of the temperature estimate has been calculated according to

$$\Delta T_{\mathrm{Fb}}(\Gamma_m, \Delta\Gamma_m, \Omega_m, \Delta\Omega_m, \dots) = \sqrt{\left(\frac{\partial T}{\partial \Gamma_m}\right)^2 \Delta\Gamma_m^2 + \left(\frac{\partial T}{\partial \Omega_m}\right)^2 \Delta\Omega_m^2 + \cdots}, \tag{4.61}$$

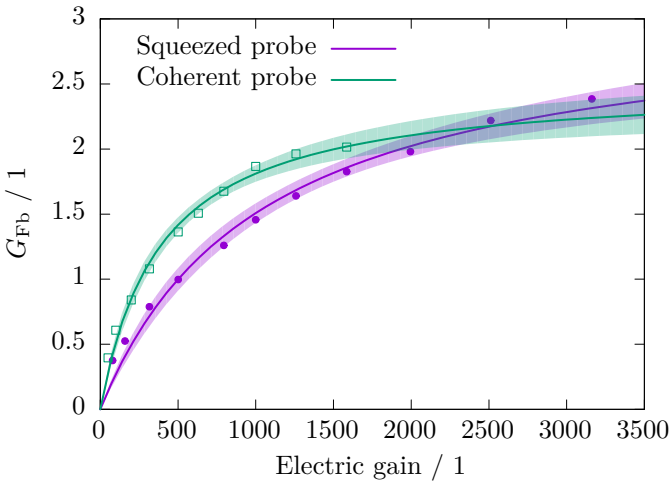

Figure 4.14: Feedback gain G_{Fb} as a function of the set electric gain for both probe states. Higher gain settings were chosen for the squeezed probe, as more gain is required to reach the optimal temperature at a higher initial SNR. Applying gain settings beyond the point leads to squashing, which is a regime where the correlations between the electronic noise and the mechanics dominate the system. The clearly visible nonlinear behaviour was caused by the influence of neighbouring mechanical modes: At high gain, those modes experienced a phase shift (cf. figure 4.8) different to the FFM, which eventually led to heating those modes. The positive feedback consequently saturated the amplifiers. A shading around the solid lines represents the 95 % confidence level of the prediction band.

where a prepended 'Δ' denotes the uncertainty estimate of the respective quantity.

4.3.3 Results

In a first experiment, we implemented feedback cooling using a coherent probe state with a power of 8.5 µW. The results are illustrated in figure 4.15, where we cooled from ambient temperature down to the limit set by the imprecision noise corresponding to the quantum noise of a coherent state. By means of attenuation measurements and balanced detection we verified the quantum origin of the noise [16], i.e. identified it as pure vacuum noise. As the feedback gain was increased, the effective temperature of the mechanical mode decreased to 149 K. Increasing the gain further led to heating of the mechanical oscillator, as the shot noise of the probing field eventually dominates the control. This feedback effect is known as squashing and was discussed in a quantum mechanical framework by Shapiro et al. [254]. An experimental verification can be found in various later publications [169, 224] and in figure 4.16.

The demonstration of squeezed light enhanced cooling is presented in figure 4.15. Here, we used the same coherent excitation as for the coherent state cooling experiment, but the quantum fluctuations of the probe beam were suppressed below vacuum noise. The detected noise suppression of the generated squeezed state was −1.9 dB, limited by evanescent coupling and propagation losses in the tapered fibre. An overview of the named factors is given in section 4.3.2.

Despite the losses an increase in measurement rate[15] of $\mu_{\mathrm{sqz}}/\mu_{\mathrm{coh}} = 1.55$ was achieved, and by applying the electronic feedback a clear suppression of the thermally excited mechanical displacement fluctuations was observed, ultimately reaching the squeezed noise level 1.9 dB below shot noise. As a result of employing quantum-enhanced feedback cooling, the mechanical mode

[15] The measurement rate characterises the rate at which the information about the mechanical position is transferred to the optical phase output. It is given by [37] $\mu = \Gamma_m |C_{\mathrm{eff}}|^2$. According to the definition, μ vanishes in the sideband resolved regime.

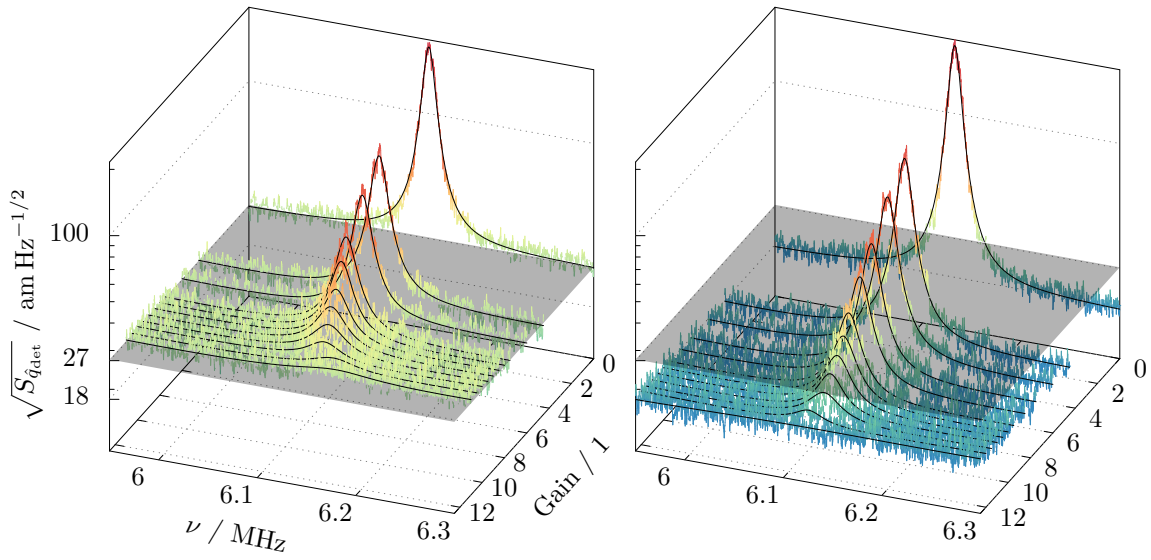

Figure 4.15: Evolution of the mechanical resonance under different gain settings. Left: Coherent state probe. Right: Squeezed state probe. Spectra were corrected for detector dark noise. A grey plane represents the optical shot noise level. The spectra are arranged proportional to the electronic gain that was set for the recording. Solid black lines represent fits to a Lorentzian distribution (4.60) and were used to infer the bandwidth and central frequency.

was cooled to an effective temperature of 130 K, more than 12 % lower than the minimum temperature achieved using coherent light.

A complementary characterisation of the demonstrated cooling scheme is provided by examining the time-domain phase space trajectory of the mechanical oscillator. Due to the large bandwidth of the homodyne detector compared to the mechanical dissipation rate Γ_m, this could be monitored in real-time [37, 129]. For this a simultaneous down-mixing of the homodyne photocurrent with two in-quadrature signals and subsequent low-pass filtering[16] at a frequency of Γ_m was applied to the digitalised data. The recorded thermal trajectories are visualised in figure 4.17(a). Both probing strategies result in a significant confinement of the oscillator's random excursions in phase space when subject to feedback cooling. While the enhancement by using squeezed light is not directly obvious from the phase space trajectories the effect is more pronounced by considering the marginal quadrature distributions depicted in figure 4.17(b), revealing a 12.6 % reduction in the variance of the cooled oscillator's position for the squeezed light probe, which is in good agreement with the temperature reduction.

The resulting temperature estimates as function of inferred feedback gain are presented in figure 4.18. A clear cooling improvement is observed for increasing gain until the thermal noise spectrum reaches the measurement imprecision noise level, after which the mechanical oscillator begins to heat up due to measurement noise being imprinted on its motion. As theoretically predicted, the reduced imprecision noise of the squeezed probe shifts the onset of heating towards larger feedback gain values, enabled quantum enhanced cooling to temperatures below the limit

[16] A finite impulse response filter, a top hat filter and a first order low pass had been applied to the data with corner frequencies around Γ_m. As the recording's SNR is rather low, a larger bandwidth immediately means more noise, while a smaller bandwidth is equivalent to smoothing the data. Both effects have been studied by Harris et al. [132].

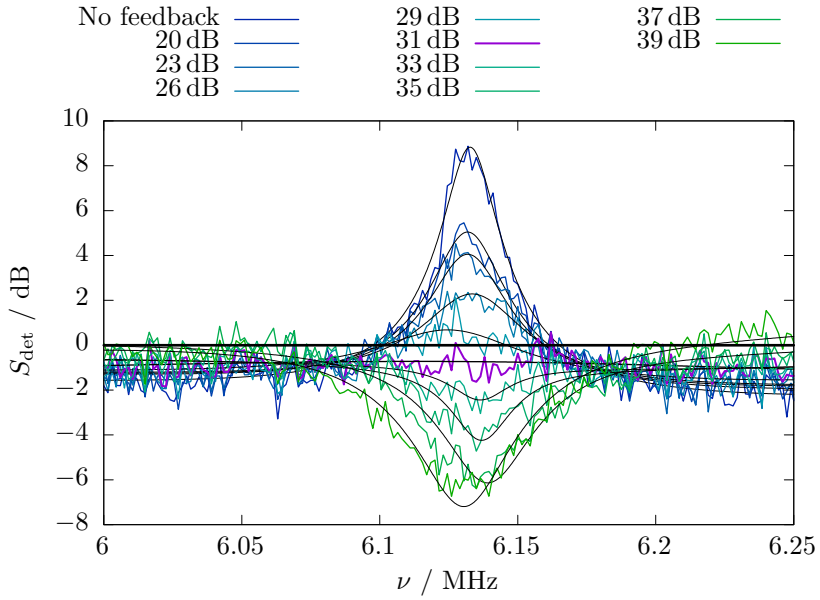

Figure 4.16: Spectral densities recorded with gain settings leading to the squashing effect. This is an effect of the in-loop measurement, correlating the mechanical motion and the measurement noise [169, 254]. The spectra are normalised to the optical shot noise level, marked by a bold line. Close-by mechanical modes led to the wings on the left and right side of the main peak.

set by shot noise.

Enhanced robustness via anti-squeezing

We already motivated the use of anti-squeezing for increasing the robustness of a displacement measurement on page 88. To support the idea, an example will be given on recent experimental implementation.

It was stated that the requirement of achieving high efficiencies for detecting the probe beam presents a serious constraint for quantum feedback control experiments. Indeed, with the experimentally realised efficiency reported by Wilson et al. [287] of $\eta = 23\,\%$, even when achieving a cooperativity $C \gg n_{\mathrm{th}}$, the minimum mechanical occupancy that could be achieved with coherent light is limited to, as given in equation (4.44b),

$$n_{\mathrm{min}} = \frac{1}{2\sqrt{0.23}} - 1/2 \approx 0.5. \tag{4.62}$$

If amplitude- rather than phase squeezing is used, the contribution of vacuum noise entering the phase quadrature due to inefficiencies is suppressed relative to the amplified noise of the phase quadrature. This results in a higher effective efficiency for feedback control experiments of

$$\eta_{\mathrm{eff}} = \frac{1}{1 + \frac{1-\eta}{2\eta\,\mathrm{Var}_c}}, \tag{4.63}$$

where $\mathrm{Var}_c = (2\,\mathrm{Var}_{\mathrm{det}} + \eta - 1)/(2\eta)$ denotes the intracavity variance of the optical field. We see that when $\mathrm{Var}_c \gg (1-\eta)/2\eta$, η_{eff} approaches unity.

As an example, assuming an intracavity phase anti-squeezing variance 9 dB above shot noise, the effective cooling efficiency of Wilson et al. could be increased to $\eta_{\mathrm{eff}} = 0.7$, allowing, in principle, cooling to an occupancy of $n_{\mathrm{min}} = 0.1$.

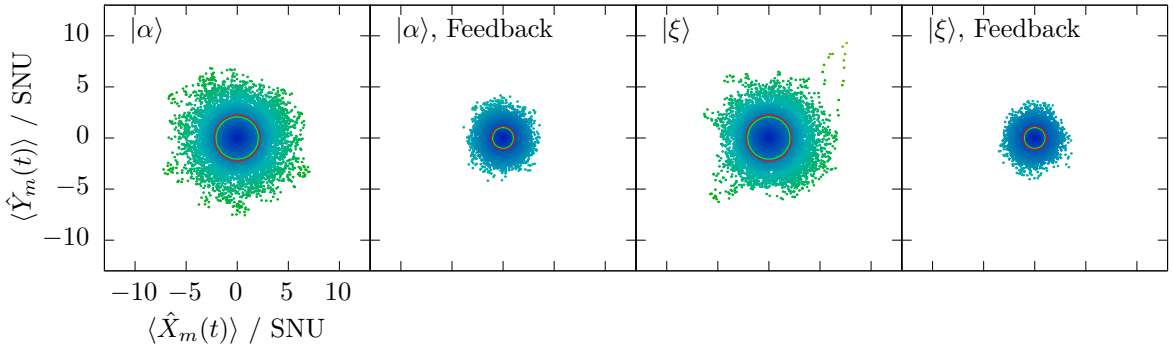

(a) Phase space trajectories

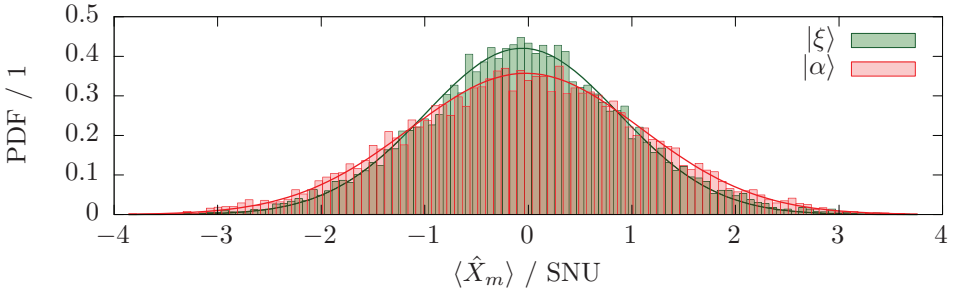

(b) Histograms of trajectories with feedback

Figure 4.17: (a) Phase space trajectory of the mechanical oscillator's position, normalised to shot noise units (SNU). The position operator $\hat{Q}$ has been decomposed into the quadratures $\cos(\Omega_m t)\hat{X}_m + \sin(\Omega_m t)\hat{Y}_m$ [37, p. 157] to span the phase space. As the bandwidth of the detector is much larger than the mechanical dissipation rate, it was possible to monitor the thermal evolution of the oscillator in real-time. $|\alpha\rangle$ and $|\xi\rangle$ refer to the coherent and squeezed state probe, respectively. Thin red circles represent the standard deviation of the distribution recorded with $|\alpha\rangle$, green circles visualise the same quantity when the mechanical mode is probed with $|\xi\rangle$. (b) The histogram shows the marginal distribution along the $\hat{X}_m$ quadrature of the cooled mechanical mode, comparing the squeezed (green) and the coherent (red) probe. Solid lines represent fits to the data, assuming a normal distribution, such that the vertical axis is scaled to be a probability density function (PDF), with the same normalisation to unity as in the phase space plots.

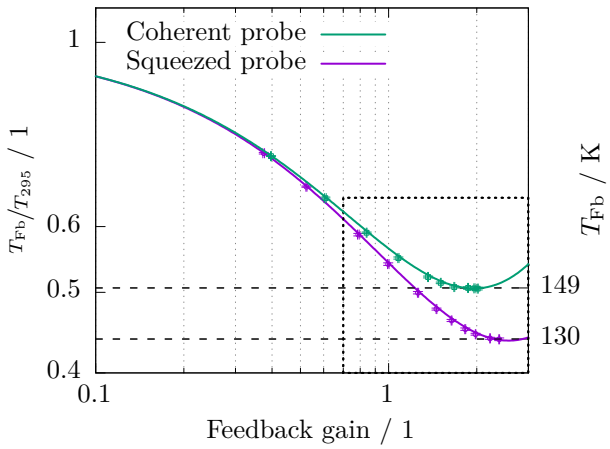

(a) Temperature comparison

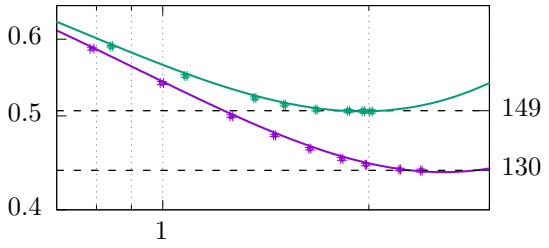

(b) Zoom into marked region

Figure 4.18: (a) Temperature ratio between the cooled and uncooled mechanical resonances (left axis) and the absolute effective temperatures T_{Fb} (right axis) versus the feedback gain G_{Fb}. Without feedback cooling, the temperature was 295 K. The effective temperature was determined, in accordance to the fluctuation-dissipation theorem, by integrating the spectral density of the oscillator's displacement. Error bars were derived from a standard uncertainty propagation method, given by equation (4.61). Solid lines calculated via equation (4.41). (b) A zoom into the region framed by a dashed rectangle in the upper plot. For higher gain settings, a squashing effect was observed, as shown in figure 4.16.

4.4 Conclusion and outlook

We demonstrated a feedback cooling scheme based on the use of a non-classical optical probe field for controlling a mechanical oscillator in the unresolved sideband regime. The combination of a squeezed state probe field and real-time feedback improved the cooling efficiency by more than 12 %, compared with a coherent probe field, to an effective temperature of 130 K.

Our results pave the way for quantum feedback control schemes that can enable an efficient interface for quantum information networks [100], and allow the standard quantum limit of force measurements to be surpassed via squeezing-enhanced measurements [175].

The absolute cooling achieved in the present demonstration is only modest compared to state-of-the-art [287], the main limitations being the relatively poor optomechanical cooperativity provided by the flexural mode and the requirement for operating in the under-coupled regime to preserve squeezing.

To improve the absolute cooling performance, an optomechanical system with enhanced cooperativity, and a realisation of a higher coupling and detection efficiencies for the squeezed mode are suggested. For instance, operating the system of Wilson et al. [287]

- in the undercoupled regime ($C/n_c = 0.62$ at a coupling efficiency of $\eta_c = 0.028$, where n_c is the intracavity photon number of 10^4) so that the injected squeezed light reflects from the cavity with high efficiency,
- with unity detection efficiency, and
- starting from 650 mK,

enables cooling to an occupation number $n_{\mathrm{th}} = 1.7$ phonons. Using an amplitude squeezed probe with an input squeezing of -9 dB, the occupation number could be lowered to $n_{\mathrm{th}} = 0.4$. This increases the chance of finding the system in ground state from ca. 31 % to 52 %.

We anticipate that the full benefit of squeezing-enhanced feedback cooling could be harnessed using recently developed tethered membrane mechanical oscillators [213] in conjunction with a high quality optical cavity, or alternatively, by implementation in state-of-the-art optomechanical systems in the microwave regime [66].

Besides the demonstrated cooling effect, our demonstration lays the foundation for more advanced schemes including squeezing-enhanced quantum backaction evasion[17] which in turn can be used to prepare mechanically squeezed states in the weak coupling regime and for generation of non-Gaussian mechanical quantum states. As an example, combining an optical input state squeezed by -10 dB with active feedback in a pulsed backaction evading scheme [140], it is possible to squeeze the mechanical oscillator by -10 dB for an interaction strength of $\chi = 4g_0\sqrt{n_c}/\kappa = 1$, while for a coherent state input, $\chi \geq \sqrt{10}$ is required to squeeze the mechanics by the same amount.

More immediately, the squeezing-enhanced sensing can improve techniques such as magnetometry based on microtoroids [102]. Here, a magnetostrictive material is embedded into the microtoroid, thereby coupling external magnetic fields to the mechanics.

[17] Backaction evasion is also referred to as quantum non-demolition measurements. The underlying idea is to gather information about, e.g., a particle's momentum without altering its further evolution. From a mathematical point of view, such a measurement can be identified via the Hamiltonian $\hat{\mathcal{H}}$: If an operator, observable by some coupling to a detector, can be identified to commute with $\hat{\mathcal{H}}$, this operator is a backaction free observable. The concept of backaction evasion was proposed in the 1970s, again in the context of gravitational wave interferometers, by Thorne et al. [269] and Braginskiĭ et al. [41].

5 | Phase insensitive quantum amplifiers in Gaussian channels

5.1 Introduction

At the end of every sensing protocol, the acquired information is extracted by some detection scheme. Such a scheme is technically limited by, e.g., electronic dark noise or, for a homodyne-like technique, the maximal local oscillator power. In a broader sense, this is an issue encountered in communication technology: Communication nowadays relies on the use of light, at least when it comes to transmission speed and information density. Regardless of the actual media which is guiding the light, propagation losses constrain the named quantities [139, 241]. Therefore the signal has to be amplified along the transmission channel to sent information over distances of hundredths of kilometres.

To simply increase the ingoing signal power is inappropriate from two perspectives: First, with an increasing demand of information exchange, the demanded power will increase, eventually to a point where technical and economical bounds are reached. Second, with the emerging field of quantum communication, especially quantum cryptography, the signal power is required to be on the order of the shot noise [243]. Any additional technical noise, that is noise which is not demanded to fulfil the laws of quantum mechanics, can constrain the benefits of quantum communication. Thus optical amplifiers have to be designed and used to accommodate for the challenges posed by it.

Apart from technical applications, the amplification of quantum states has been of interest to study fundamental aspects of quantum mechanics. To highlight those aspects, the problem of cloning quantum states, so-to-say the essence of amplification [84, 241, 290], is outlined: We start with a source of entangled particles, both carrying a spin, as depicted in figure 5.1, such that $|\psi\rangle = 1/\sqrt{2}(|\uparrow_A,\uparrow_B\rangle + |\downarrow_A,\downarrow_B\rangle)$. One particle is sent to Alice, the other one to Bob. Alice measures the spin of the particle in a coordinate system of her choice, thereby collapsing the wavefunction, e.g. $|\psi\rangle \to |\uparrow_A,\uparrow_B\rangle$. Before Bob measures the spin of the particle sent to him, let us assume he is able to clone the particle. This enables him to determine the spin of the particle and thus the alignment of Alice' measurement apparatus with more and more certainty, the more clones he created. In conclusion, Bob and Alice could communicate information without being bound by the speed of light. According to special relativity, it is safe to call such a conclusion unphysical.

The research on quantum amplifiers attracted attention shortly after the invention of the laser: Theoretical studies proofed that a phase-preserving, linear amplifier inevitably adds noise to the signal [54, 57, 182]. For optical amplifiers, this limitation was verified experimentally in 1993 [172]. The cause for the additional noise is that a quantum description of an amplifier requires a second input mode, next to the signal mode, which itself must have at least zero-point

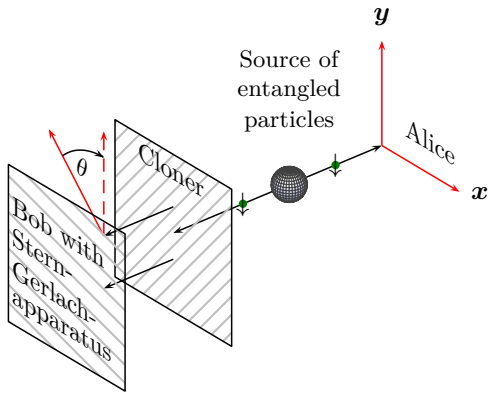

Figure 5.1: A sketch to explain the problem of cloning quantum states. Alice detects the particle in an orientation of her choice. Then, Bob produces a number of clones of the particle sent to him. Finally, he performs a Stern–Gerlach experiment under different angles θ. By doing so, he can determine the orientation of Alice's setup. Given a long enough separation, this would allow for superluminal communication.

fluctuations. Mathematically, the need of a second input mode – and consequently a second output mode – is readily explained: The naïve definition of $\hat{a}_{\text{out}} = g\hat{a}_{\text{in}}$, where g is the gain factor of the amplifier, can not maintain the commutation relation and is thus consistent with unitarity. To overcome this issue, a second mode has to be added [57]. In figure 5.3, a model of the amplifier is depicted. Assuming a phase insensitive amplifier void of technical noise and a single coherent input state, the best performance at high gain is found to be a halving of the signal-to-noise ratio [57, 158, 172].

We conducted a theoretical analysis of an amplified channel with the motivation of improving the transmission of information by introducing classical or quantum correlations between the two input modes. As the comparison between classical and quantum correlations resulted in promising findings, we studied additional cases of signal generation and detection schemes in channels with phase insensitive amplifiers.

In contrast to the mentioned phase i nsensitive amplifiers, where a phase change of the input does not alter the transformation, phase sensitive amplifiers are not restricted by the no-cloning theorem and have been used for e.g. noise reduction and optical cloning experiments [166, 171, 172]. In this analysis, we focus on phase insensitive amplifiers. Unless necessary for clarity, the qualifier 'phase insensitive' will be omitted from here on.

Chapter structure This chapter starts with a delineation of the analysis to motivate its key concept, which is the application of mutual information. It is followed by general definitions, which are then applied in the case study to various channel configurations. Next, the cases are compared visually and we conclude the study with a summary of the main results.

5.2 Approach of the analysis

To compare the performance of different input states and uses of an amplifier, the mutual information of the channel is evaluated. The advantage of this measure over others, such as the signal-to-noise ratio, is that mutual information has been studied in the context of information processing extensively and offers strict bounds on the maximum achievable performance.

The mutual information quantifies the relation between two random variables A and B; in our scenario these variables represent the in- and output of a communication channel. In a noiseless channel, A maps to B. Generally, the transmission through a physical channel is noisy, and we learn from the conditional probability $\mathrm{p}_{B|A}(b|a)$ how likely it is to get a specific outcome b from

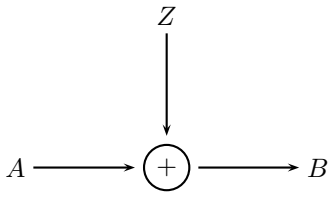

Figure 5.2: Model of a Gaussian channel. The letters A, B, Z refer to random variables and follow a Gaussian distribution.

a specific a. Given a physical channel, $\mathrm{p}_{B|A}$ is fixed, so the game is to tailor p_A to maximise the "usability", i.e. the bits per channel use, of that channel.

For discrete variables, the mutual information is defined as [74]

$$I(A;B) = \sum_{a\in A}\sum_{b\in B} \mathrm{p}(a,b)\log\left(\frac{\mathrm{p}(a,b)}{\mathrm{p}(a)\,\mathrm{p}(b)}\right). \tag{5.1}$$

While $\mathrm{p}(a,b)$ is the joint distribution[1], $\mathrm{p}(a)$ is the marginal one. With a given Wigner distribution W introduced on page 15, this definition can be applied to quantum states via

$$\mathrm{p}(x) = \int W(x,y)\,\mathrm{d}y. \tag{5.2}$$

Looking at the definition (5.1), the mutual information vanishes the more independent the marginal distributions are, as in the limiting case of complete independence $\mathrm{p}(a,b) = \mathrm{p}(a)\,\mathrm{p}(b)$.

The supremum of the mutual information is denoted by the channel capacity C. It is

$$C = \sup_{\mathrm{p}_A(a)} I(A;B), \tag{5.3}$$

where $\mathrm{p}_A(a)$ is the input distribution. The notation of the supremum instead of maximum is not found in all definitions, but the set of p_A might only have a supremum.

In case of Gaussian channels, which will be defined below, the mutual information is given by [74]

$$I = \frac{1}{2}\log\left(1+\frac{S}{N}\right), \tag{5.4}$$

with S is the signal power (or simply signal) and N the noise of the channel. Further, it is

$$\langle B^2\rangle = \langle (A+Z)^2\rangle = S+N, \tag{5.5}$$

where the noise variable Z, in accordance to Cover and Thomas [74], was introduced. The model is shown in figure 5.2. Regarding the dimension of I, the base of the logarithm tells the measure. Using the base 2, the unit is bit; in base e, the conversion $1\,\mathrm{bit} = \log_e 2\,\mathrm{nat}$ can be used.

5.3 General mathematical definitions

The scheme of the amplifier is outlined in figure 5.3. First, we collect all necessary transformations and operators to perform the calculations.

[1] $\mathrm{p}(a,b)$ is given by $\mathrm{p}_{B|A}(b|a)\,\mathrm{p}_A(a)$ [44].

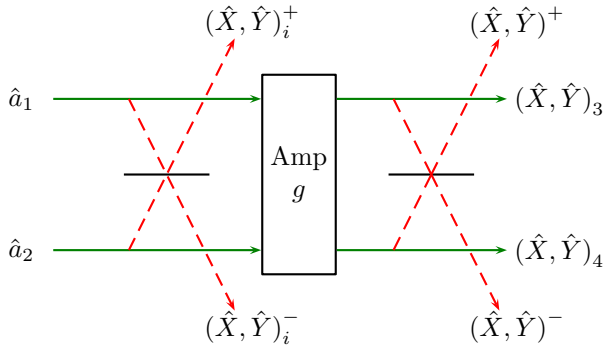

Figure 5.3: Mapping of the in- and outputs of a quantum amplifier. Two in- and outputs are required to maintain unitarity. The index notation is used in subsequent calculations. An i abbreviates initial. Green lines indicate direct in- and output modes, while dashed lines follow modes created by interfering the original ones on a beam splitter.

5.3.1 Transformations and quantum operators

Here, the fundamental transformation and operators introduced in section 1.2.1 are summarised to prevent from too many cross-references.

- The $50:50$ beam splitter is introduced as

$$M_{1/2} = \frac{1}{\sqrt{2}} \begin{bmatrix} 1 & 1 \\ -1 & 1 \end{bmatrix}. \tag{5.6}$$

  Its diagonal represents the transmitted mode.

- A variable beam splitter is employed to model losses. We define it as

$$M_\eta = \begin{bmatrix} \sqrt{\eta} & \sqrt{\eta-1} \\ -\sqrt{\eta-1} & \sqrt{\eta} \end{bmatrix}. \tag{5.7}$$

  The lossless case is given by $\eta = 1$.

- The electromagnetic field quadrature operators are

$$\hat{X} = \frac{\hat{a}+\hat{a}^\dagger}{\sqrt{2}}, \quad \hat{Y} = \frac{\hat{a}-\hat{a}^\dagger}{\imath\sqrt{2}}, \tag{5.8a}$$

$$[\hat{X},\hat{Y}] = \imath, \tag{5.8b}$$

  and the according ladder operators read

$$\hat{a} = \frac{\hat{X}+\imath\hat{Y}}{\sqrt{2}}, \quad \hat{a}^\dagger = \frac{\hat{X}-\imath\hat{Y}}{\sqrt{2}}, \tag{5.9a}$$

$$[\hat{a},\hat{a}^\dagger] = 1. \tag{5.9b}$$

  Only in ambiguous cases, an explicit unity operator is added to equations, such that commutator relations appear to carry only a scalar on the right hand side. Substituting the

field operators in the number operator,

$$\begin{aligned}\hat{n} = \hat{a}^\dagger\hat{a} &= \frac{1}{2}(\hat{X} - \imath\hat{Y})(\hat{X} + \imath\hat{Y}) \\ &= \frac{1}{2}(\hat{X}^2 + \hat{Y}^2 - 1).\end{aligned} \tag{5.10}$$

Conversely,

$$\hat{X}^2 = \frac{1}{2}\big(\hat{a}^2 + \hat{a}^{\dagger 2} + 2\hat{a}^\dagger\hat{a} + 1\big), \tag{5.11a}$$

$$\hat{Y}^2 = -\frac{1}{2}\big(\hat{a}^2 + \hat{a}^{\dagger 2} - 2\hat{a}^\dagger\hat{a} - 1\big). \tag{5.11b}$$

- The quadratures after the first beam splitter in figure 5.3 read:

$$\hat{X}_i^\pm = \frac{1}{\sqrt{2}}\Big(\hat{X}_1 \pm \hat{X}_2\Big) \tag{5.12a}$$

$$\hat{Y}_i^\pm = \frac{1}{\sqrt{2}}\Big(\hat{Y}_1 \pm \hat{Y}_2\Big) \tag{5.12b}$$

Superscripts denote one of the two output ports. For the second order, we have

$$(\hat{X}_i^\pm)^2 = \frac{1}{2}\Big(\hat{X}_1^2 + \hat{X}_2^2 \pm 2\hat{X}_1\hat{X}_2\Big), \tag{5.13a}$$

$$(\hat{Y}_i^\pm)^2 = \frac{1}{2}\Big(\hat{Y}_1^2 + \hat{Y}_2^2 \pm 2\hat{Y}_1\hat{Y}_2\Big). \tag{5.13b}$$

The number operators are:

$$\hat{n}_i^\pm = \frac{\hat{n}_1 + \hat{n}_2}{2} \pm \frac{1}{4}\Big(\{\hat{X}_1, \hat{X}_2\} + \{\hat{Y}_1, \hat{Y}_2\} + \imath[\hat{X}_1, \hat{Y}_2] + \imath[\hat{X}_2, \hat{Y}_1]\Big). \tag{5.14}$$

A pair of curly brackets denotes the anti-commutator.

- The modes after the phase insensitive amplifier read [54, 57]:

$$\hat{a}_3 = \sqrt{g}\hat{a}_1 + \sqrt{g-1}\hat{a}_2^\dagger, \tag{5.15a}$$

$$\hat{a}_4 = \sqrt{g}\hat{a}_2 + \sqrt{g-1}\hat{a}_1^\dagger. \tag{5.15b}$$

After the amplifier, the quadratures read:

$$\hat{X}_3 = \sqrt{g}\hat{X}_1 + \sqrt{g-1}\hat{X}_2, \quad \hat{X}_4 = \sqrt{g}\hat{X}_2 + \sqrt{g-1}\hat{X}_1, \tag{5.16a}$$

$$\hat{Y}_3 = \sqrt{g}\hat{Y}_1 - \sqrt{g-1}\hat{Y}_2, \quad \hat{Y}_4 = \sqrt{g}\hat{Y}_2 - \sqrt{g-1}\hat{Y}_1. \tag{5.16b}$$

A negative sign in the $\hat{Y}$ quadrature comes from the relation equation (5.15); it is lost when (erroneously) just propagating $\hat{X}$ and $\hat{Y}$ instead of the field operators. For the second orders:

$$\hat{X}_3^2 = g\hat{X}_1^2 + (g-1)\hat{X}_2^2 + 2\sqrt{g^2-g}\hat{X}_1\hat{X}_2, \tag{5.17a}$$

$$\hat{X}_4^2 = g\hat{X}_2^2 + (g-1)\hat{X}_1^2 + 2\sqrt{g^2-g}\hat{X}_1\hat{X}_2, \tag{5.17b}$$

$$\hat{Y}_3^2 = g\hat{Y}_1^2 + (g-1)\hat{Y}_2^2 - 2\sqrt{g^2-g}\hat{Y}_1\hat{Y}_2, \tag{5.17c}$$

$$\hat{Y}_4^2 = g\hat{Y}_2^2 + (g-1)\hat{Y}_1^2 - 2\sqrt{g^2-g}\hat{Y}_1\hat{Y}_2. \tag{5.17d}$$

- Placing a beam splitter after the amplifier leads to:

$$\xi^{\pm} = \sqrt{g} \pm \sqrt{g-1}, \tag{5.18a}$$
$$\hat{X}^{\pm} = \xi^{\pm} \hat{X}_i^{\pm}, \tag{5.18b}$$
$$\hat{Y}^{\pm} = \xi^{\mp} \hat{Y}_i^{\pm}. \tag{5.18c}$$

  For the second orders:

$$\Xi^{\pm} = (\xi^{\pm})^2 = 2g - 1 \pm 2\sqrt{g^2 - g}, \tag{5.19a}$$
$$(\hat{X}^{\pm})^2 = \Xi^{\pm} (\hat{X}_i^{\pm})^2, \tag{5.19b}$$
$$(\hat{Y}^{\pm})^2 = \Xi^{\mp} (\hat{Y}_i^{\pm})^2. \tag{5.19c}$$

Equipped with the basic operators and transformation, the actual channel properties are treated next. From this, we know how to extract the mutual information of a specific channel configuration.

5.3.2 Channel properties

Next to the operators, we define the properties of the channel. Figure 5.2 outlines the in- and outputs.

- As mentioned, we deal with Gaussian channels. The noise and losses are Gaussian, as is the modulation. Also, we draw the alphabet from a such distribution. In phase space, this can be envisioned as a normal distribution of coherent states. The signal state is thus described as

$$\hat{\rho} = \sum_i f_i |\alpha_i\rangle\langle\alpha_i|, \tag{5.20}$$

  whereas f_i is drawn from a multivariate Gaussian distribution.

- The signal power S is given by the variance [74], i.e. "size", of the alphabet. In turn, we start by writing

$$\operatorname{Var}\hat{\rho} = \operatorname{tr}(\hat{\rho}\hat{X}^2) + \operatorname{tr}(\hat{\rho}\hat{Y}^2) - \operatorname{tr}(\hat{\rho}\hat{X})^2 - \operatorname{tr}(\hat{\rho}\hat{Y})^2 \tag{5.21}$$

  for a two dimensional modulation. The variance is the constraint for the choice of the modulation, and for comparison it is useful to express it in terms of the photon number. This connection is drawn from equation (5.10):

$$\begin{aligned}\langle\hat{n}\rangle &= \frac{1}{2}\Big(\operatorname{tr}(\hat{\rho}\hat{X}^2) + \operatorname{tr}(\hat{\rho}\hat{Y}^2) - 1\Big) \\ &= \frac{1}{2}\Big(\operatorname{Var}\hat{X} + \langle\hat{X}^2\rangle + \operatorname{Var}\hat{Y} + \langle\hat{Y}^2\rangle - 1\Big).\end{aligned} \tag{5.22}$$

  The employed alphabet can be defined to be centred about the phase space origin, such that

$$\langle\hat{n}\rangle = \frac{1}{2}\Big(\operatorname{Var}\hat{X} + \operatorname{Var}\hat{Y} - 1\Big). \tag{5.23}$$

  Finally, we remember that to follow equation (5.5), one has to differentiate between a signal S and a noise part N of the total input first. Hence the shot noise needs to be subtracted

from (5.23). This way, the power put into the modulation can be expressed in terms of the photon number. Conversely, the variance of the quantum fluctuations are separated from the classical fluctuations generated by the sender Alice:

$$\langle \hat{n} \rangle = \frac{1}{2}\Big(\operatorname{Var} X_S + \operatorname{Var} \hat{X}_N + \operatorname{Var} Y_S + \operatorname{Var} \hat{Y}_N - 1\Big). \tag{5.24}$$

- Throughout the chapter, quantum and classical operators are distinguished by hats. Subscripts define whether the variance stems from noise (N) or the signal (S). We can also separate $\langle \hat{n} \rangle$ into a signal and noise part as

$$\langle n_S \rangle = \frac{1}{2}(\operatorname{Var} X_S + \operatorname{Var} Y_S) \tag{5.25a}$$

and

$$\langle \hat{n}_N \rangle = \frac{1}{2}\Big(\operatorname{Var} \hat{X}_N + \operatorname{Var} \hat{Y}_N - 1\Big). \tag{5.25b}$$

The difference in measuring I in terms of $\langle \hat{n} \rangle$ – the total photon number – or $\langle n_S \rangle$ – the photons used for signal modulation – will become clear when squeezed states, i.e. states with variable noise characteristics, are used.

5.4 Study of different communication channels

Equipped with the definitions, different cases to compare the mutual information are calculated to determine the optimal usage of the amplified channel.

5.4.1 Direct detection

1D modulation, homodyne detection The most simple case is when the modulation is along one quadrature, there are no losses in the channel, and the detection happens along the same quadrature. To apply equation (5.4), we need to identify the signal S and noise N. Given a coherent input state and, in accordance with the definition of $\hat{X}$ and $\hat{Y}$,

$$N = \langle \alpha | \hat{X}_N^2 | \alpha \rangle = \frac{1}{2}. \tag{5.26}$$

S is expressed by the variance of the alphabet, i.e. $\operatorname{Var} X_S = \langle X_S^2 \rangle$. Equation (5.24) is used to formulate the result in terms of photon numbers, so we have

$$\begin{aligned} I_{1,\mathrm{m}} &= \frac{1}{2}\log\left(1 + \frac{\langle X_S^2 \rangle}{1/2}\right) \\ &= \frac{1}{2}\log\big(1 + 2\langle X_S^2 \rangle\big), \end{aligned}$$

with $\langle \hat{n} \rangle = \frac{1}{2}\big(\langle X_S^2 \rangle + 2 \times \frac{1}{2} - 1\big) \Leftrightarrow \langle X_S^2 \rangle = 2\langle \hat{n} \rangle$,

$$= \frac{1}{2}\log(1 + 4\langle \hat{n} \rangle). \tag{5.27}$$

In terms of $\langle n_S \rangle$, the result is the same, as, according to equation (5.25b), $\langle \hat{n}_N \rangle = \frac{1}{2}(\frac{1}{2} + \frac{1}{2} - 1)$, so $\langle \hat{n}_N \rangle$ vanishes.

2D modulation, heterodyne detection In this case, a modulation of the field is applied to both quadratures. Accordingly, a heterodyne scheme is applied to detect the signal. This implies that the quadratures are measured independently, i.e.

$$I_{2,\mathrm{t}} = \sum_{O\in\{X_S,Y_S\}} \frac{1}{2}\log\left(1+\frac{\langle O^2\rangle}{1/2}\right). \tag{5.28}$$

N is still 1/2, as the shot noise is not changed due to the beam splitter in front of the individual detections. The signal is however attenuated by the beam splitter transformation. Equations (5.13) tells how the transformation reads. Similar to the one dimensional case, the quadratures are split into a classical signal and a quantum noise part, the former indicated with a S subscript. On the example of the $\hat{X}$ quadrature,

$$\begin{aligned}\langle\hat{X}^2\rangle &= \frac{1}{2}\langle\hat{X}_1^2+\hat{X}_2^2\rangle\\ \Leftrightarrow \langle X_S^2\rangle &= \frac{1}{2}\langle X_{1S}^2\rangle,\end{aligned} \tag{5.29}$$

where $\hat{X}_1$ is the ingoing signal and $\hat{X}_2$ the vacuum port of the beam splitter. The calculation for $\langle Y_S^2\rangle$ is equivalent. In sum,

$$I_{2,\mathrm{t}} = \sum_{O\in\{X_S,Y_S\}} \frac{1}{2}\log(1+2\langle\hat{n}_O\rangle). \tag{5.30}$$

To make this result comparable to the one dimensional case, we have to decide how many photons are "put" into the signals of $\hat{X}$ and $\hat{Y}$. By realising that the maximum of the function $\log x + \log y$ is found when $x = y$, the best combination is placing an equal amount of photons in both quadratures. Thus, for a subsequent visual comparison

$$I_{2,\mathrm{t}} = \log(1+\langle\hat{n}\rangle). \tag{5.31}$$

is used. Just as in the previous case, the result is the same in terms of $\langle n_S\rangle$.

1D modulation, single-mode squeezing, homodyne detection Changing from a coherent to a "proper" quantum state, we calculate I for a squeezed state input. For a brief introduction to squeezed states, the reader may refer to page 10. All necessary mathematical properties are summarised next.

Equivalent to the previous cases, the information is encoded as a Gaussian modulation. To make best use of resources, the squeezed quadrature is the same as the modulated (and detected) one – $\hat{X}$. So for the noise,

$$\langle\hat{X}_N^2\rangle = \frac{1}{2}\,\mathrm{e}^{-2r} \tag{5.32}$$

To relate the squeezing parameter r to the photons constituting the state, we use [114]

$$\hat{S}^\dagger(\gamma) = \hat{S}(-\gamma), \tag{5.33a}$$

$$\hat{S}^\dagger\hat{a}\hat{S} = \cosh(r)\hat{a} - \sinh(r)\hat{a}^\dagger, \quad \hat{S}^\dagger\hat{a}^\dagger\hat{S} = \cosh(r)\hat{a}^\dagger - \sinh(r)\hat{a}, \tag{5.33b}$$

to arrive at

$$\langle\hat{n}\rangle = \sinh(r)^2. \tag{5.34}$$

Substituting $\langle\hat{n}\rangle$ in equation (5.32),

$$\langle\hat{X}_N^2\rangle = \frac{1}{2\Big(\sqrt{\langle\hat{n}_\gamma\rangle}+\sqrt{1+\langle\hat{n}_\gamma\rangle}\Big)^2}, \tag{5.35}$$

where the squeezing photon number $\langle\hat{n}_\gamma\rangle$ was introduced to differentiate between the resources used for squeezing and the actual signal modulation.

The signal is given by

$$\begin{aligned}\langle\hat{n}\rangle &= \frac{1}{2}\left(\langle X_S^2\rangle + \frac{1}{2}\big(\mathrm{e}^{-2r}+\mathrm{e}^{2r}\big)-1\right)\\ \Leftrightarrow \langle X_S^2\rangle &= 2\langle\hat{n}\rangle - \cosh(2r) + 1.\end{aligned}$$

Converting r into a photon number,

$$\begin{aligned}\langle X_S^2\rangle &= 2\langle\hat{n}\rangle - (1+2\langle\hat{n}_\gamma\rangle)+1\\ &= 2(\langle\hat{n}\rangle - \langle\hat{n}_\gamma\rangle).\end{aligned} \tag{5.36}$$

But here, $\langle\hat{n}\rangle \neq \langle n_S\rangle$, because

$$\langle\hat{n}_N\rangle = \frac{1}{2}(\cosh(2r)-1) = \langle\hat{n}_\gamma\rangle. \tag{5.37}$$

Gathering the signal and noise terms results into

$$I_{1,\mathrm{m},\gamma} = \frac{1}{2}\log\left(1+4(\langle\hat{n}\rangle-\langle\hat{n}_\gamma\rangle)\left(\sqrt{\langle\hat{n}_\gamma\rangle}+\sqrt{1+\langle\hat{n}_\gamma\rangle}\right)^2\right) \tag{5.38a}$$

$$= \frac{1}{2}\log\left(1+4\langle n_S\rangle\left(\sqrt{\langle\hat{n}_\gamma\rangle}+\sqrt{1+\langle\hat{n}_\gamma\rangle}\right)^2\right). \tag{5.38b}$$

A later section will treat the optimal combination of signal-versus-squeezing photons.

5.4.2 Lossy channel

For a more realistic scenario, channel losses are introduced. This is modelled by a variable-beam-splitter transformation given by equation (5.7).

1D modulation, homodyne detection As done in the previous case, we transform the $\hat{X}$ quadrature and arrive at

$$\begin{aligned}\langle\hat{X}^2\rangle &= \langle\eta\hat{X}_1^2 + (1-\eta)\hat{X}_2^2\rangle\\ \Leftrightarrow \langle X_S^2\rangle &= \eta\langle X_{1S}^2\rangle \quad \text{with} \quad 0\leq\eta\leq 1.\end{aligned} \tag{5.39}$$

With the same argument as in the previous analysis, $N = 1/2$. Substitution into the mutual information yields

$$I_{1,\mathrm{m},\eta} = \frac{1}{2}\log(1+\eta 4\langle\hat{n}\rangle). \tag{5.40}$$

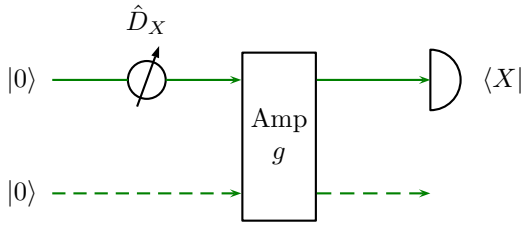

Figure 5.4: Scheme of a Gaussian channel with an one dimensional signal modulation $\hat{D}$, amplification and homodyne detection of the modulated quadrature. This scheme represents the common approach of quantum amplifiers, where one in- and one output mode are not accessible. These modes are due to, e.g., phononic excitations in a fibre based amplifier [158].

2D modulation, heterodyne detection Combining the two preceding cases,

$$I_{2,\mathrm{t},\eta} = \sum_{O\in\{X_S,Y_S\}} \frac{1}{2}\log(1+\eta 2\langle\hat{n}_O\rangle). \tag{5.41}$$

Again, the best information is achieved when the size of the alphabet is the same in both quadratures, which yields

$$I_{2,\mathrm{t},\eta} = \log(1+\eta\langle\hat{n}\rangle). \tag{5.42}$$

5.4.3 Amplified channel

Now we turn to the question how an amplification affects the mutual information.

1D modulation, homodyne detection In the first case, input mode 1 is used for sending in a one dimensional signal. Accordingly, one output is used and probed via homodyne detection. Figure 5.4 illustrates this case. For exemplification, the analytic solutions of the Wigner functions for all four modes are shown in figure 5.5.

Starting with the noise, equation (5.17) yields

$$\langle\hat{X}_N^2\rangle = \frac{g}{2} + \frac{1}{2}(g-1) = g - \frac{1}{2}. \tag{5.43}$$

For $X_S = \hat{X} - \hat{X}_N$ it is

$$\begin{aligned}\langle X_S^2\rangle + g - \frac{1}{2} &= g\langle X_{1S}^2\rangle + \frac{g}{2} + \frac{1}{2}(g-1)\\ \Leftrightarrow \langle X_S^2\rangle &= g\langle X_{1S}^2\rangle.\end{aligned} \tag{5.44}$$

So the mutual information is

$$I_{1,\mathrm{m},g} = \frac{1}{2}\log\left(1+\frac{g2\langle\hat{n}\rangle}{g-1/2}\right). \tag{5.45}$$

For the high gain limit,

$$I_{1,\mathrm{m},\infty} = \frac{1}{2}\log(1+2\langle\hat{n}\rangle), \tag{5.46}$$

equivalent to a transmission through a channel with 50 % losses.

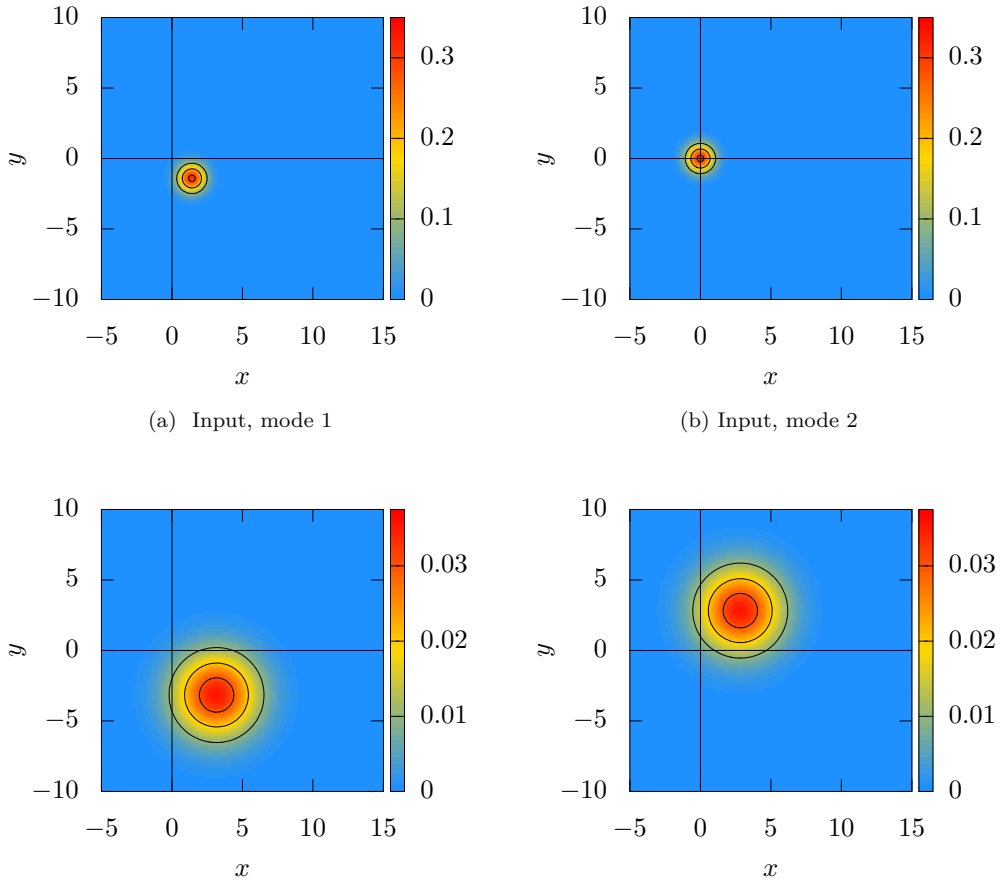

(a) Input, mode 1

(b) Input, mode 2

(c) Output, mode 3

(d) Output, mode 4

Figure 5.5: Wigner functions $W(x, y)$ for the input and output modes of the case depicted in figure 5.4. The gain set for the calculation is 5. To map in- to output, relations (5.16) are used. Modes 3 and 4 show an amplification, but at the cost of an increased noise. Quantitatively, this is expressed by equation (5.45). The state's amplitude is $\alpha_1 = 1 + \imath$ (cf. equation (1.48)) corresponding to a two dimensional modulation. It is chosen only to highlight the difference between the two output modes.

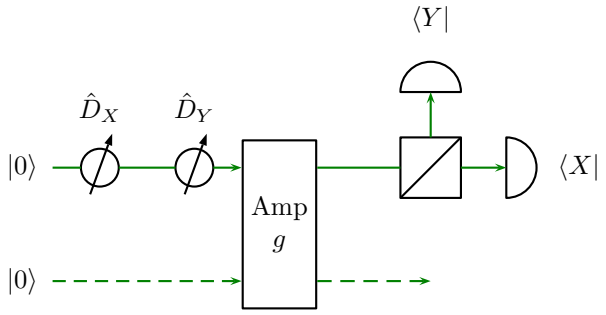

Figure 5.6: Extension of the scheme presented in figure 5.4: Here, a two dimensional signal modulation and detection protocol is applied.

2D modulation, heterodyne detection Extending the modulation into $\hat{Y}$ and performing, as shown in figure 5.6 a heterodyne detection instead, the previous results are combined to

$$I_{2,\mathrm{t},g} = \log\left(1 + \frac{g/2\langle\hat{n}\rangle}{g/2}\right) = \log(1 + \langle\hat{n}\rangle) \tag{5.47}$$

Surprisingly, the amplification cancels out, implying that the noise added by the amplification does not grow faster than the actual displacement of the input state.

1D modulation, single-mode squeezing, homodyne detection Following the standard procedure, we have

$$\langle\hat{X}_N^2\rangle = \frac{g}{2}\,\mathrm{e}^{-2r} + \frac{1}{2}(g-1) \tag{5.48a}$$

$$= \frac{g}{2\left(\sqrt{\langle\hat{n}_\gamma\rangle} + \sqrt{1+\langle\hat{n}_\gamma\rangle}\right)^2} + \frac{1}{2}(g-1), \tag{5.48b}$$

and, from equation (5.36),

$$\begin{aligned}\langle X_S^2\rangle &= g(2\langle\hat{n}\rangle - \cosh(2r) + 1)\\ &= g2(\langle\hat{n}\rangle - \langle\hat{n}_\gamma\rangle).\end{aligned} \tag{5.49}$$

This yields

$$I_{1,\mathrm{m},\gamma,g} = \frac{1}{2}\log\left(1 + \frac{4g(\langle\hat{n}\rangle - \langle\hat{n}_\gamma\rangle)}{g - 1 + g\left(\sqrt{\langle\hat{n}_\gamma\rangle} + \sqrt{1+\langle\hat{n}_\gamma\rangle}\right)^{-2}}\right) \tag{5.50a}$$

$$= \frac{1}{2}\log\left(1 + \frac{4g\langle n_S\rangle}{g - 1 + g\left(\sqrt{\langle\hat{n}_\gamma\rangle} + \sqrt{1+\langle\hat{n}_\gamma\rangle}\right)^{-2}}\right). \tag{5.50b}$$

As now two photon numbers are describing the mutual information, it is natural to ask for the optimum. In a next section, this optimum will be determined and a visual comparison for the maximum achievable I given.

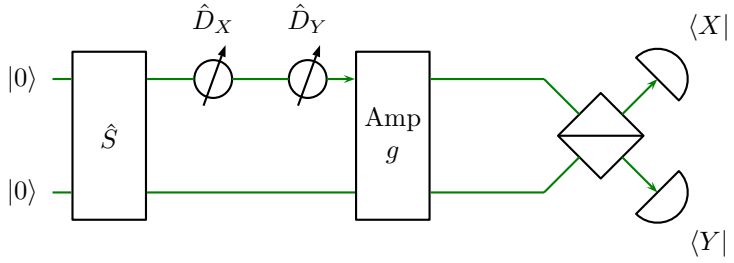

Figure 5.7: Scheme of Gaussian channel with a two-mode squeezer, entangling the input modes. After modulating the signal, the state is amplified. Before detecting, the outputs are combined on a beam splitter to form a Bell-type detection scheme [114].

2D modulation, two-mode squeezing, Bell-type detection One way to use the amplifier in a better way, compared to what is presented above, is to feed the amplifier with a two-mode squeezed state [8, 185]. The signal is then modulated as in the previous examples, that is as a displacement of one of the two modes. Experiments using this state in combination with optical amplifiers have been conducted recently [128, 166], however the authors did not evaluate their findings in terms of the mutual information.

First, let the quadrature operators be introduced as [114, 181]

$$\hat{X} = \frac{\hat{a}_1 + \hat{a}_1^\dagger + \hat{a}_2 + \hat{a}_2^\dagger}{2} = \frac{1}{\sqrt{2}}\Big(\hat{X}_1 + \hat{X}_2\Big), \tag{5.51a}$$

$$\hat{Y} = \frac{\hat{a}_1 - \hat{a}_1^\dagger + \hat{a}_2 - \hat{a}_2^\dagger}{\imath 2} = \frac{1}{\sqrt{2}}\Big(\hat{Y}_1 + \hat{Y}_2\Big) \tag{5.51b}$$

to fulfil $[\hat{X}, \hat{Y}] = \imath$. This also results in maintaining the shot noise unit of 1/2. The variances read

$$\operatorname{Var}\hat{X} = \frac{1}{2}\,\mathrm{e}^{-2r}, \quad \operatorname{Var}\hat{Y} = \frac{1}{2}\,\mathrm{e}^{2r} \tag{5.52}$$

for squeezing along the $\hat{X}$ quadrature, which is true for both single and two-mode squeezing.

The photon number in both modes is, again equal to single-mode squeezing,

$$\langle\hat{n}_1\rangle = \langle\hat{n}_2\rangle = \sinh(r)^2. \tag{5.53}$$

For the following equations, and indexing of the field operators, mind that the squeezing operator $\hat{S}$ acts on both modes. The result of equation (5.53) can be recovered via

$$\langle\gamma|\hat{n}|\gamma\rangle = \langle 0|\hat{S}^\dagger\hat{a}^\dagger\hat{a}\hat{S}|0\rangle \tag{5.54}$$

and reminding that, in addition to equation (5.33),

$$\hat{S}^\dagger\hat{a}_1\hat{S} = \cosh(r)\hat{a}_1 - \sinh(r)\hat{a}_2^\dagger, \tag{5.55a}$$

$$\hat{S}^\dagger\hat{a}_2\hat{S} = \cosh(r)\hat{a}_2 - \sinh(r)\hat{a}_1^\dagger. \tag{5.55b}$$

To measure the signal, the $\hat{X}^+$ and $\hat{Y}^-$ quadratures are probed. For the noise,

$$\begin{aligned}\langle\hat{X}_N^2\rangle &= \Xi^+\frac{1}{2}\Big(\langle\hat{X}_1^2\rangle + \langle\hat{X}_2^2\rangle + 2\langle\hat{X}_1\hat{X}_2\rangle\Big)\\ &= \Xi^+\frac{1}{2}\,\mathrm{e}^{-2r}\end{aligned} \tag{5.56a}$$

and

$$\begin{aligned}\langle \hat{Y}_N^2 \rangle &= \Xi^+ \frac{1}{2}\Big(\langle \hat{Y}_1^2 \rangle + \langle \hat{Y}_2^2 \rangle - 2\langle \hat{Y}_1 \hat{Y}_2 \rangle\Big) \\ &= \Xi^+ \frac{1}{2}\,\mathrm{e}^{-2r}\,. \end{aligned} \tag{5.56b}$$

Note that the signs in the exponent are equal. The sign change between the quadratures, as in equation (5.52), would be recovered when measuring $\hat{Y}^+$ instead of $\hat{Y}^-$. Let us convert r into photon numbers next, remembering equation (5.53): That each of the modes contains $\sinh(r)^2$ photons. Then,

$$\mathrm{e}^{-2r} = \mathrm{e}^{-2\,\mathrm{arcsinh}\left(\sqrt{\langle \hat{n}_\gamma \rangle/2}\right)} = \frac{2}{\left(\sqrt{\langle \hat{n}_\gamma \rangle} + \sqrt{2 + \langle \hat{n}_\gamma \rangle}\right)^2}. \tag{5.57}$$

For the signal,

$$\langle X_S^2 \rangle = \Xi^+ \frac{1}{2}\langle X_{1S}^2 \rangle \tag{5.58a}$$

and

$$\langle Y_S^2 \rangle = \Xi^+ \frac{1}{2}\langle Y_{1S}^2 \rangle. \tag{5.58b}$$

In which mode (number 1 or 2) the signal modulation takes place is of no matter.

Substituting the signal and noise terms into equation (5.4) yields

$$\begin{aligned} I_{2,\mathrm{b},g,\gamma} &= \sum_{O\in\{X_S,Y_S\}} \frac{1}{2}\log\left(1 + \frac{\langle O^2 \rangle}{\Xi^+ \exp(-2r)/2}\right) \\ &= \sum_{O\in\{X_S,Y_S\}} \frac{1}{2}\log\left(1 + (\langle \hat{n}_O \rangle - \langle \hat{n}_N \rangle)\left(\sqrt{\langle \hat{n}_\gamma \rangle} + \sqrt{2 + \langle \hat{n}_\gamma \rangle}\right)^2\right) \\ &= \sum_{O\in\{X_S,Y_S\}} \frac{1}{2}\log\left(1 + \left(\langle \hat{n}_O \rangle - \frac{\langle \hat{n}_\gamma \rangle}{2}\right)\left(\sqrt{\langle \hat{n}_\gamma \rangle} + \sqrt{2 + \langle \hat{n}_\gamma \rangle}\right)^2\right) \qquad (5.59a) \\ &= \sum_{O\in\{X_S,Y_S\}} \frac{1}{2}\log\left(1 + \langle n_O \rangle\left(\sqrt{\langle \hat{n}_\gamma \rangle} + \sqrt{2 + \langle \hat{n}_\gamma \rangle}\right)^2\right), \qquad (5.59b) \end{aligned}$$

where the squeezing photon number $\langle \hat{n}_\gamma \rangle$ and equation (5.36) are applied. If no squeezing is used, the mutual information is the same as for case $I_{2,\mathrm{t}}$ (2D modulation, heterodyne detection), that is the amplification cancels out. For an equal modulation of both quadratures,

$$\begin{aligned} I_{2,\mathrm{b},g,\gamma} &= \log\left(1 + \frac{1}{2}\left(\langle \hat{n}_O \rangle - \frac{\langle \hat{n}_\gamma \rangle}{2}\right)\left(\sqrt{\langle \hat{n}_\gamma \rangle} + \sqrt{2 + \langle \hat{n}_\gamma \rangle}\right)^2\right) \qquad (5.60a) \\ &= \log\left(1 + \frac{\langle n_S \rangle}{2}\left(\sqrt{\langle \hat{n}_\gamma \rangle} + \sqrt{2 + \langle \hat{n}_\gamma \rangle}\right)^2\right). \qquad (5.60b) \end{aligned}$$

The optimal balance of $\langle n_S \rangle$ and $\langle \hat{n}_\gamma \rangle$ is calculated in a later later section.

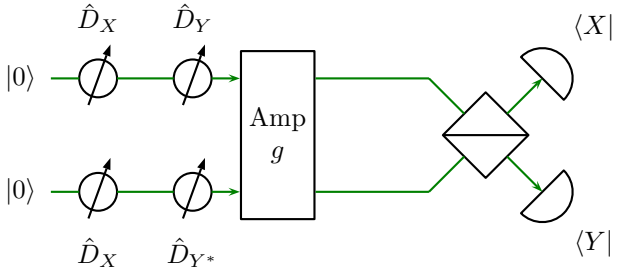

Figure 5.8: Further extension of the scheme presented in figure 5.4: The signal is modulated in both input modes equally, but with a conjugation of the phase quadrature. As in the previous example in figure 5.7, a Bell-type detection scheme is employed to extract the information.

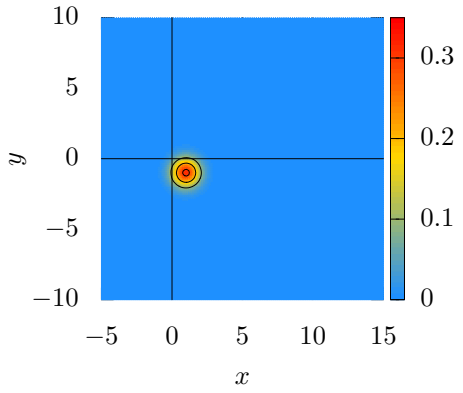

(a) Input, mode 1

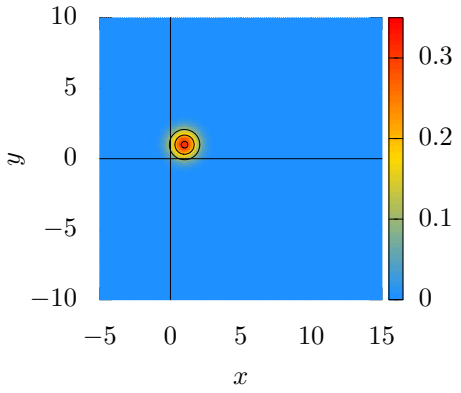

(b) Input, mode 2

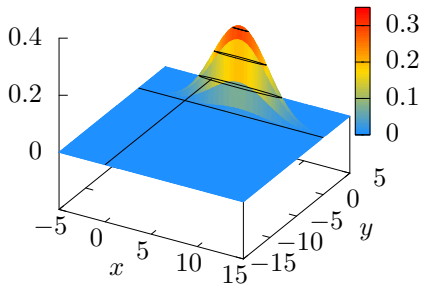

(c) Output, mode +

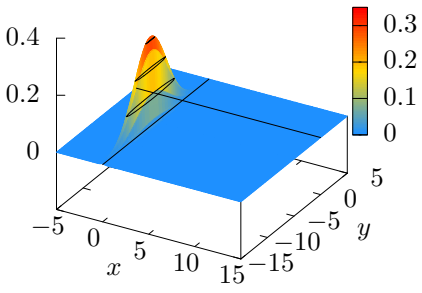

(d) Output, mode −

Figure 5.9: Wigner functions $W(x, y)$ for the in- and output modes of the case shown in figure 5.8. As in figure 5.5, $g = 5$. The signal amplitude is halved compared to what is shown in graph 5.5(a) to provide a fair comparison. For output +: $\langle \hat{X} \rangle = \sqrt{18 + 8\sqrt{5}}$, $\langle \hat{Y} \rangle = 0$, $\operatorname{Var} \hat{X} = 9/2 + 2\sqrt{5}$ and $\operatorname{Var} \hat{Y} = 9/2 - 2\sqrt{5}$, equalling a squeezing degree of $V_s = 10 \log_{10}(\operatorname{Var} \hat{Y} / \frac{1}{2}) \approx -12.5\,\mathrm{dB}$.

Classically correlated input, Bell-type detection Here we examine the case where the input state is $|\alpha_1, \alpha_2^*\rangle$, i.e. the quadrature a m p l i t u d e s of the state are correlated, but there are no quantum correlations involved. As obvious this is to point out, as important it is for the analysis. An illustration of this case can be found in figure 5.8.

We use the $\hat{X}^+, \hat{Y}^-$ quadratures to probe the correlations. Starting with the noise, one finds that (similar to equation (5.56))

$$\begin{aligned}\langle \hat{X}_N^2 \rangle &= \Xi^+ \frac{1}{2}\Big(\langle \hat{X}_1^2 \rangle + \langle \hat{X}_2^2 \rangle + 2\langle \hat{X}_1 \hat{X}_2 \rangle\Big) \\ &= \Xi^+ \frac{1}{2}\Big(1 + 2\Big(\langle X_{1S} X_{2S} \rangle + \langle X_{1S} \hat{X}_{2N} \rangle + \langle \hat{X}_{1N} X_{2S} \rangle + \langle \hat{X}_{1N} \hat{X}_{2N} \rangle\Big)\Big) \\ &= \frac{\Xi^+}{2}\left(= g - \frac{1}{2} + \sqrt{g^2 - g}\right) \end{aligned} \tag{5.61a}$$

and

$$\langle \hat{Y}_N^2 \rangle = \frac{\Xi^+}{2}. \tag{5.61b}$$

Expectation values of first and second order For the signal, let us list the expectation values first. We introduce $\langle \hat{O} \rangle$ as a short hand notation for $\langle \beta_2, \alpha_1 | \hat{O} | \alpha_1, \beta_2 \rangle$.

- The expectation values in front of the amplifier are:

$$\langle \hat{X}_1 \rangle = \sqrt{2}\Re(\alpha), \quad \langle \hat{X}_2 \rangle = \sqrt{2}\Re(\beta), \tag{5.62a}$$
$$\langle \hat{Y}_1 \rangle = \sqrt{2}\Im(\alpha), \quad \langle \hat{Y}_2 \rangle = \sqrt{2}\Im(\beta), \tag{5.62b}$$
$$\langle \hat{X}_i^\pm \rangle = \Re(\alpha) \pm \Re(\beta), \tag{5.62c}$$
$$\langle \hat{Y}_i^\pm \rangle = \Im(\alpha) \pm \Im(\beta). \tag{5.62d}$$

  For all operators $\hat{O}$ in equations (5.62):

$$\mathrm{Var}(\hat{O}) = 1/2. \tag{5.63}$$

- The expectation values directly after the amplifier read:

$$\langle \hat{X}_3 \rangle = \sqrt{g}\langle \hat{X}_1 \rangle + \sqrt{g-1}\langle \hat{X}_2 \rangle, \quad \langle \hat{X}_4 \rangle = \sqrt{g}\langle \hat{X}_2 \rangle + \sqrt{g-1}\langle \hat{X}_1 \rangle, \tag{5.64a}$$
$$\langle \hat{Y}_3 \rangle = \sqrt{g}\langle \hat{Y}_1 \rangle - \sqrt{g-1}\langle \hat{Y}_2 \rangle, \quad \langle \hat{Y}_4 \rangle = \sqrt{g}\langle \hat{Y}_2 \rangle - \sqrt{g-1}\langle \hat{Y}_1 \rangle, \tag{5.64b}$$

  and after re-combination at a beam splitter

$$\langle \hat{X}^\pm \rangle = \xi^\pm \langle \hat{X}_i^\pm \rangle, \tag{5.65a}$$
$$\langle \hat{Y}^\pm \rangle = \xi^\mp \langle \hat{Y}_i^\pm \rangle. \tag{5.65b}$$

  For the operators $\hat{O}$ in equations (5.64)

$$\mathrm{Var}(\hat{O}) = g - 1/2, \tag{5.66}$$

  and for the operators in equations (5.65)

$$\mathrm{Var}\, \hat{X}^\pm = \Xi^\pm/2, \tag{5.67a}$$
$$\mathrm{Var}\, \hat{Y}^\pm = \Xi^\mp/2. \tag{5.67b}$$

- For completeness, we check the noise figure [78]

$$\frac{\mathrm{SNR_o}}{\mathrm{SNR_i}} = \frac{\langle\hat{O}_\mathrm{o}\rangle^2\langle\hat{O}_\mathrm{i}^2\rangle - \langle\hat{O}_\mathrm{i}\rangle^2\langle\hat{O}_\mathrm{o}\rangle^2}{\langle\hat{O}_\mathrm{i}\rangle^2\langle\hat{O}_\mathrm{o}^2\rangle - \langle\hat{O}_\mathrm{i}\rangle^2\langle\hat{O}_\mathrm{o}\rangle^2}, \tag{5.68}$$

  where $\hat{O}_\mathrm{i}$ refers to some input- and $\hat{O}_\mathrm{o}$ to an output quadrature. The SNR is defined as $\langle\hat{O}\rangle^2/\operatorname{Var}\hat{O}$. Evaluating the noise figure for any combination of the quadratures $(\hat{X},\hat{Y})^\pm$ from figure 5.3, it turns out that the noise figure is always unity regardless of the amplification, which rephrases finding (5.47).

Evaluating the signal for the mutual information The signal we are able to measure in the respective modes are the sum and differences of the real and imaginary parts of the state amplitude.

$$\begin{aligned}\langle X_S^2\rangle + \langle\hat{X}_N^2\rangle &= \Xi^+\frac{1}{2}\Big(\langle\hat{X}_1^2\rangle + \langle\hat{X}_2^2\rangle + 2\langle\hat{X}_1\hat{X}_2\rangle\Big)\\ &= \Xi^+\frac{1}{2}\big(\langle X_{1S}^2\rangle + \langle X_{S2}^2\rangle + 1 + 2\langle X_{1S}X_{2S}\rangle\big) \qquad (5.69a)\\ \langle Y_S^2\rangle + \langle\hat{Y}_N^2\rangle &= \Xi^+\frac{1}{2}\big(\langle Y_{1S}^2\rangle + \langle Y_{S2}^2\rangle + 1 - 2\langle Y_{1S}Y_{2S}\rangle\big). \qquad (5.69b)\end{aligned}$$

For

$$\begin{aligned}\langle\alpha^*,\alpha|\hat{X}_1\hat{X}_2|\alpha,\alpha^*\rangle &= 2\Re(\alpha)^2, \qquad (5.70a)\\ \langle\alpha^*,\alpha|\hat{Y}_1\hat{Y}_2|\alpha,\alpha^*\rangle &= -2\Im(\alpha)^2, \qquad (5.70b)\end{aligned}$$

but, to stress it, there are only classical correlations involved in the signal modulation. Thus

$$\begin{aligned}\langle X_S^2\rangle &= \Xi^+\frac{1}{2}\big(\langle X_{1S}^2\rangle + \langle X_{S2}^2\rangle + 2\langle X_{1S}X_{2S}\rangle\big), \qquad (5.71a)\\ \langle Y_S^2\rangle &= \Xi^+\frac{1}{2}\big(\langle Y_{1S}^2\rangle + \langle Y_{S2}^2\rangle - 2\langle Y_{1S}Y_{2S}\rangle\big) \qquad (5.71b)\end{aligned}$$

are the simplified expressions. Now we insert the correlations and arrive at

$$\begin{aligned}\langle X_S^2\rangle &= \Xi^+ 2\langle X_{1S}^2\rangle, \qquad (5.72a)\\ \langle Y_S^2\rangle &= \Xi^+ 2\langle Y_{1S}^2\rangle, \qquad (5.72b)\end{aligned}$$

where the index 1 was kept, however it would read the same for the other index. Substitution of the noise and signal power into the mutual information yields

$$\begin{aligned}I_{2,\mathrm{b},g,\mathrm{cc}} &= \sum_{O\in\{X_S,Y_S\}}\frac{1}{2}\log\left(1+\frac{4\Xi^+\langle\hat{n}_O\rangle}{\Xi^+/2}\right)\\ &= \sum_{O\in\{X_S,Y_S\}}\frac{1}{2}\log(1+8\langle\hat{n}_O\rangle). \qquad (5.73)\end{aligned}$$

Just as for the noise figure, the gain of the amplifier does not enter the expression for the mutual information. Assuming an equal modulation of both quadratures and an equal distribution of photons into the two inputs,

$$I_{2,\mathrm{b},g,\mathrm{cc}} = \log(1+2\langle\hat{n}\rangle). \tag{5.74}$$

Classically correlated input, two-mode squeezing, Bell-type detection Combining the results from the last two cases, the mutual information is now evaluated for two-mode squeezing carrying a classically correlated signal.

The noise is equal to case $I_{2,\mathrm{b},g,\gamma}$, given in equation (5.56).

For the signal, the result is given already in equation (5.73), as all non-classical noise terms cancel.

In total, we have

$$I_{2,\mathrm{b},g,\mathrm{cc},\gamma} = \sum_{O\in\{X_S,Y_S\}} \frac{1}{2}\log\left(1+\frac{\langle O^2\rangle}{\Xi^+\,\mathrm{e}^{-2r}/2}\right)$$
$$= \sum_{O\in\{X_S,Y_S\}} \frac{1}{2}\log\left(1+4\left(\langle\hat{n}_O\rangle-\frac{\langle\hat{n}_\gamma\rangle}{2}\right)\mathrm{e}^{2r}\right) \tag{5.75a}$$
$$= \sum_{O\in\{X_S,Y_S\}} \frac{1}{2}\log\bigl(1+4\langle n_S\rangle\,\mathrm{e}^{2r}\bigr). \tag{5.75b}$$

For a modulation scheme equal in both quadratures and modes,

$$I_{2,\mathrm{b},g,\mathrm{cc},\gamma} = \log\left(1+2\left(\langle\hat{n}_O\rangle-\frac{\langle\hat{n}_\gamma\rangle}{2}\right)\mathrm{e}^{2r}\right) \tag{5.76a}$$
$$= \log\bigl(1+2\langle n_S\rangle\,\mathrm{e}^{2r}\bigr). \tag{5.76b}$$

Converting the squeezing parameter into a photon number, we use equation (5.57). Substitution yields

$$I_{2,\mathrm{b},g,\mathrm{cc},\gamma} = \log\left(1+\left(\langle\hat{n}_O\rangle-\frac{\langle\hat{n}_\gamma\rangle}{2}\right)\left(\sqrt{\langle\hat{n}_\gamma\rangle}+\sqrt{2+\langle\hat{n}_\gamma\rangle}\right)^2\right) \tag{5.77a}$$
$$= \log\left(1+\langle n_S\rangle\left(\sqrt{\langle\hat{n}_\gamma\rangle}+\sqrt{2+\langle\hat{n}_\gamma\rangle}\right)^2\right). \tag{5.77b}$$

The optimal I in terms of $\langle n_S\rangle$ and $\langle\hat{n}_\gamma\rangle$ is treated next.

5.4.4 Optimal photon number distribution

For input states exhibiting quantum correlations, additional resources are required. These resources can be measured in terms of photon numbers and have to be taken into account when comparing I. The question of how to distribute the photons into the actual signal modulation and squeezing generation will be answered. The approach is given in depth for the case of single-mode squeezing and is then applied to the other two.

Single-mode squeezing, direct detection

First of all, we note that equation (5.38a) is monotonously growing in both dimensions. To arrive at a meaningful answer for the question of how to distribute the photons, we have to set a condition under which $\langle n_S\rangle$ and $\langle\hat{n}_\gamma\rangle$ are shuffled around to maximise I. A natural choice of the condition, with a being the upper bound, is

$$0 < \langle n_S\rangle + \langle\hat{n}_\gamma\rangle \leq a. \tag{5.78}$$

The optimisation respects a linear combination of the photon numbers as an upper bound for the usable channel power.

Starting with the fact that the function is growing monotonously, the optimal photon number distribution has to be found on that bound. Thus, we substitute

$$I(\langle n_S\rangle, \langle \hat{n}_\gamma\rangle) = I(\langle n_S\rangle, a - \langle n_S\rangle) \tag{5.79}$$

for the optimisation. Next I is differentiated with respect to $\langle n_S\rangle$ to locate the maximum of $I(\langle n_S\rangle, a - \langle n_S\rangle)$, yielding

$$\langle n_S\rangle = \frac{a(1+a)}{1+2a} \tag{5.80a}$$

and, repeating the procedure for $\langle \hat{n}_\gamma\rangle$,

$$\langle \hat{n}_\gamma\rangle = \frac{a^2}{1+2a} \tag{5.80b}$$

for the optimal balance under the linear constraint (5.78). The results are shown in figure 5.10.

Two-mode squeezing, amplification, Bell-type detection

Following the same approach as above, the optimal balance can be calculated for the case on page 118. The assumption is that the modulation is distributed equally in both quadratures; otherwise the mutual information would not reach the same level as argued in the referenced section. The balance under a linear constraint is given by

$$\langle n_S\rangle = \frac{a(2+a)}{2+2a} \tag{5.81a}$$

and, conversely for $\langle \hat{n}_\gamma\rangle$,

$$\langle \hat{n}_\gamma\rangle = \frac{a^2}{2+2a} \tag{5.81b}$$

Two-mode squeezing, classically correlated inputs, amplification, Bell-type detection

Finally the case on page 123 is checked for its optimal distribution of photons. It is found that the same condition as in equation (5.81).

5.4.5 Visual comparison

Figures 5.11 and 5.12 summarise the preceding results. The interpretation of the index notation is repeated in table 5.1.

5.5 Conclusion

Our study on phase insensitive quantum amplifiers in Gaussian channels revealed two particular features:

First, when using a two dimensional signal modulation in one input mode and, as depicted in figure 5.6, a heterodyne detection after the amplifier, the additional noise due to the amplification

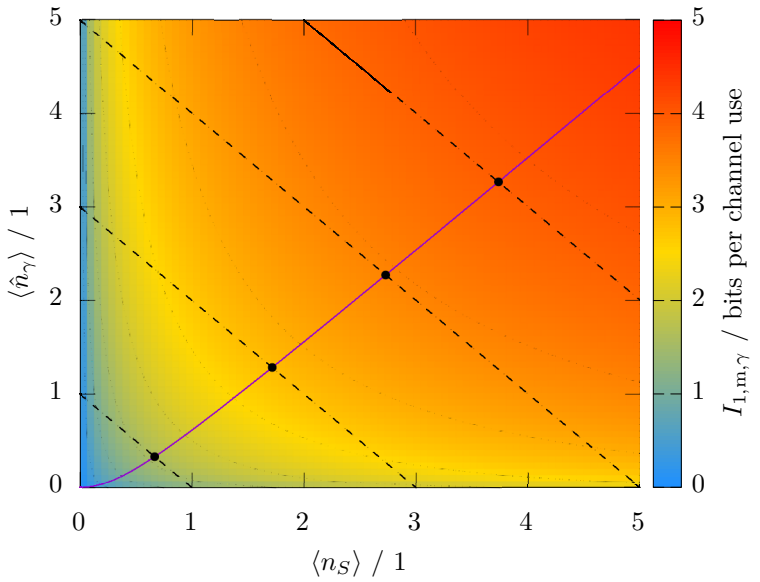

Figure 5.10: Mutual information of a Gaussian channel with a single-mode squeezed state, in the absence of losses, and homodyne detection. The axes represent the photons invested into squeezing and signal modulation. Dashed lines represent the boundary condition (5.78) under which the optimal balance has been computed. Four examples of different total photon number bounds are shown. The solid line corresponds to the optimal balance found by the optimisation.

Notation	Case
$I_{1,\mathrm{m},g}$	1D modulation, homodyne detection, gain.
$I_{1,\mathrm{m},\gamma}$	1D modulation, homodyne detection, single-mode squeezing.
$I_{2,\mathrm{t},\eta}$	2D modulation, heterodyne detection, losses.
$I_{2,\mathrm{b},g,\gamma}$	2D modulation, Bell-type detection, gain, two-mode squeezing.
$I_{2,\mathrm{b},g,\mathrm{cc}}$	2D modulation, Bell-type detection, gain, classical correlations.
$I_{2,\mathrm{b},g,\mathrm{cc},\gamma}$	Combination of $I_{2,\mathrm{b},g,\gamma}$ and $I_{2,\mathrm{b},g,\mathrm{cc}}$.

Table 5.1: Examples of the notation abbreviating the different cases treated in this chapter.

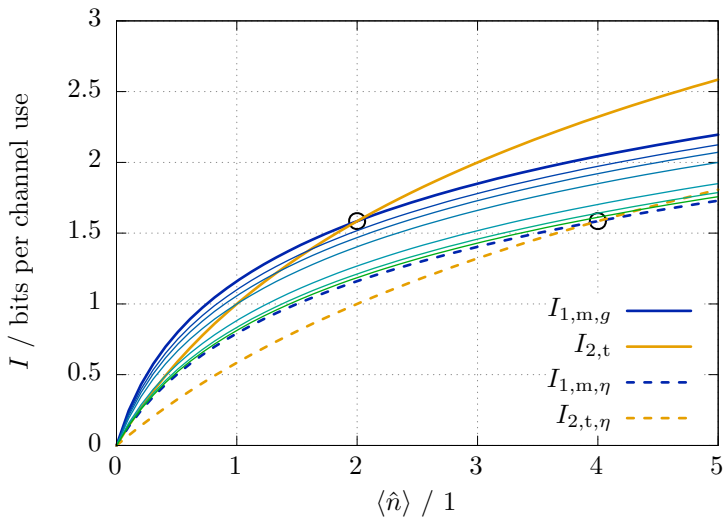

Figure 5.11: A comparison of the mutual information for a 1D modulation with homodyne-, and a 2D modulation scheme with heterodyne detection. Blue to green coloured lines represent homodyne-, orange symbolises heterodyne detection. Dashed lines represent a lossy-channel model, with $\eta = 50\,\%$. The higher the gain setting, the stronger the shift to a green colour for $I_{1,\mathrm{m},g}$, reaching its maximum at $g = 12$. $I_{2,\mathrm{t},g}$ is omitted as it equals $I_{2,\mathrm{m}}$ (cf. equation (5.47).) In general, the 2D modulation wins for a larger number of photons. A circle labels the point when both schemes perform equally.

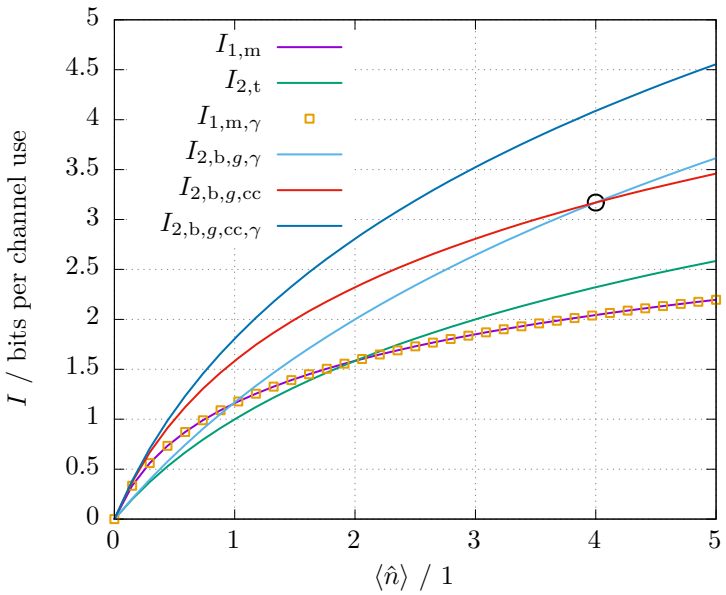

Figure 5.12: Additional comparison of the mutual information for given cases. Cases $I_{1,\mathrm{m}}$ and $I_{2,\mathrm{t}}$ are equal to figure 5.11 and shown again as a benchmark. For cases that involve squeezing, the optimal distribution of $\langle\hat{n}_\gamma\rangle$ and $\langle n_S\rangle$ is used. Taking into account both resources, the single-mode squeezing case $I_{1,\mathrm{m},\gamma}$ performs equal to the coherent state scheme, which was found in the context of channel capacity by Takeoka and Guha [265]. The circle denotes the point when the use of a two-mode squeezer instead of classical correlations is advantageous. Having up to four photons available, using only classical correlations is preferable. Finally, the case of combining classical and quantum correlations is shown and yields the best mutual information.

process has no effect on the mutual information. This effect can be appreciated by considering the effect of the two dimensional modulation in combination with the phase insensitivity: The noise caused by the amplification is distributed equally over the state, such that the two dimensional signal modulation "suffers" shares the noise contribution. Next, the beam splitter in the heterodyne detection causes a halving of the signal, but that equally applies to the amplified noise. In total, the noise grows as fast as the signal, such that g cancels in equation (5.47).

Comparing this case with a one dimensional signal modulation and homodyne detection, the latter is outperformed latest, i.e. for $g = 0$ at $\langle\hat{n}\rangle = 2$, which can also be observed in figure 5.11. From an experimental point of view, the implementation, at least on a small scale, of a two dimensional modulation and heterodyne detection is rather quick to realise: A second modulator and a second detector is necessary. However, the fact that this finding has not been applied before might indicate conceptual difficulties that need to be ruled out first.

Second, a classically correlated signal generation can yield a higher mutual information than a two-mode squeezed input, i.e. a state exhibiting quantum correlations. Depicted in figure 5.12, the total photon number in the channel has to be larger than four to arrive at a better performance using a two-mode squeezer. Given this four-photon bound, the finding means an experimental advantage as the resources for a two-mode squeezer are considerably higher than for a classical correlation, where the signal modulators have to be only electronically connected. An application for our finding are protocols where low photon numbers are usually encountered, such as a teleportation protocol combing discrete and continuous variable regimes [9]. Even though we restricted this analysis to phase insensitive amplifiers, it is important to note that the mutual information of the classically correlated case can be also achieved with two phase sensitive amplifiers: This type of amplifier acts like a squeezer and does not add noise to an input state [54, 57], if the input signal is in the appropriate field quadrature. This equality can also be understood by figure 5.9: The output modes are squeezed only along the quadrature axes, thereby mimicking two individual single-mode squeezers. An experimental verification of this

result can be attempted by using a two-mode squeezer[2] as the amplifier, as here both input and output modes are accessible easily.

[2]Such a device can be realised via spontaneous parametric down-conversion of type II. Instead of using a crystal made for a type I down-conversion, where the emitted photons share the same polarisation, a type II down-conversion process generates photon pairs with perpendicular polarisations. These polarisations represent the two output modes [8, 294].

A | Appendix

A.1 Laser beam profiler

Regardless of the actual purpose, the most crucial task of an optics experiment is the beam alignment. Next to the direction, the transversal profile of the laser beam is the key to, amongst others, high coupling efficiencies into optical fibres and high visibilities in interferograms. As commercial beam profilers are rather expensive and standard charge-coupled device (CCD) cameras were available in the group, a program has been written to meet the demands of a fast and user-friendly beam profiler. The source code was published online under the GNU General Public License 3 [245].

This section outlines the program's functionality and features.

Design

The beam profiling software is an assembly of six parts:

1. A nonlinear fit routine. It is not restricted to a profiling task, but optimised by tuning the routine's parameters. By combining a local [190] and a global [203] optimisation method, the confidence in the result is improved over one-way approaches[1]. At the end of the routine, the Hessian of the function under minimisation is inverted to estimate the standard deviation of the parameters. The model applied here assumes that each data point (i.e. pixel) contributes equally to the uncertainty of the fit, and that these measurement uncertainties, governed by a Gaussian model, are furthermore independent of each other. Under these assumptions, the estimated standard deviation reads [225]

$$\delta a_j = \underbrace{\sqrt{\frac{f(x, \boldsymbol{a}_{\text{fit}})}{P-N}}}_{s} \sqrt{|C_{j,j}|}\frac{1}{a_j}. \tag{A.1}$$

   The value f is the minimum value, i.e. the minimum sum of squares. N is the number of parameters that are to be fitted. $|C_{j,j}|$ is an absolute entry in the inverted Hessian. a_j is the parameter for which the error is to be estimated, with P being the total number of data points. The denominator of $P-N$ takes into account that f is a sum of P residuals. N accounts approximately for the fact that N parameters are fit to the data. Omitting the $-N$ means underestimating s. A typical output of the fit routine can be seen in figure A.6 on page 135

2. The next part is a 3D visualisation using OpenGL [216] as an interface to the graphics card. To support various operating systems, freeglut [105] is used as an additional interface between the actual program and OpenGL. As the visualisation is written entirely for the purpose of handling 3D data, this approach is both very fast and portable. P o r t a b l e, as the visualisation comes without making use of other libraries and non-ISO C++ calls. Four (non)typical recorded beam shapes are presented in figure A.8.

3. A class that deals with managing the two former parts and estimating the beam parameters when a new image is acquired. This class can be seen as the backbone of the software and makes use of OpenMP [217], OpenCV [215] and the C++11 thread model. Figure A.1 illustrates the threads and their communication channels. Exploiting the speed of a compiled language, a live beam profiling along image manipulation and thread handling is

[1] During my Bachelor thesis at the Max Planck Institute for gravitational physics in Hannover, PD Dr. Gerhard Heinzel introduced me into the art of fitting. The fit routines used in this program are a progression of what he showed me during my stay.

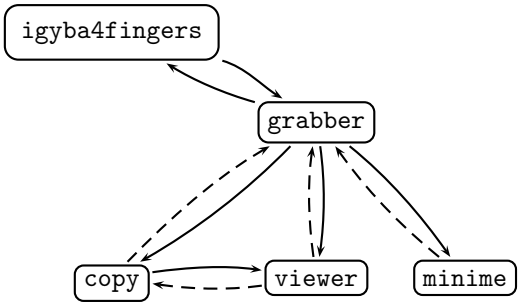

Figure A.1: An overview of the threads used in the software. The main thread `igyba4fingers` handles the GUI and the communication between the `grabber` thread, which main purpose is the communication to the hardware. `grabber` also sends information to the GUI, e.g. hardware statistics. Three threads process the data received by `grabber`: `minime` is called when the user decides to do start a nonlinear fit routine to estimate the beam parameters. `viewer` visualises the data via an OpenGL interface. Finally, the `copy` thread takes image data from `grabber` and pushes it into the memory of `viewer`. `copy` thus acts as a buffer between the visualisation and frame grabbing thread, such that both `grabber` and `viewer` don't have to wait for each other. Dashed lines in the communication diagram depict channels which only communicate signal states, e.g. to signal that a certain process has finished.

realised by this class. At a resolution of 1280×1024 pixel, five images per second can be analysed and displayed on a standard office PC. By selecting an area of interest, this rate can be increased easily.

4. A camera handler. At the time of writing, only a class for *Thorlabs* cameras was written. However, other camera models can be included easily, as the class structure can be inherited by other hardware.

5. A graphical user interface (GUI). wxWidgets [103] was chosen as the interface, as it supports many operating system, is lightweight and, compared to some other GUIs, fully open source. Figure A.7 on page 136 presents one panel of the GUI.

Introduction to the physics of beam profiling

The purpose of this introduction is to give a coherent picture of the program, not a full treatment of laser beam profiles. Figure A.2 depicts and summarises all parameters and the propagation of a Gaussian laser beam. More information about the theory of Gaussian beams can be found in a number of excellent books [133, 255, 294].

The starting point is a multivariate normal distribution, as it is the most general form to describe a Gaussian laser beam. Physically, this means that the beam's wavefront is, in general, elliptical. Hermite- or Laguerre Gaussian modes of such a multivariate beam have been studied theoretically [49], but due to the increase of parameters they are more complex to handle.

Multivariate normal distribution formalism

The most concise notation of the model reads

$$f(\boldsymbol{r}) = \frac{1}{\sqrt{(2\pi)^2 \det \Sigma}} \exp\left(-\frac{1}{2}(\boldsymbol{r}-\boldsymbol{\mu})^{\mathrm{T}} \cdot \Sigma^{-1} \cdot (\boldsymbol{r}-\boldsymbol{\mu})\right), \tag{A.2}$$

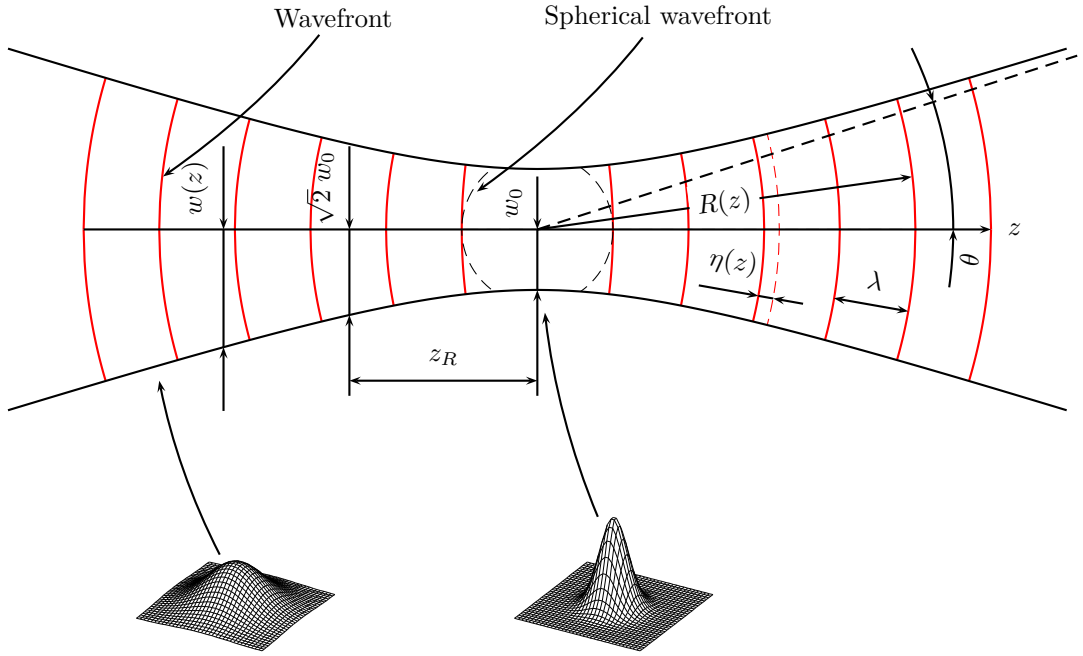

Figure A.2: A model of the propagation of a Gaussian laser beam. The propagation is calculated for a wavelength of $\lambda = 809\,\mathrm{nm}$ and a waist of $0.8\,\mathrm{mm}$. The radius $w(z)$ of the beam is given at a drop of the intensity by $\mathrm{e}^{-2} \approx 86.5\,\%$. w_0 denotes the beam waist. The Rayleigh range $z_R = \pi w_0^2/\lambda$ is the position where the waist is widened by a factor of $\sqrt{2}$. $R(z)$ is the radius of curvature of the beam's wavefront. An additional phase shift is due to focussing the beam and called the Gouy phase, here denoted as $\eta(z)$. A dashed line visualises what the effect of this phase shift is. The far field angle θ is measured with respect to the radius (and not the full opening angle). The beam radius at some position z is fixed by knowing the Rayleigh range z_R and the beam waist w_0. Along the direction of propagation, the evolution reads $w(z) = w_0\sqrt{1 + (z/z_R)^2}$. The propagation length is $\pm 6.5\,\mathrm{m}$.

where Σ is a real symmetric 2×2 positive-definite matrix – the covariance matrix –, $\boldsymbol{\mu}$ is a real valued two dimensional vector, called the centroid or first moment, and $\boldsymbol{r}$ is the point where the distribution is to be evaluated. The power of two in the factor of 2π comes from the dimensionality of our problem. To extract the describing parameters of the distribution, two formulas have to be solved:

1. Calculate the first moment to get $\boldsymbol{\mu}$. Letting $\boldsymbol{r}$ be parametrised by x, y, we can write

$$\mu_i = \frac{\iint i f(\boldsymbol{r}) \, \mathrm{d}x \, \mathrm{d}y}{\iint f(\boldsymbol{r}) \, \mathrm{d}x \, \mathrm{d}y} \tag{A.3}$$

   for the centroid $\boldsymbol{\mu}$ along the $i \in \{x, y\}$ direction. The norm has to be calculated for this expression and should be stored for the next step when working it out numerically.

2. Compute the second moment to retrieve the covariance matrix Σ. The expression

$$\sigma_{ij} = \frac{\iint (i - \mu_i)(j - \mu_j) f(\boldsymbol{r}) \, \mathrm{d}x \, \mathrm{d}y}{\iint f(\boldsymbol{r}) \, \mathrm{d}x \, \mathrm{d}y} \tag{A.4}$$

   results in three scalars when evaluating it for the different combinations of $i, j \in \{x, y\}$. The diagonal entries satisfy $\sigma_{ii} \geq 0$, while $\sigma_{xy} < \pm\sqrt{\sigma_{xx}\sigma_{yy}}$.

Expression (A.2) almost holds for the amplitude of a Gaussian laser beam. The difference is that the variance of a Gaussian beam with a radius of w is $w^2/2$. If it would follow the definition of a 'normal' normal distribution, it had read simply w^2. As we are concerned about the intensity, an additional scaling factor has to be taken into account, leaving us with a variance of $w^2/4$.

The impact of the rescaling on the normalisation factor in equation (A.2) is easy to remember: The factor of 2 in the denominator is lifted to the numerator.

These scaling factors in combination are found to be a source of confusion, but I regard the explicit comparison to a multivariate normal distribution as an appropriate approach for a coherent description.

Example of an elliptical Gaussian beam

As a simple example, a specific expression of equation (A.2) – applied to the Gaussian beam formalism – might read

$$f(x, y) = \frac{2}{\pi w_x w_y} \exp\Big(-2\Big((x/w_x)^2 + (y/w_y)^2\Big)\Big) \tag{A.5}$$

with w_i denoting the beam radius in the direction of i. In this example, we have

$$\boldsymbol{\mu} = \begin{pmatrix} 0 \\ 0 \end{pmatrix}, \tag{A.6a}$$

$$\Sigma = \begin{pmatrix} \sigma_{xx} & \sigma_{xy} \\ \sigma_{xy} & \sigma_{yy} \end{pmatrix} = \begin{pmatrix} w_x^2/4 & 0 \\ 0 & w_y^2/4 \end{pmatrix}. \tag{A.6b}$$

Making it explicit, the results from substituting expression (A.5) in equation (A.4) thus have to be multiplied by 4 to get the square of the respective beam radius.

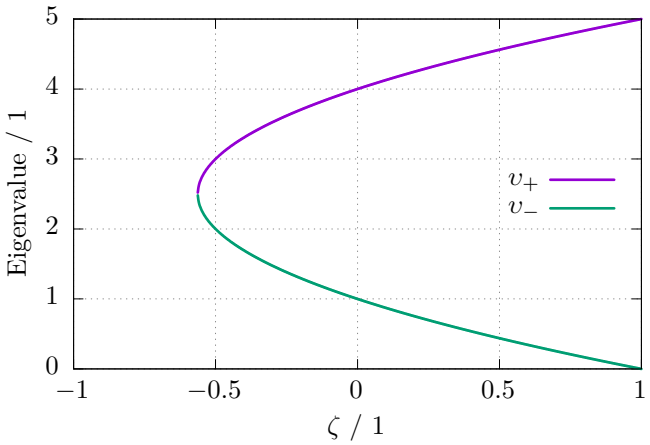

Figure A.3: The value set of $\upsilon_\pm$ for $\sigma_{xx} = 1, \sigma_{yy} = 4$ under variation of the correlation, defined in equation (A.10). In general, $\upsilon_\pm > 0$, as Σ is positive-definite, also leading to $|\zeta| < 1$.

Adding rotation to the beam

When adding a rotation of the ellipse circumscribing the beam, things get a bit more interesting. The result is that the covariance matrix won't be diagonal any longer. By evaluating the second moment, we arrive at measures that tell about the beam radius along the axes of – and in 45° to – the g l o b a l coordinate system. The global system is in this case given by the orientation of the camera used to record the beam. Using it as a reference might be fine, but it could be of interest to know about the minor and major axes of the ellipse, plus the angle of rotation of the ellipse.

In the source code and herein, I refer to the minor and major axes as the m a i n axes in contrast to the aforementioned global axes. So to get the measures along the main axes, either an explicit rotation of the ellipse is computed or the eigenvalues $\upsilon_\pm$ of Σ are calculated. The latter approach is less expensive and thus pursued. Refer to figure A.3 for an example of their value set. Explicitly evaluating the eigenvalues of

$$\Sigma = \begin{pmatrix} \sigma_{xx} & \sigma_{xy} \\ \sigma_{xy} & \sigma_{yy} \end{pmatrix} \tag{A.7}$$

yields

$$\upsilon_\pm = \frac{1}{2}\left(\sigma_{xx} + \sigma_{yy} \pm \sqrt{\sigma_{xx}^2 + 4\sigma_{xy}^2 - 2\sigma_{xx}\sigma_{yy} + \sigma_{yy}^2}\right), \tag{A.8}$$

visualised in figure A.4. If, instead of the covariance matrix, the beam radii w_x and w_y are known at the point of evaluating the eigenvalues, we just have to transform them according to:

$$\sigma_{xx} = w_x^2/4 \tag{A.9a}$$
$$\sigma_{yy} = w_y^2/4 \tag{A.9b}$$
$$\sigma_{xy} = w_{xy}/4 = w_x w_y \zeta/4. \tag{A.9c}$$

Here, the correlation $\zeta \in \mathbb{R}, -1 < \zeta < 1$ was introduced. It has to be calculated when evaluating the second moment as it is defined as

$$\zeta = \frac{\sigma_{xy}}{\sqrt{\sigma_{xx}\sigma_{yy}}}. \tag{A.10}$$

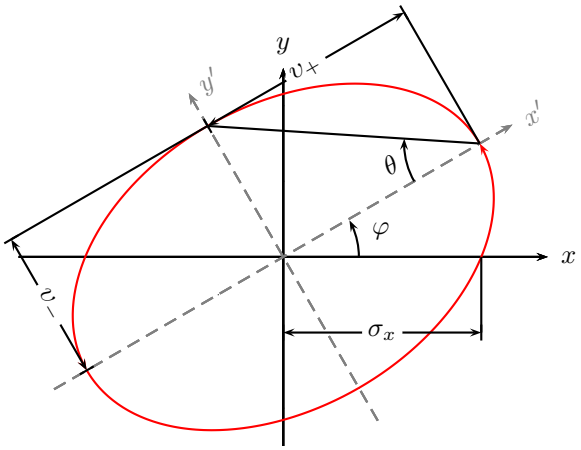

Figure A.4: The characteristic parameters of an ellipse. Axes x, y correspond to what I call the global coordinate system (given by the camera sensor) while x', y' is the main coordinate system, oriented towards the ellipse' major and minor axis.

The advantage of displaying the correlations instead of σ_{xy} is that its interpretation appears to be more intuitive, a bit easier, as it is a normed value. The case $|\zeta| = 1$ corresponds to a infinitely stretched out ellipse and can be used as a sanity check. ζ's sign finally tells about the rotation of the ellipse.

Additional information of the shape

Other values that are convenient to display are

$$\varphi = \frac{1}{2} \arctan\left(\frac{2\sigma_{xy}}{\sigma_{xx} - \sigma_{yy}}\right) \tag{A.11a}$$

$$\theta = \arctan\left(\frac{b'}{a'}\right) \tag{A.11b}$$

where φ is the angle between the main and the global coordinate system, as depicted in figure A.4. To express the eccentricity of the ellipse, θ might be used. In terms of readability, I prefer to use

$$\theta \stackrel{\text{def}}{=} \begin{cases} \sqrt{1 - \frac{\upsilon_+}{\upsilon_-}} & \text{if } \upsilon_- > \upsilon_+ \\ \sqrt{1 - \frac{\upsilon_-}{\upsilon_+}} & \text{else} \end{cases} \tag{A.12}$$

as a figure of the eccentricity. Figure A.5 highlights the reasoning: It vanishes when the eigenvalues are equal.

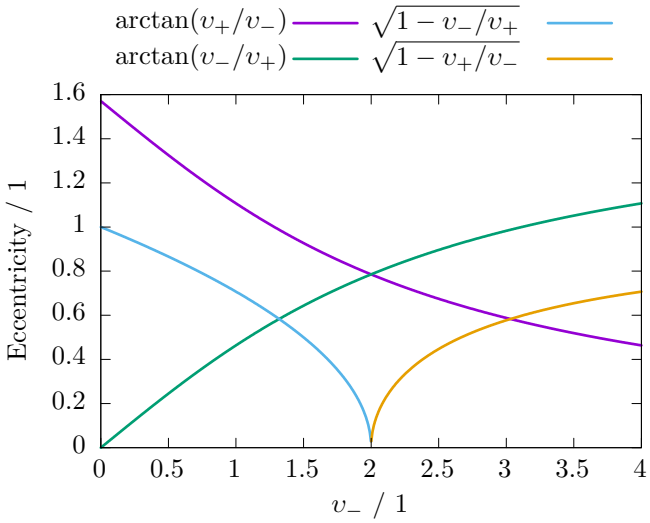

Figure A.5: Comparing the definitions of the eccentricity. Variable names are in accordance to figure A.4. υ_+ is set to 2.

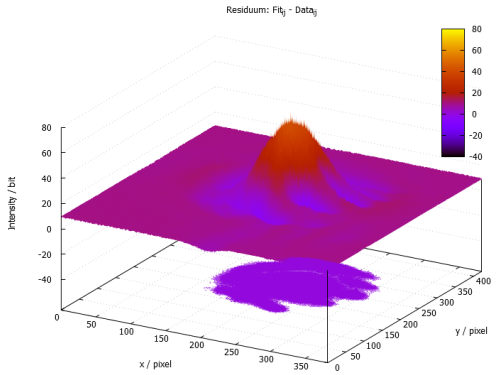

(c) Difference

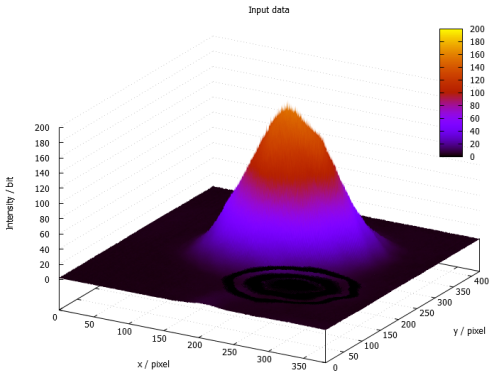

(a) Input

Figure A.6: Plots automatically generated by the fit routine. (a) Recorded beam profile. (b) Fit of equation (A.2) to the recorded profile. (c) Difference between the input and fit model.
Next to the results printed in the heading of the fit result, statistical data is written to a text file. The ripples visible in the difference between the input and the data fit stem from interference effects caused by a cover slide fixed to the sensor chip.

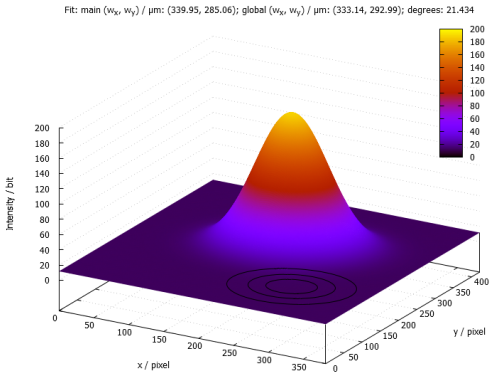

(b) Data fit

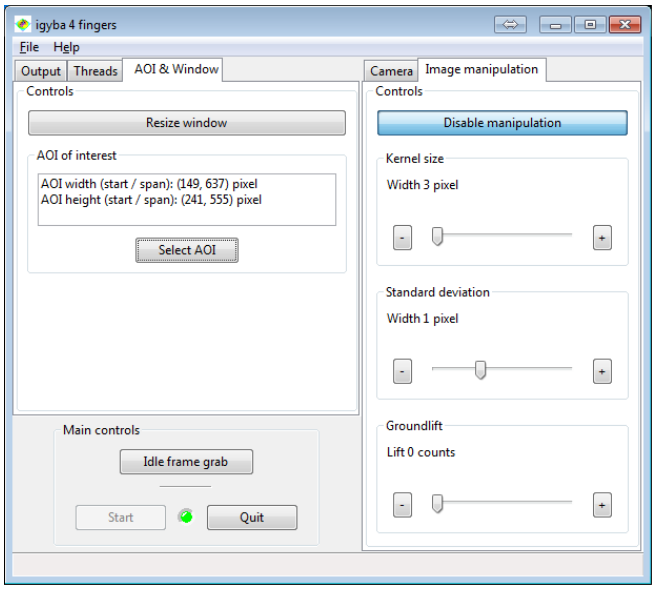

Figure A.7: Part of the graphical user interface of the beam profiler. Shown here is the image manipulation module to smooth the acquired image and correct for noise. On the left, the area of interest can be changed to analyse only a part of the acquired data.

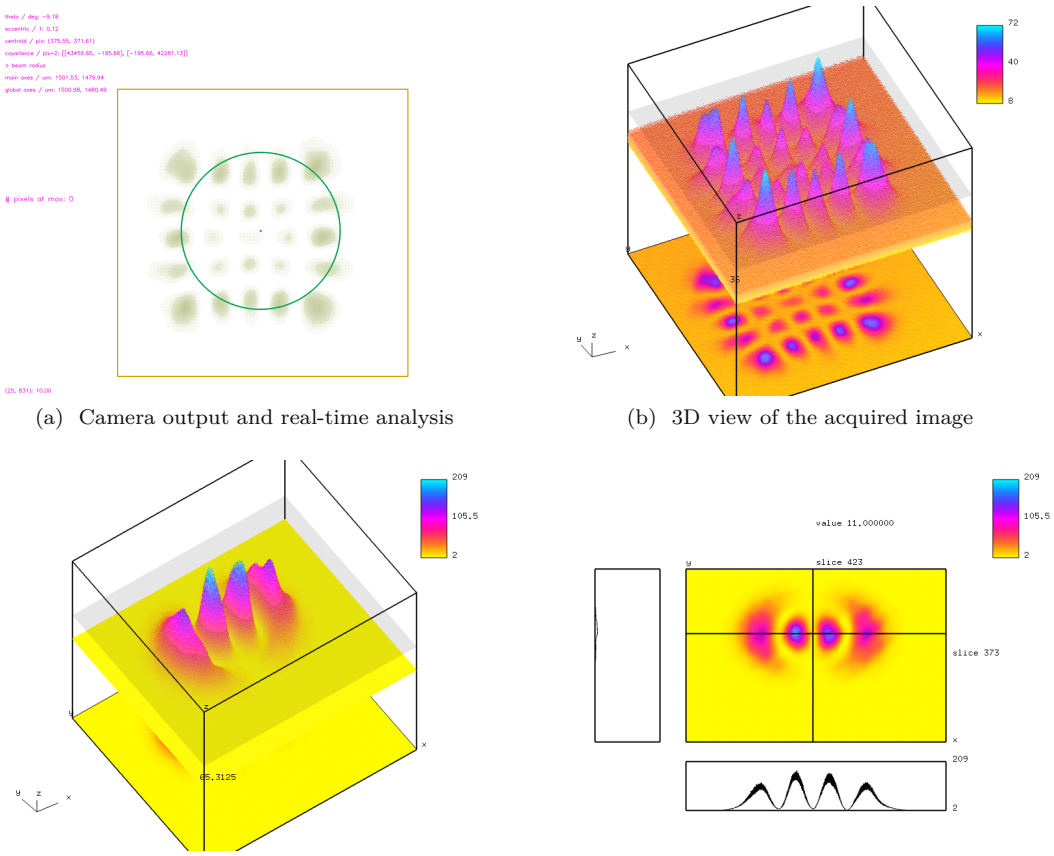

(a) Camera output and real-time analysis

(b) 3D view of the acquired image

(c) 3D view of a Laguerre Gaussian '11' beam

(d) 2D view with cross section

Figure A.8: Different examples of the visualisation capabilities of the beam profiler software. For the purpose of a homogeneous presentation, the images are colour inverted.
Image (a) shows an example of a higher order mode of a mode cleaning cavity. The yellow rectangle is the area of interest selected by the user. A green ellipse represents the real-time analysis of the beam radius, which is, in the case for higher order modes, not particularly meaningful. Figure (b) shows the same data but represented in 3D and in false colours. The view point can be manipulated by the user. Just as the analysis, the 3D view is updated in real time to monitor the dynamics of the beam detected by the camera. Figure (c) shows a similar case, while figure (d) highlights another feature of the visualisation module: The data is shown on a map, and the user can select a point on it to display cross sections.

A.2 Probing transfer functions of closed loop systems

Herein the measurement of open loop transfer functions is derived when the system under investigation can only be operated as a closed loop. For our purpose the best example is an optical cavity locked to a certain transmission or reflection, that is: It is locked to a certain cavity length. The system is defined as to behave linearly around this bias (or lock) point. Mandatory for the presented scheme to work is thus an at least somewhat working control loop; this contrasts the common approach of probing the open loop transfer function b e f o r e operating in a closed loop mode[2]. However, the measurement will enable the characterisation and consequently an optimisation of the system, consisting of a servomechanism, a piezo with a voltage supply and finally a photodetector.

Transfer function

The fundamental equation for modelling systems depicted in figure A.9 is an input-output relation as

$$G = \frac{x_{\text{out}}}{x_{\text{in}}}. \tag{A.13}$$

G is understood as the transfer function, it propagates an input x_{in} to an output x_{out}. The

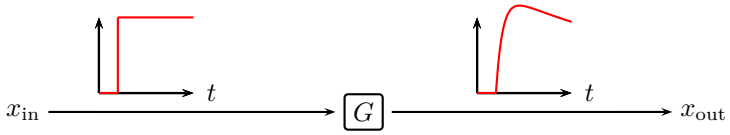

Figure A.9: Scheme of the input-output relation of a transfer function G. The insets represent a typical transient response. The vertical axes might have different dimensions as G's dimension doesn't have to be unity.

space of G is given by the space where the Laplace transform ($\mathscr{L}(x(t)) = \int_0^\infty x(t)\exp(-st)\,\mathrm{d}t$ with $s \in \mathbb{C}$) converges and yields analytic functions [44]. To arrive at the transient description, an inverse Laplace transform has to be performed on G. Before going on, I'd like to note that, even though the mathematical handling of transfer function using the 'Laplace formalism' turns out to be very convenient, it is only applicable when a linear model exists. Nonlinear models have to be either linearised (like it is done for the locked cavity case) or other methods have to be applied. The second assumption is that the system is time invariant, that is the system behaviour doesn't change overnight.

Describing a closed loop system is done by accounting for the different contributions shown in figure A.10, such that

$$\begin{aligned} x_{\text{out}} &= G_1 x_{\text{in}} - G_1 G_2 x_{\text{out}} \\ &= \frac{G_1}{1 + G_1 G_2} x_{\text{in}}. \end{aligned} \tag{A.14}$$

The fraction can be now regarded as the overall transfer function G. In addition, we

[2]Self-oscillation due to positive feedback in closed loop systems can lead to damaging involved components. To prevent from self-oscillation, the system is preferably characterised in an open loop configuration. From this characterisation, all system parameters can be derived and used to set the optimal control parameters [184].

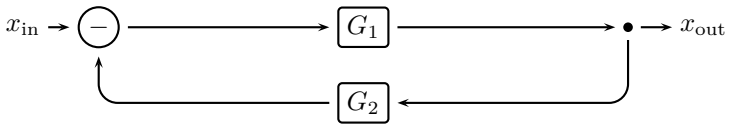

Figure A.10: Block diagram of a system operated as a closed loop. The first node subtracts the respective inputs, giving rise to a negative feedback operation. The dot in front of the output represents a pick-up node.

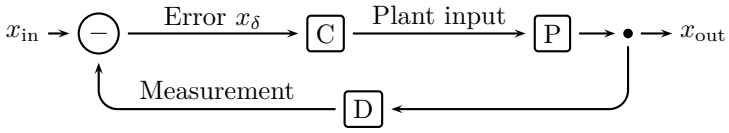

Figure A.11: Extended model of a (negative) feedback loop system. First, a desired value is set by the user, then subtracted from the measured value and subsequently amplified by a controller. The signal is then send to the plant which eventually closes the loop.

- G_1 the forward,
- G_2 the backward,
- G_1G_2 the open loop transfer function G_0.

A bit more realism

From the generic model presented above, a specification is done by identifying the individual transfer functions $G_1, G_2, \ldots$ with certain entities: The controller C, the plant P and the detector D. In between these constituents, a conversion of the dimension is usually implicated, e.g. the detector converts optical power (Watt) to an electrical potential (Volt).

A controller is the device regarded as the one to be tuneable, it is the operator's task to optimise its transfer function to accommodate for stability and speed of the control loop. We commonly refer to it as the servo (short for servomechanism). The detector is the device that picks up the plant's action and sends it back to the controller. If the detector's response is much faster than the plant to a stimulus, one can neglect its transfer function to decrease the complexity of the analysis. Finally, the plant is the part which is to be controlled and so its transfer function is regarded to be constant. Knowing the plant's transfer function is the key for a proper actuation of the system. Figure A.11 comprising the aforementioned elements.

The model is, so far, somewhat ideal as it assumes that the only input into the system is our target value. To account for disturbances, e.g. temperature drifts biasing a certain point in the system, more nodes have to be added to the model. A block diagram of a system with two "disturbance inputs" is shown figure A.12. There's no point in stopping from adding more disturbance along the other links – apart from the convenience of drawing only what's necessary for the following explanations.

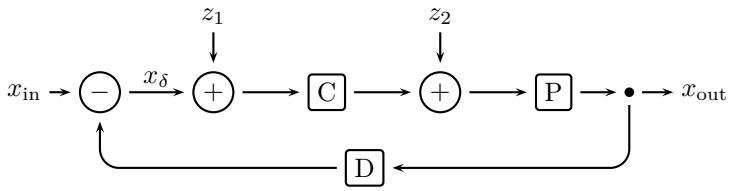

Figure A.12: An extension of the block diagram in figure A.11. Two disturbance variables z_1 and z_2 have been added to it.

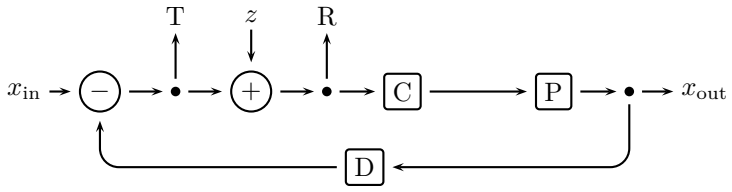

Figure A.13: Block diagram which shows how to probe the open loop transfer function. The pick-up nodes T and R refer to the inputs of a network analyser. Labels might differ, of importance is that the mode is set to display 'T/R'. z is the stimulus from the analyser's function generator assumed to be known.

Transfer functions in closed loop operation

As motivated in the beginning, we apply the definitions to probe the open loop and the plant's transfer function in a closed loop operation.

Open loop transfer function

We start with the open loop measurement. To perform this measurement on a "text-book system", the feedback connection has simply to be broken up. In a system with a bias point such as an optical cavity, we have to mimic this by breaking the system virtually. A scheme which is able to achieve this is given in figure A.13. By using the network analyser's capability of probing two points of a system at a time and displaying the fraction of these points, a given circuit can by virtually broken in two. The analysis of the full circuit is

$$\begin{aligned} x_{\text{out}} &= x_{\text{in}} G_{\text{C}} G_{\text{P}} - x_{\text{out}} \underbrace{G_{\text{C}} G_{\text{P}} G_{\text{D}}}_{G_0} + z G_{\text{C}} G_{\text{P}} \\ \Leftrightarrow x_{\text{out}}(1 + G_0) &= z G_{\text{C}} G_{\text{P}} + x_{\text{in}} G_{\text{C}} G_{\text{P}} \\ \Leftrightarrow x_{\text{out}} &= (z + x_{\text{in}}) \frac{G_{\text{C}} G_{\text{P}}}{1 + G_0} \end{aligned} \tag{A.15}$$

As expected, it carries the structure of equation (A.14). Checking for the pick-up nodes T and R, we find

$$x_{\text{T}} = x_{\text{in}} - z G_0 - x_{\text{out}} G_{\text{D}} \tag{A.16a}$$

$$x_{\text{R}} = x_{\text{in}} + z - x_{\text{out}} G_{\text{D}}. \tag{A.16b}$$

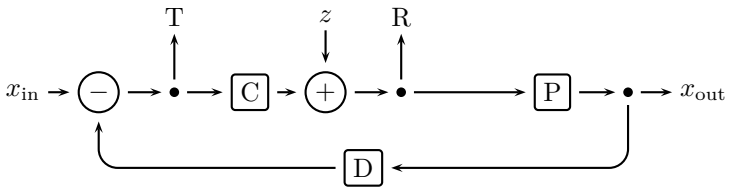

Figure A.14: Block diagram which shows how to measure the plant and detector transfer function.

To single out G_0, the signals have to be subtract from each other. The disturbance z is then cancelled as it is generated by the network analyser.

A network analyser commonly offers an option to display the fraction – instead of the subtraction – of T and R. However, the use of a gain and phase analysis, usually in terms of a Bode plot, will yield to the result since multiplicative complex transfer function are additive in this representation: The amplitudes are additive using logarithmic scales, the phase add naturally.

Plant and detector transfer function

When breaking up the system as shown in figure A.14, one singles out the controller. The pick-up nodes will then read

$$x_{\mathrm{T}} = x_{\mathrm{in}} - zG_{\mathrm{P}}G_{\mathrm{D}} - x_{\mathrm{out}}G_{\mathrm{D}} \tag{A.17a}$$

$$x_{\mathrm{R}} = x_{\mathrm{in}}G_{\mathrm{C}} + z - x_{\mathrm{out}}G_{\mathrm{D}}G_{\mathrm{C}}. \tag{A.17b}$$

Reminding that the probing only works for an already locked system with a fixed bias point, and furthermore a vanishing influence of the detector, the terms involving x_{in} and x_{out} can be neglected, leaving us with the middle term. Then, the argument runs as in the previous probing of G_0.

Application notes

When measuring the transfer function as described, special care should be taken regarding the amplitude of z. Especially the measurement of G_0 requires some attention, as the amplitude can easily drive the plant (i.e. the piezo actuator) out of its bias point.

In section A.3, schematics for the required electronics can be found. The electronics were tested and found to behave linearly in the small signal regime (35 mV at 50 Ω) up to 200 kHz.

Example

To optimise the stability of a mode cleaning cavity or phase shifter locked by a servo, the transfer function of $G_{\mathrm{D}}G_{\mathrm{P}}$, according to figure A.14, should be measured first. An example of such a recording is shown in figure A.15. It was taken for the mode cleaning cavity built for the pump beam of the squeezed state source. As can be seen, the system is stable up to about 6 kHz. Afterwards, several resonances prevent from a stable operation of the cavity. Thus, we can't expect to compensate fluctuations at higher frequencies, but we can however optimise the servo: First, to make sure that the gain of the servo is low at the resonances to prevent from positive feedback (i.e. to provide a high gain margin [184]), and second to have a enough gain at lower frequencies to compensate also weak disturbances.

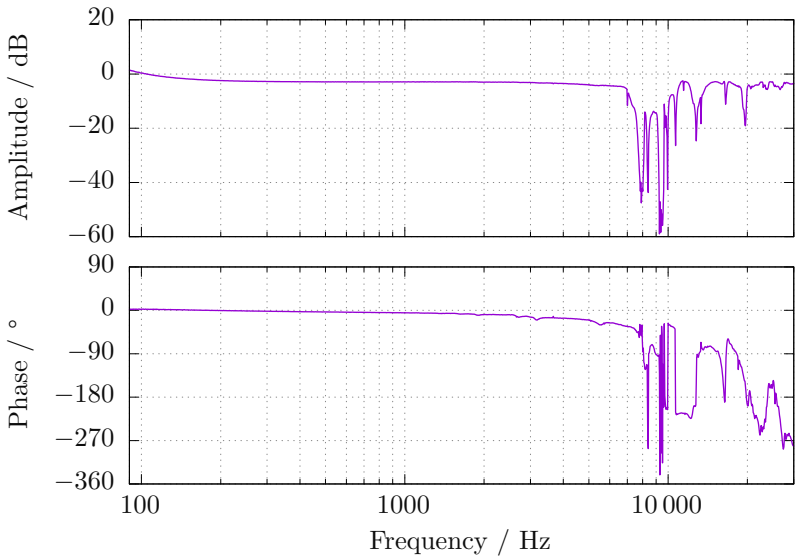

Figure A.15: A plant and detector transfer function recorded according to scheme A.14. The probed system is the mode cleaning cavity shown in figure 3.9 used for the squeezed state experiments. An *Agilent* E5061B electronic network analyser was employed for the measurement.

The open loop transfer function G_0 tells how the servo "handles" the response $G_\mathrm{D}G_\mathrm{P}$. Figure A.16 contains three curves: A first measurement was taken with the standard servo design (refer to section A.3 for a schematic). The gain was set such that the resonance just below 10 kHz is not, or barely, amplified. As the resonance was quite pronounced, the overall gain was required to be set to a rather low level, in turn limiting the servo's bandwidth to 3 kHz. This can be seen from the fact that the amplitude is below 0 dB above 3 kHz. Next, a transfer function was calculated to enhance the performance of the servo. The strong resonance at 10 kHz was compensated with a notch filter. Resonances beyond that frequency were damped with a low-pass filter. An integrator with a corner frequency of 1 kHz in combination with an overall gain of 6 dB provided a high sensitivity at lower frequencies.

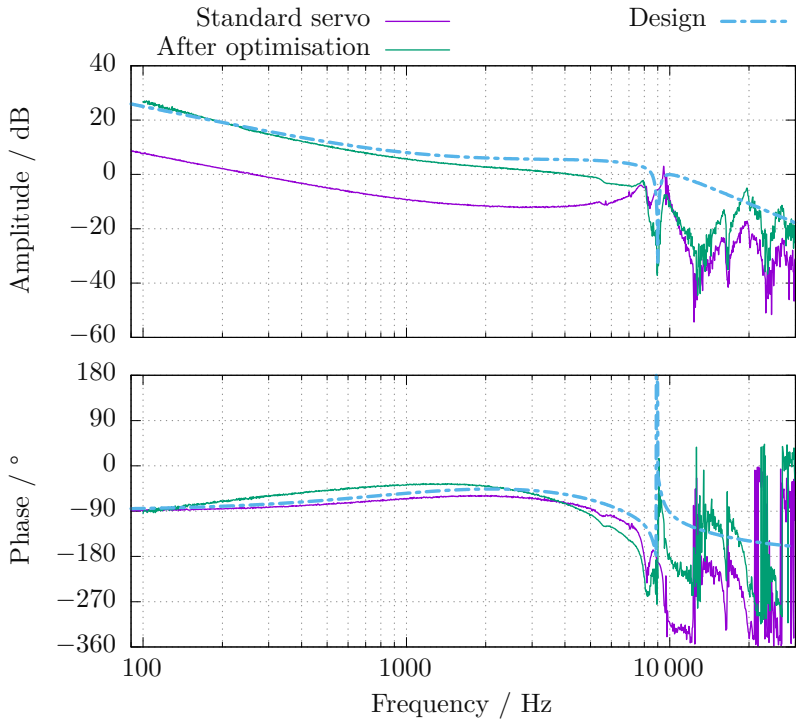

Figure A.16: Open loop transfer function for the same system as in figure A.15. The transfer function before and after optimisation, along with the intended behaviour, is shown. The model parts and parameters are: Integrator frequency 1 kHz, low-pass corner frequency 8 kHz with $\mathcal{Q} = 0.8$, and a notch filter at 9 kHz with $\mathcal{Q} = 800$.

A.3 Electronics

Not only due to special requirements such as noise performance and tunability, but also for practical reasons as size and a global cable management, several electronics have been developed during this thesis. Especially the usage of differential signals [142] showed to decrease the noise in error signals of phase- and cavity locks, such that the required signal power to overcome the noise floor dropped: The required optical signal power to lock the squeezer cavity dropped from 4 mW by more than a factor of 10.

Two schematics, developed together with Tobias Gehring, proved to be helpful for various applications and are appended in the following. The circuits were printed on a surface-mount device (SMD) board. Ruben Grigoryan gave helpful advice for the board design, test boards have been made by Anders Poulsen.

Servomechanism schematic

The first device is a servomechanism (or short servo) to control cavity and phase locks, fitted onto an euro card with SMD components.

- The servo features
  - adjustable gain,
  - two twin-T notch filters,
  - two universal integrator / differentiator circuits with analogue integrated-circuit (IC) switches,
  - one second order Sallen–Key low-pass filter.
- Additional features are
  - a ramp generator with additional trigger output, adjustable frequency and amplitude.
  - an adjustable offset.
  - an inverter with analogue IC switch.
  - a differential (symmetric) in- and output.
  - a single ended output.
  - a monitor output.

The standard procedure is to equip the circuits with standard components and optimise filters and the controllers by measuring transfer functions of the device which is to be controlled. The necessary circuit for probing such transfer functions is shown in the next section A.3.

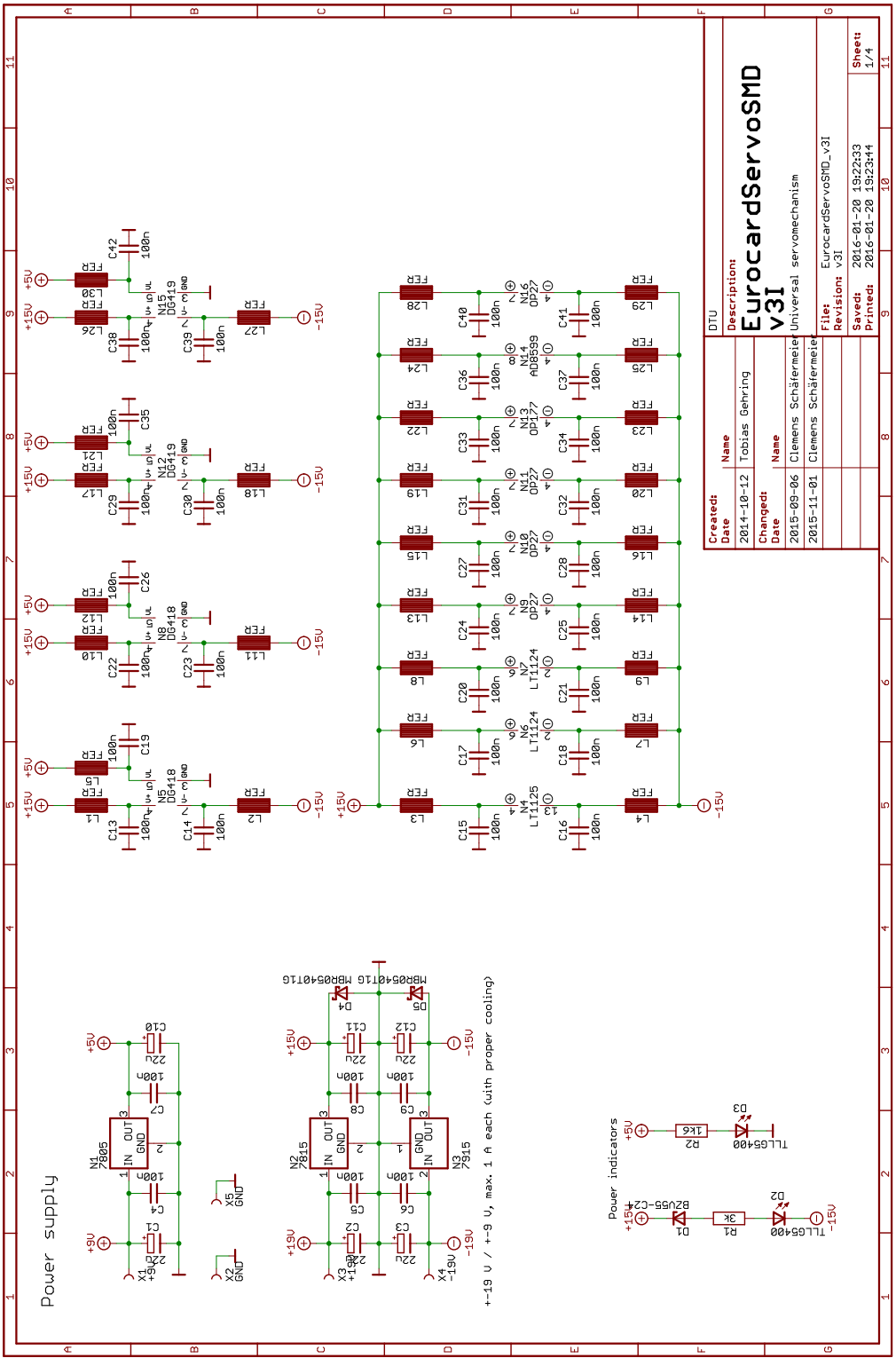
EurocardServoSMD
v3I
Universal servomechanism
DTU
Power supply
+-19 V / +-9 V, max. 1 A each (with proper cooling)
Power indicators

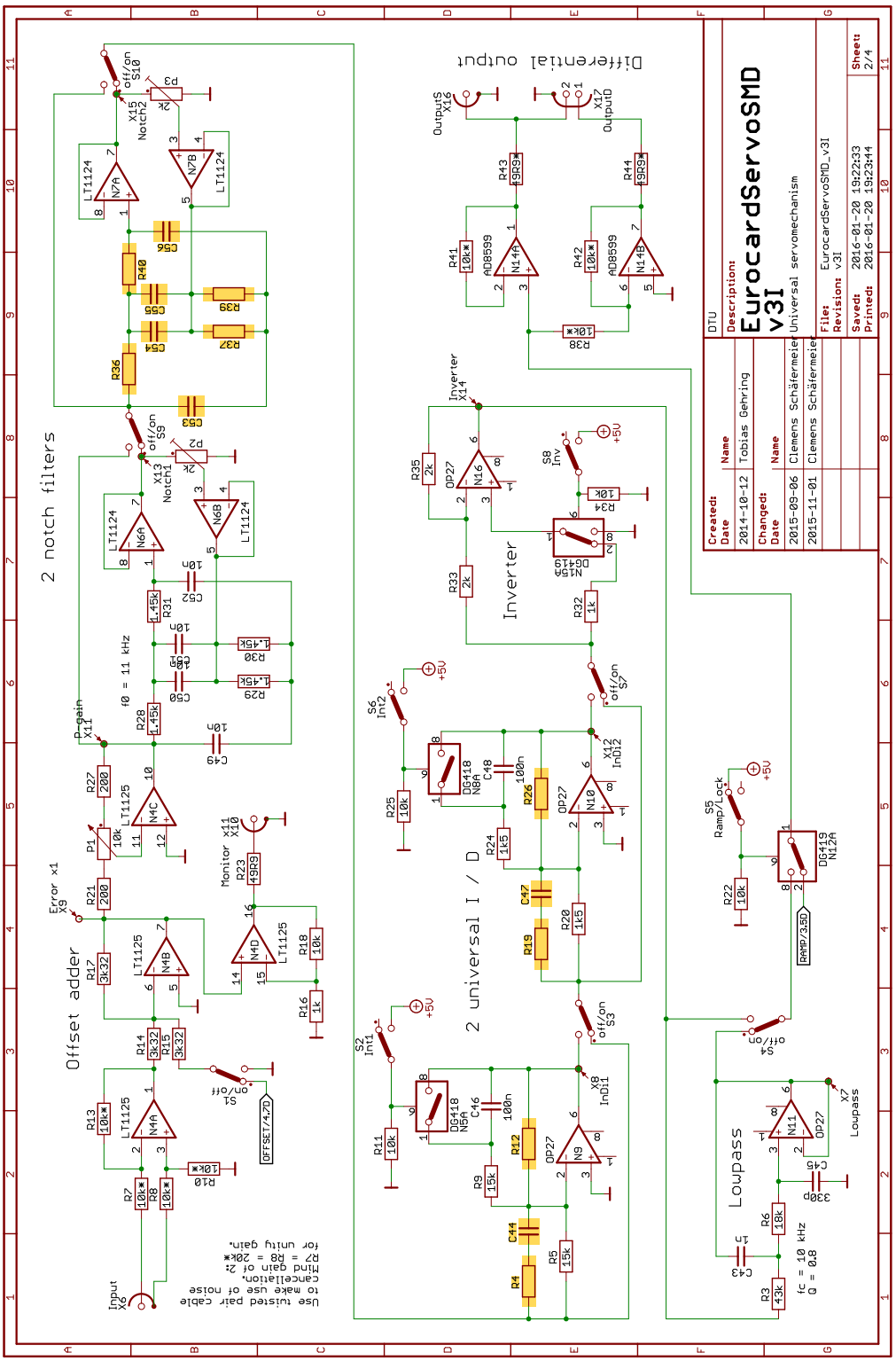
EurocardServoSMD
v3I
Universal servomechanism
DTU
Tobias Gehring
Clemens Schäfermeier
Clemens Schäfermeier
2 notch filters
Offset adder
2 universal I / D
Inverter
Differential output
Loupass
Use twisted pair cable to make use of noise cancellation.
Find gain of 2:
R7 = R8 = 20k*
for unity gain.

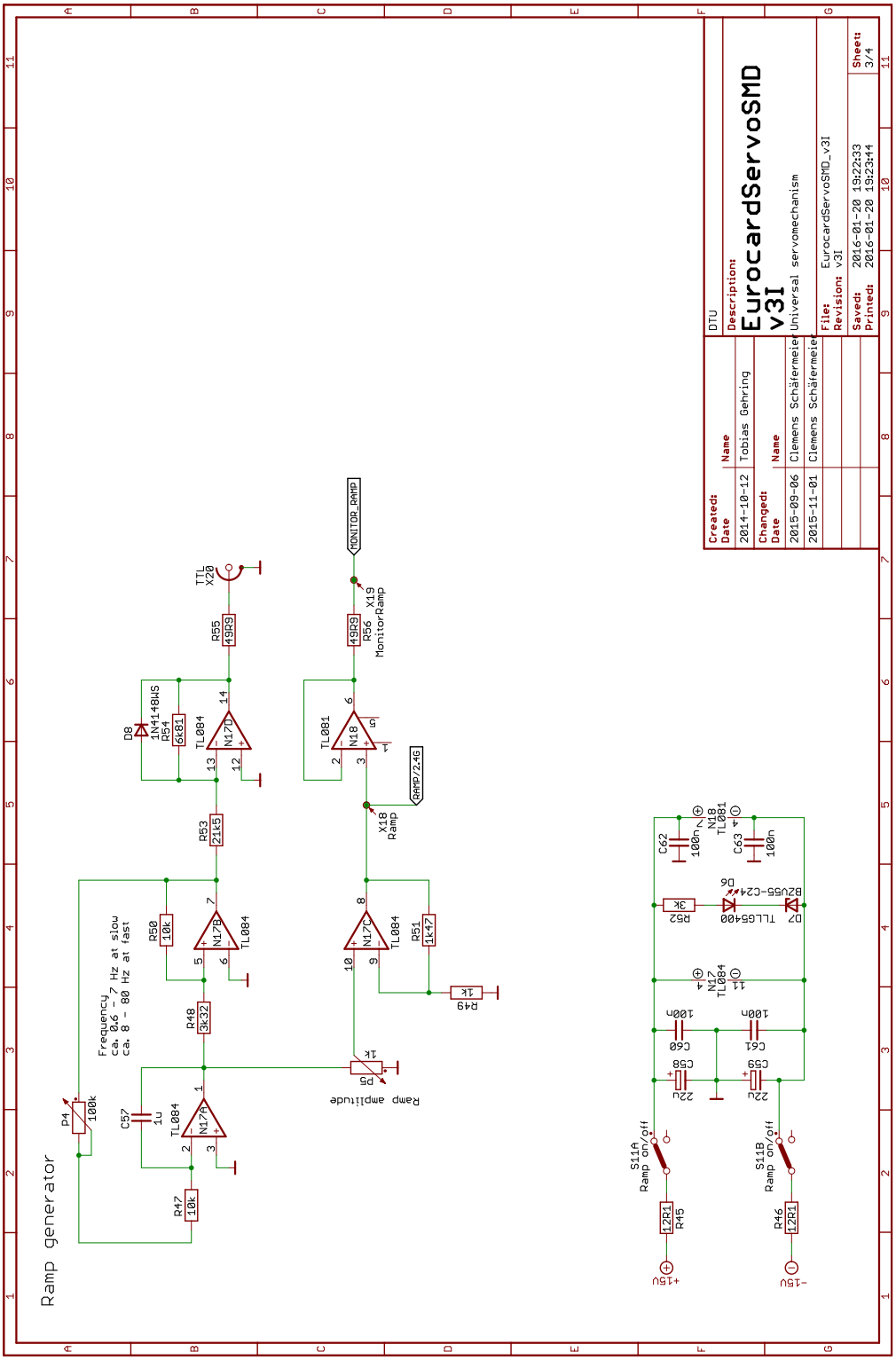
Ramp generator
Frequency
ca. 0.6 - 7 Hz at slow
ca. 8 - 80 Hz at fast
Ramp amplitude
MONITOR_RAMP
RAMP/2.46
EurocardServoSMD
v3I
Universal servomechanism
DTU
Tobias Gehring
Clemens Schäfermeier
Clemens Schäfermeier
EurocardServoSMD_v3I
2014-10-12
2015-09-06
2015-11-01
2016-01-20 19:22:33
2016-01-20 19:23:44
3/4

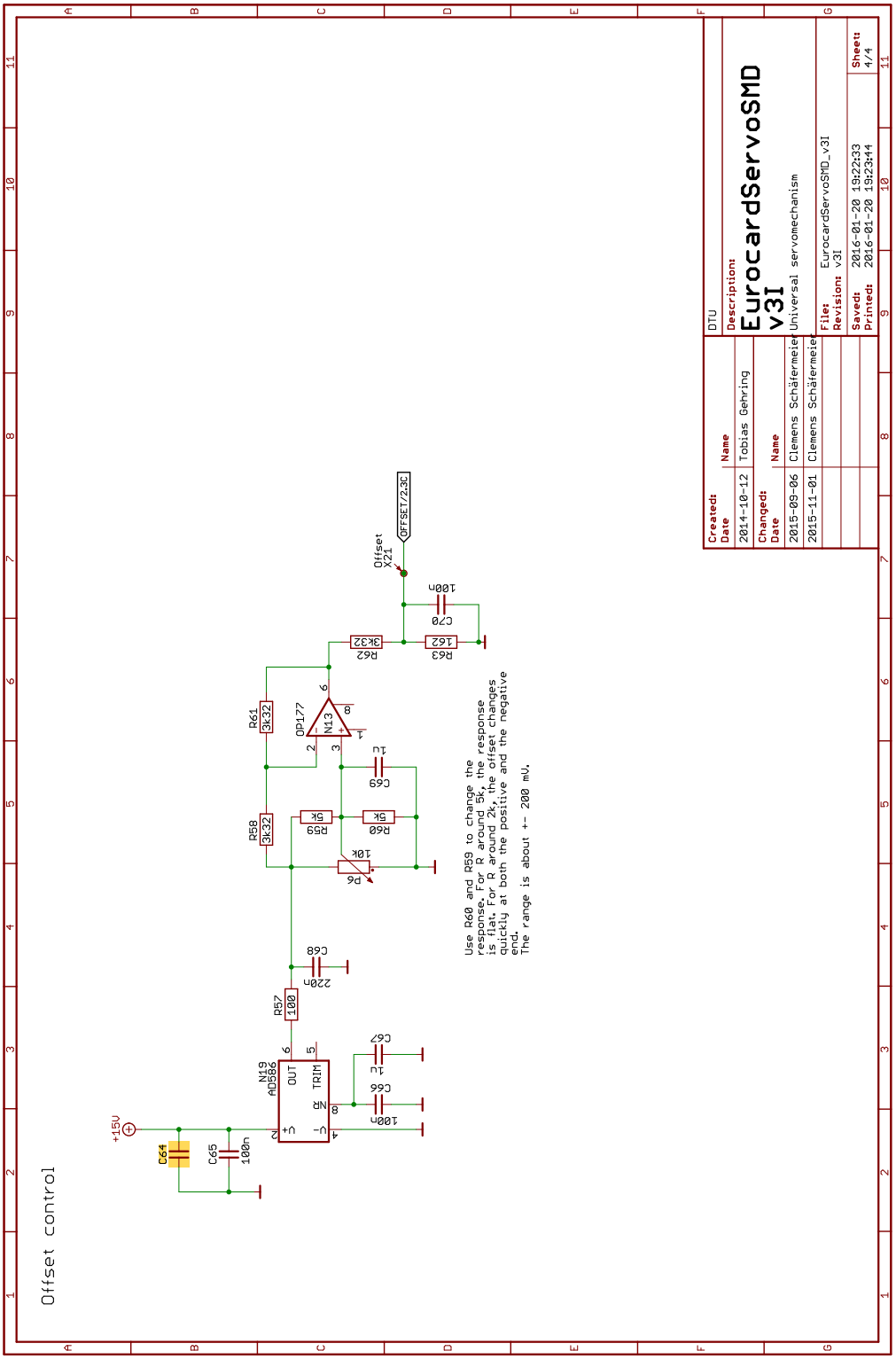
Offset control
+15V
C64
C65
100n
N19
AD586
OUT
TRIM
C66
100n
C67
1u
R57
100
C68
220n
R58
3k32
R59
5k
R60
5k
P6
10k
R61
3k32
OP177
N13
C69
1u
R62
3k32
R63
162
C70
100n
Offset
X21
OFFSET/2.3C
Use R60 and R59 to change the
response. For R around 5k, the response
is flat. For R around 2k, the offset changes
quickly at both the positive and the negative
end.
The range is about +- 200 mV.
DTU
EurocardServoSMD
v3I
Universal servomechanism
EurocardServoSMD_v3I
v3I
Created:
Date
2014-10-12
Name
Tobias Gehring
Changed:
Date
2015-09-06
2015-11-01
Name
Clemens Schäfermeier
Clemens Schäfermeier
File:
Revision:
Saved:
2016-01-20 19:22:33
Printed:
2016-01-20 19:23:44
Sheet:
4/4

Adder schematic

To probe open loop transfer functions of systems which can not be accessed without being actually closed, the system's circuit has to be broken virtually. Details can be found in section A.2. To do so, the following schematic was developed. Two version have been devised, to be usable for both single ended and differential signals. They feature:

- Addition of two signals, whereas
  - one is differential- (symmetric) and one single ended (pseudosymmetric), or,
  - both are single ended. A copy of the schematic is found on page 150 and 151.
- Two buffer outputs.
- A differential- and a single ended output.
- A buffer circuit for a differential input with a differential- and a single ended output.

Printed next is the single ended version.

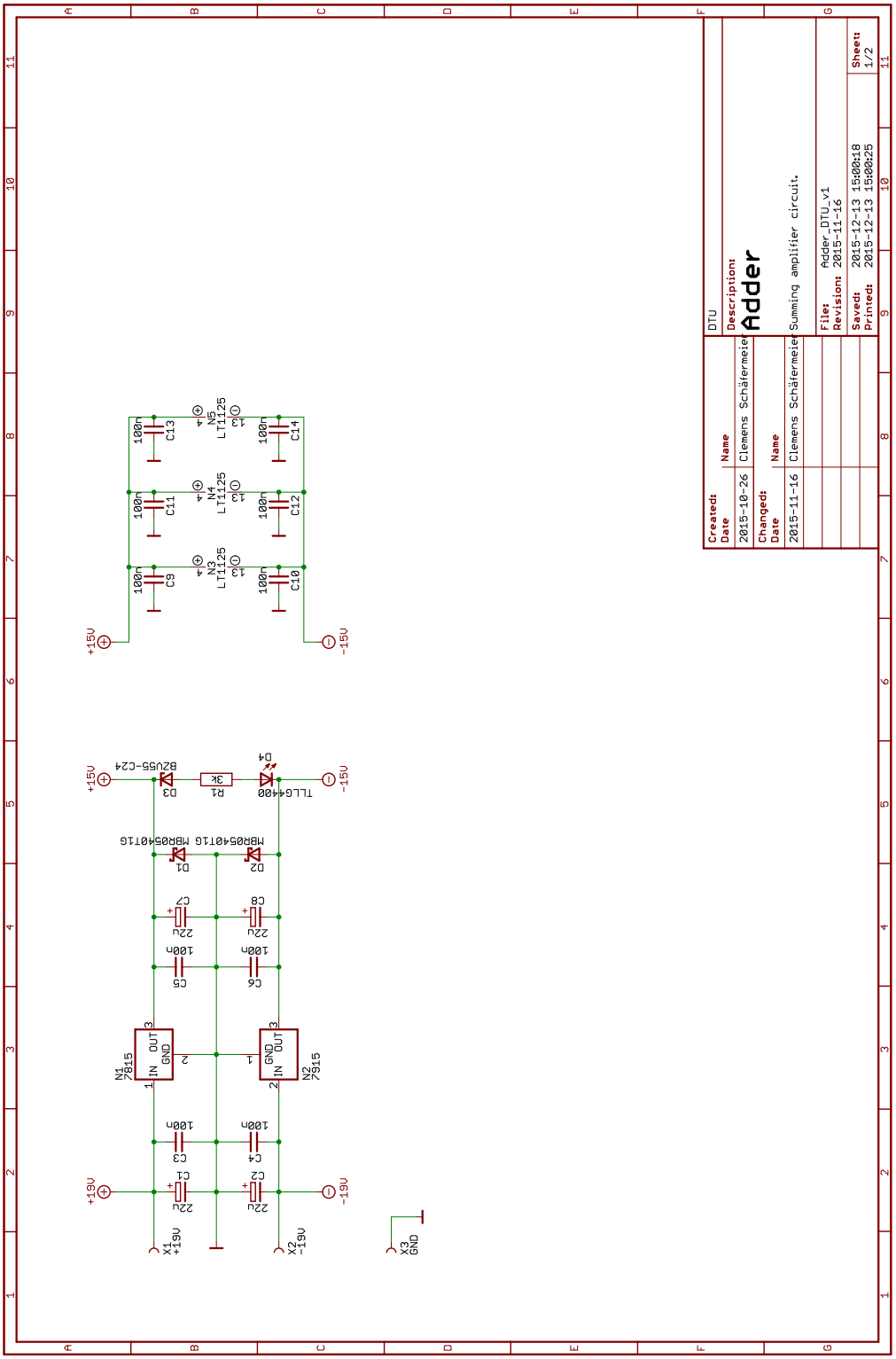
DTU
Adder
Summing amplifier circuit.
Created: Date 2015-10-26 Name Clemens Schätermeier
Changed: Date 2015-11-16 Name Clemens Schätermeier
File: Adder_DTU_v1
Revision: 2015-11-16
Saved: 2015-12-13 15:00:18
Printed: 2015-12-13 15:00:25
Sheet: 1/2
+15V
-15V
+19V
-19V
GND
N1 7815 IN GND OUT
N2 7915 GND IN OUT
N3 LT1125
N4 LT1125
N5 LT1125
C1 22u
C2 22u
C3 100n
C4 100n
C5 100n
C6 100n
C7 22u
C8 22u
C9 100n
C10 100n
C11 100n
C12 100n
C13 100n
C14 100n
D1 MBR0540T1G
D2 MBR0540T1G
D3 BZV55-C24
D4 TLLG4400
R1 3k
X1 +19V
X2 -19V
X3 GND

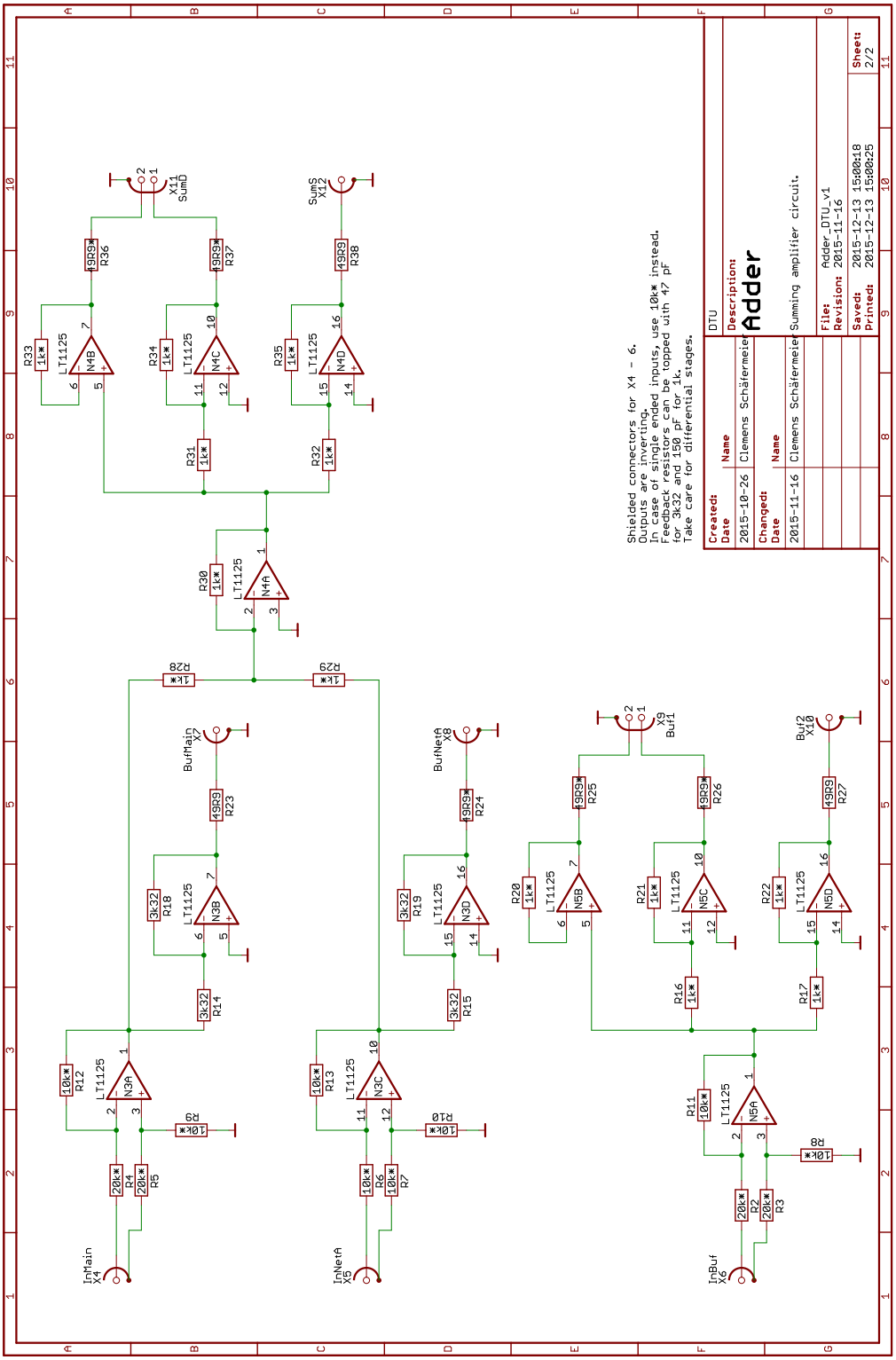
Shielded connectors for X4 - 6.
Outputs are inverting.
In case of single ended inputs, use 10k* instead.
Feedback resistors can be topped with 47 pF
for 3k32 and 150 pF for 1k.
Take care for differential stages.
DTU
Description:
Adder
Summing amplifier circuit.
Created: Date 2015-10-26 Name Clemens Schätermeier
Changed: Date 2015-11-16 Name Clemens Schätermeier
File: Adder_DTU_v1
Revision: 2015-11-16
Saved: 2015-12-13 15:00:18
Printed: 2015-12-13 15:00:25
Sheet: 2/2
X11 Sum0
Sum5 X12
BufMain X7
BufNetA X8
X9 Buf1
Buf2 X10
InMain X4
InNetA X5
InBuf X6
LT1125
R33 1k*
R34 1k*
R35 1k*
R36 49R9*
R37 49R9*
R38 49R9
R31 1k*
R32 1k*
R30 1k*
R28 1k*
R29 1k*
R23 49R9
R24 49R9*
R25 49R9*
R26 49R9*
R27 49R9
R18 3k32
R19 3k32
R14 3k32
R15 3k32
R20 1k*
R21 1k*
R22 1k*
R16 1k*
R17 1k*
R12 10k*
R13 10k*
R11 10k*
R9 10k*
R10 10k*
R8 10k*
R4 20k*
R5 20k*
R6 10k*
R7 10k*
R2 20k*
R3 20k*

A.4 Mechanical drawings

For different experiments, special mechanical solutions have been devised and realised either because ready-made components were not available or too expensive. Poul Erik Andersen and Erik Hansen from the department's machine shop processed the various parts. In this section, the idea and an overview schematic of a selection of realised designs is presented. Following solutions were crucial for our projects:

- Page 154 shows a portable interferometer for white and coherent light interferometry. The device is used to profile fibre tips with an indentation to form a micro cavity [89]. In contrast to the other designs, the assembly consists entirely of off-the-shelf parts which are given in the parts list[3].

  A Visual-C++ program was written to analyse the interferograms recorded by a CCD camera and actuate the piezo-driven stage simultaneously. Various approaches for the analysis had been compared: A Fourier transform based approach [264] and two phase shift based techniques. The advantage of the former is that no moving parts are required. However to increase the transversal resolution, a close fringe spacing is necessary. This can be accomplished by tilting the sample, which also leads to a decreased signal-to-noise ratio. Phase shift based techniques rely on a precise control of the sample, but overcome the mentioned issues. Amongst those techniques, the Carré and Hariharan algorithm, a four- and a five-step based technique, respectively, had been tested [187]. The Hariharan algorithm was finally chosen as the additional image improves the robustness and provides simple means to evaluate a 'quality map' to judge the spatial uncertainty of the result. For all of these techniques, a phase unwrapping algorithm has to be applied on its output. This was solved via processing the wrapped phase data with a fast Fourier transform method [32]. For a final evaluation of the reconstructed sample profile, a fit to Zernike polynomials [211], common in optical metrology, via singular value decomposition [225] had been implemented.

  The assembly features a footprint of 250 mm × 300 mm and is stable enough to perform white light interferometry. For coherent light interferometry, the fibre coupler (part 15) is used in combination with an appropriate mirror in the reference arm (mounted on part 22). For white light interferometry, an incandescent light source was coupled via a flexible house directly to the beam splitter cube (part 19). When profiling glass surfaces, an uncoated, wedged glass flat was mounted in the reference arm to enhance the fringe visibility by matching the reflectivity to the fibre tip and to mitigate multiple reflections.

- Page 155 shows a mirror mount with a piezo-electric actuator. A high resonance frequency and a large clearance for the beam were the main requirements. The first feature enables a fast actuation of the mirror and thereby the phase of the reflected light, while the latter is important to ease the alignment. However, both requirements play against each other to a certain extend, as a large mirror support allows for high stiffness thus a high pressure in the cut-out region while narrowing down the clearance for the light. This was solved by two additional cut-outs. The structure was optimised via a finite element analysis and the resonances are damped with the wedged back plate.

- Pages 156 to 157 illustrates the assembly constructed for the squeezed light experiments. A compact design, high mechanical stability, thermal insulation, minimal expenditure in manufacturing and an easy alignment were the set points. Apart from the thermal insulation, which was realised by a proper choice of materials, the other features are implemented

[3] The data for the models was published and is available from the manufacturing company.

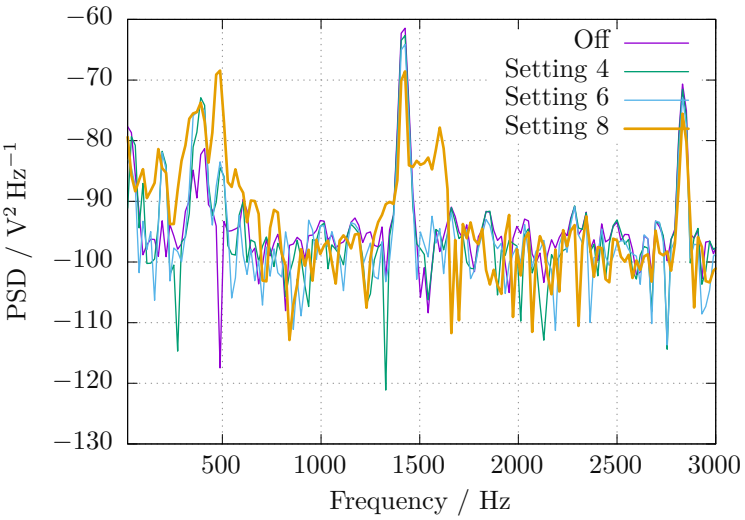

Figure A.17: Power spectral density (PSD) of an interferometric measurement conducted under the flow module. A Michelson interferometer with an arm length of 50 cm was constructed on the table under the flow module to test for vibrations and inhomogeneous air flow. A significant influence was found to occur only at the maximum air speed. The measurement was corrected for dark noise.

by the construction: The cavity length can be changed by replacing a spacer (part 13), deviations of ±0.6 mm from the designated transversal position of the mirror (part 7) can be adjusted by set screws (part 23). For cost effectiveness, the spacer and the back plate (part 11) were made from PMMA instead of glass, as stated in the parts list.

- Page 158 illustrates an assembly designed for shipping optical fibres and glass flats to optical coating companies and maintaining the parts during the respective coating process. The fibres (part 8) are mounted into blocks (part 1) with an alignment tool (not shown) to be flush with the remaining components. The assembly can be mounted with 42 fibres and 3 optical flats. A monitor flat can be mounted as well to control the coating process. Caps (part 35) protect the mounted fibre tips during alignment runs necessary to adjust the process. An outer barrel (not shown) is mounted around the assembly to protect fibres during shipping, as cleanness is the top-most requirement for a high yield.

- Page 159 illustrates a housing constructed for various experiments requiring a clean environment. An optical table is shown in the drawing as a reference. The windows are stabilised with counter weights on the ceiling. The flow module (part 5) is mounted on the ceiling as well to minimise mechanical vibrations. Set-up in a basement room without special air filters (ISO 9), the clean room class was measured to be ISO 5 (according to ISO 14644-1 clean room standards). Figure A.17 further shows the outcome of an interferometric measurement inside the housing when the flow module is switched on. Inhomogeneities in the air flow and mechanical vibrations between the two arms of the interferometer could be tested this way. It was found that, apart from the highest setting, the influence of the flow module on this test was negligible.

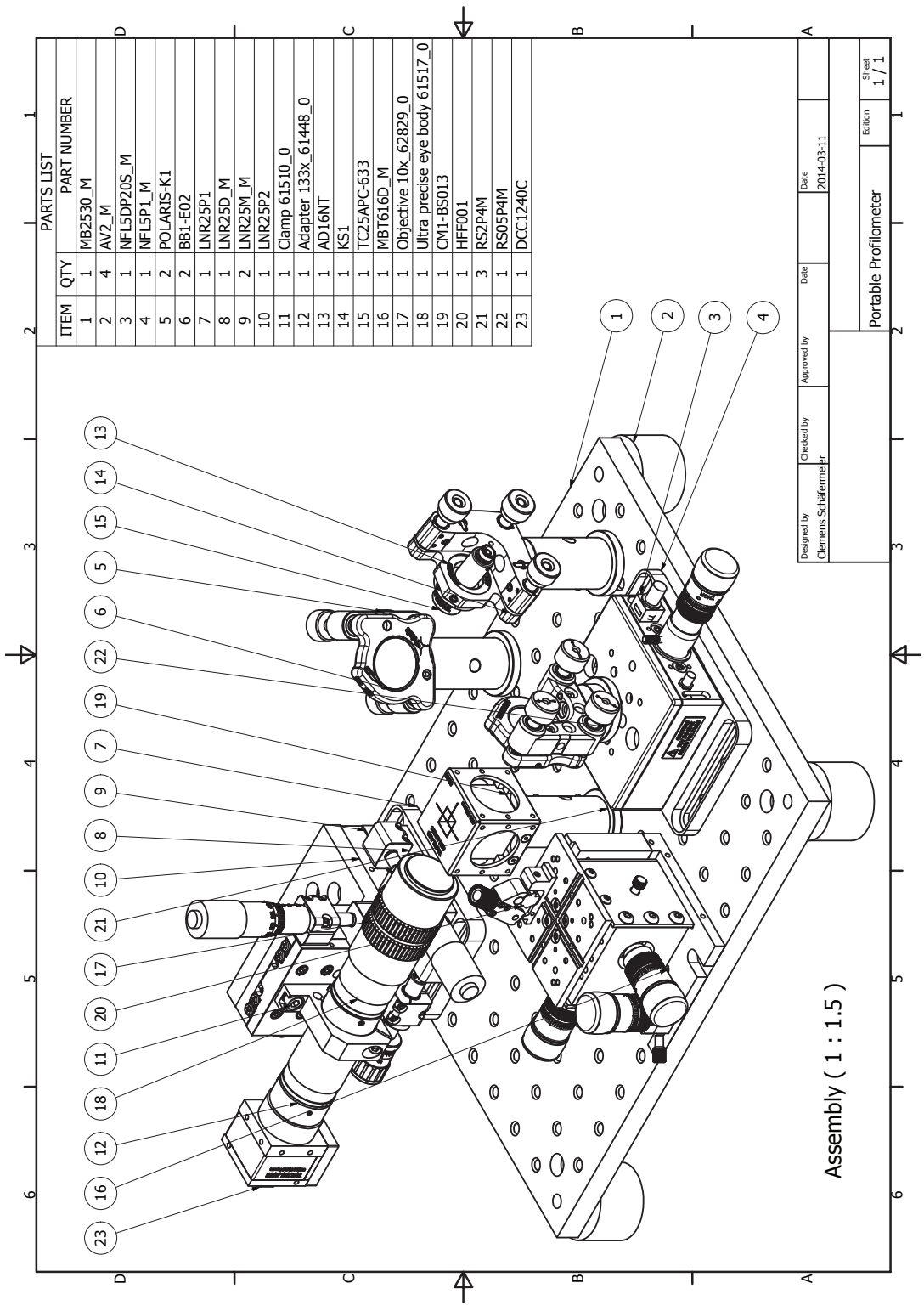
PARTS LIST
ITEM QTY PART NUMBER
1 1 MB2530_M
2 4 AV2_M
3 1 NFL5DP20S_M
4 1 NFL5P1_M
5 2 POLARIS-K1
6 2 BB1-E02
7 1 LNR25P1
8 1 LNR25D_M
9 2 LNR25M_M
10 1 LNR25P2
11 1 Clamp 61510_0
12 1 Adapter 133x_61448_0
13 1 AD16NT
14 1 KS1
15 1 TC25APC-633
16 1 MBT616D_M
17 1 Objective 10x_62829_0
18 1 Ultra precise eye body 61517_0
19 1 CM1-BS013
20 1 HFF001
21 3 RS2P4M
22 1 RS05P4M
23 1 DCC1240C
Designed by Clemens Schäfermeier
Checked by
Approved by
Date
Date 2014-03-11
Portable Profilometer
Edition
Sheet 1 / 1
Assembly (1 : 1.5)

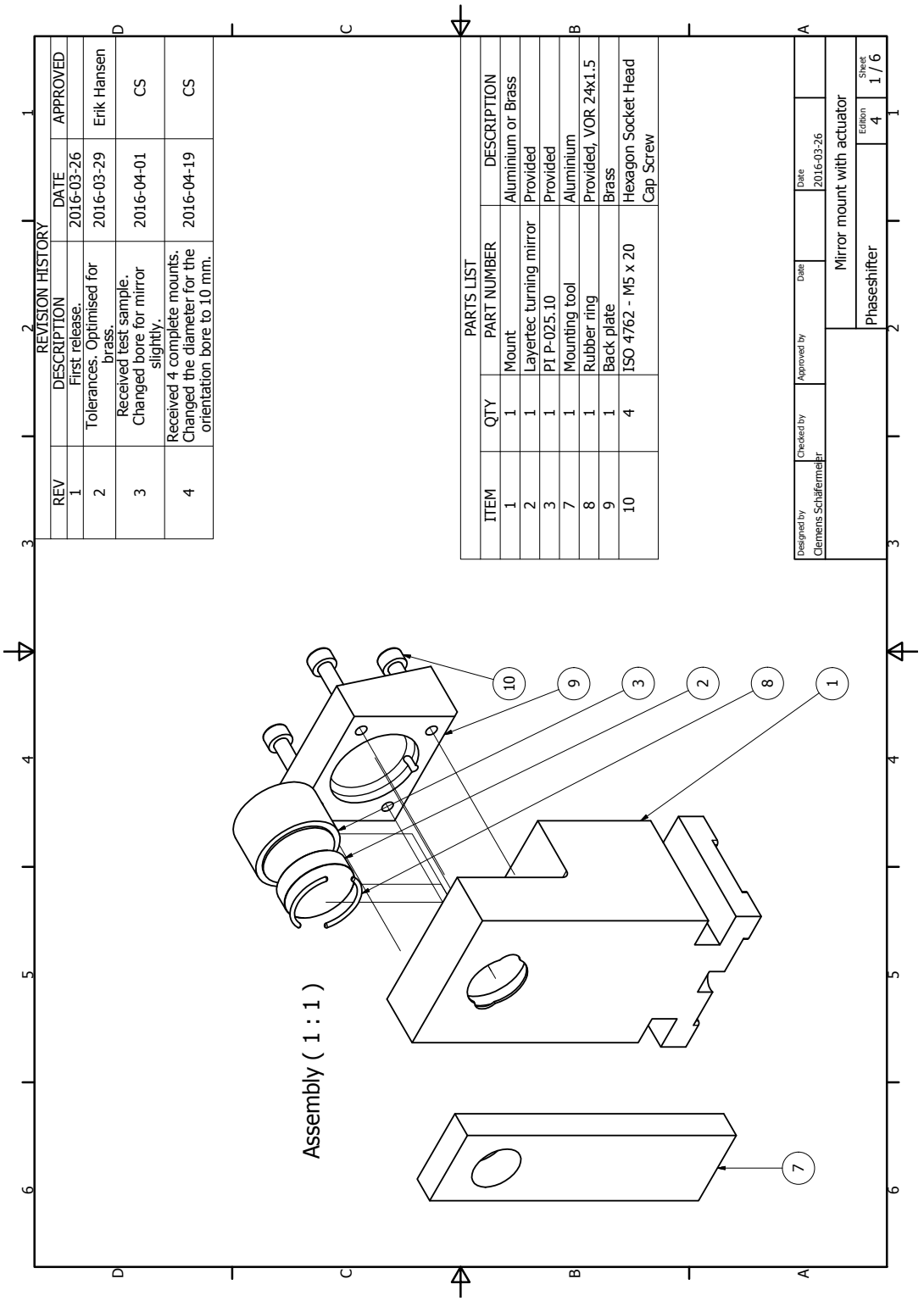
REVISION HISTORY
REV | DESCRIPTION | DATE | APPROVED
1 | First release. | 2016-03-26 |
2 | Tolerances. Optimised for brass. | 2016-03-29 | Erik Hansen
3 | Received test sample. Changed bore for mirror slightly. | 2016-04-01 | CS
4 | Received 4 complete mounts. Changed the diameter for the orientation bore to 10 mm. | 2016-04-19 | CS
PARTS LIST
ITEM | QTY | PART NUMBER | DESCRIPTION
1 | 1 | Mount | Aluminium or Brass
2 | 1 | Layertec turning mirror | Provided
3 | 1 | PI P-025.10 | Provided
7 | 1 | Mounting tool | Aluminium
8 | 1 | Rubber ring | Provided, VOR 24x1.5
9 | 1 | Back plate | Brass
10 | 4 | ISO 4762 - M5 x 20 | Hexagon Socket Head Cap Screw
Assembly (1 : 1)
Designed by Clemens Schäfermeier
Checked by
Approved by
Date
Date 2016-03-26
Mirror mount with actuator
Phaseshifter
Edition 4
Sheet 1 / 6

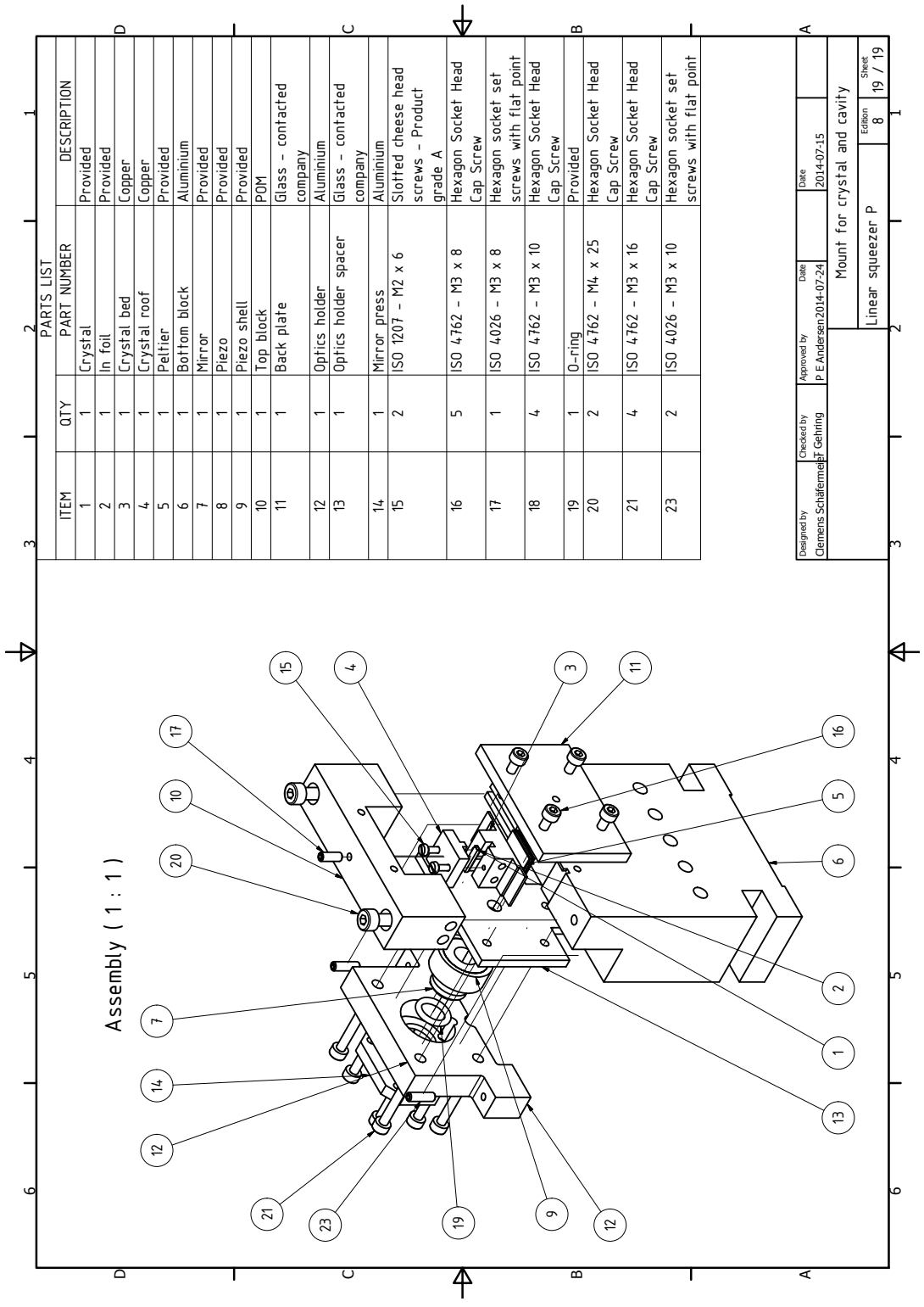
PARTS LIST
ITEM | QTY | PART NUMBER | DESCRIPTION
1 | 1 | Crystal | Provided
2 | 1 | In foil | Provided
3 | 1 | Crystal bed | Copper
4 | 1 | Crystal roof | Copper
5 | 1 | Peltier | Provided
6 | 1 | Bottom block | Aluminium
7 | 1 | Mirror | Provided
8 | 1 | Piezo | Provided
9 | 1 | Piezo shell | Provided
10 | 1 | Top block | POM
11 | 1 | Back plate | Glass - contacted company
12 | 1 | Optics holder | Aluminium
13 | 1 | Optics holder spacer | Glass - contacted company
14 | 1 | Mirror press | Aluminium
15 | 2 | ISO 1207 - M2 x 6 | Slotted cheese head screws - Product grade A
16 | 5 | ISO 4762 - M3 x 8 | Hexagon Socket Head Cap Screw
17 | 1 | ISO 4026 - M3 x 8 | Hexagon socket set screws with flat point
18 | 4 | ISO 4762 - M3 x 10 | Hexagon Socket Head Cap Screw
19 | 1 | O-ring | Provided
20 | 2 | ISO 4762 - M4 x 25 | Hexagon Socket Head Cap Screw
21 | 4 | ISO 4762 - M3 x 16 | Hexagon Socket Head Cap Screw
23 | 2 | ISO 4026 - M3 x 10 | Hexagon socket set screws with flat point
Assembly (1 : 1)
Designed by Clemens Schäfermeier
Checked by Ulf Gehring
Approved by P E Andersen
Date 2014-07-24
Date 2014-07-15
Mount for crystal and cavity
Linear squeezer P
Edition 8
Sheet 19 / 19

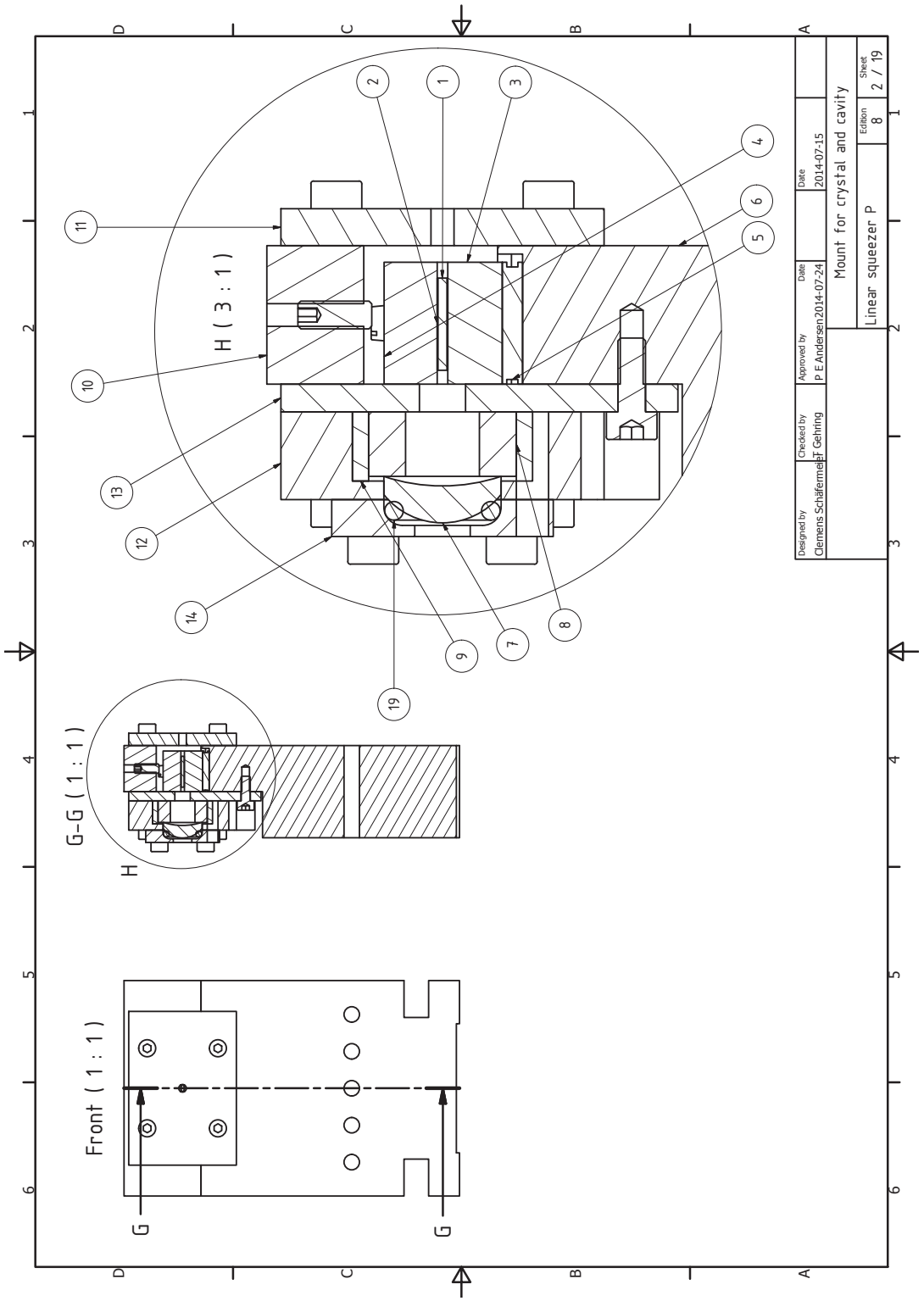
H (3 : 1)
G-G (1 : 1)
Front (1 : 1)
Designed by
Clemens Schäfermeier
Checked by
T Gehring
Approved by
P E Andersen
Date
2014-07-24
Date
2014-07-15
Mount for crystal and cavity
Linear squeezer P
Edition
8
Sheet
2 / 19

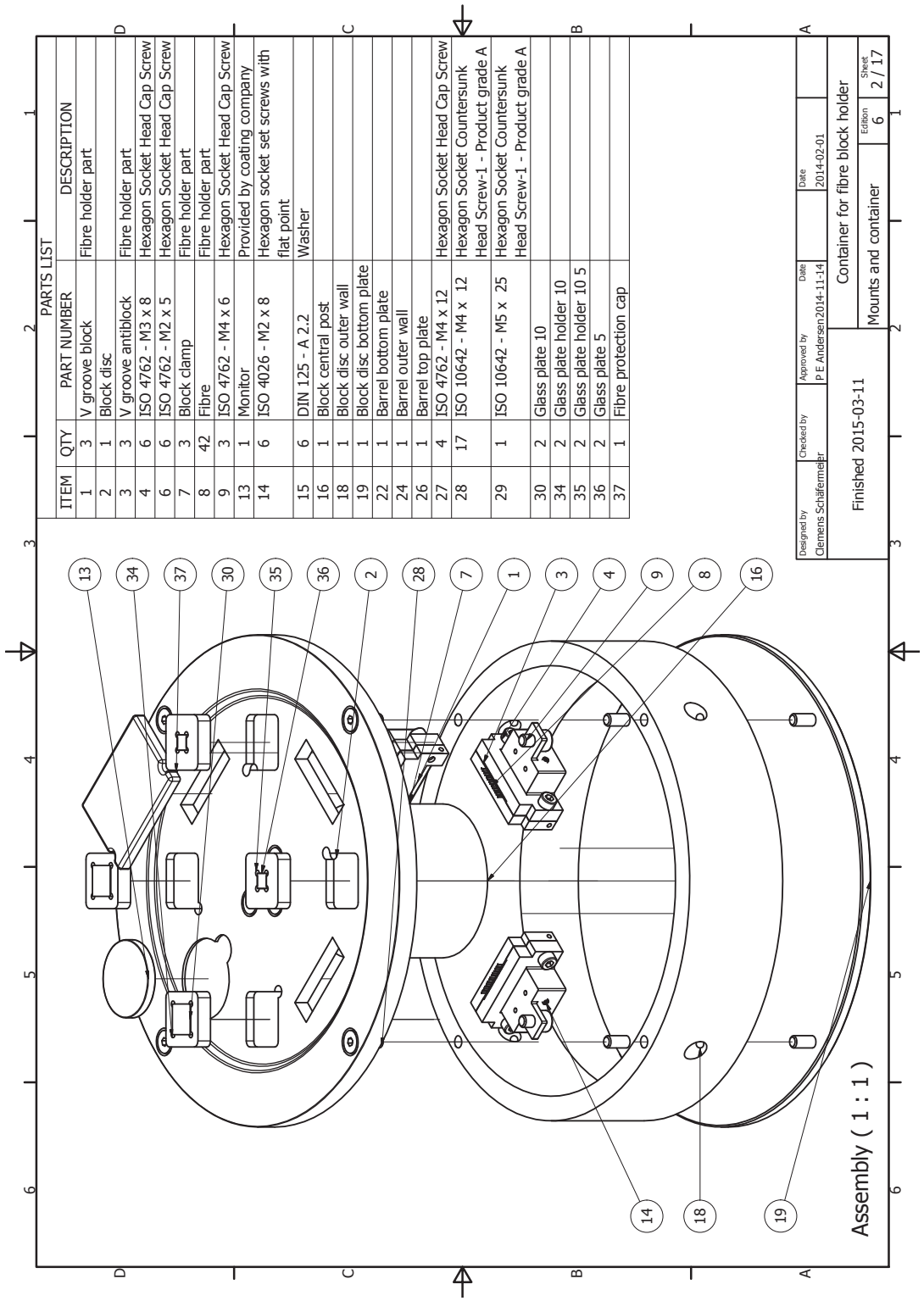

PARTS LIST

ITEM	QTY	PART NUMBER	DESCRIPTION
1	3	V groove block	Fibre holder part
2	1	Block disc	
3	3	V groove antiblock	Fibre holder part
4	6	ISO 4762 - M3 x 8	Hexagon Socket Head Cap Screw
6	6	ISO 4762 - M2 x 5	Hexagon Socket Head Cap Screw
7	3	Block clamp	Fibre holder part
8	42	Fibre	Fibre holder part
9	3	ISO 4762 - M4 x 6	Hexagon Socket Head Cap Screw
13	1	Monitor	Provided by coating company
14	6	ISO 4026 - M2 x 8	Hexagon socket set screws with flat point
15	6	DIN 125 - A 2.2	Washer
16	1	Block central post	
18	1	Block disc outer wall	
19	1	Block disc bottom plate	
22	1	Barrel bottom plate	
24	1	Barrel outer wall	
26	1	Barrel top plate	
27	4	ISO 4762 - M4 x 12	Hexagon Socket Head Cap Screw
28	17	ISO 10642 - M4 x 12	Hexagon Socket Countersunk Head Screw-1 - Product grade A
29	1	ISO 10642 - M5 x 25	Hexagon Socket Countersunk Head Screw-1 - Product grade A
30	2	Glass plate 10	
34	2	Glass plate holder 10	
35	2	Glass plate holder 10 5	
36	2	Glass plate 5	
37	1	Fibre protection cap	

Designed by: Clemens Schäfermeier | Checked by: | Approved by: P E Andersen | Date: 2014-11-14 | Date: 2014-02-01

Finished 2015-03-11

Container for fibre block holder

Mounts and container

Edition 6 | Sheet 2 / 17

Assembly (1 : 1)

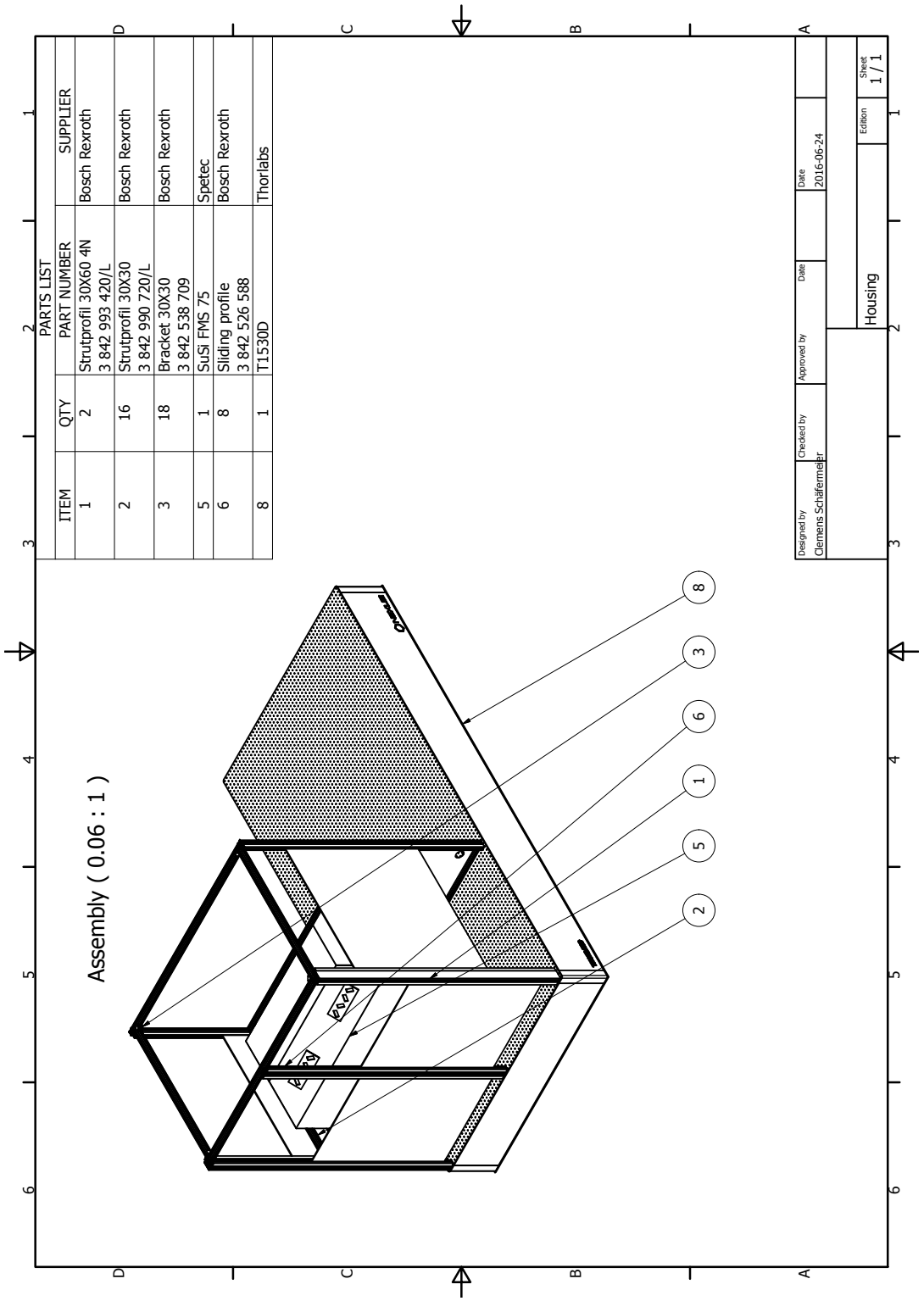
PARTS LIST
ITEM | QTY | PART NUMBER | SUPPLIER
1 | 2 | Strutprofil 30X60 4N 3 842 993 420/L | Bosch Rexroth
2 | 16 | Strutprofil 30X30 3 842 990 720/L | Bosch Rexroth
3 | 18 | Bracket 30X30 3 842 538 709 | Bosch Rexroth
5 | 1 | SuSi FMS 75 | Spetec
6 | 8 | Sliding profile 3 842 526 588 | Bosch Rexroth
8 | 1 | T1530D | Thorlabs
Assembly (0.06 : 1)
Designed by
Clemens Schäfermeier
Checked by
Approved by
Date
2016-06-24
Housing
Edition
Sheet
1 / 1

A.5 Calculation of Fisher information for phase measurements

The expression evaluated for figure 3.4 are summarised below.

Regardless of the state, the Fisher information is derived by propagating the input state's Wigner function through the interferometer. Two transformations are sufficient to accomplish the propagation: The phase shift transformation (3.9) and the variable-beam-splitter transformation (5.7). The transformed Wigner function is then substituted into equation equation (3.26) to yield $\mathrm{p}(x|\phi)$. Finally, one may calculate the integral form of equation (3.10), i.e.

$$F(\phi) = \int_x \mathrm{p}(x|\phi)\left(\frac{\partial}{\partial\phi}\ln \mathrm{p}(x|\phi)\right)^2 \mathrm{d}x. \tag{A.18}$$

For a coherent state input $|\alpha,\beta\rangle$ described the by Wigner function

$$\begin{aligned} W(x_1,y_1,x_2,y_2,\alpha,\beta) = \frac{1}{\pi^2}\times \\ \exp\Big(-2|\alpha|^2 - x_1^2 - y_1^2 + 2\imath\sqrt{2}\alpha y_1 + 2\sqrt{2}(x_1 - \imath y_1)\Re(\alpha)\Big)\times \\ \exp\Big(-2|\beta|^2 - x_2^2 - y_2^2 + 2\imath\sqrt{2}\beta y_2 + 2\sqrt{2}(x_2 - \imath y_2)\Re(\beta)\Big), \end{aligned} \tag{A.19}$$

the Fisher information of the output modes (cf. figure 3.2) reads

$$F_6(\phi,\alpha,\beta) = F_7(\phi,\alpha,\beta) = -\frac{1}{4}\,\mathrm{e}^{-2\imath\phi}\big(-\mathrm{e}^{2\imath\phi}(\alpha+\beta) + \alpha^* + \beta^*\big)^2. \tag{A.20}$$

To calculate F for $|1,0\rangle$, we start with the Wigner function

$$W(x_1,y_1,x_2,y_2) = \frac{1}{\pi^2}\big(2y_1^2 + 2x_1^2 - 1\big)\,\mathrm{e}^{-\left(y_1^2+y_2^2+x_1^2+x_2^2\right)} \tag{A.21}$$

and arrive at

$$F_6(\phi) = \frac{\sin(\phi)^2\left(\sqrt{2\pi}\,\mathrm{e}^{\frac{1}{2}\tan(\phi/2)^2}\left(|c(\phi)|^2+1\right)^2\left(\operatorname{erf}\left(\frac{1}{\sqrt{2}|c(\phi)|}\right)-1\right) + \frac{4|c(\phi)|^3}{\cos(\phi)+1}\right)}{4(\cos(\phi)-1)|c(\phi)|^5}, \tag{A.22a}$$

$$F_7(\phi) = \left(\operatorname{erfc}\left(\frac{1}{\sqrt{2}|\tan(\phi/2)|}\right)\frac{\sqrt{2\pi}\,\mathrm{e}^{\frac{1}{2}c(\phi)^2}}{\cos(\phi)+1} - |\tan(\phi/2)|\right)|\tan(\phi/2)|^{-3}, \tag{A.22b}$$

where $c(\phi) = \cot(\phi/2)$. The numerator of $F_6(\phi)$ contains terms which are quickly diverging for $\phi \to \pi$, thus a numerical evaluation for $\phi \gtrsim \pi - 1/4$ requires an increase in numerical precision (compared to standard machine precision) or a rewriting of the expression.

The Wigner function for $|1,1\rangle$ is

$$W(x_1,y_1,x_2,y_2) = \frac{1}{\pi^2}\big(2y_1^2 + 2x_1^2 - 1\big)\big(2y_2^2 + 2x_2^2 - 1\big)\,\mathrm{e}^{-\left(y_1^2+y_2^2+x_1^2+x_2^2\right)}. \tag{A.23}$$

Complex analysis helps to find a closed expression for

$$F_6(\phi) = F_7(\phi) = \frac{1}{2\sqrt{\pi}}\int_{-\infty}^{\infty}\frac{\mathrm{e}^{-x^2}\big(4x^4 - 12x^2 + 3\big)^2\sin(2\phi)^2}{(-4x^4 + 12x^2 - 3)\cos(2\phi) + 4(x^4+x^2) + 3}\,\mathrm{d}x, \tag{A.24}$$

however a numerical evaluation of the integral showed to be faster.

Finally, for a single-mode squeezed state $|\xi\rangle$, we consider a "single mode interferometer", i.e. the state is directly subject to a phase shift without splitting it into two modes. As a squeezed state carries, compared to Fock states, already a defined phase information, the interference with a local oscillator in a homodyne detection is sufficient to provide a frame of reference to measure the Fisher information (and even more generally, perform a state tomography). Since we saw that squeezed states are susceptible to losses, a variable beam splitter transformation was included into the analysis. Compared to the previous Fock state cases, the integrals are all Gaussian such that one arrives at a less complex expression:

$$F(\phi, r, \eta, \varphi) = 2\left(\frac{\eta \sinh(2r)\sin(2\phi - 2\varphi)}{1 - \eta - \eta\sinh(2r)\cos(2\phi - 2\varphi) + \eta\cosh(2r)}\right)^2. \tag{A.25}$$

List of Figures

List of Tables

Bibliography

[1] E. Abbe. "XV.–The Relation of Aperture and Power in the Microscope (continued)*". In: *Journal of the Royal Microscopical Society* **3**.6 (1883), pp. 790–812. ISSN: 1365-2818. DOI: 10.1111/j.1365-2818.1883.tb05956.x. URL: http://dx.doi.org/10.1111/j.1365-2818.1883.tb05956.x (cit. on p. 4).

[2] A. Abragam. *The Principles of Nuclear Magnetism*. 2nd ed. International Series of Monographs on Physics. Clarendon Press, 1982. ISBN: 9780198520146 (cit. on p. 20).

[3] G. S. Agarwal. *Quantum optics*. 1st ed. Cambridge University Press, 2012. ISBN: 9781107006409 (cit. on pp. 74, 78).

[4] I. Aharonovich, A. D. Greentree and S. Prawer. "Diamond photonics". In: *Nature Photonics* **5** (7 2011), pp. 397–405. DOI: 10.1038/nphoton.2011.54. URL: http://www.nature.com/nphoton/journal/v5/n7/full/nphoton.2011.54.html (cit. on p. 17).

[5] T. Aichele, A. I. Lvovsky and S. Schiller. "Optical mode characterization of single photons prepared by means of conditional measurements on a biphoton state". In: *The European Physical Journal D - Atomic, Molecular, Optical and Plasma Physics* **18**.2 (2002), pp. 237–245. ISSN: 1434-6079. DOI: 10.1140/epjd/e20020028. URL: http://link.springer.com/article/10.1140/epjd/e20020028 (cit. on p. 38).

[6] R. Albrecht et al. "Narrow-band single photon emission at room temperature based on a single nitrogen-vacancy center coupled to an all-fiber-cavity". In: *Applied Physics Letters* **105**.7 (2014). DOI: 10.1063/1.4893612. URL: http://scitation.aip.org/content/aip/journal/apl/105/7/10.1063/1.4893612 (cit. on pp. 21, 33).

[7] D. W. Allan. "Statistics of atomic frequency standards". In: *Proceedings of the IEEE* **54**.2 (Feb. 1966), pp. 221–230. DOI: 10.1109/PROC.1966.4634. URL: http://ieeexplore.ieee.org/xpl/articleDetails.jsp?arnumber=1446564 (cit. on p. 61).

[8] U. L. Andersen, T. Gehring, C. Marquardt and G. Leuchs. "30 years of squeezed light generation". In: *Physica Scripta* **91**.5 (2016), p. 053001. URL: http://stacks.iop.org/1402-4896/91/i=5/a=053001 (cit. on pp. 53, 118, 127).

[9] U. L. Andersen and T. C. Ralph. "High-Fidelity Teleportation of Continuous-Variable Quantum States Using Delocalized Single Photons". In: *Phys. Rev. Lett.* **111** (5 Aug. 2013), p. 050504. DOI: 10.1103/PhysRevLett.111.050504. URL: http://link.aps.org/doi/10.1103/PhysRevLett.111.050504 (cit. on p. 126).

[10] P. M. Anisimov et al. "Quantum Metrology with Two-Mode Squeezed Vacuum: Parity Detection Beats the Heisenberg Limit". In: *Phys. Rev. Lett.* **104** (10 Mar. 2010), p. 103602. DOI: 10.1103/PhysRevLett.104.103602. URL: http://link.aps.org/doi/10.1103/PhysRevLett.104.103602 (cit. on p. 35).

[11] F. Apfelbeck. "Low-Temperature Investigations of Silicon Vacancy Color Centers in Diamond NanoCrystals". MA thesis. München: LMU, 2015 (cit. on p. 29).

[12] F. Arecchi and R. Bonifacio. “Theory of optical maser amplifiers”. In: *IEEE Journal of Quantum Electronics* **1**.4 (July 1965), pp. 169–178. DOI: 10.1109/JQE.1965.1072212. URL: http://ieeexplore.ieee.org/xpl/articleDetails.jsp?arnumber=1072212 (cit. on p. 53).

[13] D. K. Armani, T. J. Kippenberg, S. M. Spillane and K. J. Vahala. “Ultra-high-Q toroid microcavity on a chip”. In: *Nature* **421**.6926 (Feb. 2003), pp. 925–928. DOI: 10.1038/nature01371. URL: http://www.nature.com/nature/journal/v421/n6926/full/nature01371.html (cit. on p. 73).

[14] M. Aspelmeyer, T. J. Kippenberg and F. Marquardt. “Cavity optomechanics”. In: *Rev. Mod. Phys.* **86** (4 Dec. 2014), pp. 1391–1452. DOI: 10.1103/RevModPhys.86.1391. URL: http://link.aps.org/doi/10.1103/RevModPhys.86.1391 (cit. on pp. 72–76, 78, 80).

[15] D. D. Awschalom, R. Epstein and R. Hanson. “The Diamond Age Diamond Age of Spintronics”. In: *Scientific American* **297** (4 2007), pp. 84–91. DOI: 10.1038/scientificamerican1007-84. URL: http://www.nature.com/scientificamerican/journal/v297/n4/full/scientificamerican1007-84.html (cit. on p. 17).

[16] H.-A. Bachor and T. Ralph. *A Guide to Experiments in Quantum Optics*. 2nd ed. Wiley-VCH, 2004. ISBN: 3-527-40393-0 (cit. on pp. 8–10, 13, 14, 38, 54, 74, 100).

[17] T. Bagci et al. “Optical detection of radio waves through a nanomechanical transducer”. In: *Nature* **507** (Mar. 2014), pp. 81–85. DOI: 10.1038/nature13029. URL: http://www.nature.com/nature/journal/v507/n7490/full/nature13029.html (cit. on p. 72).

[18] C. Baker and M. Rochette. “A generalized heat-brush approach for precise control of the waist profile in fiber tapers”. In: *Opt. Mater. Express* **1**.6 (Oct. 2011), pp. 1065–1076. DOI: 10.1364/OME.1.001065. URL: http://www.osapublishing.org/ome/abstract.cfm?URI=ome-1-6-1065 (cit. on p. 73).

[19] G. Balasubramanian et al. “Ultralong spin coherence time in isotopically engineered diamond”. In: *Nature Materials* **8**.5 (May 2009). DOI: 10.1038/nmat2420. URL: http://www.nature.com/nmat/journal/v8/n5/full/nmat2420.html (cit. on p. 17).

[20] P. E. Barclay, K.-M. C. Fu, C. Santori, A. Faraon and R. G. Beausoleil. “Hybrid Nanocavity Resonant Enhancement of Color Center Emission in Diamond”. In: *Phys. Rev. X* **1** (1 Sept. 2011), p. 011007. DOI: 10.1103/PhysRevX.1.011007. URL: http://link.aps.org/doi/10.1103/PhysRevX.1.011007 (cit. on p. 18).

[21] B. Barish and R. Weiss. “LIGO and the Detection of Gravitational Waves”. In: *Phys. Today* **52** (10 Oct. 1999), pp. 44–50. DOI: 10.1063/1.882861. URL: http://scitation.aip.org/content/aip/magazine/physicstoday/article/52/10/10.1063/1.882861 (cit. on p. 72).

[22] J. A. Barnes et al. “Characterization of Frequency Stability”. In: *IEEE Transactions on Instrumentation and Measurement* **IM-20**.2 (May 1971), pp. 105–120. ISSN: 0018-9456. DOI: 10.1109/TIM.1971.5570702 (cit. on p. 61).

[23] S. M. Barnett, D. T. Pegg and J. Jeffers. “Bayes’ theorem and quantum retrodiction”. In: *Journal of Modern Optics* **47**.11 (2000), pp. 1779–1789. DOI: 10.1080/09500340008232431. URL: http://www.tandfonline.com/doi/abs/10.1080/09500340008232431 (cit. on p. 43).

[24] S. D. Barrett and P. Kok. “Efficient high-fidelity quantum computation using matter qubits and linear optics”. In: *Phys. Rev. A* **71** (6 June 2005), p. 060310. DOI: 10.1103/PhysRevA.71.060310. URL: http://link.aps.org/doi/10.1103/PhysRevA.71.060310 (cit. on p. 18).

[25] K. Beha, A. Batalov, N. B. Manson, R. Bratschitsch and A. Leitenstorfer. "Optimum Photoluminescence Excitation and Recharging Cycle of Single Nitrogen-Vacancy Centers in Ultrapure Diamond". In: *Phys. Rev. Lett.* **109** (9 Aug. 2012), p. 097404. DOI: 10.1103/PhysRevLett.109.097404. URL: http://link.aps.org/doi/10.1103/PhysRevLett.109.097404 (cit. on p. 17).

[26] V. B. Berestetskii, E. M. Lifshitz and L. P. Pitaevskii. *Quantum Electrodynamics*. 2nd ed. Course of Theoretical Physics 4. Butterworth-Heinemann, 1982. ISBN: 978-0-7506-3371-0 (cit. on pp. 7, 23).

[27] A. A. Berni. "Continuous Variables Quantum Information in Noisy Environments". PhD thesis. Technical University of Denmark, Dec. 2014 (cit. on pp. 43, 46, 59).

[28] H. Bernien et al. "Heralded entanglement between solid-state qubits separated by three metres". In: *Nature* **497** (7447 May 2013), pp. 86–90. DOI: 10.1038/nature12016. URL: http://www.nature.com/nature/journal/v484/n7392/full/nature10900.html (cit. on p. 18).

[29] R. Betzholz, J. M. Torres and M. Bienert. "Quantum optical master equation for solid-state quantum emitters". In: *Phys. Rev. A* **90** (6 Dec. 2014), p. 063818. DOI: 10.1103/PhysRevA.90.063818. URL: http://link.aps.org/doi/10.1103/PhysRevA.90.063818 (cit. on pp. 22, 24).

[30] K. M. Birnbaum, A. Boca, R. Miller, A. D. Boozer, T. E. Northup and H. J. Kimble. "Photon blockade in an optical cavity with one trapped atom". In: *Nature* **436**.7047 (2005), pp. 87–90. DOI: 10.1038/nature03804. URL: http://www.nature.com/nature/journal/v436/n7047/abs/nature03804.html (cit. on p. 33).

[31] E. D. Black. "An introduction to Pound–Drever–Hall laser frequency stabilization". In: *American Journal of Physics* **69**.1 (2001), pp. 79–87. DOI: 10.1119/1.1286663. URL: http://scitation.aip.org/content/aapt/journal/ajp/69/1/10.1119/1.1286663 (cit. on pp. 55, 80).

[32] D. J. Bone. "Fourier fringe analysis: the two-dimensional phase unwrapping problem". In: *Appl. Opt.* **30**.25 (Sept. 1991), pp. 3627–3632. DOI: 10.1364/AO.30.003627. URL: http://ao.osa.org/abstract.cfm?URI=ao-30-25-3627 (cit. on p. 152).

[33] M. Born and P. Jordan. "Zur Quantenmechanik". German. In: *Zeitschrift für Physik* **34**.1 (1925), pp. 858–888. ISSN: 0044-3328. DOI: 10.1007/BF01328531. URL: http://dx.doi.org/10.1007/BF01328531 (cit. on p. 7).

[34] M. Born and E. Wolf. *Principles of Optics*. 6th ed. Pergamon Press, 1986. ISBN: 0-08-026481-6 (cit. on pp. 6, 34).

[35] M. Born. "Zur Quantenmechanik der Stoßvorgänge". German. In: *Zeitschrift für Physik* **37**.12 (1926), pp. 863–867. ISSN: 0044-3328. DOI: 10.1007/BF01397477. URL: http://link.springer.com/article/10.1007%2FBF01397477 (cit. on p. 42).

[36] A. N. Boto, P. Kok, D. S. Abrams, S. L. Braunstein, C. P. Williams and J. P. Dowling. "Quantum Interferometric Optical Lithography: Exploiting Entanglement to Beat the Diffraction Limit". In: *Phys. Rev. Lett.* **85** (13 Sept. 2000), pp. 2733–2736. DOI: 10.1103/PhysRevLett.85.2733. URL: http://link.aps.org/doi/10.1103/PhysRevLett.85.2733 (cit. on p. 34).

[37] W. P. Bowen and G. J. Milburn. *Quantum Optomechanics*. CRC Press, 2016. ISBN: 9781482259155 (cit. on pp. 11, 54, 72, 74, 75, 78, 85, 87, 88, 96, 97, 99–101, 103).

[38] R. W. Boyd, ed. *Nonlinear Optics*. 3rd ed. Academic Press, 2008. ISBN: 978-0123694706 (cit. on pp. 53, 54).

[39] V. B. Braginskiĭ. "Classical and Quantum Restrictions on the Detection of Weak Disturbances of a Macroscopic Oscillator". In: *Soviet Journal of Experimental and Theoretical Physics* **26** (Apr. 1968), pp. 831–834 (cit. on p. 72).

[40] V. B. Braginskiĭ and A. B. Manukin. "Ponderomotive Effects of Electromagnetic Radiation". In: *Soviet Journal of Experimental and Theoretical Physics* **25** (Oct. 1967), pp. 653–655 (cit. on p. 72).

[41] V. B. Braginskiĭ and Y. I. Vorontsov. "Quantum-mechanical limitations in macroscopic experiments and modern experimental technique". In: *Soviet Physics Uspekhi* **17**.5 (1975), p. 644. URL: http://stacks.iop.org/0038-5670/17/i=5/a=R02 (cit. on p. 105).

[42] B. Brandstätter et al. "Integrated fiber-mirror ion trap for strong ion-cavity coupling". In: *Review of Scientific Instruments* **84**.12 (2013). DOI: 10.1063/1.4838696. URL: http://scitation.aip.org/content/aip/journal/rsi/84/12/10.1063/1.4838696 (cit. on p. 33).

[43] H.-P. Breuer and F. Petruccione. *The Theory of Open Quantum Systems*. Oxford University Press, 2007. ISBN: 9780199213900 (cit. on pp. 22, 23).

[44] I. N. Bronshtein, K. . Semendyayev, G. Musiol and H. Mühlig. *Handbook of Mathematics*. 5th ed. Springer-Verlag, 2007. ISBN: 978-3-540-72121-5 (cit. on pp. 9, 14, 41, 44, 82, 108, 138).

[45] S. W. Brown and S. C. Rand. "Site symmetry analysis of the 738 nm defect in diamond". In: *Journal of Applied Physics* **78**.6 (1995), pp. 4069–4075. DOI: 10.1063/1.359864. URL: http://scitation.aip.org/content/aip/journal/jap/78/6/10.1063/1.359864 (cit. on p. 19).

[46] M. J. Burek, D. Ramos, P. Patel, I. W. Frank and M. Lončar. "Nanomechanical resonant structures in single-crystal diamond". In: *Applied Physics Letters* **103**.13, 131904 (2013). DOI: 10.1063/1.4821917. URL: http://scitation.aip.org/content/aip/journal/apl/103/13/10.1063/1.4821917 (cit. on p. 21).

[47] P. Busch, P. Lahti and R. F. Werner. "Proof of Heisenberg's Error-Disturbance Relation". In: *Phys. Rev. Lett.* **111** (16 Oct. 2013), p. 160405. DOI: 10.1103/PhysRevLett.111.160405. URL: http://link.aps.org/doi/10.1103/PhysRevLett.111.160405 (cit. on p. 34).

[48] K. E. Cahill and R. J. Glauber. "Density Operators and Quasiprobability Distributions". In: *Phys. Rev.* **177** (5 Jan. 1969), pp. 1882–1902. DOI: 10.1103/PhysRev.177.1882. URL: http://link.aps.org/doi/10.1103/PhysRev.177.1882 (cit. on p. 15).

[49] Y. Cai and Q. Lin. "Decentered elliptical Hermite–Gaussian beam". In: *J. Opt. Soc. Am. A* **20**.6 (June 2003), pp. 1111–1119. DOI: 10.1364/JOSAA.20.001111. URL: http://josaa.osa.org/abstract.cfm?URI=josaa-20-6-1111 (cit. on p. 130).

[50] B. Calkins et al. "High quantum-efficiency photon-number-resolving detector for photonic on-chip information processing". In: *Opt. Express* **21**.19 (Sept. 2013), pp. 22657–22670. DOI: 10.1364/OE.21.022657. URL: http://www.opticsexpress.org/abstract.cfm?URI=oe-21-19-22657 (cit. on p. 38).

[51] J. Capmany and C. R. Fernández-Pousa. "Quantum model for electro-optical phase modulation". In: *J. Opt. Soc. Am. B* **27**.6 (June 2010), A119–A129. DOI: 10.1364/JOSAB.27.00A119. URL: http://josab.osa.org/abstract.cfm?URI=josab-27-6-A119 (cit. on p. 66).

[52] T. Carmon, H. Rokhsari, L. Yang, T. J. Kippenberg and K. J. Vahala. "Temporal Behavior of Radiation-Pressure-Induced Vibrations of an Optical Microcavity Phonon Mode". In: *Phys. Rev. Lett.* **94** (22 June 2005), p. 223902. DOI: 10.1103/PhysRevLett.94.223902. URL: http://link.aps.org/doi/10.1103/PhysRevLett.94.223902 (cit. on p. 73).

[53] W. B. Case. "Wigner functions and Weyl transforms for pedestrians". In: *American Journal of Physics* **76**.10 (2008), pp. 937–946. DOI: 10.1119/1.2957889. URL: http://scitation.aip.org/content/aapt/journal/ajp/76/10/10.1119/1.2957889 (cit. on p. 40).

[54] C. M. Caves. "Quantum limits on noise in linear amplifiers". In: *Phys. Rev. D* **26** (8 Oct. 1982), pp. 1817–1839. DOI: 10.1103/PhysRevD.26.1817. URL: http://link.aps.org/doi/10.1103/PhysRevD.26.1817 (cit. on pp. 106, 110, 126).

[55] C. M. Caves. "Quantum-mechanical noise in an interferometer". In: *Phys. Rev. D* **23** (8 Apr. 1981), pp. 1693–1708. DOI: 10.1103/PhysRevD.23.1693. URL: http://link.aps.org/doi/10.1103/PhysRevD.23.1693 (cit. on pp. 35, 45, 49, 51).

[56] C. M. Caves. "Quantum-Mechanical Radiation-Pressure Fluctuations in an Interferometer". In: *Phys. Rev. Lett.* **45** (2 July 1980), pp. 75–79. DOI: 10.1103/PhysRevLett.45.75. URL: http://link.aps.org/doi/10.1103/PhysRevLett.45.75 (cit. on p. 72).

[57] C. M. Caves, J. Combes, Z. Jiang and S. Pandey. "Quantum limits on phase-preserving linear amplifiers". In: *Phys. Rev. A* **86** (6 Dec. 2012), p. 063802. DOI: 10.1103/PhysRevA.86.063802. URL: http://link.aps.org/doi/10.1103/PhysRevA.86.063802 (cit. on pp. 106, 107, 110, 126).

[58] C. M. Caves and B. L. Schumaker. "New formalism for two-photon quantum optics. I. Quadrature phases and squeezed states". In: *Phys. Rev. A* **31** (5 May 1985), pp. 3068–3092. DOI: 10.1103/PhysRevA.31.3068. URL: http://link.aps.org/doi/10.1103/PhysRevA.31.3068 (cit. on p. 54).

[59] N. J. Cerf, G. Leuchs and E. S. Polzik, eds. *Quantum Information with Continuous Variables of Atoms and Light*. Imperial College Press, 2007. ISBN: 978-1-86094-760-5 (cit. on p. 51).

[60] I. Chakrabarty. "Fisher Information: Quantum Uncertainty Relation". In: *arXiv* (Nov. 2005). arXiv: 0511169 [quant-ph]. URL: https://arxiv.org/abs/quant-ph/0511169 (cit. on p. 44).

[61] J. Chan et al. "Laser cooling of a nanomechanical oscillator into its quantum ground state". In: *Nature* **478** (Oct. 2011), pp. 89–92. DOI: 10.1038/nature10461. URL: http://www.nature.com/nature/journal/v478/n7367/full/nature10461.html (cit. on p. 82).

[62] J. I. Cirac and P. Zoller. "Laser cooling of trapped ions in a squeezed vacuum". In: *Phys. Rev. A* **47** (3 Mar. 1993), pp. 2191–2195. DOI: 10.1103/PhysRevA.47.2191. URL: http://link.aps.org/doi/10.1103/PhysRevA.47.2191 (cit. on p. 73).

[63] J. I. Cirac and P. Zoller. "Quantum Computations with Cold Trapped Ions". In: *Phys. Rev. Lett.* **74** (20 May 1995), pp. 4091–4094. DOI: 10.1103/PhysRevLett.74.4091. URL: http://link.aps.org/doi/10.1103/PhysRevLett.74.4091 (cit. on p. 72).

[64] C. D. Clark and C. B. Dickerson. "The 1.681 eV centre in polycrystalline diamond". In: *Surface and Coatings Technology* **47**.1 (1991), pp. 336–343. ISSN: 0257-8972. DOI: 10.1016/0257-8972(91)90299-C. URL: http://www.sciencedirect.com/science/article/pii/025789729190299C (cit. on p. 18).

[65] C. D. Clark, H. Kanda, I. Kiflawi and G. Sittas. “Silicon defects in diamond”. In: *Phys. Rev. B* **51** (23 June 1995), pp. 16681–16688. DOI: 10.1103/PhysRevB.51.16681. URL: http://link.aps.org/doi/10.1103/PhysRevB.51.16681 (cit. on p. 18).

[66] J. B. Clark, F. Lecocq, R. W. Simmonds, J. Aumentado and J. D. Teufel. “Observation of strong radiation pressure forces from squeezed light on a mechanical oscillator”. In: *Nature Physics* **12**.7 (Mar. 2016), pp. 683–687. DOI: 10.1038/nphys3701. URL: http://www.nature.com/nphys/journal/v12/n7/full/nphys3701.html (cit. on p. 105).

[67] P. F. Cohadon, A. Heidmann and M. Pinard. “Cooling of a Mirror by Radiation Pressure”. In: *Phys. Rev. Lett.* **83** (16 Oct. 1999), pp. 3174–3177. DOI: 10.1103/PhysRevLett.83.3174. URL: http://link.aps.org/doi/10.1103/PhysRevLett.83.3174 (cit. on p. 73).

[68] M. J. Collett and C. W. Gardiner. “Squeezing of intracavity and traveling-wave light fields produced in parametric amplification”. In: *Phys. Rev. A* **30** (3 Sept. 1984), pp. 1386–1391. DOI: 10.1103/PhysRevA.30.1386. URL: http://link.aps.org/doi/10.1103/PhysRevA.30.1386 (cit. on p. 53).

[69] M. J. Collett and R. Loudon. “Output properties of parametric amplifiers in cavities”. In: *J. Opt. Soc. Am. B* **4**.10 (Oct. 1987), pp. 1525–1534. DOI: 10.1364/JOSAB.4.001525. URL: http://josab.osa.org/abstract.cfm?URI=josab-4-10-1525 (cit. on p. 53).

[70] M. J. Collett, R. Loudon and C. W. Gardiner. “Quantum Theory of Optical Homodyne and Heterodyne Detection”. In: *Journal of Modern Optics* **34**.6-7 (1987), pp. 881–902. URL: http://www.tandfonline.com/doi/abs/10.1080/09500348714550811 (cit. on p. 14).

[71] A. T. Collins, L. Allers, C. J. H. Wort and G. A. Scarsbrook. “The annealing of radiation damage in De Beers colourless CVD diamond”. In: *Diamond and Related Materials* **3**.4 (1994). Proceedings of the 4th European Conference on Diamond, Diamond-like and Related Materials, pp. 932–935. ISSN: 0925-9635. DOI: 10.1016/0925-9635(94)90302-6. URL: http://www.sciencedirect.com/science/article/pii/0925963594903026 (cit. on p. 18).

[72] A. T. Collins, A. Connor, C.-H. Ly, A. Shareef and P. M. Spear. “High-temperature annealing of optical centers in type-I diamond”. In: *Journal of Applied Physics* **97**.8, 083517 (2005). DOI: 10.1063/1.1866501. URL: http://scitation.aip.org/content/aip/journal/jap/97/8/10.1063/1.1866501 (cit. on p. 27).

[73] T. Corbitt et al. “Optical Dilution and Feedback Cooling of a Gram-Scale Oscillator to 6.9 mK”. In: *Phys. Rev. Lett.* **99** (16 Oct. 2007), p. 160801. DOI: 10.1103/PhysRevLett.99.160801. URL: http://link.aps.org/doi/10.1103/PhysRevLett.99.160801 (cit. on p. 73).

[74] T. M. Cover and J. A. Thomas. *Elements of Information Theory*. 2nd ed. John Wiley & Sons, 2006. ISBN: 978-0-471-24195-9 (cit. on pp. 108, 111).

[75] H. Cramér. *Mathematical Methods of Statistics*. Princeton University Press, 1999. ISBN: 9780691005478 (cit. on pp. 41, 44).

[76] A. D. Cronin, J. Schmiedmayer and D. E. Pritchard. “Optics and interferometry with atoms and molecules”. In: *Rev. Mod. Phys.* **81** (3 July 2009), pp. 1051–1129. DOI: 10.1103/RevModPhys.81.1051. URL: http://link.aps.org/doi/10.1103/RevModPhys.81.1051 (cit. on p. 34).

[77] W. Crookes. “On Attraction and Repulsion Resulting from Radiation”. In: *Philosophical Transactions of the Royal Society of London* **164** (1874), pp. 501–527. DOI: 10.1098/rstl.1874.0015. URL: http://rstl.royalsocietypublishing.org/content/164/501.short (cit. on p. 72).

[78] G. M. D'Ariano, C. Macchiavello and M. G. A. Paris. "Amplification under the Standard Quantum Noise Limit". In: *Phys. Rev. Lett.* **73** (24 Dec. 1994), pp. 3187–3190. DOI: 10.1103/PhysRevLett.73.3187. URL: http://link.aps.org/doi/10.1103/PhysRevLett.73.3187 (cit. on p. 122).

[79] A. Datta, L. Zhang, N. Thomas-Peter, U. Dorner, B. J. Smith and I. A. Walmsley. "Quantum metrology with imperfect states and detectors". In: *Phys. Rev. A* **83** (6 June 2011), p. 063836. DOI: 10.1103/PhysRevA.83.063836. URL: http://link.aps.org/doi/10.1103/PhysRevA.83.063836 (cit. on p. 35).

[80] V. A. Davydov et al. "Production of nano- and microdiamonds with Si-V and N-V luminescent centers at high pressures in systems based on mixtures of hydrocarbon and fluorocarbon compounds". In: *JETP Letters* **99**.10 (2014), pp. 585–589. ISSN: 1090-6487. DOI: 10.1134/S002136401410004X. URL: http://dx.doi.org/10.1134/S002136401410004X (cit. on pp. 21, 27).

[81] C. L. Degen, M. Poggio, H. J. Mamin and D. Rugar. "Nuclear Spin Relaxation Induced by a Mechanical Resonator". In: *Phys. Rev. Lett.* **100** (13 Apr. 2008), p. 137601. DOI: 10.1103/PhysRevLett.100.137601. URL: http://link.aps.org/doi/10.1103/PhysRevLett.100.137601 (cit. on p. 72).

[82] R. Demkowicz-Dobrzanski et al. "Quantum phase estimation with lossy interferometers". In: *Phys. Rev. A* **80** (1 July 2009), p. 013825. DOI: 10.1103/PhysRevA.80.013825. URL: http://link.aps.org/doi/10.1103/PhysRevA.80.013825 (cit. on p. 35).

[83] U. F. S. D'Haenens-Johansson et al. "Optical properties of the neutral silicon split-vacancy center in diamond". In: *Phys. Rev. B* **84** (24 Dec. 2011), p. 245208. DOI: 10.1103/PhysRevB.84.245208. URL: http://link.aps.org/doi/10.1103/PhysRevB.84.245208 (cit. on p. 19).

[84] D. Dieks. "Communication by EPR devices". In: *Physics Letters A* **92**.6 (1982), pp. 271–272. ISSN: 0375-9601. DOI: 10.1016/0375-9601(82)90084-6. URL: http://www.sciencedirect.com/science/article/pii/0375960182900846 (cit. on p. 106).

[85] A. Dietrich et al. "Isotopically varying spectral features of silicon-vacancy in diamond". In: *New Journal of Physics* **16**.11 (2014), p. 113019. URL: http://stacks.iop.org/1367-2630/16/i=11/a=113019 (cit. on pp. 19, 21).

[86] P. A. M. Dirac. *The Principles of Quantum Mechanics*. 4th ed. Oxford University Press, 1988. ISBN: 978-0-19-852011-5 (cit. on pp. 7, 8, 23).

[87] Direction de la Recherche Scientifique et Technologique. *Histoire de la mesure*. French. URL: http://www.metrologie-francaise.fr/fr/histoire/histoire-mesure.asp (visited on 24/07/2016) (cit. on p. 4).

[88] E. Distante, M. Ježek and U. L. Andersen. "Deterministic Superresolution with Coherent States at the Shot Noise Limit". In: *Phys. Rev. Lett.* **111** (3 July 2013), p. 033603. DOI: 10.1103/PhysRevLett.111.033603. URL: http://link.aps.org/doi/10.1103/PhysRevLett.111.033603 (cit. on pp. 35, 45, 48, 51, 70, 71).

[89] M. S. E. Djurhuus and M. S. Møller-Kristensen. "Fabrication and white light profilometry of spherical mirrors for micro-cavities". Bachelor thesis. Technical University of Denmark, June 2015 (cit. on p. 152).

[90] M. W. Doherty, N. B. Manson, P. Delaney, F. Jelezko, J. Wrachtrup and L. C. L. Hollenberg. "The nitrogen-vacancy colour centre in diamond". In: *Physics Reports* **528**.1 (2013), pp. 1–45. ISSN: 0370-1573. DOI: 10.1016/j.physrep.2013.02.001. URL: http://www.sciencedirect.com/science/article/pii/S0370157313000562 (cit. on p. 17).

[91] U. Dorner et al. “Optimal Quantum Phase Estimation”. In: *Phys. Rev. Lett.* **102** (4 Jan. 2009), p. 040403. DOI: 10.1103/PhysRevLett.102.040403. URL: http://link.aps.org/doi/10.1103/PhysRevLett.102.040403 (cit. on p. 35).

[92] J. P. Dowling and G. J. Milburn. “Quantum technology: the second quantum revolution”. In: *Philosophical Transactions of the Royal Society of London A: Mathematical, Physical and Engineering Sciences* **361**.1809 (2003), pp. 1655–1674. ISSN: 1364-503X. DOI: 10.1098/rsta.2003.1227. URL: http://rsta.royalsocietypublishing.org/content/361/1809/1655 (cit. on p. 17).

[93] R. W. P. Drever et al. “Laser phase and frequency stabilization using an optical resonator”. In: *Applied Physics B* **31**.2 (1983), pp. 97–105. ISSN: 1432-0649. DOI: 10.1007/BF00702605. URL: http://dx.doi.org/10.1007/BF00702605 (cit. on p. 55).

[94] T. Eberle et al. “Quantum Enhancement of the Zero-Area Sagnac Interferometer Topology for Gravitational Wave Detection”. In: *Phys. Rev. Lett.* **104** (25 June 2010), p. 251102. DOI: 10.1103/PhysRevLett.104.251102. URL: http://link.aps.org/doi/10.1103/PhysRevLett.104.251102 (cit. on pp. 38, 51).

[95] A. M. Edmonds, M. E. Newton, P. M. Martineau, D. J. Twitchen and S. D. Williams. “Electron paramagnetic resonance studies of silicon-related defects in diamond”. In: *Phys. Rev. B* **77** (24 June 2008), p. 245205. DOI: 10.1103/PhysRevB.77.245205. URL: http://link.aps.org/doi/10.1103/PhysRevB.77.245205 (cit. on p. 18).

[96] A. Ekert. “Quantum interferometers as quantum computers”. In: *Physica Scripta* **1998**.T76 (1998), p. 218. URL: http://stacks.iop.org/1402-4896/1998/i=T76/a=031 (cit. on p. 35).

[97] B. Fang et al. “Metrology with Atom Interferometry: Inertial Sensors from Laboratory to Field Applications”. In: *Journal of Physics: Conference Series* **723**.1 (2016), p. 012049. URL: http://stacks.iop.org/1742-6596/723/i=1/a=012049 (cit. on p. 5).

[98] T. Feng and B. D. Schwartz. “Characteristics and origin of the 1.681 eV luminescence center in chemical-vapor-deposited diamond films”. In: *Journal of Applied Physics* **73**.3 (1993), pp. 1415–1425. DOI: 10.1063/1.353239. URL: http://scitation.aip.org/content/aip/journal/jap/73/3/10.1063/1.353239 (cit. on p. 18).

[99] A. Ferraro, S. Olivares and M. G. A. Paris. “Gaussian states in continuous variable quantum information”. In: *arXiv* (Mar. 2005). arXiv: 0503237 [quant-ph]. URL: https://arxiv.org/abs/quant-ph/0503237 (cit. on pp. 16, 38).

[100] R. Filip. “Quantum interface to a noisy system through a single kind of arbitrary Gaussian coupling with limited interaction strength”. In: *Phys. Rev. A* **80** (2 Aug. 2009), p. 022304. DOI: 10.1103/PhysRevA.80.022304. URL: http://link.aps.org/doi/10.1103/PhysRevA.80.022304 (cit. on p. 105).

[101] M. Fleischhauer, A. Imamoglu and J. P. Marangos. “Electromagnetically induced transparency: Optics in coherent media”. In: *Rev. Mod. Phys.* **77** (2 July 2005), pp. 633–673. DOI: 10.1103/RevModPhys.77.633. URL: http://link.aps.org/doi/10.1103/RevModPhys.77.633 (cit. on p. 20).

[102] S. Forstner et al. “Cavity Optomechanical Magnetometer”. In: *Phys. Rev. Lett.* **108** (12 Mar. 2012), p. 120801. DOI: 10.1103/PhysRevLett.108.120801. URL: http://link.aps.org/doi/10.1103/PhysRevLett.108.120801 (cit. on p. 105).

[103] A. S. Foundation. *wxWidgets*. Version 3.0.2. Oct. 2014. URL: https://www.wxwidgets.org/ (cit. on p. 130).

[104] P. A. Franken, A. E. Hill, C. W. Peters and G. Weinreich. "Generation of Optical Harmonics". In: *Phys. Rev. Lett.* **7** (4 Aug. 1961), pp. 118–119. DOI: 10.1103/PhysRevLett.7.118. URL: http://link.aps.org/doi/10.1103/PhysRevLett.7.118 (cit. on p. 53).

[105] *freeglut*. Version 3.0.0. Mar. 2015. URL: http://freeglut.sourceforge.net/ (cit. on p. 129).

[106] A. Freise and K. A. Strain. "Interferometer Techniques for Gravitational-Wave Detection". In: *Living Rev. Relativity* **13** (2010). DOI: doi:10.12942/lrr-2010-1. URL: http://www.livingreviews.org/lrr-2010-1 (cit. on pp. 55, 66, 81).

[107] L. Galleani. "The dynamic Allan variance II: a fast computational algorithm". In: *IEEE Transactions on Ultrasonics, Ferroelectrics, and Frequency Control* **57**.1 (Jan. 2010), pp. 182–188. DOI: 10.1109/TUFFC.2010.1396. URL: http://ieeexplore.ieee.org/xpl/articleDetails.jsp?arnumber=5361540 (cit. on p. 61).

[108] Y. Gao, P. M. Anisimov, C. F. Wildfeuer, J. Luine, H. Lee and J. P. Dowling. "Super-resolution at the shot-noise limit with coherent states and photon-number-resolving detectors". In: *J. Opt. Soc. Am. B* **27**.6 (June 2010), A170–A174. DOI: 10.1364/JOSAB.27.00A170. URL: http://josab.osa.org/abstract.cfm?URI=josab-27-6-A170 (cit. on p. 45).

[109] C. W. Gardiner and M. J. Collett. "Input and output in damped quantum systems: Quantum stochastic differential equations and the master equation". In: *Phys. Rev. A* **31** (6 June 1985), pp. 3761–3774. DOI: 10.1103/PhysRevA.31.3761. URL: http://link.aps.org/doi/10.1103/PhysRevA.31.3761 (cit. on pp. 77, 78).

[110] C. Gardiner and P. Zoller, eds. *Quantum Noise*. 3rd ed. Springer-Verlag, 2004. ISBN: 978-3-540-22301-6 (cit. on p. 53).

[111] C. Gardiner and C. Savage. "A multimode quantum theory of a degenerate parametric amplifier in a cavity". In: *Optics Communications* **50**.3 (1984), pp. 173–178. ISSN: 0030-4018. DOI: 10.1016/0030-4018(84)90342-0. URL: http://www.sciencedirect.com/science/article/pii/0030401884903420 (cit. on p. 54).

[112] T. Gehring(Eberle). "Realization of Finite-Size Quantum Key Distribution based on Einstein-Podolsky-Rosen Entangled Light". Dissertation. Gottfried Wilhelm Leibniz Universität Hannover, July 2013 (cit. on pp. 59, 61, 62, 64, 67).

[113] C. Genes, D. Vitali, P. Tombesi, S. Gigan and M. Aspelmeyer. "Ground-state cooling of a micromechanical oscillator: Comparing cold damping and cavity-assisted cooling schemes". In: *Phys. Rev. A* **77** (3 Mar. 2008), p. 033804. DOI: 10.1103/PhysRevA.77.033804. URL: http://link.aps.org/doi/10.1103/PhysRevA.77.033804 (cit. on pp. 73, 74).

[114] C. C. Gerry and P. L. Knight. *Introductory Quantum Optics*. 1st ed. Cambridge University Press, 2005. ISBN: 978-0-521-52735-4 (cit. on pp. 6, 8, 10, 12, 15, 23–25, 27, 29, 34, 35, 39, 53, 74, 77, 113, 118).

[115] V. Giovannetti, S. Lloyd and L. Maccone. "Advances in quantum metrology". In: *Nature Photonics* **5** (4 Mar. 2011), pp. 222–229. URL: http://dx.doi.org/10.1038/nphoton.2011.35 (cit. on pp. 35, 43).

[116] V. Giovannetti, S. Lloyd and L. Maccone. "Quantum-Enhanced Measurements: Beating the Standard Quantum Limit". In: *Science* **306**.5700 (2004), pp. 1330–1336. ISSN: 0036-8075. DOI: 10.1126/science.1104149. URL: http://science.sciencemag.org/content/306/5700/1330 (cit. on p. 35).

[117] R. J. Glauber. "Coherent and Incoherent States of the Radiation Field". In: *Phys. Rev.* **131** (6 Sept. 1963), pp. 2766–2788. URL: http://link.aps.org/doi/10.1103/PhysRev.131.2766 (cit. on p. 8).

[118] J. Goldstein et al. *Scanning Electron Microscopy and X-ray Microanalysis*. 3rd ed. Springer US, 2003. ISBN: 978-0-306-47292-3 (cit. on p. 28).

[119] V. Gorini, A. Kossakowski and E. C. G. Sudarshan. "Completely positive dynamical semigroups of N-level systems". In: *Journal of Mathematical Physics* **17**.5 (1976), pp. 821–825. DOI: 10.1063/1.522979. URL: http://scitation.aip.org/content/aip/journal/jmp/17/5/10.1063/1.522979 (cit. on p. 23).

[120] M. L. Gorodetksy, A. Schliesser, G. Anetsberger, S. Deleglise and T. J. Kippenberg. "Determination of the vacuum optomechanical coupling rate using frequency noise calibration". In: *Opt. Express* **18**.22 (Oct. 2010), pp. 23236–23246. DOI: 10.1364/OE.18.023236. URL: http://www.opticsexpress.org/abstract.cfm?URI=oe-18-22-23236 (cit. on p. 97).

[121] A. A. Gorokhovsky, A. V. Turukhin, R. R. Alfano and W. Phillips. "Photoluminescence vibrational structure of Si center in chemical-vapor deposited diamond". In: *Applied Physics Letters* **66**.1 (1995), pp. 43–45. DOI: 10.1063/1.114176. URL: http://scitation.aip.org/content/aip/journal/apl/66/1/10.1063/1.114176 (cit. on p. 18).

[122] J. P. Goss, P. R. Briddon, M. J. Rayson, S. J. Sque and R. Jones. "Vacancy-impurity complexes and limitations for implantation doping of diamond". In: *Phys. Rev. B* **72** (3 July 2005), p. 035214. DOI: 10.1103/PhysRevB.72.035214. URL: http://link.aps.org/doi/10.1103/PhysRevB.72.035214 (cit. on p. 18).

[123] J. P. Goss, R. Jones, S. J. Breuer, P. R. Briddon and S. Öberg. "The Twelve-Line 1.682 eV Luminescence Center in Diamond and the Vacancy-Silicon Complex". In: *Phys. Rev. Lett.* **77** (14 Sept. 1996), pp. 3041–3044. DOI: 10.1103/PhysRevLett.77.3041. URL: http://link.aps.org/doi/10.1103/PhysRevLett.77.3041 (cit. on pp. 18, 19).

[124] M. Gould, E. R. Schmidgall, S. Dadgostar, F. Hatami and K.-M. C. Fu. "Efficient Extraction of Zero-Phonon-Line Photons from Single Nitrogen-Vacancy Centers in an Integrated GaP-on-Diamond Platform". In: *Phys. Rev. Applied* **6** (1 July 2016), p. 011001. DOI: 10.1103/PhysRevApplied.6.011001. URL: http://link.aps.org/doi/10.1103/PhysRevApplied.6.011001 (cit. on p. 18).

[125] R. Graham, D. F. Walls and W. Zhang. "Laser cooling in a squeezed vacuum". In: *Phys. Rev. A* **44** (11 Dec. 1991), pp. 7777–7784. DOI: 10.1103/PhysRevA.44.7777. URL: http://link.aps.org/doi/10.1103/PhysRevA.44.7777 (cit. on p. 73).

[126] A. D. Greentree. "Viewpoint: Diamond and Silicon Get Entangled". In: *Physics* **7**.93 (2014). DOI: 10.1103/Physics.7.93. URL: http://physics.aps.org/articles/pdf/10.1103/Physics.7.93 (cit. on p. 20).

[127] A. Gruber, A. Dräbenstedt, C. Tietz, L. Fleury, J. Wrachtrup and C. v. Borczyskowski. "Scanning Confocal Optical Microscopy and Magnetic Resonance on Single Defect Centers". In: *Science* **276**.5321 (1997), pp. 2012–2014. ISSN: 0036-8075. DOI: 10.1126/science.276.5321.2012. URL: http://science.sciencemag.org/content/276/5321/2012 (cit. on p. 17).

[128] X. Guo, N. Liu, X. Li, Y. Liu and Z. Y. Ou. "Noise figure improvement and quantum information tapping in a fiber optical parametric amplifier with correlated quantum fields". In: *arXiv* (Apr. 2015). arXiv: 1504.07345 [quant-ph]. URL: http://arxiv.org/abs/1504.07345 (cit. on p. 118).

[129] Y. Hadjar, P. F. Cohadon, C. G. Aminoff, M. Pinard and A. Heidmann. "High-sensitivity optical measurement of mechanical Brownian motion". In: *EPL (Europhysics Letters)* **47**.5 (1999), p. 545. URL: http://stacks.iop.org/0295-5075/47/i=5/a=545 (cit. on p. 101).

[130] B. Hage. "Purification and distillation of continuous variable entanglement". Dissertation. Gottfried Wilhelm Leibniz Universität Hannover, Jan. 2010 (cit. on pp. 59, 61, 67).

[131] L. T. Hall, C. D. Hill, J. H. Cole and L. C. L. Hollenberg. "Ultrasensitive diamond magnetometry using optimal dynamic decoupling". In: *Phys. Rev. B* **82** (4 July 2010), p. 045208. DOI: 10.1103/PhysRevB.82.045208. URL: http://link.aps.org/doi/10.1103/PhysRevB.82.045208 (cit. on p. 17).

[132] G. I. Harris, D. L. McAuslan, E. Sheridan, Y. Sachkou, C. Baker and W. P. Bowen. "Laser cooling and control of excitations in superfluid helium". In: *Nature Physics* **12**.8 (Apr. 2016), pp. 788–793. DOI: 10.1038/nphys3714. URL: http://www.nature.com/nphys/journal/v12/n8/full/nphys3714.html (cit. on p. 101).

[133] E. Hecht. *Optics*. 4th ed. Addison-Wesley Longman, 2002. ISBN: 0-321-18878-0 (cit. on pp. 4, 13, 25, 34, 35, 67, 130).

[134] W. Heisenberg. *Die physikalischen Prinzipien der Quantentheorie*. German. 5th ed. S. Hirzel Verlag, 2008. ISBN: 978-3-7776-1616-2 (cit. on p. 34).

[135] C. W. Helstrom. "Minimum mean-squared error of estimates in quantum statistics". In: *Physics Letters A* **25**.2 (1967), pp. 101–102. ISSN: 0375-9601. DOI: 10.1016/0375-9601(67)90366-0. URL: http://www.sciencedirect.com/science/article/pii/0375960167903660 (cit. on p. 43).

[136] C. W. Helstrom. "Quantum detection and estimation theory". In: *Journal of Statistical Physics* **1**.2 (1969), pp. 231–252. ISSN: 1572-9613. DOI: 10.1007/BF01007479. URL: http://dx.doi.org/10.1007/BF01007479 (cit. on p. 35).

[137] B. Hensen et al. "Loophole-free Bell inequality violation using electron spins separated by 1.3 kilometres". In: *Nature* **526**.7575 (Oct. 2015), pp. 682–686. DOI: 10.1038/nature15759. URL: http://www.nature.com/nature/journal/v526/n7575/full/nature15759.html (cit. on p. 17).

[138] C. Hepp et al. "Electronic Structure of the Silicon Vacancy Color Center in Diamond". In: *Phys. Rev. Lett.* **112** (3 Jan. 2014), p. 036405. DOI: 10.1103/PhysRevLett.112.036405. URL: http://link.aps.org/doi/10.1103/PhysRevLett.112.036405 (cit. on p. 19).

[139] M. Hilbert and P. López. "The World's Technological Capacity to Store, Communicate, and Compute Information". In: *Science* **332**.6025 (Apr. 2011), pp. 60–65. URL: http://www.sciencemag.org/content/332/6025/60 (cit. on p. 106).

[140] U. B. Hoff, J. Kollath-Bönig, J. S. Neergaard-Nielsen and U. L. Andersen. "Measurement-Induced Macroscopic Superposition States in Cavity Optomechanics". In: *Phys. Rev. Lett.* **117** (14 Sept. 2016), p. 143601. DOI: 10.1103/PhysRevLett.117.143601. URL: http://link.aps.org/doi/10.1103/PhysRevLett.117.143601 (cit. on p. 105).

[141] U. B. Hoff et al. "Quantum-enhanced micromechanical displacement sensitivity". In: *Opt. Lett.* **38**.9 (May 2013), pp. 1413–1415. DOI: 10.1364/OL.38.001413. URL: http://ol.osa.org/abstract.cfm?URI=ol-38-9-1413 (cit. on p. 74).

[142] P. Horowitz and W. Hill. *The Art Of Electronics*. 2nd ed. Cambridge University Press, 1989. ISBN: 978-0521370950 (cit. on pp. 12, 144).

[143] D. A. Howe. *Total Variance Explained*. Joint Meeting of the 13th European Frequency and Time Forum and the 1999 IEEE International Frequency Control Symposium. 1999. URL: http://www.tf.nist.gov/timefreq/general/pdf/1307.pdf (visited on 12/08/2016) (cit. on p. 61).

[144] Z. Hradil, R. Myška, T. Opatrný and J. Bajer. "Entropy of phase measurement: Quantum phase via quadrature measurement". In: *Phys. Rev. A* **53** (6 June 1996), pp. 3738–3742. DOI: 10.1103/PhysRevA.53.3738. URL: http://link.aps.org/doi/10.1103/PhysRevA.53.3738 (cit. on p. 43).

[145] S. F. Huelga, C. Macchiavello, T. Pellizzari, A. K. Ekert, M. B. Plenio and J. I. Cirac. "Improvement of Frequency Standards with Quantum Entanglement". In: *Phys. Rev. Lett.* **79** (20 Nov. 1997), pp. 3865–3868. DOI: 10.1103/PhysRevLett.79.3865. URL: http://link.aps.org/doi/10.1103/PhysRevLett.79.3865 (cit. on p. 35).

[146] E. H. Huntington et al. "Demonstration of the spatial separation of the entangled quantum sidebands of an optical field". In: *Phys. Rev. A* **71** (4 Apr. 2005), p. 041802. DOI: 10.1103/PhysRevA.71.041802. URL: http://link.aps.org/doi/10.1103/PhysRevA.71.041802 (cit. on p. 54).

[147] J. R. Hutchinson. "Axisymmetric Flexural Vibrations of a Thick Free Circular Plate". In: *Journal of Applied Mechanics* **46** (1 Mar. 1979), pp. 139–144. DOI: 10.1115/1.3424485. URL: http://dx.doi.org/10.1115/1.3424485 (cit. on p. 76).

[148] S. D. Huver, C. F. Wildfeuer and J. P. Dowling. "Entangled Fock states for robust quantum optical metrology, imaging, and sensing". In: *Phys. Rev. A* **78** (6 Dec. 2008), p. 063828. DOI: 10.1103/PhysRevA.78.063828. URL: http://link.aps.org/doi/10.1103/PhysRevA.78.063828 (cit. on p. 47).

[149] K. Iakoubovskii, G. J. Adriaenssens and M. Nesladek. "Photochromism of vacancy-related centres in diamond". In: *Journal of Physics: Condensed Matter* **12**.2 (2000), p. 189. URL: http://stacks.iop.org/0953-8984/12/i=2/a=308 (cit. on p. 18).

[150] Y. Israel, I. Afek, S. Rosen, O. Ambar and Y. Silberberg. "Experimental tomography of NOON states with large photon numbers". In: *Phys. Rev. A* **85** (2 Feb. 2012), p. 022115. DOI: 10.1103/PhysRevA.85.022115. URL: http://link.aps.org/doi/10.1103/PhysRevA.85.022115 (cit. on p. 38).

[151] K. Jacobs. *Quantum Measurement Theory and its Applications*. Cambridge University Press, 2014. ISBN: 9781107025486 (cit. on p. 72).

[152] K. D. Jahnke. "Low temperature spectroscopy of single colour centres in diamond". Dissertation. Universität Ulm, Mar. 2015 (cit. on pp. 21, 30).

[153] K. D. Jahnke et al. "Electron–phonon processes of the silicon-vacancy centre in diamond". In: *New Journal of Physics* **17**.4 (2015), p. 043011. URL: http://stacks.iop.org/1367-2630/17/i=4/a=043011 (cit. on pp. 20, 26).

[154] U. Jantzen et al. "Nanodiamonds carrying silicon-vacancy quantum emitters with almost lifetime-limited linewidths". In: *New Journal of Physics* **18**.7 (2016), p. 073036. URL: http://stacks.iop.org/1367-2630/18/i=7/a=073036 (cit. on pp. 29, 30).

[155] K. Jiang, H. Lee, C. C. Gerry and J. P. Dowling. "Super-resolving quantum radar: Coherent-state sources with homodyne detection suffice to beat the diffraction limit". In: *Journal of Applied Physics* **114**.19, 193102 (2013). DOI: 10.1063/1.4829016. URL: http://scitation.aip.org/content/aip/journal/jap/114/19/10.1063/1.4829016 (cit. on p. 47).

[156] R.-B. Jin et al. "Detection-dependent six-photon NOON state interference". In: *arXiv* (July 2016). arXiv: 1607.00926 [quant-ph]. URL: http://arxiv.org/abs/1607.00926v1 (cit. on p. 38).

[157] J. R. Johansson, P. D. Nation and F. Nori. "QuTiP 2: A Python framework for the dynamics of open quantum systems". In: *Computer Physics Communications* **184**.4 (2013), pp. 123–1240. ISSN: 0010-4655. DOI: 10.1016/j.cpc.2012.11.019. URL: http://www.sciencedirect.com/science/article/pii/S0010465512003955 (cit. on p. 24).

[158] V. Josse, M. Sabuncu, N. J. Cerf, G. Leuchs and U. L. Andersen. "Universal Optical Amplification without Nonlinearity". In: *Phys. Rev. Lett.* **96** (16 Apr. 2006), p. 163602. DOI: 10.1103/PhysRevLett.96.163602. URL: http://link.aps.org/doi/10.1103/PhysRevLett.96.163602 (cit. on pp. 107, 115).

[159] M. Kacprowicz, R. Demkowicz-Dobrzanski, W. Wasilewski, K. Banaszek and I. A. Walmsley. "Experimental quantum-enhanced estimation of a lossy phase shift". In: *Nature Photonics* **4** (6 June 2010), pp. 357–360. DOI: 10.1038/nphoton.2010.39. URL: http://dx.doi.org/10.1038/nphoton.2010.39 (cit. on p. 35).

[160] H. Kaupp, C. Deutsch, H.-C. Chang, J. Reichel, T. W. Hänsch and D. Hunger. "Scaling laws of the cavity enhancement for nitrogen-vacancy centers in diamond". In: *Phys. Rev. A* **88** (5 Nov. 2013), p. 053812. DOI: 10.1103/PhysRevA.88.053812. URL: http://link.aps.org/doi/10.1103/PhysRevA.88.053812 (cit. on p. 33).

[161] H. Kaupp et al. "Purcell-enhanced single-photon emission from nitrogen-vacancy centers coupled to a tunable microcavity". In: *arXiv* (2016). arXiv: 1606.00167v2 [quant-ph]. URL: https://arxiv.org/abs/1606.00167v2 (cit. on p. 18).

[162] T. A. Kennedy, J. S. Colton, J. E. Butler, R. C. Linares and P. J. Doering. "Long coherence times at 300 K for nitrogen-vacancy center spins in diamond grown by chemical vapor deposition". In: *Applied Physics Letters* **83**.20 (2003), pp. 4190–4192. DOI: 10.1063/1.1626791. URL: http://scitation.aip.org/content/aip/journal/apl/83/20/10.1063/1.1626791 (cit. on p. 17).

[163] H. Kerdoncuff. "Squeezing-enhanced feedback cooling of a microresonator". PhD thesis. Technical University of Denmark, Oct. 2015 (cit. on pp. 74, 80, 92, 97).

[164] H. Kerdoncuff, U. B. Hoff, G. I. Harris, W. P. Bowen and U. L. Andersen. "Squeezing-enhanced measurement sensitivity in a cavity optomechanical system". In: *Annalen der Physik* **527**.1-2 (2015), pp. 107–114. ISSN: 1521-3889. DOI: 10.1002/andp.201400171. URL: http://dx.doi.org/10.1002/andp.201400171 (cit. on p. 80).

[165] D. Kleckner and D. Bouwmeester. "Sub-kelvin optical cooling of a micromechanical resonator". In: *Nature* **444** (June 2006), pp. 75–78. URL: http://www.nature.com/nature/journal/v444/n7115/full/nature05231.html (cit. on p. 73).

[166] J. Kong, F. Hudelist, Z. Y. Ou and W. Zhang. "Cancellation of Internal Quantum Noise of an Amplifier by Quantum Correlation". In: *Phys. Rev. Lett.* **111** (3 July 2013), p. 033608. DOI: 10.1103/PhysRevLett.111.033608. URL: http://link.aps.org/doi/10.1103/PhysRevLett.111.033608 (cit. on pp. 107, 118).

[167] R. Kumar, E. Barrios, A. MacRae, E. Cairns, E. H. Huntington and A. I. Lvovsky. "Versatile Wideband Balanced Detector for Quantum Optical Homodyne Tomography". In: *Optics Communications* **285**.24 (2012), pp. 5259–5267. ISSN: 0030-4018. URL: http://www.sciencedirect.com/science/article/pii/S0030401812008255 (cit. on pp. 14, 62).

[168] W. E. Lamb. "Anti-photon". In: *Applied Physics B* **60**.2 (1995), pp. 77–84. ISSN: 1432-0649. DOI: 10.1007/BF01135846. URL: http://dx.doi.org/10.1007/BF01135846 (cit. on p. 5).

[169] K. H. Lee, T. G. McRae, G. I. Harris, J. Knittel and W. P. Bowen. "Cooling and Control of a Cavity Optoelectromechanical System". In: *Phys. Rev. Lett.* **104** (12 Mar. 2010), p. 123604. DOI: 10.1103/PhysRevLett.104.123604. URL: http://link.aps.org/doi/10.1103/PhysRevLett.104.123604 (cit. on pp. 73, 86, 100, 102).

[170] M. Lesik et al. "Production of bulk NV centre arrays by shallow implantation and diamond CVD overgrowth". In: *physica status solidi (a)* (2016). ISSN: 1862-6319. DOI: 10.1002/pssa.201600219. URL: http://dx.doi.org/10.1002/pssa.201600219 (cit. on p. 17).

[171] J. A. Levenson, I. Abram, T. Rivera, P. Fayolle, J. C. Garreau and P. Grangier. "Quantum optical cloning amplifier". In: *Phys. Rev. Lett.* **70** (3 Jan. 1993), pp. 267–270. DOI: 10.1103/PhysRevLett.70.267. URL: http://link.aps.org/doi/10.1103/PhysRevLett.70.267 (cit. on p. 107).

[172] J. A. Levenson, I. Abram, T. Rivera and P. Grangier. "Reduction of quantum noise in optical parametric amplification". In: *J. Opt. Soc. Am. B* **10**.11 (Nov. 1993), pp. 2233–2238. DOI: 10.1364/JOSAB.10.002233. URL: http://josab.osa.org/abstract.cfm?URI=josab-10-11-2233 (cit. on pp. 106, 107).

[173] T. Li, S. Kheifets and M. G. Raizen. "Millikelvin cooling of an optically trapped microsphere in vacuum". In: *Nature Physics* **7**.7 (2011), pp. 527–530. DOI: 10.1038/nphys1952. URL: http://www.nature.com/nphys/journal/v7/n7/full/nphys1952.html (cit. on p. 73).

[174] E. M. Lifshitz and L. P. Pitaevskii. *Statistical Physics*. 3rd ed. Vol. 5.1. Course of Theoretical Physics. Pergamon Press, 1980. ISBN: 0-08-023038-5 (cit. on pp. 87, 97).

[175] LIGO Scientific Collaboration. "Enhanced sensitivity of the LIGO gravitational wave detector by using squeezed states of light". In: *Nature Photonics* **7** (July 2013), pp. 613–619. DOI: 10.1038/nphoton.2013.177. URL: http://www.nature.com/nphoton/journal/v7/n8/abs/nphoton.2013.177.html (cit. on p. 105).

[176] LIGO Scientific Collaboration. "Observation of a kilogram-scale oscillator near its quantum ground state". In: *New Journal of Physics* **11**.7 (2009), p. 073032. URL: http://dx.doi.org/10.1088/1367-2630/11/7/073032 (cit. on p. 73).

[177] LIGO Scientific Collaboration. "Observation of Gravitational Waves from a Binary Black Hole Merger". In: *Phys. Rev. Lett.* **116** (6 Feb. 2016), p. 061102. DOI: 10.1103/PhysRevLett.116.061102. URL: http://link.aps.org/doi/10.1103/PhysRevLett.116.061102 (cit. on pp. 34, 72).

[178] G. Lindblad. "On the generators of quantum dynamical semigroups". In: *Communications in Mathematical Physics* **48**.2 (1976), pp. 119–130. ISSN: 1432-0916. DOI: 10.1007/BF01608499. URL: http://dx.doi.org/10.1007/BF01608499 (cit. on p. 23).

[179] A. E. Lita, A. J. Miller and S. W. Nam. "Counting near-infrared single-photons with 95% efficiency". In: *Opt. Express* **16**.5 (Mar. 2008), pp. 3032–3040. DOI: 10.1364/OE.16.003032. URL: http://www.opticsexpress.org/abstract.cfm?URI=oe-16-5-3032 (cit. on p. 38).

[180] L. B. Loeb. *The Kinetic Theory of Gases*. 3rd ed. Dover Publications, 2004. ISBN: 978-0486495729 (cit. on p. 72).

[181] R. Loudon. *The Quantum Theory Of Light*. 3rd ed. Oxford University Press, 2000. ISBN: 978-0198501763 (cit. on pp. 12, 27, 35, 74, 118).

[182] W. H. Louisell. *Radiation and noise in quantum electronics*. McGraw-Hill physical and quantum electronics series. McGraw-Hill, 1964. ISBN: 978-0070387614 (cit. on p. 106).

[183] W. H. Louisell, A. Yariv and A. E. Siegman. "Quantum Fluctuations and Noise in Parametric Processes. I." In: *Phys. Rev.* **124** (6 Dec. 1961), pp. 1646–1654. DOI: 10.1103/PhysRev.124.1646. URL: http://link.aps.org/doi/10.1103/PhysRev.124.1646 (cit. on p. 53).

[184] H. Lutz and W. Wendt. *Taschenbuch der Regelungstechnik*. German. 7th ed. Harri Deutsch Verlag, 2007. ISBN: 978-3817118076 (cit. on pp. 85, 138, 141).

[185] A. I. Lvovsky. "Squeezed light". In: *arXiv* (Jan. 2014). arXiv: 1401.4118v1 [quant-ph]. URL: http://arxiv.org/abs/1401.4118v1 (cit. on pp. 14, 53, 54, 118).

[186] A. I. Lvovsky, H. Hansen, T. Aichele, O. Benson, J. Mlynek and S. Schiller. "Quantum State Reconstruction of the Single-Photon Fock State". In: *Phys. Rev. Lett.* **87** (5 July 2001), p. 050402. DOI: 10.1103/PhysRevLett.87.050402. URL: http://link.aps.org/doi/10.1103/PhysRevLett.87.050402 (cit. on p. 38).

[187] D. Malacara, ed. *Optical Shop Testing*. 3rd ed. John Wiley & Sons, 2007. ISBN: 978-0-471-48404-2 (cit. on pp. 34, 152).

[188] Z. Malkin. "Application of the Allan Variance to Time Series Analysis in Astrometry and Geodesy: A Review". In: *IEEE Transactions on Ultrasonics, Ferroelectrics, and Frequency Control* **63**.4 (Apr. 2016), pp. 582–589. ISSN: 0885-3010. DOI: 10.1109/TUFFC.2015.2496337. URL: http://dx.doi.org/10.1109/TUFFC.2015.2496337 (cit. on p. 61).

[189] S. Mancini, D. Vitali and P. Tombesi. "Optomechanical Cooling of a Macroscopic Oscillator by Homodyne Feedback". In: *Phys. Rev. Lett.* **80** (4 Jan. 1998), pp. 688–691. DOI: 10.1103/PhysRevLett.80.688. URL: http://link.aps.org/doi/10.1103/PhysRevLett.80.688 (cit. on pp. 73, 82).

[190] D. W. Marquardt. "An Algorithm for the Least-Squares Estimation of Nonlinear Parameters". In: *SIAM Journal of Applied Mathematics* **11**.2 (1963), pp. 431–441. DOI: 10.1137/0111030. URL: http://epubs.siam.org/doi/abs/10.1137/0111030 (cit. on p. 129).

[191] W. Marshall, C. Simon, R. Penrose and D. Bouwmeester. "Towards Quantum Superpositions of a Mirror". In: *Phys. Rev. Lett.* **91** (13 Sept. 2003), p. 130401. DOI: 10.1103/PhysRevLett.91.130401. URL: http://link.aps.org/doi/10.1103/PhysRevLett.91.130401 (cit. on p. 72).

[192] A. A. Michelson. "The relative motion of the Earth and of the luminiferous ether". In: *American Journal of Science*. 3rd ser. **22**.128 (1881), pp. 120–129. DOI: 10.2475/ajs.s3-22.128.120. URL: http://www.ajsonline.org/content/s3-22/128/120.short (cit. on p. 34).

[193] A. A. Michelson and E. W. Morley. "On the relative motion of the Earth and the luminiferous ether". In: *American Journal of Science*. 3rd ser. **34**.203 (1887), pp. 333–345. DOI: 10.2475/ajs.s3-34.203.333. URL: http://www.ajsonline.org/content/s3-34/203/333.short (cit. on p. 34).

[194] M. Mičuda et al. "Highly stable polarization independent Mach-Zehnder interferometer". In: *Review of Scientific Instruments* **85**.8, 083103 (2014). DOI: 10.1063/1.4891702. URL: http://scitation.aip.org/content/aip/journal/rsi/85/8/10.1063/1.4891702 (cit. on p. 63).

[195] M. Minsky. "Memoir on inventing the confocal scanning microscope". In: *Scanning* **10**.4 (1988), pp. 128–138. ISSN: 1932-8745. DOI: 10.1002/sca.4950100403. URL: http://dx.doi.org/10.1002/sca.4950100403 (cit. on p. 25).

[196] G. P. Miroshnichenko and A. V. Gleim. "Quantum Hamiltonian theory of an electro-optical modulator". In: *Optics and Spectroscopy* **119**.1 (2015), pp. 92–97. ISSN: 1562-6911. DOI: 10.1134/S0030400X1507019X. URL: http://dx.doi.org/10.1134/S0030400X1507019X (cit. on p. 66).

[197] M. W. Mitchell, J. S. Lundeen and A. M. Steinberg. “Super-resolving phase measurements with a multiphoton entangled state”. In: *Nature* **429** (6988 May 2004), pp. 161–164. URL: http://dx.doi.org/10.1038/nature02493 (cit. on pp. 35, 38).

[198] W. Mlak and M. Słociński. “Quantum phase and circular operators”. In: *Universitatis Iagellonicae Acta Mathematica* (29 1992), pp. 133–144. URL: http://www.emis.de/journals/UIAM/actamath/PDF/29-133-144.pdf (cit. on p. 6).

[199] S. S. Moliver. “Electronic structure of neutral silicon-vacancy complex in diamond”. In: *Technical Physics* **48**.11 (2003), pp. 1449–1453. ISSN: 1090-6525. DOI: 10.1134/1.1626778. URL: http://dx.doi.org/10.1134/1.1626778 (cit. on p. 31).

[200] A. Monras. “Optimal phase measurements with pure Gaussian states”. In: *Phys. Rev. A* **73** (3 Mar. 2006), p. 033821. DOI: 10.1103/PhysRevA.73.033821. URL: http://link.aps.org/doi/10.1103/PhysRevA.73.033821 (cit. on pp. 38, 43).

[201] C. R. Müller et al. “Evading Vacuum Noise: Wigner Projections or Husimi Samples?” In: *Phys. Rev. Lett.* **117** (7 Aug. 2016), p. 070801. DOI: 10.1103/PhysRevLett.117.070801. URL: http://link.aps.org/doi/10.1103/PhysRevLett.117.070801 (cit. on p. 16).

[202] T. Müller et al. “Optical signatures of silicon-vacancy spins in diamond”. In: *Nature Communications* **5**.3328 (Feb. 2014). DOI: 10.1038/ncomms4328. URL: http://www.nature.com/articles/ncomms4328 (cit. on p. 21).

[203] J. A. Nelder and R. Mead. “A Simplex Method for Function Minimization”. In: *The Computer Journal* **7** (1965), pp. 308–313. DOI: 10.1093/comjnl/7.4.308. URL: http://comjnl.oxfordjournals.org/content/7/4/308.full.pdf+html (cit. on p. 129).

[204] K. Nemoto et al. “Photonic Quantum Networks formed from NV^- centers”. In: *Scientific Reports* **6** (May 2016). DOI: 10.1038/srep26284. URL: http://www.nature.com/articles/srep26284 (cit. on p. 17).

[205] E. Neu, M. Fischer, S. Gsell, M. Schreck and C. Becher. “Fluorescence and polarization spectroscopy of single silicon vacancy centers in heteroepitaxial nanodiamonds on iridium”. In: *Phys. Rev. B* **84** (20 Nov. 2011), p. 205211. DOI: 10.1103/PhysRevB.84.205211. URL: http://link.aps.org/doi/10.1103/PhysRevB.84.205211 (cit. on pp. 19, 27).

[206] E. Neu et al. “Low-temperature investigations of single silicon vacancy colour centres in diamond”. In: *New Journal of Physics* **15**.4 (2013), p. 043005. URL: http://stacks.iop.org/1367-2630/15/i=4/a=043005 (cit. on p. 21).

[207] E. Neu et al. “Low temperature investigations and surface treatments of colloidal narrowband fluorescent nanodiamonds”. In: *Journal of Applied Physics* **113**.20 (2013). DOI: 10.1063/1.4807398. URL: http://scitation.aip.org/content/aip/journal/jap/113/20/10.1063/1.4807398 (cit. on p. 21).

[208] E. Neu et al. “Narrowband fluorescent nanodiamonds produced from chemical vapor deposition films”. In: *Applied Physics Letters* **98**.24, 243107 (2011). DOI: 10.1063/1.3599608. URL: http://scitation.aip.org/content/aip/journal/apl/98/24/10.1063/1.3599608 (cit. on pp. 18, 21).

[209] E. F. Nichols and G. F. Hull. “A Preliminary Communication on the Pressure of Heat and Light Radiation”. In: *Phys. Rev. (Series I)* **13** (5 Nov. 1901), pp. 307–320. DOI: 10.1103/PhysRevSeriesI.13.307. URL: http://link.aps.org/doi/10.1103/PhysRevSeriesI.13.307 (cit. on p. 72).

[210] S. Nimmrichter, K. Hornberger and K. Hammerer. "Optomechanical Sensing of Spontaneous Wave-Function Collapse". In: *Phys. Rev. Lett.* **113** (2 July 2014), p. 020405. DOI: 10.1103/PhysRevLett.113.020405. URL: http://link.aps.org/doi/10.1103/PhysRevLett.113.020405 (cit. on p. 72).

[211] R. J. Noll. "Zernike polynomials and atmospheric turbulence". In: *J. Opt. Soc. Am.* **66**.3 (Mar. 1976), pp. 207–211. DOI: 10.1364/JOSA.66.000207. URL: http://www.osapublishing.org/abstract.cfm?URI=josa-66-3-207 (cit. on p. 152).

[212] D. D. Nolte. "The tangled tale of phase space". In: *Physics Today* **63**.4 (2010), p. 33. DOI: 10.1063/1.3397041. URL: http://scitation.aip.org/content/aip/magazine/physicstoday/article/63/4/10.1063/1.3397041 (cit. on p. 15).

[213] R. A. Norte, J. P. Moura and S. Gröblacher. "Mechanical Resonators for Quantum Optomechanics Experiments at Room Temperature". In: *Phys. Rev. Lett.* **116** (14 Apr. 2016), p. 147202. DOI: 10.1103/PhysRevLett.116.147202. URL: http://link.aps.org/doi/10.1103/PhysRevLett.116.147202 (cit. on p. 105).

[214] L. Novotny and B. Hecht. *Principles of Nano-Optics*. 2nd ed. Cambridge University Press, 2012. ISBN: 9781107005464 (cit. on p. 25).

[215] *OpenCV*. Version 2.4.11. Feb. 2015. URL: http://opencv.org/ (cit. on p. 129).

[216] *OpenGL*. Version 4.1. July 2010. URL: https://www.opengl.org/ (cit. on p. 129).

[217] *OpenMP*. Version 4.0. July 2013. URL: http://openmp.org/wp/ (cit. on p. 129).

[218] A. Ourjoumtsev. "Étude théorique et expérimentale de superpositions quantiques cohérentes et d'états intriqués non-Gaussiens de la lumière". French. Thèse. Université Paris-Sud XI, Nov. 2007 (cit. on p. 61).

[219] R. Paschotta. *Optical Heterodyne Detection*. Encyclopedia entry. http://www.rp-photonics.com/optical_heterodyne_detection.html: RP Photonics Consulting GmbH, Mar. 2016 (cit. on p. 12).

[220] A. Peres. *Quantum Theory: Concepts and Methods*. Kluwer Academic Publishers, 2002. ISBN: 0-792-33632-1 (cit. on p. 7).

[221] R. W. Peterson et al. "Laser Cooling of a Micromechanical Membrane to the Quantum Backaction Limit". In: *Phys. Rev. Lett.* **116** (6 Feb. 2016), p. 063601. DOI: 10.1103/PhysRevLett.116.063601. URL: http://link.aps.org/doi/10.1103/PhysRevLett.116.063601 (cit. on p. 83).

[222] I. Pikovski, M. R. Vanner, M. Aspelmeyer, M. S. Kim and Č. Brukner. "Probing Planck-scale physics with quantum optics". In: *Nature Physics* **8** (May 2012), pp. 393–397. DOI: 10.1038/nphys2262 (cit. on p. 72).

[223] M. Pinard, Y. Hadjar and A. Heidmann. "Effective mass in quantum effects of radiation pressure". In: *The European Physical Journal D - Atomic, Molecular, Optical and Plasma Physics* **7**.1 (1999), pp. 107–116. DOI: 10.1007/s100530050354. URL: http://dx.doi.org/10.1007/s100530050354 (cit. on p. 84).

[224] M. Poggio, C. L. Degen, H. J. Mamin and D. Rugar. "Feedback Cooling of a Cantilever's Fundamental Mode below 5 mK". In: *Phys. Rev. Lett.* **99** (1 July 2007), p. 017201. DOI: 10.1103/PhysRevLett.99.017201. URL: http://link.aps.org/doi/10.1103/PhysRevLett.99.017201 (cit. on pp. 73, 86, 99, 100).

[225] W. H. Press, S. A. Teukolsky, W. T. Vetterling and B. P. Flannery. *Numerical Recipes in C: The Art of Scientific Computing*. 2nd ed. Cambridge University Press, 1992. ISBN: 0-521-43108-5 (cit. on pp. 129, 152).

[226] T. P. Purdy, R. W. Peterson and C. A. Regal. "Observation of Radiation Pressure Shot Noise on a Macroscopic Object". In: *Science* **339** (2013), pp. 801–804. DOI: 10.1126/science.1231282. URL: http://science.sciencemag.org/content/339/6121/801 (cit. on p. 83).

[227] J. G. Rarity et al. "Two-photon interference in a Mach-Zehnder interferometer". In: *Phys. Rev. Lett.* **65** (11 Sept. 1990), pp. 1348–1351. DOI: 10.1103/PhysRevLett.65.1348. URL: http://link.aps.org/doi/10.1103/PhysRevLett.65.1348 (cit. on p. 35).

[228] K. J. Resch et al. "Time-Reversal and Super-Resolving Phase Measurements". In: *Phys. Rev. Lett.* **98** (22 May 2007), p. 223601. DOI: 10.1103/PhysRevLett.98.223601. URL: http://link.aps.org/doi/10.1103/PhysRevLett.98.223601 (cit. on pp. 35, 45).

[229] O. Reynolds. "On Certain Dimensional Properties of Matter in the Gaseous State." In: *Philosophical Transactions of the Royal Society of London* **170** (1879), pp. 727–845. DOI: 10.1098/rstl.1879.0078. URL: http://rstl.royalsocietypublishing.org/content/170/727.short (cit. on p. 72).

[230] J. Riedrich-Möller et al. "Deterministic Coupling of a Single Silicon-Vacancy Color Center to a Photonic Crystal Cavity in Diamond". In: *Nano Letters* **14**.9 (2014), pp. 5281–5287. DOI: 10.1021/nl502327b. URL: http://pubs.acs.org/doi/abs/10.1021/nl502327b (cit. on p. 21).

[231] H. P. Robertson. "The Uncertainty Principle". In: *Phys. Rev.* **34** (1 July 1929), pp. 163–164. DOI: 10.1103/PhysRev.34.163. URL: http://link.aps.org/doi/10.1103/PhysRev.34.163 (cit. on p. 9).

[232] L. J. Rogers et al. "Multiple intrinsically identical single-photon emitters in the solid state". In: *Nature Communications* **5**.4739 (2014). DOI: 10.1038/ncomms5739. URL: http://www.nature.com/articles/ncomms5739 (cit. on pp. 21, 30, 31).

[233] L. J. Rogers et al. "All-Optical Initialization, Readout, and Coherent Preparation of Single Silicon-Vacancy Spins in Diamond". In: *Phys. Rev. Lett.* **113** (26 Dec. 2014), p. 263602. DOI: 10.1103/PhysRevLett.113.263602. URL: http://link.aps.org/doi/10.1103/PhysRevLett.113.263602 (cit. on pp. 20, 21).

[234] L. J. Rogers et al. "Electronic structure of the negatively charged silicon-vacancy center in diamond". In: *Phys. Rev. B* **89** (23 June 2014), p. 235101. DOI: 10.1103/PhysRevB.89.235101. URL: http://link.aps.org/doi/10.1103/PhysRevB.89.235101 (cit. on pp. 19, 20).

[235] O. Romero-Isart. "Quantum superposition of massive objects and collapse models". In: *Phys. Rev. A* **84** (5 Nov. 2011), p. 052121. DOI: 10.1103/PhysRevA.84.052121. URL: http://link.aps.org/doi/10.1103/PhysRevA.84.052121 (cit. on p. 72).

[236] A. Royer. "Wigner function as the expectation value of a parity operator". In: *Phys. Rev. A* **15** (2 Feb. 1977), pp. 449–450. DOI: 10.1103/PhysRevA.15.449. URL: http://link.aps.org/doi/10.1103/PhysRevA.15.449 (cit. on p. 47).

[237] L. A. Rozema, A. Darabi, D. H. Mahler, A. Hayat, Y. Soudagar and A. M. Steinberg. "Violation of Heisenberg's Measurement-Disturbance Relationship by Weak Measurements". In: *Phys. Rev. Lett.* **109** (10 Sept. 2012), p. 100404. DOI: 10.1103/PhysRevLett.109.100404. URL: http://link.aps.org/doi/10.1103/PhysRevLett.109.100404 (cit. on p. 34).

[238] A. H. Safavi-Naeini, J. Chan, J. T. Hill, T. P. M. Alegre, A. Krause and O. Painter. "Observation of Quantum Motion of a Nanomechanical Resonator". In: *Phys. Rev. Lett.* **108** (3 Jan. 2012), p. 033602. DOI: 10.1103/PhysRevLett.108.033602. URL: http://link.aps.org/doi/10.1103/PhysRevLett.108.033602 (cit. on p. 83).

[239] J. J. Sakurai. *Modern quantum mechanics*. Revised edition. Addison-Wesley Publishing Company, 1994. ISBN: 0-201-53929-2 (cit. on p. 40).

[240] B. C. Sanders. "Quantum dynamics of the nonlinear rotator and the effects of continual spin measurement". In: *Phys. Rev. A* **40** (5 Sept. 1989), pp. 2417–2427. DOI: 10.1103/PhysRevA.40.2417. URL: http://link.aps.org/doi/10.1103/PhysRevA.40.2417 (cit. on p. 35).

[241] N. Sangouard, C. Simon, H. de Riedmatten and N. Gisin. "Quantum repeaters based on atomic ensembles and linear optics". In: *Rev. Mod. Phys.* **83** (1 Mar. 2011), pp. 33–80. DOI: 10.1103/RevModPhys.83.33. URL: http://link.aps.org/doi/10.1103/RevModPhys.83.33 (cit. on p. 106).

[242] M. Sasaki and S. Suzuki. "Multimode theory of measurement-induced non-Gaussian operation on wideband squeezed light: Analytical formula". In: *Phys. Rev. A* **73** (4 Apr. 2006), p. 043807. DOI: 10.1103/PhysRevA.73.043807. URL: http://link.aps.org/doi/10.1103/PhysRevA.73.043807 (cit. on p. 62).

[243] V. Scarani, H. Bechmann-Pasquinucci, N. J. Cerf, M. Dušek, N. Lütkenhaus and M. Peev. "The security of practical quantum key distribution". In: *Rev. Mod. Phys.* **81** (3 Sept. 2009), pp. 1301–1350. DOI: 10.1103/RevModPhys.81.1301. URL: http://link.aps.org/doi/10.1103/RevModPhys.81.1301 (cit. on p. 106).

[244] C. Schäfermeier. *alvar*. Version 1.0. Aug. 2015. URL: https://github.com/fys-clesch/alvar (cit. on p. 61).

[245] C. Schäfermeier. *igyba*. Version 1.0. Aug. 2015. URL: https://github.com/fys-clesch/igyba (cit. on p. 129).

[246] C. Schäfermeier. "Towards quantum key distribution in an atmospheric channel". Master thesis. Fachhochschule Münster & Max Planck Institute for the science of light, Oct. 2012 (cit. on p. 5).

[247] G. Schaller. *Open Quantum Systems Far from Equilibrium*. Springer, 2014. ISBN: 978-3-319-03876-6 (cit. on pp. 22, 23).

[248] A. Schliesser, G. Anetsberger, R. Rivière, O. Arcizet and T. J. Kippenberg. "High-sensitivity monitoring of micromechanical vibration using optical whispering gallery mode resonators". In: *New Journal of Physics* **10**.9 (2008), p. 095015. URL: http://stacks.iop.org/1367-2630/10/i=9/a=095015 (cit. on pp. 73, 98).

[249] A. Schliesser, P. Del'Haye, N. Nooshi, K. J. Vahala and T. J. Kippenberg. "Radiation Pressure Cooling of a Micromechanical Oscillator Using Dynamical Backaction". In: *Phys. Rev. Lett.* **97** (24 Dec. 2006), p. 243905. DOI: 10.1103/PhysRevLett.97.243905. URL: http://link.aps.org/doi/10.1103/PhysRevLett.97.243905 (cit. on p. 73).

[250] A. Schließer. "Cavity Optomechanics and Optical Frequency Comb Generation with Silica Whispering-Gallery-Mode Microresonators". Dissertation. Ludwig Maximilian University of Munich, Oct. 2009 (cit. on p. 73).

[251] C. Schmidt et al. "Nonlinear thermal effects in optical microspheres at different wavelength sweeping speeds". In: *Opt. Express* **16**.9 (Apr. 2008), pp. 6285–6301. DOI: 10.1364/OE.16.006285. URL: http://www.opticsexpress.org/abstract.cfm?URI=oe-16-9-6285 (cit. on p. 73).

[252] E. Schrödinger. "Are There Quantum Jumps? Part II". In: *British Journal for the Philosophy of Science* **3**.11 (1952), pp. 233–242. URL: http://www.jstor.org/stable/685266 (cit. on pp. 4, 5).

[253] M. Schukraft et al. “Invited Article: Precision nanoimplantation of nitrogen vacancy centers into diamond photonic crystal cavities and waveguides”. In: *APL Photonics* **1**.2 (2016), p. 020801. DOI: 10.1063/1.4948746. URL: http://scitation.aip.org/content/aip/journal/app/1/2/10.1063/1.4948746 (cit. on pp. 5, 17).

[254] J. H. Shapiro, P. Kumar, B. E. A. Saleh, M. C. Teich, G. Saplakoglu and S.-T. Ho. “Theory of light detection in the presence of feedback”. In: *J. Opt. Soc. Am. B* **4**.10 (Oct. 1987), pp. 1604–1620. DOI: 10.1364/JOSAB.4.001604. URL: http://josab.osa.org/abstract.cfm?URI=josab-4-10-1604 (cit. on pp. 100, 102).

[255] A. E. Siegman. *Lasers*. University Science Books, 1986. ISBN: 978-0935702118 (cit. on pp. 53, 59, 62, 67, 80, 81, 95, 130).

[256] A. Sipahigil et al. “Indistinguishable Photons from Separated Silicon-Vacancy Centers in Diamond”. In: *Phys. Rev. Lett.* **113** (11 Sept. 2014), p. 113602. DOI: 10.1103/PhysRevLett.113.113602. URL: http://link.aps.org/doi/10.1103/PhysRevLett.113.113602 (cit. on pp. 19, 31).

[257] J. L. Skinner and D. Hsu. “Pure dephasing of a two-level system”. In: *The Journal of Physical Chemistry* **90**.21 (1986), pp. 4931–4938. DOI: 10.1021/j100412a013. URL: http://dx.doi.org/10.1021/j100412a013 (cit. on pp. 20, 22).

[258] K. E. Spear and J. P. Dismukes, eds. *Synthetic diamond: Emerging CVD science and technology*. Wiley, 1994. ISBN: 978-0-471-53589-8 (cit. on p. 17).

[259] J. Stachel. “Fresnel’s (Dragging) Coefficient as a Challenge to 19th Century Optics of Moving Bodies”. In: *The Universe of General Relativity*. Ed. by A. J. Kox and J. Eisenstaedt. 3rd ed. Birkhäuser, 2005. Chap. 1 (cit. on p. 34).

[260] H. Sternschulte, K. Thonke, R. Sauer, P. C. Münzinger and P. Michler. “1.681-eV luminescence center in chemical-vapor-deposited homoepitaxial diamond films”. In: *Phys. Rev. B* **50** (19 Nov. 1994), pp. 14554–14560. DOI: 10.1103/PhysRevB.50.14554. URL: http://link.aps.org/doi/10.1103/PhysRevB.50.14554 (cit. on p. 18).

[261] H. Sternschulte et al. “Uniaxial stress and Zeeman splitting of the 1.681 eV optical center in a homoepitaxial CVD diamond film”. In: *Diamond and Related Materials* **4**.10 (1995), pp. 1189–1192. ISSN: 0925-9635. DOI: 10.1016/0925-9635(95)00298-7. URL: http://www.sciencedirect.com/science/article/pii/0925963595002987 (cit. on p. 19).

[262] D. Stoler. “Equivalence Classes of Minimum Uncertainty Packets”. In: *Phys. Rev. D* **1** (12 June 1970), pp. 3217–3219. DOI: 10.1103/PhysRevD.1.3217. URL: http://link.aps.org/doi/10.1103/PhysRevD.1.3217 (cit. on p. 51).

[263] D. B. Sullivan. “Time and frequency measurement at NIST: the first 100 years”. In: *Frequency Control Symposium and PDA Exhibition, 2001. Proceedings of the 2001 IEEE International*. 2001, pp. 4–17. DOI: 10.1109/FREQ.2001.956152. URL: http://ieeexplore.ieee.org/xpl/articleDetails.jsp?arnumber=956152 (cit. on p. 17).

[264] M. Takeda, H. Ina and S. Kobayashi. “Fourier-transform method of fringe-pattern analysis for computer-based topography and interferometry”. In: *J. Opt. Soc. Am.* **72**.1 (Jan. 1982), pp. 156–160. DOI: 10.1364/JOSA.72.000156. URL: http://www.osapublishing.org/abstract.cfm?URI=josa-72-1-156 (cit. on p. 152).

[265] M. Takeoka and S. Guha. “Capacity of optical communication in loss and noise with general quantum Gaussian receivers”. In: *Phys. Rev. A* **89** (4 Apr. 2014), p. 042309. DOI: 10.1103/PhysRevA.89.042309. URL: http://link.aps.org/doi/10.1103/PhysRevA.89.042309 (cit. on p. 126).

[266] M. A. Taylor and W. P. Bowen. "Quantum metrology and its application in biology". In: *arXiv* (Sept. 2014). arXiv: 1409.0950 [quant-ph]. URL: https://arxiv.org/abs/1409.0950 (cit. on pp. 34, 38).

[267] M. A. Taylor et al. "Biological measurement beyond the quantum limit". In: *Nature Photonics* **7** (3 Mar. 2013), pp. 229–233. DOI: 10.1038/nphoton.2012.346. URL: http://dx.doi.org/10.1038/nphoton.2012.346 (cit. on p. 38).

[268] D. G. Tempel and A. Aspuru-Guzik. "Relaxation and dephasing in open quantum systems time-dependent density functional theory: Properties of exact functionals from an exactly-solvable model system". In: *Chemical Physics* **391**.1 (2011), pp. 130–142. ISSN: 0301-0104. DOI: 10.1016/j.chemphys.2011.03.014. URL: http://www.sciencedirect.com/science/article/pii/S0301010411000905 (cit. on p. 24).

[269] K. S. Thorne, R. W. P. Drever, C. M. Caves, M. Zimmermann and V. D. Sandberg. "Quantum Nondemolition Measurements of Harmonic Oscillators". In: *Phys. Rev. Lett.* **40** (11 Mar. 1978), pp. 667–671. DOI: 10.1103/PhysRevLett.40.667. URL: http://link.aps.org/doi/10.1103/PhysRevLett.40.667 (cit. on p. 105).

[270] M. Tinkham. *Group Theory and Quantum Mechanics*. Dover, 1964. ISBN: 9780486432472 (cit. on p. 19).

[271] G. M. Tino and M. A. Kasevich, eds. *Atom Interferometry*. Vol. 188. Proceedings of the International School of Physics "Enrico Fermi". IOS Press Ebooks, 2014. ISBN: 978-1-61499-447-3 (cit. on p. 5).

[272] F. Treussart et al. "Evidence for intrinsic Kerr bistability of high-Q microsphere resonators in superfluid helium". In: *The European Physical Journal D - Atomic, Molecular, Optical and Plasma Physics* **1**.3 (1998), pp. 235–238. ISSN: 1434-6079. DOI: 10.1007/PL00021556. URL: http://dx.doi.org/10.1007/PL00021556 (cit. on p. 73).

[273] Ulm-IQO. *QuDi*. URL: https://github.com/Ulm-IQO/qudi (cit. on p. 26).

[274] Q. P. Unterreithmeier, E. M. Weig and J. P. Kotthaus. "Universal transduction scheme for nanomechanical systems based on dielectric forces". In: *Nature* **458**.7241 (Feb. 2009), pp. 1001–1004. DOI: 10.1038/nature07932. URL: http://www.nature.com/nature/journal/v458/n7241/full/nature07932.html (cit. on p. 73).

[275] J. A. Vaccaro and A. Joshi. "Position-momentum and number-phase Wigner functions and their respective displacement operators". In: *Physics Letters A* **243**.1 (1998), pp. 13–19. ISSN: 0375-9601. DOI: 10.1016/S0375-9601(98)00187-X. URL: http://www.sciencedirect.com/science/article/pii/S037596019800187X (cit. on p. 16).

[276] J. A. Vaccaro and D. T. Pegg. "Wigner function for number and phase". In: *Phys. Rev. A* **41** (9 May 1990), pp. 5156–5163. DOI: 10.1103/PhysRevA.41.5156. URL: http://link.aps.org/doi/10.1103/PhysRevA.41.5156 (cit. on p. 16).

[277] K. J. Vahala. "Optical microcavities". In: *Nature* **424**.6950 (2003), pp. 839–846. DOI: 10.1038/nature01939. URL: http://www.nature.com/nature/journal/v424/n6950/abs/nature01939.html (cit. on p. 33).

[278] D. Vitali, S. Mancini, L. Ribichini and P. Tombesi. "Mirror quiescence and high-sensitivity position measurements with feedback". In: *Phys. Rev. A* **65** (6 May 2002), p. 063803. DOI: 10.1103/PhysRevA.65.063803. URL: http://link.aps.org/doi/10.1103/PhysRevA.65.063803 (cit. on p. 72).

[279] I. I. Vlasov et al. "Molecular-sized fluorescent nanodiamonds". In: *Nature Nanotechnology* **9**.1 (2014), pp. 54–58. DOI: 10.1038/nnano.2013.255. URL: http://dx.doi.org/10.1038/nnano.2013.255 (cit. on p. 21).

[280] D. F. Walls and G. J. Milburn. *Quantum Optics*. 2nd ed. Springer-Verlag, 2008. ISBN: 978-3-540-28573-1 (cit. on pp. 9, 10, 12, 15).

[281] H. Walther, B. T. H. Varcoe, B.-G. Englert and T. Becker. "Cavity quantum electrodynamics". In: *Reports on Progress in Physics* **69**.5 (2006), p. 1325. URL: http://stacks.iop.org/0034-4885/69/i=5/a=R02 (cit. on p. 77).

[282] C. Wang, C. Kurtsiefer, H. Weinfurter and B. Burchard. "Single photon emission from SiV centres in diamond produced by ion implantation". In: *Journal of Physics B: Atomic, Molecular and Optical Physics* **39**.1 (2006), p. 37. URL: http://stacks.iop.org/0953-4075/39/i=1/a=005 (cit. on p. 18).

[283] G. D. Watkins. "Defects in irradiated silicon: EPR of the tin-vacancy pair". In: *Phys. Rev. B* **12** (10 Nov. 1975), pp. 4383–4390. DOI: 10.1103/PhysRevB.12.4383. URL: http://link.aps.org/doi/10.1103/PhysRevB.12.4383 (cit. on p. 19).

[284] M. J. Weber, ed. *Handbook of Optical Materials*. Laser and Optical Science and Technology Series. CRC Press, 2002. ISBN: 978-0-8493-3512-9 (cit. on p. 27).

[285] C. Weedbrook et al. "Gaussian quantum information". In: *Rev. Mod. Phys.* **84** (2 May 2012), pp. 621–669. DOI: 10.1103/RevModPhys.84.621. URL: http://link.aps.org/doi/10.1103/RevModPhys.84.621 (cit. on pp. 16, 40).

[286] J. Wenger, J. Fiurášek, R. Tualle-Brouri, N. J. Cerf and P. Grangier. "Pulsed squeezed vacuum measurements without homodyning". In: *Phys. Rev. A* **70** (5 Nov. 2004), p. 053812. DOI: 10.1103/PhysRevA.70.053812. URL: http://link.aps.org/doi/10.1103/PhysRevA.70.053812 (cit. on pp. 61, 62).

[287] D. J. Wilson, V. Sudhir, N. Piro, R. Schilling, A. Ghadimi and T. J. Kippenberg. "Measurement-based control of a mechanical oscillator at its thermal decoherence rate". In: *Nature* **524**.7565 (2015), pp. 325–329. DOI: 10.1038/nature14672. URL: http://www.nature.com/nature/journal/v524/n7565/abs/nature14672.html (cit. on pp. 73, 88, 102, 105).

[288] H. M. Wiseman and G. J. Milburn. *Quantum Measurement and Control*. Cambridge University Press, 2014. ISBN: 9781107424159 (cit. on pp. 23, 72).

[289] S. A. Wolf, I. Rosenberg, R. Rapaport and N. Bar-Gill. "Purcell-enhanced optical spin readout of nitrogen-vacancy centers in diamond". In: *Phys. Rev. B* **92** (23 Dec. 2015), p. 235410. DOI: 10.1103/PhysRevB.92.235410. URL: http://link.aps.org/doi/10.1103/PhysRevB.92.235410 (cit. on pp. 17, 18).

[290] W. K. Wootters and W. H. Zurek. "A single quantum cannot be cloned". In: *Nature* **299** (5886 Oct. 1982), pp. 802–803. URL: http://dx.doi.org/10.1038/299802a0 (cit. on p. 106).

[291] J. Worrall. "The pressure of light: The strange case of the vacillating 'crucial experiment'". In: *Studies in History and Philosophy of Science Part A* **13**.2 (1982), pp. 133–171. ISSN: 0039-3681. DOI: 10.1016/0039-3681(82)90023-1. URL: http://www.sciencedirect.com/science/article/pii/0039368182900231 (cit. on p. 72).

[292] X. Xu, M. Gullans and J. M. Taylor. "Quantum nonlinear optics near optomechanical instabilities". In: *Phys. Rev. A* **91** (1 Jan. 2015), p. 013818. DOI: 10.1103/PhysRevA.91.013818. URL: http://link.aps.org/doi/10.1103/PhysRevA.91.013818 (cit. on p. 78).

[293] Y. Yamamoto and H. A. Haus. "Preparation, measurement and information capacity of optical quantum states". In: *Rev. Mod. Phys.* **58** (4 Oct. 1986), pp. 1001–1020. DOI: 10.1103/RevModPhys.58.1001. URL: http://link.aps.org/doi/10.1103/RevModPhys.58.1001 (cit. on p. 51).

[294] A. Yariv. *Quantum Electronics*. 3rd ed. John Wiley & Sons, 1989. ISBN: 978-0-471-60997-1 (cit. on pp. 53, 59, 127, 130).

[295] L. Yong-Chun, H. Yu-Wen, W. C. Wei and X. Yun-Feng. "Review of cavity optomechanical cooling". In: *Chinese Physics B* **22**.11 (2013), p. 114213. URL: http://stacks.iop.org/1674-1056/22/i=11/a=114213 (cit. on pp. 73, 82).

[296] H.-I. Yoo and J. H. Eberly. "Dynamical theory of an atom with two or three levels interacting with quantized cavity fields". In: *Physics Reports* **118**.5 (1985), pp. 239–337. ISSN: 0370-1573. DOI: 10.1016/0370-1573(85)90015-8. URL: http://www.sciencedirect.com/science/article/pii/0370157385900158 (cit. on p. 20).

[297] K. Young. Private communication. Product specialist at *Newport Corporation*. June 2016 (cit. on p. 95).

[298] H. P. Yuen and V. W. S. Chan. "Noise in homodyne and heterodyne detection". In: *Opt. Lett.* **8**.3 (Mar. 1983), pp. 177–179. URL: http://ol.osa.org/abstract.cfm?URI=ol-8-3-177 (cit. on p. 14).

[299] H. P. Yuen. "Two-photon coherent states of the radiation field". In: *Phys. Rev. A* **13** (6 June 1976), pp. 2226–2243. DOI: 10.1103/PhysRevA.13.2226. URL: http://link.aps.org/doi/10.1103/PhysRevA.13.2226 (cit. on p. 51).

[300] A. M. Zaitsev. *Optical Properties of Diamond*. Springer, 2001. ISBN: 978-3-540-66582-3 (cit. on p. 18).

[301] A. M. Zaitsev. "Vibronic spectra of impurity-related optical centers in diamond". In: *Phys. Rev. B* **61** (19 May 2000), pp. 12909–12922. DOI: 10.1103/PhysRevB.61.12909. URL: http://link.aps.org/doi/10.1103/PhysRevB.61.12909 (cit. on p. 17).

[302] H. Zhang et al. "Silicon-Vacancy Color Centers in Nanodiamonds: Cathodoluminescence Imaging Markers in the Near Infrared". In: *Small* **10**.10 (2014), pp. 1908–1913. ISSN: 1613-6829. DOI: 10.1002/smll.201303582. URL: http://dx.doi.org/10.1002/smll.201303582 (cit. on p. 21).

[303] P. Zoller et al. "Quantum information processing and communication". In: *The European Physical Journal D - Atomic, Molecular, Optical and Plasma Physics* **36**.2 (2005), pp. 203–228. ISSN: 1434-6079. DOI: 10.1140/epjd/e2005-00251-1. URL: http://dx.doi.org/10.1140/epjd/e2005-00251-1 (cit. on p. 72).

Related publications

Listed are those publications this thesis is based on.

1. U. Jantzen, A. B. Kurz, D. S. Rudnicki, C. S., K. D. Jahnke, U. L. Andersen, V. A. Davydov, V. N. Agafonov, A. Kubanek, L. J. Rogers and F. Jelezko. "Nanodiamonds carrying quantum emitters with almost lifetime-limited linewidths".

   In: *New Journal of Physics* **18**.7 (2016), p. 073036.

2. C. S., H. Kerdoncuff, U. B. Hoff, H. Fu, A. Huck, J. Bilek, G. I. Harris, W. P. Bowen, T. Gehring and U. L. Andersen. "Quantum enhanced feedback cooling of a mechanical oscillator".

   As of today: Accepted (Nature Communications). Preprint in: arXiv:1605.05949 [quant-ph] (2016).

3. C. S., M. Ježek, T. Gehring and U. L. Andersen. "Phase measurements exhibiting super sensitivity and super resolution features".

   In: Conference on Lasers and Electro-Optics. Optical Society of America, 2016, FF1C.4.

4. C. S. and U. L. Andersen. "Correlated classical states outperform squeezed states in communication over Gaussian channels".

   In: Conference on Lasers and Electro-Optics. Optical Society of America, 2016, JTu5A.28.

5. K. Marshall, C. S. Jacobsen, C. S., T. Gehring, C. Weedbrook and U. L. Andersen. "Practical Quantum Computing on Encrypted Data".

   As of today: Accepted (Nature Communications). Preprint in: arXiv:1607.07372 [quant-ph] (2016).